Author:
Wu, Xun

Title:
Behaviour of pseudo-ductile thin-ply angle-ply laminates under different loading conditions

Behaviour of pseudo-ductile thin-ply angle-ply laminates under different loading conditions

Xun Wu

Bristol Composites Institute (ACCIS)

Department of Aerospace Engineering

Faculty of Engineering

University of Bristol

Bristol, BS8 1TR, United Kingdom

A dissertation submitted to the University of Bristol in accordance with the requirements of the degree of Doctor of Philosophy in the Faculty of Engineering.

September 2018

Word Count: 41475

Abstract

Thin ply angle-ply laminates with central 0° plies, that have previously shown pseudo-ductility in tensile loading, have been experimental investigated under several different load cases. These include open-hole tension, compression, bending, fatigue loading and bearing loading, since the design of carbon fibre composite structures is often limited by their behaviour under these load cases and the failure is often catastrophic in many of these load cases. The behaviour of these laminates under different loadings were found to be significantly affected by a combination of prepreg properties, layups and angles in angle-ply. An overall promising behaviour has been observed, including a reduced notch-sensitivity in open-hole tension, compressive fibre fragmentation, progressive failure in bending via fibre fragmentation in the specific sequences on the tensile and compressive sides of the beam, good fatigue performance in both pristine and damaged specimen and gradual failure in bearing.

Laminates with two different configurations, namely $[\pm 26_5/0]_s$ and $[\pm 25_2/0]_s$, and containing different fibre types, were designed and investigated under unnotched and open-hole tensile loading. Both configurations have shown pseudo-ductile stress-strain responses under unnotched tension, with similar damage mechanisms of 0° ply fragmentation and localised dispersed delamination found in the laminates. In terms of open-hole behaviour, the $[\pm 25_2/0]_s$ laminate has been shown to be less sensitive to the presence of a notch than the $[\pm 26_5/0]_s$ laminate. The fragmentation of the central 0° ply was found to be the main mechanism according to analysis of digital image correlation and X-ray computed tomography. This fragmentation caused stress redistribution around the hole and therefore a reduced notch-sensitivity was achieved.

To achieve pseudo-ductility in compression, a $[\pm 27_7/0]_s$ laminate containing high modulus 0° plies has been designed and tested via a sandwich beam loaded in

four-point bending. The laminate exhibited a pseudo-ductile stress-strain response and gradual failure in compressive loading. The compressive fibre fragmentation in the central 0° plies, and inhibition of delamination at the 0/-27 interface using thin ply prepreg contributed to the progressive failure.

The $[\pm 27_7/0]_s$ laminate has also shown a non-linear load-displacement response and progressive failure under flexural loading. Fragmentation has been observed in both the compressive and tensile sides of the beam, where fragmentation of the central 0° plies and localised dispersed delamination on the tensile side slowed down damage accumulation on the compressive side and achieved this gradual failure.

The three laminates used previously have been tested under tension-tension fatigue loading to investigate their fatigue life and damage progression. 80% of the laminate "yield" stress has been found to be the maximum stress level that these laminates can operate without a stiffness loss up to 1×10^6 cycles. For the overloaded specimen with fractured 0° ply fibres under fatigue loading, delamination dominated damage was seen in these laminates and a comparison between each laminate was presented.

A preliminary study of the bearing behaviour of thin ply angle-ply laminates has been conducted via single- and double-bolted laminate joint configurations. Gradual failure has been exhibited in all tested laminates, which is attributed to the absence of delamination in thin ply laminates, allowing compressive damage, such as fibre microbuckling of standard modulus fibre in 0° plies, and fibre fragmentation of the high modulus fibre in 0° plies, which propagated gradually to the adjacent plies in the out-of-plane direction and multiple out-of-plane kink-bands were formed.

Acknowledgements

I would like to thank my supervisor Prof. Michael Wisnom and Dr. Jonathan Fuller, for their patient guidance, supervision, and sharing of their knowledge and experience with me during the study.

I also want to thank Prof. Paul Weaver for offering me the opportunity to be a part of the CDT programme and Sarah Hallworth for her support in the past years.

Thanks also to Ian Chorley, Guy Peam, Peter Whereat, Ian Milnes for their help and advice in the lab, and Dr. Oliver Nixon-Pearson and Dr. Yusuf Mahadik for their help on performing the X-ray computed tomography, and Dr. Bing Zhang, Dr. Mohamad Fotouhi, Dr. Hana Yu and Putu Suwarta for their daily based help.

Special recognition should be given to Jamie Hartley, whom provided me significant help on improving my English writing in the past four years, Dr. Marco Longana, whom provided me constant support on experimental work and Dr. Thomas Pozegic, whom helped me on performing Differential Scanning Calorimetry.

Lastly, I would like to give the special and biggest thank you to my dearest mum and dad, for their unconditional love and support.

This work was funded by the ACCIS Centre for Doctoral Training in Advanced Composites (grant number EP/G036772/1) and under the UK Engineering and Physical Sciences Research Council (EPSRC) Programme Grant EP/I02946X/1 on High Performance Ductile Composite Technology in collaboration with Imperial College, London.

Bristol, September 21, 2018

Authors Declaration

I declare that the work in this dissertation was carried out in accordance with the requirements of the University's Regulations and Code of Practice for Research Degree Programmes and that it has not been submitted for any other academic award. Except where indicated by specific reference in the text, the work is the candidate's own work. Work done in collaboration with, or with the assistance of, others, is indicated as such. Any views expressed in the dissertation are those of the authors.

Bristol, September 21, 2018

_____

Xun Wu

Publications

Journal Article

[1] Wu X, Fuller JD, Longana ML, Wisnom MR. Reduced notch sensitivity in pseudo-ductile CFRP thin ply angle-ply laminates with central 0° plies. Compos Part A Appl Sci Manuf 2018;111. doi:10.1016/j.compositesa.2018.05.011.

Conference Papers:

[2] Wu X, Fuller JD, Wisnom MR. Open-hole response of pseudo-ductile thin-ply angle-ply laminates. In: Proceeding of the 17th European Conference on Composites Materials., Munich, Germany, 26-30th June, 2016.

[3] Wu X, Fuller JD, Wisnom MR. Combining the non-linearity of angle-plies and fibre fragmentation in carbon fibre laminates under compressive loading. In: Proceeding of the 21st International Conference on Composites Materials., Xi'an, China, 20-35th August, 2017.

[4] Wu X, Fotouhi M, Fuller JD, Wisnom MR. Bearing failure of pseudo-ductile thin ply angle-ply laminates. In: Proceeding of the 18th European Conference on Composites Materials., Athens, Greece, 25-28th June, 2018.

List of Figures

List of Tables

Table of Contents

1. Introduction

1.1 Background

Carbon fibre reinforced plastic composites (CFRPs) have been used extensively in recent years. They offer better specific strength and stiffness, as well as improved corrosion resistance and structural efficiency, compared to more traditionally used metallics such as aluminium which are commonly used in lightweight structures. The design of carbon fibre composites can be tailored to meet the specific requirements in different applications via changing stacking sequences or constituent materials. Consequently, the mechanical properties and damage mechanisms vary for different designs. A thorough understanding of composite behaviour when subjected to different loading conditions is crucial to design composite structures.

There is a broad range of applications for carbon fibre composites, from high performance applications to commercial goods. One of the major applications of carbon fibre composites is in commercial aircraft. More than 50% of the weight in the most recent generation of aircraft, the Boeing 787 [5] and Airbus A350 XWB [6] are carbon fibre composites and the use of CFRPs reduces fuel consumption by up to 25%. It is also worth noting that composites have been used in primary structures such as wings and fuselage sections in these two aircraft. In other innovation projects, carbon fibre composites also play an important role in primary loaded structures, such as in the Interplanetary Transport System launch vehicle and the Interplanetary Spaceship developed by SpaceX [7].

Because of the high cost of carbon fibre composites, applications used to be primarily focused on the high-end aerospace industry or high-performance automobile racing. Nowadays, applications are spreading into wider industry sectors, such as oil storage, wind energy, infrastructure and sports goods. CFRPs have shown many advantages such as weight savings, design flexibility and structural efficiency. However, compared with most metals, structures made from carbon fibre often fail suddenly and catastrophically. This requires a larger safety margin when designing a structure with carbon fibre composites, which could reduce the effectiveness of the

design and material usage. For example, Figure 1.1(a) presents an example showing different failures of metal and CFRP bicycle frames. Considering a bicycle crash, carbon fibre frames can snap in half catastrophically. On the contrary, a metal bicycle frame only undergoes plastic deformation and bending, without complete fracture. It is also found that the carbon fibre structures can fail suddenly, without any warning or visual inspected damage, which requires more complex maintenance and inspection. In addition, from a comparison between the stress-strain behaviour of quasi-isotropic CFRPs and aluminium as shown in Figure 1.1(b), the plastic deformation and progressive failure can allow a higher energy absorption in ductile material such as aluminium than brittle material such as CFRP, indicating the beneficial of ductility in application of crashworthiness.

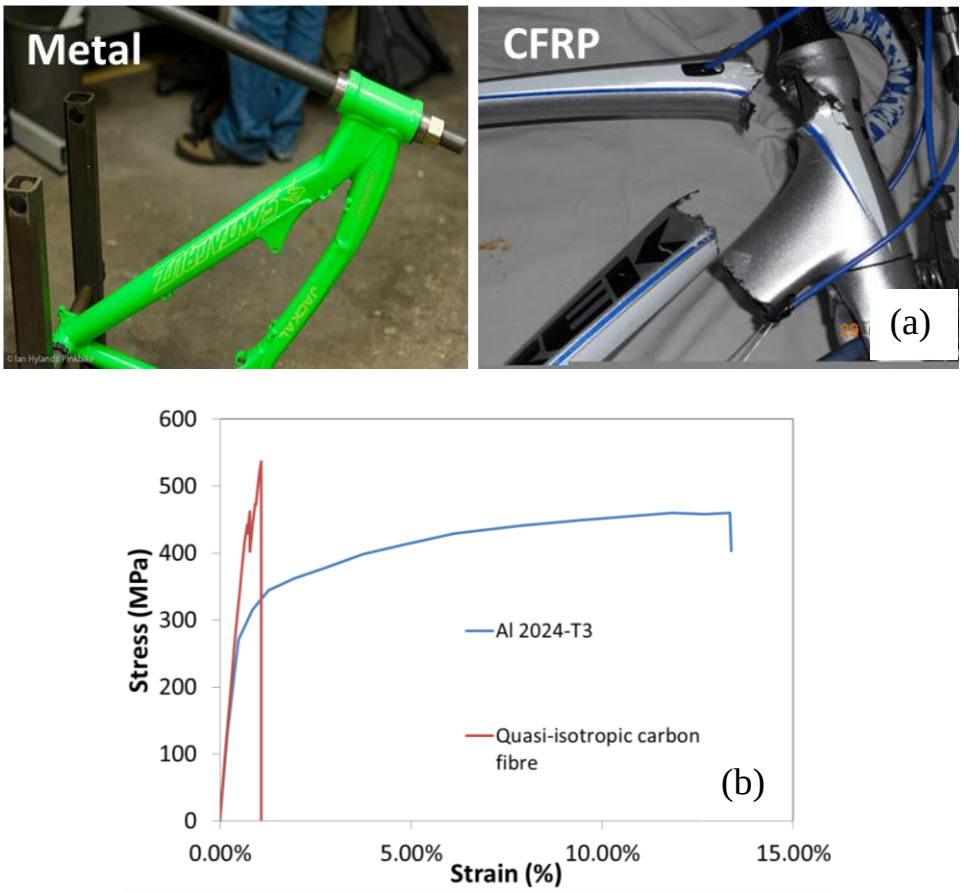

Figure 1.1: (a) An example showing the advantage of ductility: a metal bike frame underwent plastic deformation and a carbon fibre frame snapped into several parts. (b) the typical stress-strain curves for quasi-isotropic carbon fibre composites and aluminium 2024 T3.

To overcome the "inherent" brittleness of carbon fibre composites and to achieve gradual failure, several different approaches have been developed under the High Performance Ductile Composites Technology (HiPerDuCT) programme [8,9]. Three distinct themes, including a fibre reorientation concept, an aligned fibre and interfacial modification concept and ductile constituents concept have all been investigated and ductility/pseudo-ductility has been achieved using these approaches. In the fibre reorientation approach, a significant amount of pseudo-ductility has been obtained in angle-ply laminates, when using thin ply prepregs for all plies. For example, a $[\pm 25]_{ns}$ laminate made from thin ply prepreg (t = 0.03 mm) exhibited highly non-linear stress-strain behaviour in tension and achieved a pseudo-ductile strain of 1.23% (defined as the difference between the strain at the ultimate stress and at a point on the initial modulus line at the ultimate stress) as well as an ultimate stress of 927 MPa [10]. Incorporating the non-linearity of angle-ply laminates with central 0° plies, a metal-like tensile stress-strain response has been exhibited in these laminates, with an enhanced initial modulus, strains and strength [11]. Figure 1.2 shows a typical stress-strain response of the pseudo-ductile $[\pm 26_5/0]_s$ laminate. Delamination suppression of thin plies enables this response to be achieved by several distinct damage mechanisms such as progressive multiple fibre fracture (fragmentation) of the central 0° plies and localised dispersed delamination at the 0/-θ interfaces.

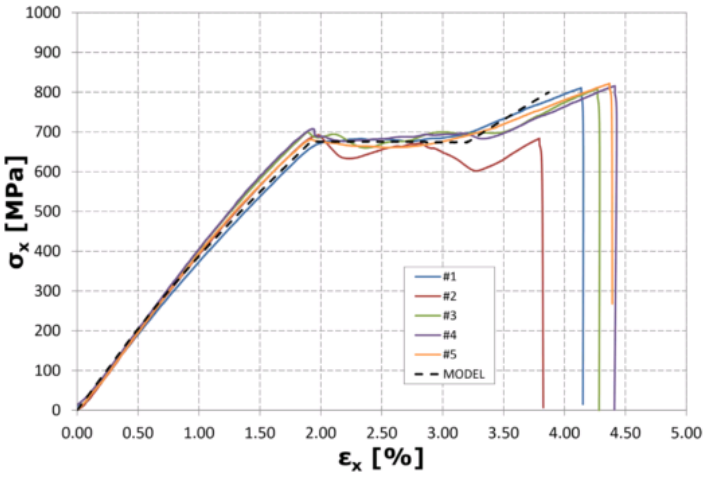

Figure 1.2: Metal-like stress-strain curves for $[\pm 26_5/0]_s$ laminates [11].

The definition of pseudo-ductility and other key measures, as used in the HiPerDuCT programme and in the current work, are presented in Figure 1.3. Two different stress-strain curves were considered here. Figure 1.3 (a) presents a stress-strain curve with a smooth transition between the elastic and non-linear region. In this condition, the "yield" stress, σ_Y is defined as the stress at the intersection between a straight line offset from the initial modulus by a strain of 0.1%, and the laminate stress-strain curve. The corresponding strain at this point is defined as the "yield" strain ε_Y. In another case presented in Figure 1.3 (b), a clear "knee" point can be seen between the elastic and the non-linear regions. The stress and strain at the knee point are selected as the "yield" stress σ_Y and the "yield" strain ε_Y. The definition of the pseudo-ductile strain, ε_d is the same in both cases, which is defined as the difference between the strain at the ultimate stress and at a point on the initial modulus line at the ultimate stress.

So far, the exploration of pseudo-ductile thin ply angle-ply laminates has primarily focused on tensile loading. To progress these laminates to a wider range of applications, their behaviour under different loading cases needs to be understood. The aim of the current work is to further investigate pseudo-ductile thin ply angle-ply laminates and to exploit their pseudo-ductility in different loading cases.

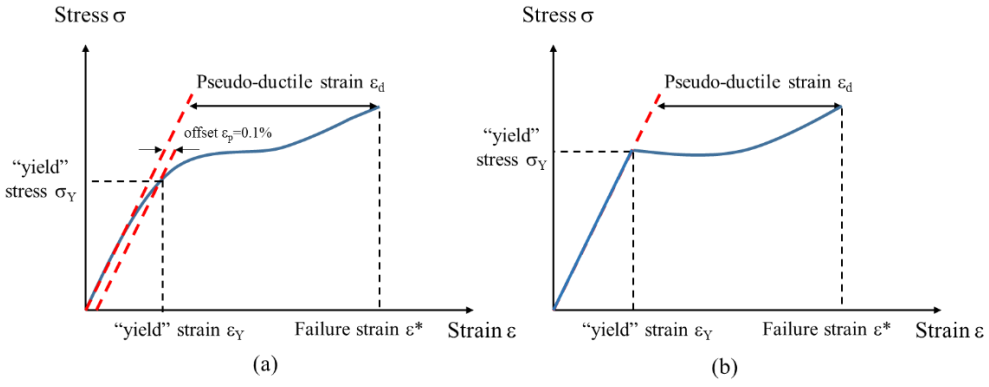

Figure 1.3: Definition of pseudo-ductile strain and other key parameters.

1.2 Summary, research scope and thesis outline

The overall aim of this PhD thesis is to understand the behaviour of thin ply angle-ply laminate with central 0° plies under different loading condition. More specifically, the following objectives are fulfilled in the present work:

- Explore in further detail thin ply angle-ply laminates with central 0° plies under static tensile loading.
- Investigate the notch-sensitivity of thin ply angle-ply laminates with central 0° plies under tensile loading.
- Explore pseudo-ductility and gradual failure of thin ply angle-ply laminates in compressive loading.
- Investigate the flexural performance of laminates with non-linear pseudo-ductile tensile and compressive behaviour.
- Investigate the fatigue life of pseudo-ductile thin ply angle-ply laminates with central 0° plies, as well as to understand the damage progression and accumulation under cyclic loading.
- Design and investigate the progressive failure in bearing loading and to understand the mechanisms of single- and double-bolt jointed laminates.

Extensive work has been carried out to fulfil the objectives above and has been presented in the following chapters:

Chapter 1 presents a background of composite materials and pseudo-ductility in carbon fibre composites.

Chapter 2 reviews several loading cases which are critical in the design of pseudo-ductile thin ply angle-ply laminates.

Chapter 3 covers an experimental and numerical investigation of thin ply angle-ply laminates under open-hole tensile loading. Detailed analysis is conducted via several different techniques and the notch sensitivity is discussed.

Chapter 4 investigates the pseudo-ductility under compressive loading using thin ply angle-ply laminates with central 0° plies. A novel compression test method via a

sandwich beam is used. Post-failure analysis is conducted to understand the damage mechanism governing the progressive compression failure.

Chapter 5 further explores the flexural behaviour of thin ply angle-ply laminates with central 0° plies. The layups selected in this study have shown pseudo-ductility in tension and compression according to the previous chapters. Assessment of the damage initiation and development are also conducted to provide information for designing the laminates to fail progressively.

Chapter 6 investigates the operation limits and fatigue life of pseudo-ductile thin ply angle-ply laminates with three different layups. In addition, the damage progression under cyclic loading is conducted through "pre-fractured" fatigue testing.

Chapter 7 describes further work on experimentally characterising the bearing strength and damage evolution within pseudo-ductile thin ply angle-ply laminates subjected to bearing loading and a method to compare bearing performance between two different pseudo-ductile laminates.

Chapter 8 concludes all the key findings from the previous chapters and presents possible future works.

2 Literature Review

2.1 An overall review of pseudo-ductile laminates

Up to now, a number of different approaches have been developed in order to achieve ductility in carbon fibre laminates, such as introducing ductile constituents, or by re-designing the architectures of carbon fibre laminates. Examples include using the extra strain generated from fibre reorientation [10–12] or making hybrid composites via either interlayer hybrids [13–20] or intermingled hybrids [21–23]. In the present study, the focus is mainly on re-designing the architectures of carbon fibre laminates.

The hybrid composites concept can be traced back to the 1970s [24] and has regained much interest in recent years. Early research on hybrid composites has shown that by hybridising two or more fibre types into a single composite, the advantages of each fibre type were retained with additional benefits. One of the main advantages is enhancement in failure strain of hybrid laminates. When testing a composite comprising both low elongation (LE) and high elongation (HE) fibres, it was found that failure would not necessarily occur at the fracture point of the LE fibre, and showed a progressive failure [25].

As a typical example of LE and HE fibre hybrid composites, carbon fibre – glass fibre hybrid composites have been studied extensively. Aveston and Kelly carried out several investigations on intermingled carbon/glass fibre epoxy hybrid composites [26]. They found that once the types of carbon and glass fibres are fixed, the behaviour of these hybrid composites is significantly determined by the fraction of glass and carbon fibres – a single fracture occurred if the amount of glass fibre was insufficient to sustain the stress at the first carbon fibre fracture. Increasing the glass content to a specific transition point resulted in multiple fractures being observed in the low elongation carbon fibre, resulting in a higher failure strain of the hybrid composite compared to an exclusively carbon fibre composite. Similar observations have also been found in interlayer hybrid composites. In interlayer hybrid composites, instead of single fibre bundle fracture, single- or multiple- fibre fractures were found across the entire width of the laminate. Again, the performance of these are determined from the glass and carbon layer fraction, and a gradual failure

without severe stiffness loss or load drop would be ideal. In the study presented by Bunsell and Harris [24], or Manders and Bader [27], for hybrid laminates with thicker carbon layers, an obvious load drop followed the first carbon layer fracture, whilst a more gradual stress-strain curve was seen in the hybrid laminate with thinner carbon layers. In addition, in these studies on hybrid composites, a so called "hybrid effect" has been reported. A clear point of the "hybrid effect" is that the tensile fracture strain of low elongation fibres in a hybrid specimen was found to be higher than the conventional unidirectional (UD) tensile testing. In addition, they found that the thinner the LE plies are or well dispersed the fibres are, the higher failure strain is.

Inspired by this, further investigations on interlayer glass-carbon hybrid laminates were carried out to design pseudo-ductile carbon fibre composites. Czel et al. successfully demonstrated pseudo-ductility in carbon fibre laminates, by hybridising glass fibre prepreg with carbon fibre prepreg [13–20,28,29]. It is worth noting that the thin ply prepregs with nominal ply thickness of 0.03mm were used in the central UD carbon layer. They found that the performance of the [$Glass_m$/$Carbon_n$/$Glass_m$] hybrid laminates was significantly reliant on the relative thickness of the carbon layers to the total glass layers [13]. In a hybrid laminate [$Glass_2$/$Carbon_n$/$Glass_2$], the laminate failed in the desired pseudo-ductile manner with a clear pseudo-yield point when there was 1 or 2 layers of carbon in the centre. When the number of carbon layers increased to 3 and 4, the specimen showed a minor load drop after the initial elastic region, followed by a stress plateau or a significant load drop due to unstable delamination. These observations are similar to the stress-strain behaviour of the hybrid laminates that have been mentioned previously. In terms of damage mechanisms and final failure modes, multiple fractures (fragmentation) uniformly distributed in the carbon layers have been observed in the laminates with 1 and 2 carbon plies and localised delamination have been seen. When the number of carbon plies increased to 3 and 4, the damage changed to delamination dominated failure. The different behaviour is caused by the different energy release rate as the thinner carbon layers release lower energy. These observations confirm the importance of using thin carbon plies – since there is a clear

shift of the damage mechanisms and failure modes between different carbon thicknesses.

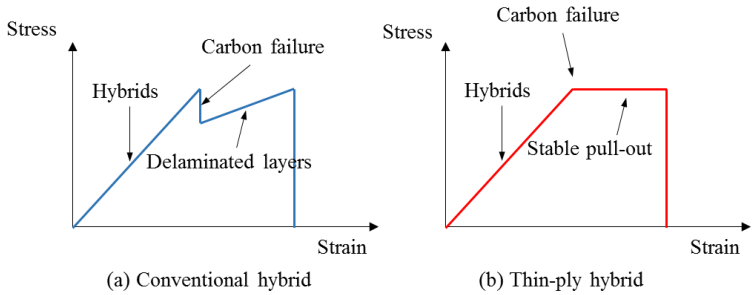

Figure 2.1: Schematic of the stress-strain curves of hybrid laminates with (a) conventional thickness ply and (b) thin ply in the carbon layer [13]. Note: the present curves only represent the shape of stress-strain curves for each laminate. A sudden load drop in stress is observed in the conventional hybrid and a stable transition is observed in thin-ply hybrid.

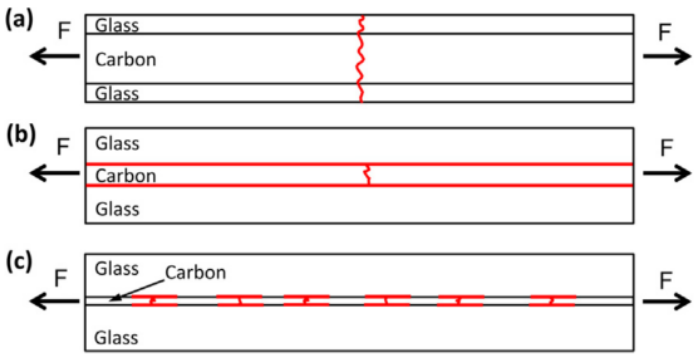

Figure 2.2: Possible failure modes of UD glass/carbon hybrid laminates, where (a) (b) shows catastrophic failure and (c) shows pseudo-ductile behaviour [13].

To understand and predict pseudo-ductility in hybrid laminates, Jalavand et al. have developed numerical and analytical models to analyse pseudo-ductile glass/carbon thin-ply UD hybrid composites [16–18]. In the numerical approach, they modelled the full damage process, such as fragmentation in the carbon layers and dispersed delamination with the assistance of cohesive elements. The results have been found to be in good agreement with the experimental stress-stress behaviour. More hybrid layups have been analysed and a so called “damage mode map” has been developed with the axes of absolute and relative carbon thicknesses.

The “damage mode map” defines the boundaries between four distinct regions – carbon fragmentation, fragmentation and localised delamination, single delamination and glass failure. Since using a numerical model to produce the “damage mode map” was computationally expensive, an analytical method was proposed. In this approach, several distinct sections of the stress-strain curve were modelled. The first failure was assumed to be the fracture of the carbon layers since there is no stress variation along the fibre direction in the linear region, followed by three possible damage modes including fragmentation in the carbon layers, delamination propagation at the carbon/glass interfaces and failure of the glass plies. The stress-strain curves and failure strain for several S-glass/carbon hybrid combinations predicted from this analytical model have shown a good agreement with the experimental results. The glass/carbon combination showing the optimised pseudo-ductile behaviour has been found to be the [S-glass/C_2/S-glass]. It achieved a pseudo-ductile strain of 1.0% whilst retaining a “yield” stress of 1130 MPa. In addition, a generally better performance of the S-glass/carbon hybrid compared to the E-glass/carbon hybrid has shown that the enhanced properties of glass layers increased the overall laminate performance.

With the assistance of the “damage mode map” as shown in Figure 2.3, and analytical predictions, a more comprehensive study was carried out on the S-glass sandwiched between a series of different carbon fibre layers, including standard, high and ultra-high modulus fibres [14]. There is a trade-off between the initial modulus, the “yield” stress and pseudo-ductile strain when designing pseudo-ductile hybrid laminates. All the configurations tested in this study have achieved pseudo-ductile strains between 0.8% and 2.6%, initial modulus between 50 GPa and 125 GPa and “yield” stresses between 500 MPa and 1400 MPa.

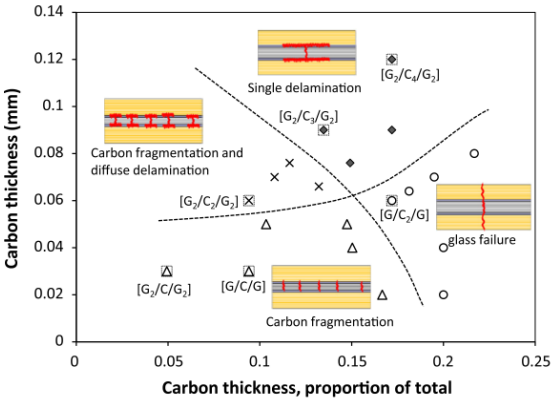

Figure 2.3: A typical example of a damage mode map for glass/carbon hybrid laminates [18].

2.2 Pseudo-ductility of thin ply angle-ply laminates

The method of using thin-ply UD glass-carbon hybrids to achieve gradual failure has been extended to all-carbon thin ply angle-ply carbon fibre laminates as many industrial applications demand it. In addition, a higher proportion of thin angle-plies can enable much greater design flexibility. The high strain to failure makes these thin ply angle-ply laminates a good replacement for the high strain material – the glass fibre plies in the hybrid glass/carbon case [10–12,30].

Much of the early work on angle-ply laminates has shown significant fibre re-orientation and a much higher strain to failure compared to UD laminates, particularly for ±45° laminates [31,32]. The failure strain of these ±45° laminates has been found to be more than 20%, which is desirable for use as a replacement of the high strain material in hybrid glass/carbon laminates [31]. However, one of the major drawbacks was its low initial modulus and strength, which were only 15 GPa and 375 MPa respectively. This limits the overall mechanical performance of pseudo-ductile thin angle-ply laminates. Therefore, Fuller et al. has focused on reducing the angle selections in angle-ply laminates, for example achieving an initial modulus of 80 GPa and strength of 1300 MPa in a ±22.5° laminate [10].

A series of works have been done in order to understand the behaviour and damage mechanisms governing angle-ply laminate failure [33–40]. Xu et al. tested

two types of $[+20_m/-20_m]_{ns}$ laminates (where m = 1, 2 and n = 8, 4) in tension experimentally and numerically [33]. A 57% increase in strength was achieved in the laminates when reducing the thickness of blocked plies, and edge delamination in the angle plies was delayed. This observation is similar to the early research on effect of the ply thickness on edge delamination and transverse cracking performed by Crossman et al. [36]. Inspired by this, Fuller and Wisnom have decided to use commercially available thin ply prepregs to replace the standard thickness ply prepreg in angle-ply laminates to achieve a better stress and strain performances in thin ply angle-ply laminates.

Thin ply prepreg is manufactured from a breakthrough new technique called spread-tow technology, first introduced by Kawabe et al. in 1997 [41] and then further developed to industry scale in composite materials in 2008 [42]. This technique enables a uniform spreading of fibre tows of sizes from 3K to 24K whilst minimising the fibre damage. Thus far, several companies can manufacture thin ply prepreg including the North Thin Ply Technology (NTPT), SK Chemical, Chomarat and the Nippon Graphite Fibre Corporation. Due to the potential benefits such as damage reduction and better design capability using thin ply prepreg, many investigations have been carried out based on these fairly new materials [43–63]. As the thickness of thin ply materials is small, to maintain the thickness requirement of structures, a large number of plies will be required, resulting in an increase of the labour and time. In addition, expensive manufacturing processes for thin ply prepregs make them a significantly more expensive option compared to regular materials

As one of the first studies on thin ply laminates, Sihn et al. have tested two different laminates named THIN and THICK, where the THIN and THICK laminates were made from prepregs with nominal ply thicknesses of 0.04 mm and 0.2 mm respectively [47]. All the laminates used QI layups and were tested in several different load cases such as unnotched tension, open-hole tension, impact and fatigue loading. In the unnotched tensile testing, they found that the THIN laminate exhibited a 10% higher strength than the THICK laminate. In addition, when the unnotched specimens were loaded in fatigue, the THIN specimens showed less than

5% reduction in both the modulus and residual strength after 50,000 cycles, whilst the THICK specimens showed a reduction up to 17% for the same applied peak stress. Also, X-ray images revealed that micro-cracks and edge-delaminations observed in the THICK laminate, were suppressed in the THIN laminate. All these experimental observations gave a good indication that when using thin prepreg, the micro-cracking and edge delamination can be suppressed in the carbon fibre laminates, as well as increasing the damage onset stress.

More in-depth investigations covering thin ply laminates or thickness scaling by using thin ply prepreg have been carried out [34–37,39–41, 42, 44, 49–53]. Yokozeki et al. have tested QI laminates with thin ply prepreg (75 gsm) and standard thickness ply prepreg (145 gsm) in static tension, tension-tension fatigue, CAI and compression testing and superior characteristics have been found in thin ply laminates in all these loading cases [49]. For example, under static tensile loading, laminates with thinner plies have shown a 20% higher strength compared with thicker plies, as well as fewer accumulated matrix cracks, which is in good agreement with the results presented by Sihn et al. [47]. Under compression loading, the compressive strength has shown a 16% increase in thin ply laminates compared with laminates with standard thickness plies. The increase in strength was attributed to a notable increase in the compressive stability of thin ply laminates. In all other work focusing on thin ply prepreg, either using thin non-crimp fabric (Chomarat C-ply [45,60] and TeXtreme [58,59]) or ultra-thin prepreg (NTPT prepreg [43,53]), the damage mechanisms such as matrix cracking and delamination were suppressed, and a better performance in terms of failure stress and strain was achieved in all these laminates. Using thin ply prepreg to replace the standard thickness ply in angle-ply laminates produces a promising non-linear stress-strain performance, higher failure strains and enlarges the design space in these laminates [63].

The studies as mentioned above have shown the potential to achieve a better non-linearity in angle-ply laminates using thin ply prepregs, as the premature failure of angle-ply laminates due to matrix cracking and delamination can be avoided. Fuller et al. have investigated thin ply angle-ply carbon fibre laminates with angles varying from 15° to 45° under static tension [10]. The material chosen for this study

was Skyflex USN020A carbon fibre/epoxy prepreg with a ply thickness of 0.03mm, consisting of Mitsubishi Rayon TR30 carbon fibre and SK chemical K50 120°C curing resin. As shown in Figure 2.4, highly non-linear stress-strain behaviour has been achieved in all these angle-ply layups. Since the $[\pm 45_5]_s$ laminate showed a low initial modulus and strength and the $[\pm 15_5]_s$ laminate showed very limited non-linearity, the primary interests were focused on the $[\pm 20_5]_s$, $[\pm 25_5]_s$, and $[\pm 30_5]_s$, laminates. The $[\pm 25_5]_s$ laminates showed a pseudo-ductile strain of 1.23% as well as a failure stress of 927 MPa. The $[\pm 30_5]_s$ laminates have a slightly lower failure stress, but the pseudo-ductile strain is more than twice that of the $[\pm 25_5]_s$ laminates. Free-edge delamination was completely suppressed in each of these thin angle-ply laminates. The absence of edge delamination enabled higher failure strains in the angle-ply laminates, as well as allowing other mechanisms, e.g. fragmentation in carbon layer as observed in [15], to develop within the laminates.

Fuller et al. further investigated thin ply angle-ply laminates via an analytical method, taking into account the large amount of fibre rotations and matrix plasticity that was observed in the experiment [12]. This method used an orthotropic plasticity model developed by Sun and Chen [64], as well as taking into account fibre rotation. A unit cell of the thin angle-ply laminates has been defined in a micromechanical model with orthotropic linear-elastic fibre properties and isotropic elastic-plastic matrix properties following the von Mises J_2-flow rule. The analytical tensile stress-strain response of $[\pm\theta_5]_s$ laminates with different angles was shown to have a good agreement with experimental results in the region lower than 2%, and only showed a slightly stiffer behaviour in the high strain region compared to the experimental results. A parametric study on parameters governing pseudo-ductility suggested that $[\pm 26_5]_s$ and $[\pm 27_5]_s$ laminates show the most promising pseudo-ductile behaviour. The result has shown that even 1° difference in ply angles brought notable differences in overall behaviour. For example, the pseudo-ductile strains for the $[\pm 26_5]_s$ and $[\pm 27_5]_s$ laminates are 1.2% and 1.47% respectively. Similar modelling work on thin angle-ply laminates can also been found in [65].

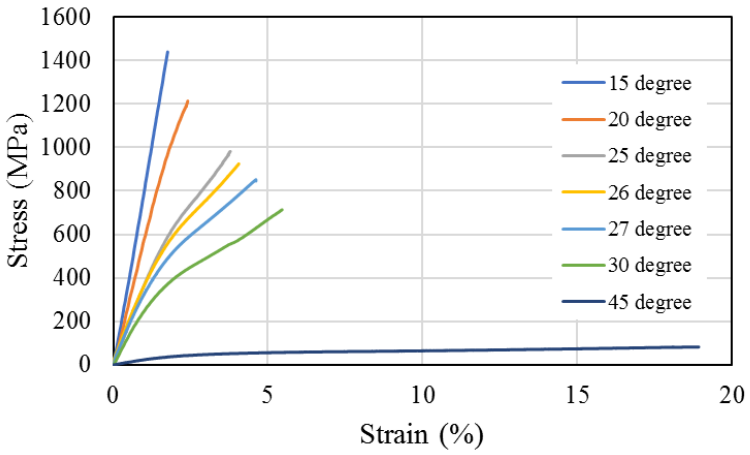

Figure 2.4: Experimental longitudinal stress-strain curves of $[\pm\theta]_n$ angle-ply laminates with angles vary between 15° and 45°. All the laminates were made of Skyflex USN020 TR30 carbon fibre prepreg with nominal ply thickness of 0.03 mm. The figure is reproduced from [10].

As pseudo-ductility and high strain to failure have been demonstrated experimentally and analytically in thin ply angle-ply laminates, these laminates have been found to be a good substitute for the glass plies in glass/carbon hybrid composites. Using thin ply prepreg in angle plies, damage has been suppressed as well as providing a larger design space. Fuller et al. have combined the analytical model for thin angle-ply laminates with the analytical model for pseudo-ductile UD hybrid laminates [18], to predict the stress-strain behaviour and failure modes of $[\pm\theta_n/0_m]_s$ laminates [11].

Similarly to the pseudo-ductile glass/carbon hybrid laminates, three distinct damage modes have been modelled in the $[\pm\theta_n/0_m]_s$ laminates, including fibre fracture/fragmentation of the central 0° plies, dispersed delamination at the 0/-θ interfaces localised to the fracture surfaces and the failure of the angle plies. The first major damage predicted to occur in the model is the fracture of the central 0° plies, once the fracture strain of the 0° ply fibre has been reached. If the angle plies adjacent to the 0° plies are strong enough, fibre fragmentation occurs. In addition, a Mode-II delamination at the 0/-θ interface has been considered in the model. The last failure mode considered in the model is failure of the angle plies, which resulted in the final failure of the laminate.

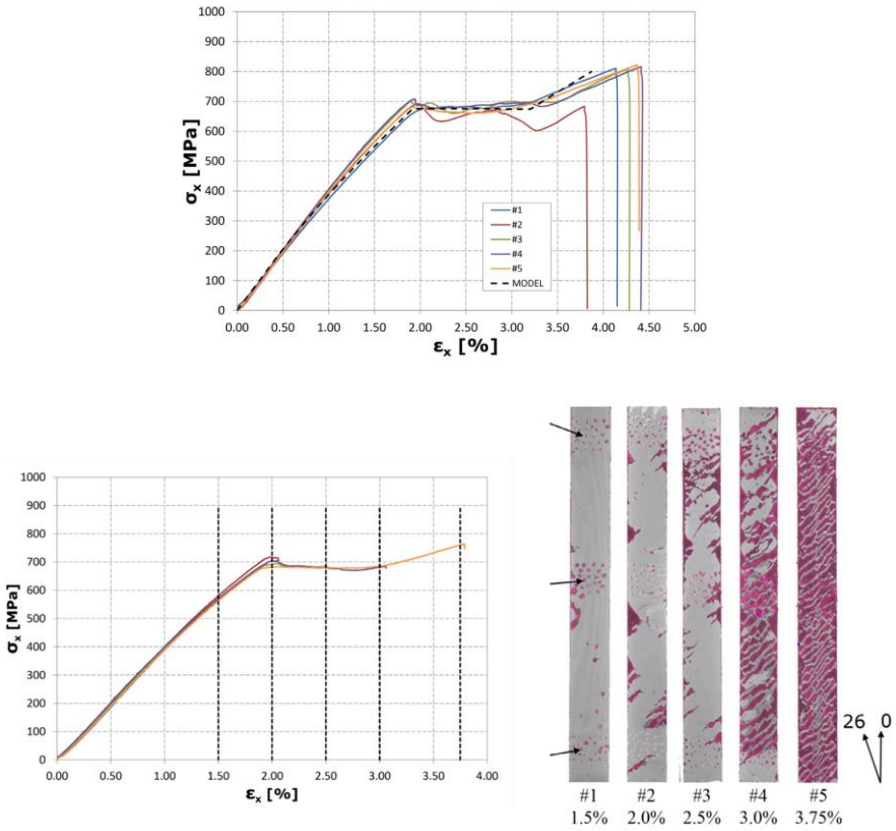

Figure 2.5: The tensile stress-strain curve and damage evolution for the $[\pm 26_5/0]_s$ laminate. The black dashed-line represents the modelling results from the same laminate. In the bottom image, the dye penetrant reflections are shown in the pink colour and suspected to be damage [11].

Laminates made from the same Skyflex USN020A prepreg with several different layups have been simulated in the model, and two of the layups - $[\pm 26_4/0]_s$ and $[\pm 26_5/0]_s$ - have been found to show good pseudo-ductile behaviour and have been tested for model validation. In the analytical prediction, the $[\pm 26_4/0]_s$ and $[\pm 26_5/0]_s$ laminates have exhibited pseudo-ductile strains of 2.01% and 1.91% respectively. In the experimental validation, all specimens from the batch of $[\pm 26_5/0]_s$ layup have shown stress-strain behaviour that is similar to the analytical prediction, exhibiting an averaged pseudo-ductile strain of 2.2% and a "yield" stress of 692 MPa. However, the $[\pm 26_4/0]_s$ layup has shown large discrepancies in the experimental results – only two specimens have shown pseudo-ductility and the rest

of them failed catastrophically at the fibre fracture strain. X-ray analysis indicated that the early failure was due to the premature failure of the angle plies, due to the localised stress being close to the strength of the angle plies. One extra pair of angle plies avoided this problem and gave a more conservative design. Figure 2.5 presents the stress-strain curve and damage evolution in the $[\pm 26_5/0]_s$ laminate. This analytical model has shown sufficient accuracy to predict the behaviour of $[\pm\theta_n/0_m]_s$ laminates made from different materials, stacking sequences and ply orientations.

Pseudo-ductility and unique damage mechanisms have been found in these thin ply angle-ply laminates with central 0° plies in tension. To progress these laminates to real applications, their behaviour in more complex loading cases needs to be understood, particular for critical loading cases that might result in premature or catastrophic failure. In this work, the following load cases – open-hole tension, compression, bending, tension-tension fatigue and bearing – are the main focuses of the present work, and their background will be presented in the following sections.

2.3 Open-hole loading of CFRP laminates

The open-hole behaviour of these pseudo-ductile thin ply angle-ply laminates needs to be understood since the presence of stress concentrations can lead to significant strength reduction and catastrophic failure. Limited work has been reported on the open-hole response of pseudo-ductile laminates [28,66,67].

Several studies have been carried out to investigate the factors and damage mechanisms that related to the notched strength of the laminates. The strength of a notched laminate is related to a variety of intrinsic and extrinsic factors, including hole size and geometry, ply thickness, laminate size, stacking sequences, material constituents, the quality of machining and some interactions between these factors [68–79].

In all these investigations, notch sensitivity has been found to be related to the damage growth within the laminate prior to final failure. Harris and Morris have tested a number of quasi-isotropic (QI) $[0/\pm 45/90]_{ns}$ laminates and cross-ply $[0/\pm 45]_{ns}$ laminates with different numbers of sub-laminates to examine the role of

delamination on the notched strength [79]. The results indicated that the strength of the $[0/\pm45/90]_s$ laminates decreased with the increasing number of sub-laminates. According to the radiographs of crack-tip damage, the decrease in the $[0/\pm45/90]_{ns}$ laminates is due to the smaller damage zone at the crack-tip in the laminate with more sub-laminates and less stress relief in the laminates. The strength of the $[0/\pm45]_{ns}$ laminates increased with the increasing number of sub-laminates, as the blocks of delamination at the +45/-45 interface have been prevented in the thicker laminates. This allowed fibre fracture and splitting developed in all plies and stress redistribute next to the notch.

In order to understand the relation between different types of damage and notched strength, Kortschot and Beaumont conducted a series of tensile tests on notched cross-ply laminates and employed an X-ray technique to monitor damage in the specimen [69,78]. All the specimens have been categorised into three batches by different ratios of total notch length to specimen width: 0.125, 0.25 and 0.5. Similar damage patterns, such as 0° ply splitting, transverse ply cracking and delamination at the 0/90 interfaces, have been observed in X-ray images from all three batches. They have measured the length of splitting and the base length of delamination and then linked these two parameters to the strength of the specimens. They concluded that the strength of these cross-ply specimens increased with the increase of splitting length since 0° plies splitting can redistribute the stress at the tip of the notch and have a significant influence on the notched strength of the laminate. Based on the damage observation, they have developed a damage-based notched strength model to predict the damage growth and notched strength.

Similar observations and conclusions have been found in many other studies [70,73–77,80]. Laminate thickness and scaling effects influencing the sub-critical damage development and notched strength have been discussed. Among all of these studies, lower notched strengths have been observed in the laminates with a lower ply thickness, a smaller number of blocked plies or sub-laminate level scaling. This is due to the damage mechanisms blunting the notch, such as 0° plies splitting, matrix cracking and triangular delamination extending from the splits being less in these laminates. Wisnom et al. [81] and Hallett et al. [70] have demonstrated that

introducing cohesive elements along the splitting route in FE analysis can effectively model the effect of the split in 0° plies.

A more extensive and comprehensive experimental testing programme on scaling of notched composites was performed by Green et al. [80]. They carried out a series of open-hole tensile tests with different hole diameters and ply thicknesses to investigate the scaling effects in notched composites. Quasi-isotropic CFRP laminates with stacking sequences $[45_m/90_m/-45_m/0_m]_{ns}$ were tested in static tension containing central holes with diameters from 3.175mm to 25.4mm. The results showed that the open-hole performance was dependent upon hole size and laminate thickness. In the ply-level scaling, the failure mode transitioned from pull-out to delamination dominated failure with the increase of ply thickness, and delamination was reduced if the ratio of hole diameter to ply thickness was increased. For sub-laminate-level scaling, less splitting in the 0° plies was observed when increasing the total number of sub-laminates, and a lower notched strength found. Overall, this study has indicated that less sub-critical damage has been found in laminates with a less ply blocking and a larger hole dimension, resulting in a larger strength reduction. The notched strength is plotted with the hole diameter and changing the thickness in Figure 2.6. This is because sub-critical damage can redistribute the stress at the hole edge and delay the onset of final failure.

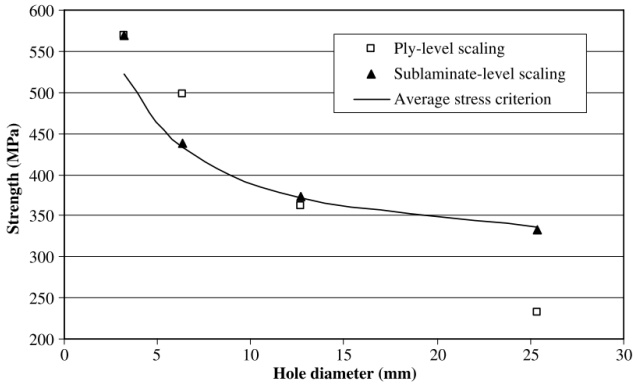

Figure 2.6: Notched strength is plotted against hole diameter for ply-level scaling and sub-laminate-level scaling laminates [80].

From the studies mentioned above, notch-sensitivity was highly related to the damage development within the laminate prior to final fracture. Subcritical damage can redistribute the stress at the notch-tip and result in a higher notched strength. However, this could be a concern with laminates using thin plies, since the damage suppression characteristic of thin plies/low thickness plies has been shown to be sensitive to notches [43,45–47,49]. The open-hole tensile strength of thin ply laminates can be at least 10% lower than the laminates made from thicker plies, whilst failing in a more brittle manner. For example, Sihn et al. presented the open-hole tensile strength of the THIN QI laminate (t = 0.04 mm) as being 10% lower than the THICK one (t = 0.20 mm) [47]. The damage of these laminates has been analysed via acoustic emission (AE) and X-ray techniques. Results have shown that more AE energy events were captured during loading and more micro-cracks were observed at the hole edge of the THICK than the THIN laminates. Figure 2.7 presents typical visual damage observations of the failed THIN and THICK specimens. Similar findings were also presented in the notched responses of non-crimp fabric thin-ply laminates by Arteiro et al. [45]. In laminates with a centre-notched or centre-drilled hole, brittle net-section failure was observed in the laminates made from thin non-crimp C-ply.

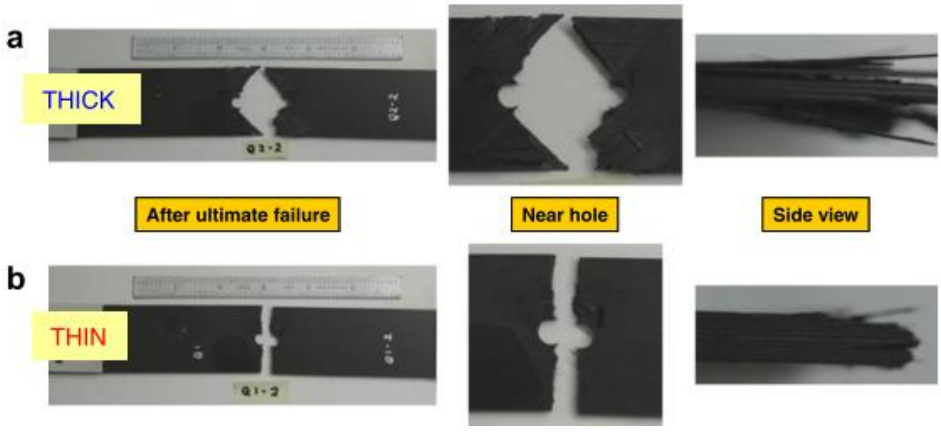

Figure 2.7: A comparison between THICK and THIN specimens after ultimate load [47].

To improve the notched performance of thin-ply laminates and maintain the benefits of using thin ply prepregs, it is necessary to design the laminate with “built

in" damage. Furtado et al. have developed a selective ply-level hybridisation concept (HYBRID) [46], which combined off-axis thin plies with standard thickness 0° plies in a QI laminate and then compared them with the THIN and THICK laminates with the same layups respectively. The HYBRID and THICK specimens exhibited very similar damage modes, including splitting along the 0° fibres and some localised delaminations across the width of the specimen next to the hole edge. The notched strength of the HYBRID laminate was higher than the THIN laminate and slightly lower than the THICK laminates. Although the notched strength of the HYBRID laminate reduced when increasing the hole dimension, the influence of hole dimension on the laminate strength was less than the THIN laminates. This study successfully demonstrated that introducing "built in" damage (e.g. 0° ply splitting) can effectively improve the notched performance of thin ply laminates without losing their unnotched tensile response.

Jalalvand et al. [28] suggested that, based on numerical modelling, the notch sensitivity can be reduced in QI laminates made from pseudo-ductile thin-ply hybrid sub-laminates. The results showed that when the ratio of pseudo-ductile strain to "yield" strain is sufficiently high, the stress concentration can be reduced since damage initiated in the pseudo-ductile thin-ply hybrid sub-laminate can re-distribute the stress around the hole. This has been experimentally demonstrated in [66,67]. These studies provide a good indication that the damage mechanisms of pseudo-ductile thin angle-ply laminates mentioned in section 2.2, e.g. fibre fragmentation, could be mechanisms in blunting notch in the thin ply specimen under open-hole tensile loading.

2.4 Compressive loading

Thin ply angle-ply laminates with central 0° plies have shown metal-like stress-strain behaviour in tensile loading. If these pseudo-ductile laminates are applied to real structures, compressive behaviour is often a critical design case since the compressive strength is often found to be lower than in tension [83]. It is essential to fully understand the compressive behaviour of these laminates so that confidence in their utilisation can be increased.

Compressive behaviour and failure modes have been investigated extensively in the past [83–98] and the results have shown that plastic microbuckling – governed by the shear instability of the fibres in the surrounding matrix - was the major compressive failure mechanism in many commercial fibre composites. In UD laminates, fibre micro-buckling is induced from the instability of fibres under compressive loading, followed by plastic deformation in the surrounding matrix. This allows the further rotation of the fibre to form a "kink-band", which contributes to the final failure. Figure 2.8 shows a typical illustration of how the "kink-band" is formed.

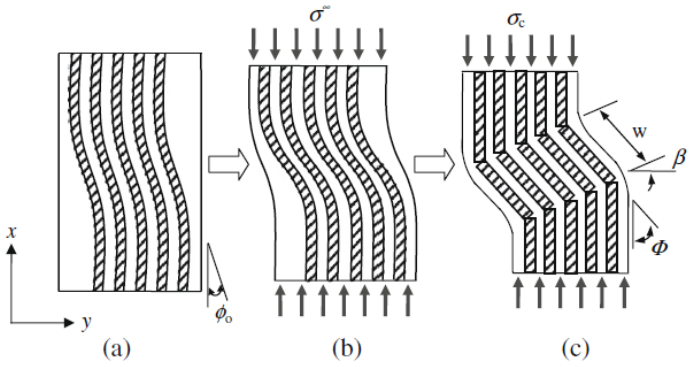

Figure 2.8: An illustration showing kinking band formation under compressive loading: (a) the initial misalignment or in-plane waviness, (b) micro-buckling of fibres and (c) formation of kink-band.

A significant number of theoretical analyses have been performed to predict the compressive strength of fibre reinforced composites. One of the earliest models to predict the compressive strength was presented by Rosen [99], where the compressive strength was related to the work done by compressing composites and the strain energy in the fibre and matrix. Jelf and Fleck [87] have extended Rosen's model which assumed an elastic buckling of an initially perfectly aligned fibre, to a more realistic elastic-perfectly plastic case, incorporating matrix strain hardening and finite fibre stiffness. Through a series of imperfection-sensitivity studies, the matrix yield strength and the initial fibre misalignment/waviness have been found to be the key factors on the compressive strength and buckling behaviour. Budiansky, Fleck et al [84], Jelf, Fleck et al. [100] and Wisnom [95] have shown that the

compressive strength reduces linearly with the increase of applied shear stress until the shear strength has been reached – it is a maximum when the shear stress is zero. Figure 2.9 shows the variation of axial compressive strength with applied shear stress. Fibre waviness and misalignment can introduce very large shear stresses, and result in shear instability under a lower applied compressive load compared with the perfectly aligned case [83,94–96]. For example, Wisnom [94] has demonstrated that the compressive strength could be reduced from 1949 MPa to 940 MPa, from only a small angle change from 0.75° to 3°.

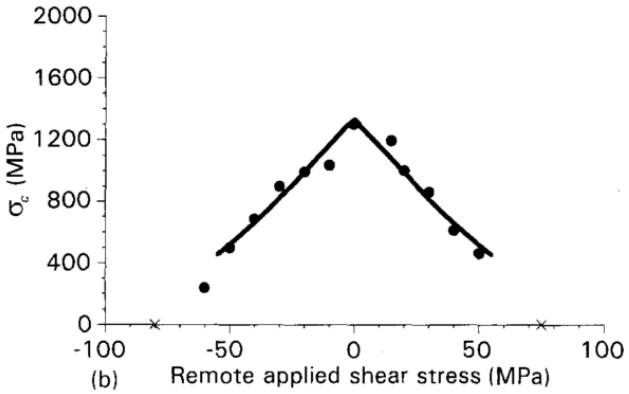

Figure 2.9: Compressive strength is plotted against matrix shear yield strength [100].

Studies on compressive behaviour of CFRPs have been extended to angle-ply laminates and the effect of angle plies on the 0° plies' failure [101–106]. The compressive strength of angle-ply laminates was found to be significantly lower than UD laminates. It decreases significantly with the increase of angle in the angle plies, and the degree of non-linearity increases [101,105,107]. In terms of failure modes, the dominant failure mode for the angle-ply laminates with a small angle (below 15°) is characterised by brooming and interlaminar cracking. When the angles lie between 15° and 45°, the laminates fail as a single fracture parallel to the fibre direction. This failure is governed by in-plane matrix shearing and high transverse tensile stress. With the further increase of angles to between 60° and 90°, failure is attributed to matrix dominated transverse compression. Fuller et al. have observed similar behaviour for the $[\pm 26_n]_s$ and $[\pm 30_n]_s$ laminates made from thin ply prepreg [63].

In the studies focused on off-axis laminates containing 0° plies, the effect of off-axis plies on 0° fibre micro-buckling has been investigated. Soutis et al. have tested cross-ply and QI laminates containing different percentages of 0° plies [97]. Failure strains of all the laminates were found to be independent of the layup, suggesting that the ±45° plies have very limited effect on the micro-buckling strain of the 0° plies. The damage modes observed in these laminates were micro-buckling of 0° plies, followed by delamination at the 0/θ interfaces. Berbinau et al. tested $[(\pm\theta/0_2)_2]_s$ laminates with θ equal to 30°, 45°, 60° and 75° [106]. Each of these specimens failed by splitting parallel to the fibres in the angle-ply layers, with fibre micro-buckling of the 0° plies and delamination between 0° and ±θ plies, where micro-buckling of the 0° plies was found to be the major mechanism and to cause the catastrophic failure. The ±45° plies provided the best lateral support among all angles. However, the difference in failure strain was less than 5% which indicated the values of θ had little effect on the 0° plies. Via a modified micro-buckling model, it was also suggested that matrix cracking and edge delamination could trigger micro-buckling in the 0° plies at a lower stress/strain in a $[(\pm\theta/0_2)_2]_s$ laminate.

From the studies discussed above, angle-ply laminates have shown a significant degree of non-linearity under compressive loading if the angles in the angle-ply were higher than 15°. However, due to the high in-plane shear stress and transverse tensile stress, angle-ply laminates have a lower compressive strength compared to UD laminates. Laminate with both off-axis plies and 0° plies tend to fail at a higher stress than monolithic angle-ply laminates, but the micro-buckling in the 0° plies and delamination at the 0/θ interface result in catastrophic failure. In the studies of thin ply laminates [49,61], if the ply is sufficiently thin, delamination can be suppressed in compressive loading. The delamination at the 0/θ interface can be avoided and a more progressive failure can be promoted in thin ply angle-ply laminates with central 0° plies. In some of the most recent works on glass/carbon hybrid composites [15,108], Czel et al. have observed progressive ply fragmentation in a compressive test of high modulus carbon fibre plies. This suggests the potential to exhibit pseudo-ductility under compression with the absence of kink-bands due to shear instability.

2.5 Bending

Flexural loading is another crucial but more complicated loading case, involving compression and tension on the top and bottom sides of the specimen respectively, as well as interlaminar stresses in the through thickness direction. This means that when laminates are loaded in flexure, their compressive, tensile and shear properties all need to be taken into consideration. The flexural strength can be the same as the tensile/compressive strength of the laminate, depending on whichever is the lower, but in most cases the flexural strength lies between these two properties due to the fact that micro-buckling can be inhibited on the compressive side of the beam by the stress gradient, and so much higher strains can be achieved in bending [109–111].

Flexural behaviour and the dominant damage modes can be significantly influenced by the laminate layup and test configuration [112–115]. Increasing the span-to-thickness ratio results in the failure mode changing from interlaminar shear failure to tensile/compressive failure [112]. For example, Davies et al. investigated the effect of flexural behaviour on three different span-to-thickness ratios of 16, 32 and 64 [113]. The flexural strength was found to increase with the increase of span-to-thickness ratio. The authors have also reported that a larger non-linearity is presented in the load-strain curves for the laminates with a ratio of 64 than 16 or 32, due to the geometrical non-linearity. Although differences have been seen in the strength and load-strain curves for the different ratios, the failure modes were similar among these cases: out-of-plane fibre micro-buckling induced compressive failure, followed by minor delamination on the compressive side of the beam. Jackson et al. have studied the layup and scale effects in the failure of laminates in flexural loading [115]. Laminates with UD, angle-ply, cross-ply and QI layups have been machined into different dimensions and tested in a hinged-pinned flexural test fixture. Different layups have exhibited different failure mechanisms in bending. UD laminates failed mainly by fibre facture and longitudinal splitting, whilst angle-ply laminates failed by transverse matrix cracking along the angle direction. Size-related effects had very little influence on the failure mechanisms of both laminates. However, in the cross-ply laminates, the failure mechanisms transited from fibre fracture of the outer 0° plies and transverse matrix cracks in the 90° plies, to delamination at the 90/0 interface. In terms of bending strength and strain, the angle-ply laminates were

influenced the most, whilst the UD laminates showed the least sensitivity to size effects.

Caminero et al. [116] have also investigated the effect of stacking sequence on flexural behaviour via a series of different layups, including UD layup $[0]_{12}$, and multi-directional layups $[0/90]_{3s}$, $[\pm45]_{3s}$, and $[0/90/\pm45_2]_{3s}$ tested in 3-point bending. Most of the layups failed catastrophically with a sudden load drop, apart from the $[\pm45]_{3s}$ laminates. The $[\pm45]_{3s}$ laminates exhibited the largest non-linearity and high strain to failure due to the scissoring of angle plies on both the compressive and tensile sides. Severe matrix cracks and delamination due to the high free-edge interlaminar stresses initiated from the tensile side and progressed to the compressive side, resulting in progressive pseudo-ductile behaviour. For the two layups with 0° plies, the damage initiated in the $[0/90]_{3s}$ and $[0/90/\pm45_2]_{3s}$ laminates is compressive micro-buckling and delamination at the 0/90 interfaces. Delamination at the ±45 interface on the tensile side was also observed. All these layups, apart from the $[\pm45]_{3s}$ laminates, failed catastrophically which is caused by the sudden compressive failure. Figure 2.10 shows the load-displacement curves and damage for cross-ply and angle-ply laminates that have been mentioned in the previous context.

From the studies above, the $[\pm45]_{3s}$ angle-ply laminate has shown favourable non-linear behaviour and gradual failure. The micro-damage accumulation and the matrix yield in the angle plies contributed to the non-linear behaviour in tensile, compressive and flexural loading. The dissimilar behaviour on the tensile and compressive sides causes a non-symmetric strain field through the thickness [117–121]. In addition, due to significant non-linear tensile and compressive stress-strain behaviour for the $[\pm45]_{3s}$ laminate, possible large deflections in the bending test and non-linear stress-strain behaviour of the fibres, linear elastic analysis is not sufficient for analysing these laminate beams [121–123]. The earliest evaluation presented by Jones [121] has shown an analysis to predict the flexural strength and modulus based on the non-linear material response, but restricted to the material with bilinear stress-strain behaviour. Wisnom [123] also developed an analytical model by assuming the non-linear tensile and compressive modulus as a linear function of strains. The predicted results have shown a good agreement with experimental results as well as

up to a 20% difference compared to the linear elastic bending theory. Some more recent work presented by Serna Moreno et al. [115,117–120] has focused on flexural behaviour analysis on the UD, cross-ply and angle-ply laminates with a dissimilar tensile and compressive modulus. In the work focused on the $[\pm 45]_{ns}$ angle-ply laminate [119], the pseudo-ductile flexural response has been investigated and predicted in more detail. In contrast to the UD, cross-ply and QI laminates, the damage initiation of the $[\pm 45]_{ns}$ angle-ply laminate started by matrix micro-cracking from the tensile side. With increasing load, the remaining plies next to the first failure plies sustained further loading and this micro-cracking propagated to the adjacent layers until complete failure occurred. The progressive damage accumulation starting from the tensile side has been shown to successfully demonstrate pseudo-ductility in flexural loading. Similar tension dominated failure has been reported in the bending work by Wisnom [114,124]. This observation gives a good indication that when pseudo-ductile thin ply angle-ply laminates are subjected to bending, the initiation of 0° ply fragmentation on the tensile side would delay the damage accumulation on the compressive side and therefore achieve a more gradual failure.

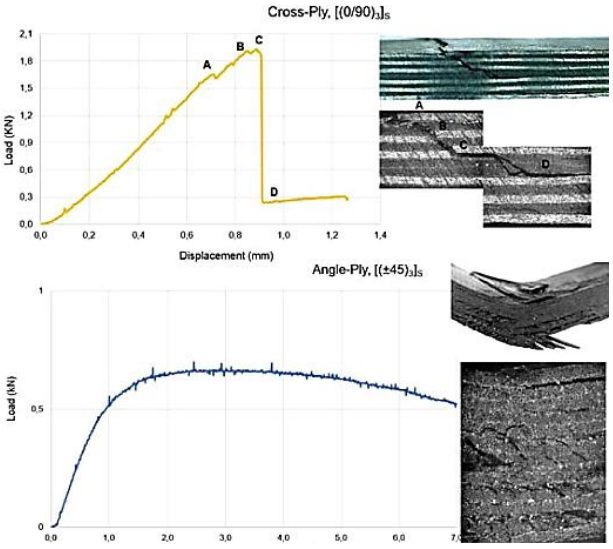

Figure 2.10: Load-displacement curves and optical damage observations for two different layups. A non-linear curve and more progressive damage development can be seen in the angle-ply laminate rather than cross-ply laminate [116].

2.6 Fatigue

Any structure made from carbon fibre composite may suffer from fatigue load in its service life, therefore the fatigue performance is another important property that needs to be understood, predicted and considered in design. In fibre reinforced composites, defects such as voids, fibre wrinkles and misalignments can be damage initiation points when subjected to fatigue loading [125]. The accumulation of damage such as matrix cracking, interfacial debonding and fibre breakage leads to more detectable damage such as delamination and splitting that can cause the eventual failure of a composite in cyclic loading.

To assess the damage that has developed during cyclic loading, residual strength and residual modulus have been found to be a common scale and the failure is assumed to have occurred at a residual strength equal to the maximum stress amplitude. Figure 2.11 shows typical degradation curves – normalised stiffness and strength against number of cycles. In these curves, the stiffness is found to be more sensitive to the damage accumulation over cyclic loading than the strength [125].

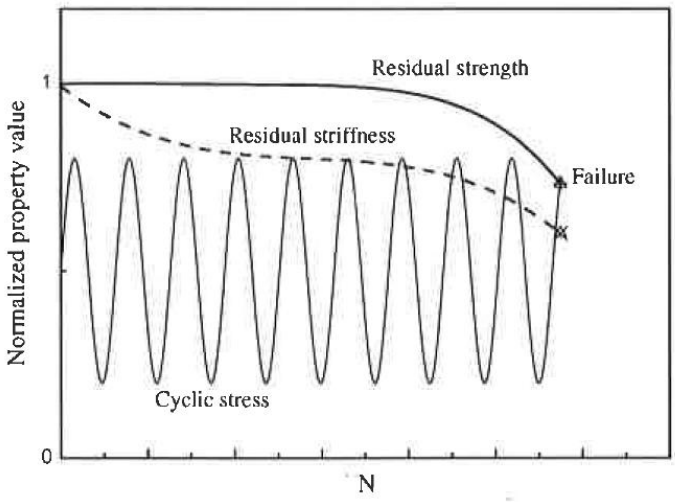

Figure 2.11: Normalised mechanical property reduction against number of cycles [125].

The fatigue life and damage accumulation are significantly influenced by numerous factors including load severity, frequency of cyclic loading, the R-ratio

(stress ratio, defined as the ratio of the minimum and maximum cyclic stresses), material constituents and laminate stacking sequence [125–139]. It is particularly worth mentioning the effect of loading frequency on fatigue life as it has been found to vary depending on stacking sequences. For example, Saff [135] has shown that when the frequency increased from 0.1Hz to 10 Hz, the fatigue life of a $[\pm 45_2]_s$ laminate at 10Hz is only one tenth of that at 0.1 Hz due to the self-generated heat. Miyano et al. [140] have developed a method on predicting fatigue life of UD carbon fibre composites. Based on the results from both the prediction and experimental validation, for a given fatigue strength, the number of cycles to failure is lower for the specimen tested at a frequency f = 0.02 Hz than at a frequency of f = 2 Hz due to the viscoelastic behaviour of polymer matrix. However, for laminates containing 0° plies, the loading frequency has less effect on fatigue life in general.

The influence of laminate configuration/stacking sequence on fatigue life has been found to be based on the damage accumulation within the laminate [130,131,141–146]. O'Brien [143,147] conducted tension-tension fatigue testing on $[0_2/\theta_2/-\theta_2]_s$ carbon fibre laminates, with θ = 15, 20, 25 and 30°. The damage sequences in all these layups are similar: matrix cracks in -θ° plies, followed by the local and edge delamination at the θ/-θ interfaces. Similar damage accumulation has also been observed in QI laminates in fatigue presented by Masters and Reifsnider [130]. For a $[0/90/\pm 45_2]_s$ laminate, the sequence of damage was transverse cracks in the 90° layer, transverse cracks in the ±45° layers and delamination at the 45/-45 interfaces at the free-edge. Some of the damage observed in fatigue specimens, such as the cracking initiated in the off-axis plies and the extensive edge delamination, have not been seen in the static specimens. This suggests that the damage accumulated at fatigue loads was transverse ply cracking and delamination, and it was more severe than that seen under static tensile loading.

Due to the significant role of damage on fatigue behaviour, Poursartip et al. have developed a model to predict the stiffness loss due to damage [145,146]. Analysis has focused on two stages: the stiffness loss was based on the delamination area and a slow stiffness reduction was attributed to the breakage of the 0° plies once

the delamination was completed. They also found that the damage growth rate is independent of the damage in the specimens at a constant applied stress level.

However, the previous investigation on thin ply laminates [47] has shown no microcracks and less edge delamination under fatigue loading compared with laminates made from standard thickness plies. This suggests that when the pseudo-ductile thin ply angle-ply laminate with central 0° plies is subjected to fatigue loading, a stiffness reduction is unlikely due to transverse cracking. As mentioned in section 2.2, the damage modes observed in these laminates under static tension were fragmentation of the central 0° plies, delamination localised to the fractured 0° plies and a small amount of edge delamination at the θ/-θ interface. Therefore, the growth of localised dispersed delamination in addition to the free edge delamination under fatigue load would be the main fatigue damage mechanisms and their effect on the reduction of laminate properties needs to be assessed.

Wisnom et al. presented more details on the delamination growth under fatigue tension loading using laminates with terminating internal plies [148] and tapered laminates [149]. These two types of laminate have been found to be prone to delamination, in both static tensile and fatigue loading. In their studies, the delamination has developed and propagated along the interface between the continuous and cut plies at a constant rate [148]. Delamination growth rate and the strain energy release rate have been estimated based on the measured modulus before and after fatigue loading. In addition, delamination growth rate has been found to vary with thickness and orientation of plies, and thinner specimens showed an increased delamination growth rate. These delamination studies are very similar to the pseudo-ductile thin ply angle-ply laminates with fractured central 0° plies loaded in fatigue, as specimen with internal cut or fractured plies favour a Mode-II delamination.

2.7 Bearing

Mechanically fastened joints are a critical part in the application of composites, since these connect different parts together and transfer the loads between them. The load

is transferred through friction produced by the laminates and bolt thread, mechanical interlocking of the bolt head and the shear force in the fastener. The failure modes of mechanically fastened joints vary based on the material, layup and geometry factors, and bearing strength is always found to be lower than the unnotched strength due to the stress concentration around the hole, therefore the bearing behaviour needs to be well understood to design joints more efficiently without any premature failure of the composite structure.

One of the common ways for determining the bearing response of laminates is via a single bolted joint. Among all the studies on bolted composite joints, net-section tension, shear, cleavage, tear-out and bearing were the five main common failure modes in laminates and are presented in Figure 2.12. Net-section tension and cleavage are often associated with bearing/bypass interaction.

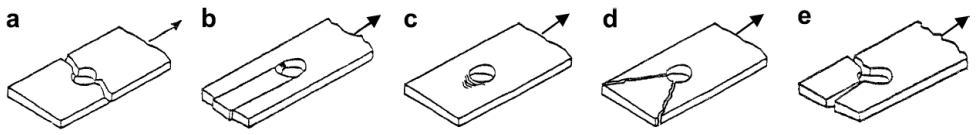

Figure 2.12: Five typical damage modes observed in bolted composite joints: (a) net-section tension, (b) shear-out, (c) bearing, (d) tear-out and (e) cleavage.

Extensive studies have been carried out to investigate the effect of geometrical parameters on bolted joint laminates [150–162]. Zhang et al. explored the effect of end distance on the bearing behaviour of a QI laminate [150]. With the end distance to diameter ratio (E/D) increasing, the failure mode transitioned from cleavage/shear failure to a progressive bearing failure. An intrinsic critical length has been selected to assess the failure mode – laminates tend to fail in cleavage if the end distance is smaller than the critical length and vice versa. An E/D ratio of 3 is recommended to be used in the design for QI laminates according to many studies. A similar trend has also been seen in the width to diameter ratio (W/D) that with the increase of this ratio, the failure mode changes from tension dominated failure to bearing failure [151,152,158,163]. Hamada et al. [152] and Park et al. [153] presented the effect of stacking sequences on bearing behaviour in more detail. Similar conclusions have been made that, for either QI or cross-ply layups, the

stacking sequences of the internal plies had limited influence on bearing strength, but the plies on the outer surface played an important role. The studies found that the laminates with 90° plies on the outer layers were stronger than those with 0° plies.

Many experimental investigations and theoretical models have been developed to understand the behaviour and damage mechanisms of bolted composite joints [151,152,155,157,164]. Wang et al. studied the bearing failure of cross-ply and QI laminates with different layups in a double shear-lap bolted joint test [151]. QI layups have shown higher bearing strengths than cross-ply laminates at the same test condition, particularly for those with 90° layers on the outer surfaces since ±45 plies improved the shear strength of the QI laminate. In terms of damage observations, out-of-plane shear cracks and delamination have been observed in all layups. The shear cracks often come in pairs and are attributed to the accumulation of fibre kinking, fibre-matrix shear and matrix compression in each ply of the laminate. In addition, a linear load-displacement response and catastrophic failure have been observed, due to the unstable delamination initiated from the shear cracks. When increasing the initial applied clamping pressure, the bearing strength has also been found to increase. Shear cracks and delamination were reduced within the specimen due to the lateral constraint from tightening the bolts. A clear comparison of bearing damage at finger tight and high clamping pressure conditions is presented in Figure 2.13 [151].

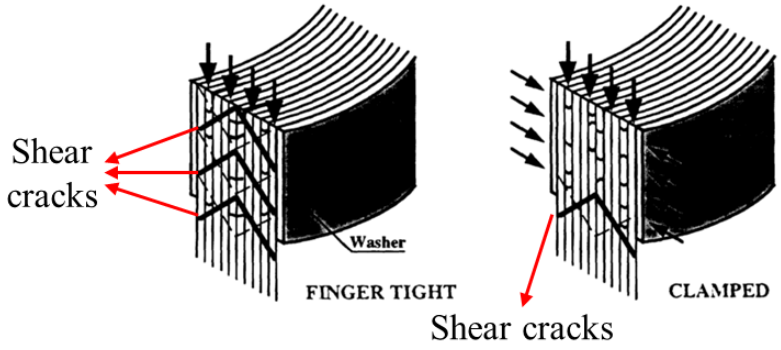

Figure 2.13: A schematic description of the bearing damage at low (finger tight) and high clamping pressures [151]. Under low clamping pressure, damage accumulates in the individual plies to form significant amounts of shear cracks in the bearing plane of the laminates; under high clamping pressure, the shear cracks are inhibited due to the restraints in the transverse direction.

Xiao et al. [157] and Sola et al. [164] further investigated in detail the role of fibre kinking in bearing tests of carbon fibre composites. In these studies, a kink-band plays a dominant role in leading to bearing failure. Fibre kinking has been shown to be the first major damage occurring within the laminates. With further applied load, the kink-band propagated in both the in-plane and out-of-plane direction (referred as out-of-plane shear cracks in [151]). These kink-bands triggered delamination located close to the outer layers of the laminate due to lack of ply constraint effects, resulting in the final failure. Figure 2.14 presents typical damage observations at the bearing plane at 60% and 75% of the maximum load respectively.

All the studies discussed above were based on laminates made from standard thickness plies. When thin ply laminates are subjected to bearing load, damage mechanisms have been found to be different from those studies above [43,45]. Thin ply laminates have shown superior bearing responses to standard thickness ply laminates (e.g. IM7/8552). Although matrix cracking and fibre kinking have been observed in these thin ply laminates, delamination has been successfully inhibited. This suggests that when the pseudo-ductile thin ply angle-ply laminates are loaded in bearing, the compressive damage in 0° plies, either fibre kinking or progressive fibre fracture, may not cause catastrophic failure of the laminate if the delamination is suppressed.

Once the number of fasteners is increased to two or more, the design and analysis of bolted joint laminates becomes more complex. It involves both the bearing behaviour at each fastener and the ability of load to bypass from one fastener to another. Each fastener needs to be designed to carry an allowable portion of the load, and premature failure in any fastener would be undesirable. Many studies have focused on testing multi-bolted laminates joints, and in addition to those factors mentioned in bearing tests, the material properties of the fixture and bolts, and the distance and alignment between adjacent holes are also important in testing multi-bolted joints [165–172].

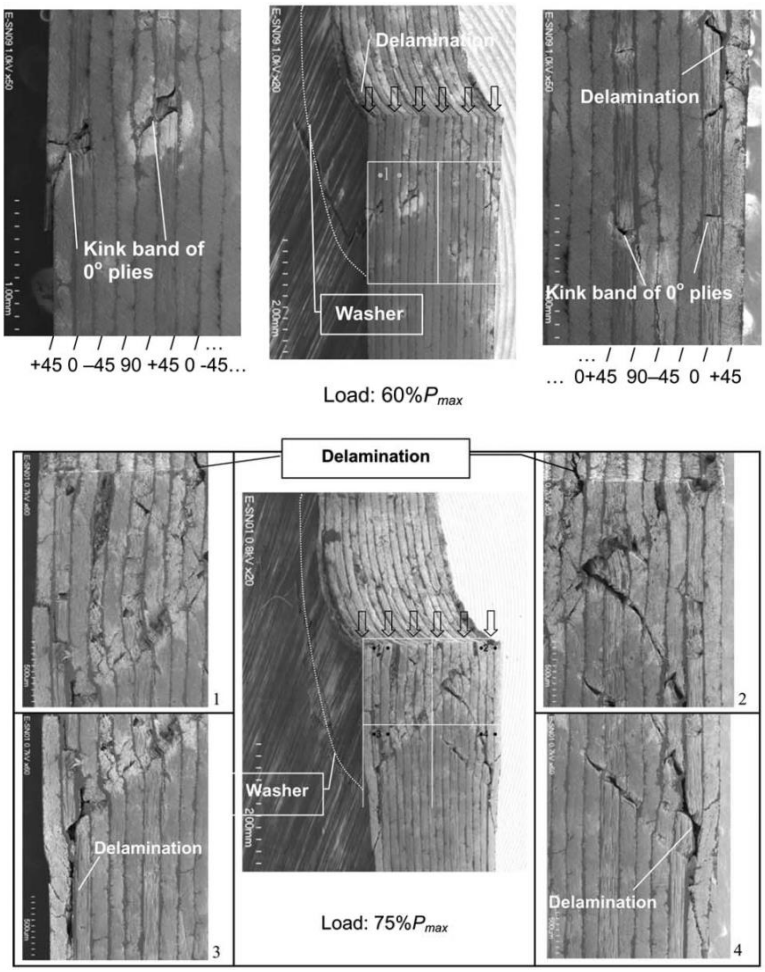

Figure 2.14: SEM images show bearing damage at 60% and 75% of the maximum load [157].

A review of the literature has shown that pseudo-ductility has been developed in thin ply angle-ply laminates with central 0° plies under tension. Damage suppression of thin ply prepreg allows damage mechanisms of fragmentation in the 0° plies and localised delamination to develop in these laminates. These pseudo-ductile laminates would be expected to take the advantage of thin-ply laminates, with their other mechanisms providing different behaviour in a range of loading conditions compared with conventional carbon fibre composites.

In open-hole tensile loading, due to the lack of damage mechanisms, thin ply laminates are found to be very sensitive to notches. Previous research has

suggested that introducing built-in damage within thin ply laminates can improve the notched performance, indicating fibre fragmentation of 0° plies of pseudo-ductile laminates could be the mechanism for redistributing the stress around the hole and achieving a better notched strength. When thin-ply angle-ply laminates are under compression, micro-buckling in the 0° plies has been found to be delayed due to the lack of matrix cracking and edge delamination. Delamination at the 0/θ interface can also be suppressed, which allows progressive fibre fractures to occur in the central 0° plies with the support from adjacent angle plies and could achieve pseudo-ductility under compression. A similar indication should also be given in bearing load. When pseudo-ductile laminates are loaded in flexure, progressive fibre fractures on both the tensile and compressive sides of the beam are observed. The initiation of 0° ply fragmentation on the tensile side would delay the damage accumulation on the compressive side and therefore achieve a more gradual failure.

3 Unnotched and open-hole response of pseudo-ductile thin-ply angle-ply laminates

This chapter presents an experimental investigation on the unnotched and open-hole tensile behaviour of pseudo-ductile thin ply angle-ply carbon fibre/epoxy laminates with central 0° plies. Laminates with two different configurations of $[\pm 26_5/0]_s$ *and* $[\pm 25_2/0]_s$ *were designed and tested under unnotched and open-hole tensile loading. Metal-like tensile stress-strain curves with a plateau were observed in both unnotched configurations. The open-hole net-section strength of the* $[\pm 25_2/0]_s$ *laminate attained 96% of the unnotched "yield" strength. Digital image correlation and X-ray CT-scan images showed that the same damage mechanisms of central 0° ply fragmentation and local dispersed delamination observed in unnotched pseudo-ductile laminates were present in the open-hole specimens of the same configuration. These damage mechanisms caused stress redistribution around the hole and reduced the notch sensitivity in pseudo-ductile laminates under open-hole tensile loading. The main factors governing the open-hole performance are also discussed.*

3.1 Introduction

Pseudo-ductility and unique damage mechanisms have been found in these thin ply angle-ply laminates in tension. However, to progress these laminates towards real applications, their open-hole behaviour needs to be understood since the presence of stress concentrations can lead to catastrophic failure and significant strength reduction.

In previous research, notch sensitivity has been found to be related to the damage within the laminate prior to the final failure. For example, Kortschot and Beaumont [78] conducted a series of tensile tests on notched cross-ply laminates and employed an X-ray machine to monitor damage in the specimen, to understand the relation between damage and notched strength of open-hole specimens. The results showed that sub-critical damage in cross-ply laminates, such as 0° ply splitting, transverse ply cracking and delamination, can redistribute the stress and have a significant influence on the notched strength of the laminate. Similar conclusions have also been found in many other studies and also it has been found that the laminates tend to be less notch sensitive when the hole size is relatively small.

However, this could be a concern with laminates using thin plies, for example pseudo-ductile thin ply angle-ply laminates, since the damage suppression characteristic in thin plies has been shown to make laminates sensitive to notches. The open-hole strength of thin ply laminates can be at least 10% lower than for thicker plies, whilst failing in a more brittle manner [47].

In the present chapter, the studies of pseudo-ductile laminates in unnotched tensile loading have been extended from laminates with all standard modulus fibre prepreg to intermediate – high modulus fibre prepreg combinations. Based on this, the open-hole tensile performance of pseudo-ductile thin ply angle-ply laminates has been investigated and the role of the damage mechanisms of these pseudo-ductile laminates on their notch sensitivity has been studied. The damage within the laminates was studied using acoustic emission and Digital Image Correlation (DIC) during testing, and ultrasonic C-scan and X-ray CT-scan techniques for post-failure analysis.

3.2 Design methods

As mentioned in the work presented by Javalvand et al. [28], in a pseudo-ductile glass-carbon hybrid QI laminate with thin carbon plies, notch sensitivity is expected to decrease with increasing ratio of pseudo-ductile strain to "yield" strain (termed strain ratio) and it can potentially be eliminated when the strain ratio is greater than 3.

Inspired by this, two different pseudo-ductile thin ply angle-ply laminate configurations were tested: one is a laminate with a strain ratio higher than 3 and other one has a low strain ratio for a contrasting study. The design of the unnotched specimens follows an analytical method developed by Fuller et al. [11].

3.2.1 Design concepts for unnotched specimens

The criteria used in the design of a pseudo-ductile $[\pm\theta_m/0_n]_s$ laminate follow the analytical method presented by Fuller et al. [11] and is briefly summarised here. The failure mode of thin ply angle-ply laminates with internal 0° plies depends on the elastic properties of the angle plies, 0° plies and their thicknesses. The possible failure modes of these laminates include failure and fragmentation of the central 0° plies, delamination initiating from fracture surface of the central 0° plies and fibre fracture of angle plies. Two types of design considerations are made here in order to promote failure in a pseudo-ductile manner:

(1) Once the fibre failure strain of the 0° plies has been reached, the central 0° plies start to fracture and the ±θ° plies have to be sufficiently strong to withstand the increased stress at the crack tip (σ_{crack}) to promote multiple fractures in the central 0° plies (termed fragmentation) that leads to gradual failure. σ_{crack} is calculated as:

$$\sigma_{crack} = K_t \sigma_x \left(\frac{t}{t_{AP}} \right) \tag{3.1}$$

where σ_x is the laminate applied stress, t_{AP} is the thickness of angle plies, t is the total laminate thickness and K_t is an assumed stress concentration factor (SCF) since the broken 0° plies can introduce a non-uniform stress distribution around

the surrounding angle plies and may lead to the fracture of these angle plies. An approximate SCF value of 1.08 predicted from a finite element analysis, was used for all of the laminates [18].

(2) The stress concentration at the crack tip promotes a Mode-II delamination at the 0/θ interface. The second design criterion is to assess the delamination stress, ensuring it is higher than the fragmentation stress to avoid the complete delamination of the specimen after the first fracture. The delamination stress σ_{del} is governed by the following equation [11], which is adapted from [17]:

$$\sigma_{del} = \frac{1}{t_{AP} + t_{UD}} \sqrt{\frac{2G_{IIc} E_x^{AP} t_{AP} (E_x^{AP} t_{AP} + E_{11} t_{UD})}{E_{11} t_{UD}}} \qquad (3.2)$$

In this equation, G_{IIc} denotes the critical Model-II fracture energy, subscripts "UD" and "AP" denote the properties of the 0° plies and angle plies respectively, and E_x^{AP} and E_{11} represent the stiffness of the angle plies and 0° plies respectively.

To achieve the required strain ratio, two approaches can be used, either by increasing the final failure strain or reducing the "yield" strain. Standard modulus fibres normally have a relatively high fracture strain, for example 1.6% for the T300 carbon fibre, a high failure strain of 6% is required for the laminate to achieve a strain ratio of 3, which is difficult to achieve in angle-ply laminates whilst retaining good strength and stiffness. Therefore, high modulus fibre prepreg has been used to replace the standard modulus fibre prepreg in the central 0° plies, since the high modulus fibres have a lower fracture strain, for example 0.5% for the TORAYCA YSH70A carbon fibre. Finally, two different laminates were selected in the present study: T300-T300 $[\pm 26_5/0]_s$ laminate, where "T300" stands for prepreg with standard modulus fibre T300, and MR60-YSH70 $[\pm 25_2/0]_s$, where "MR60" and "YSH70" denote intermediate modulus MR60 fibre and high modulus YSH70 fibre prepreg respectively. The T300-T300 laminate was based on a similar configuration presented in [11] and was used for a contrast study. In the MR60-YSH70 laminate,

since the central 0° plies were replaced by high modulus fibre prepreg, the angle plies were adjusted to ±25° to ensure that they would be strong enough to carry the stress redistribution after the fracture in the 0° plies.

3.2.2 Material selection, specimen design and manufacture

The materials used in each of the tests are commercially available spread tow carbon fibre prepregs including Skyflex USN020A with TORAYCA T300 standard modulus carbon fibre (termed T300), Skyflex UIN020A with Mitsubishi Rayon MR60 intermediate modulus fibre (termed MR60), and YSH-70A-ThinPreg120EPHTg-402 with ultra-high modulus fibre from North Thin-ply Technology (termed YSH70). The first two Skyflex prepregs from SK Chemicals used K50 low-temperature cure resin and the high modulus fibre prepreg from North Thin-ply technology uses a 120 EPHTg-402 type epoxy resin. The elastic properties for the different fibre types and cured laminates are given in Table 3.1 and Table 3.2 respectively.

Table 3.1: Key fibre properties of three different prepregs.

Fibre Type	Elastic modulus [GPa]	Tensile strain to failure [%]	Tensile strength [MPa]
TORAYCA T300 (Standard modulus) [173]	230	1.6	3530
Mitsubishi Rayon MR60 (Intermediate modulus) [174]	290	2.0	5680
TORAYCA YSH70A (High modulus) [175]	720	0.5	3630

The T300-T300 laminate was laid up from Skyflex USN020A prepreg, cured in the autoclave followed with a standard cure cycle of the Skyflex prepreg (heating up rate 3 °C/min, dwelling at 80 °C for 30 mins and holding at 125 °C for 90 mins). The MR60-YSH70 laminate was manufactured from Skyflex UIN020A prepreg and North YSH70A with a curing cycle (heating up rate 3 °C/min, dwelling

at 80 °C for 75 mins and holding at 125 °C for 165 mins). Whilst both materials could be cured at the same temperature, the North prepreg required a longer dwell period. The cure cycle of the combined MR60-YSH70 laminate was therefore selected to be the same as the longer of the two materials, to ensure complete crosslinking of both.

Table 3.2: Cured ply mechanical properties of UD laminates.

	Skyflex USN020A (T300 fibre)	Skyflex UIN020A (MR60 fibre)	YSH70A/epoxy (YSH70A fibre)
E_1 [GPa]	121 [a]	146	362
E_2 [GPa]	5.4 [a]	6.6	6.0
σ_1 [GPa]	1936 [b]	2800	1810
G_{12} [GPa]	2.76 [c]	2.97	4.00
ε_1 [%]	1.6	2.0	0.5
t [mm]	0.022	0.028	0.032
v_f [%]	52	50	50

[a] *Estimated from Rule of Mixtures*
[b] *Calculated from E_1 and ε_1*
[c] *Measured experimentally*

In order to understand the performance of the adjusted cure cycle, the degree of cure was examined by using Differential Scanning Calorimetry (DSC). Initially, DSC was performed on an uncured hybrid mixture with a mass of 10.56 mg with a ramp rate of 10 °C/min, start temperature of 35 °C and an end temperature of 250 °C (shown as black curve in Figure 3.1). An additional sample underwent an identical curing cycle that was used in this study by performing isotherms (75 mins at 80 °C; 165 mins at 125 °C) using DSC. This sample (10.86 mg) was analysed with DSC with a ramp rate of 10 °C/min and temperature ramp from 35 °C to 250 °C (shown as red curve in Figure 3.1). All samples were placed in hermetically-sealed aluminium (Tzero) pans and were analysed by a TAI Q200 DSC.

The DSC curves are shown Figure 3.1. The uncured sample is characterised by a large exothermic peak at ~146 °C which signals the irreversible crosslinking of

epoxy resin. The absence of this exothermic peak in the red curve demonstrates that the epoxy resin systems have successfully cured. In addition, the cured MR60-YSH70 laminate was examined under the microscope and no phase separation/delamination was observed. The information above indicates the compatibility of the two resins, although no chemical formulation of the above two resin systems were provided by the prepreg suppliers.

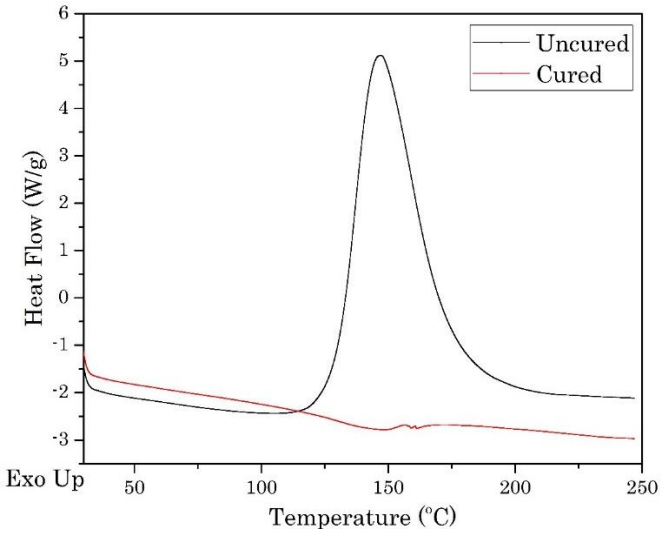

Figure 3.1: DSC signals of the uncured and cured hybrid prepreg specimens. The cured hybrid sample had undergone isothermal DSC to mimic the same curing cycle as the mechanical test samples.

The unnotched specimens for the T300-T300 $[\pm 26_5/0]_s$ and MR60-YSH70 $[\pm 25_2/0]_s$ laminates were designed according to the ASTM 3039 standard, which stipulates a parallel edge specimen of gauge length 150 mm and width 15 mm. For the open-hole specimens, a central drilled hole with diameter of 3.175 mm was used, with a width-to-diameter ratio of 5 and length-to-diameter ratio of 20, giving a specimen width of 16mm and gauge length of 64 mm. The thicknesses of the T300-T300 and MR60-YSH70 laminates were 0.48 mm and 0.25 mm respectively, which are too thin for testing in open-hole tension due to the compression across the width in the upper and lower edge of the hole that may cause undesired failure. Therefore,

the configurations of T300-T300 $[\pm 26_5/0]_{s2}$ and MR60-YSH70 $[\pm 25_2/0]_{s4}$ were used for the open-hole specimens, both with similar total thicknesses of about 1 mm. In both cases, glass fibre-epoxy end-tabs of length 40 mm were attached at each end of the specimen. The details of specimen dimensions are specified in Figure 3.2 and summarised in Table 3.3.

Table 3.3: Specimen geometries of T300-T300 $[\pm 26_5/0]_s$ and MR60-YSH70 $[\pm 25_2/0]_s$ laminates

	T300-T300 $[\pm 26_5/0]_s$		MR60-YSH70 $[\pm 25_2/0]_s$	
	Unnotched	Open-hole	Unnotched	Open-hole
Thickness [mm]	0.48	0.96	0.25	1.02
Width [mm]	15.00	16.00	15.00	16.00
Total length [mm]	230	144	230	144
Gauge length [mm]	150	64	150	64

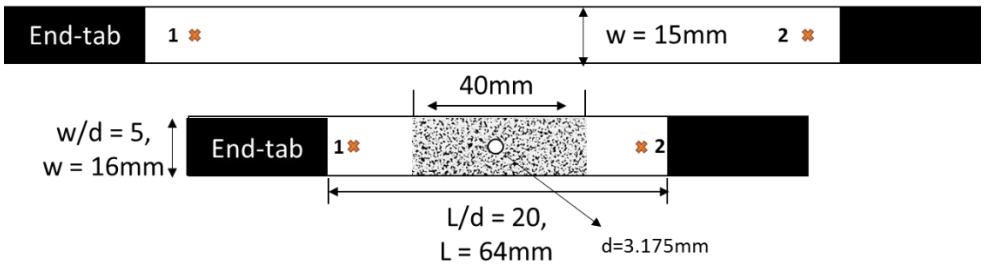

Figure 3.2: Schematic of the unnotched and open-hole tensile specimens. Orange crosses on each specimen represent the target points used for tracking longitudinal strain. In the open-hole specimen, the middle region was speckled with black and white dots for surface strain tracking by DIC.

3.2.3 Test setup and equipment

The unnotched and open-hole specimens were tested using an Instron hydraulically-actuated system with a 25 kN load cell, at loading rates of 2 mm/min and 1 mm/min respectively to give similar strain rates on the different length specimens.

In both tests, the overall strain was measured by an Imetrum Video Extensometer. Since the material properties in pseudo-ductile thin-ply angle-ply laminate cannot be treated as homogeneous in the loading direction and the damage mechanisms of fibre fracture and delamination can initiate from anywhere along the gauge length, strain gauges and extensometers are not sufficiently long in this case. The overall longitudinal strain measurements were therefore recorded by tracking targets which were set up near the top and bottom of the gauge length (the targets are shown as orange crosses in Figure 3.2) by using a Video Extensometer. A 10 mm gap was left between the targets and end-tabs to minimise the end-tab effects and allow a sufficient length to be covered in the strain measurements at the same time.

In order to evaluate the surface strain field local to the notch and to assess damage development in the open-hole specimen during loading, Digital Image Correlation (DIC) was employed. The main principle is to take images before and after deformation of the area of interest and then make a comparison between them. Two LaVision VC-Imager LX 16M CamLink (Nikon) cameras were placed in front of the specimen and zoomed in to the area of interest. The test set-up is shown in Figure 3.3. The area of interest was speckled with black & white paint and strains during loading were tracked by the cameras based on the deformation of these speckled patterns. The DIC measurement specifications are summarised in Table 3.4. It is also worth noting that the imaging apparatus for the T300-T300 laminates was set-up to be able to cover the whole specimen area. To perform the DIC measurement on the MR60-YSH70 specimens, once it was ascertained that the non-uniform strain field was only in a small region around the open hole, the field of view was reduced to increase spatial and strain resolution.

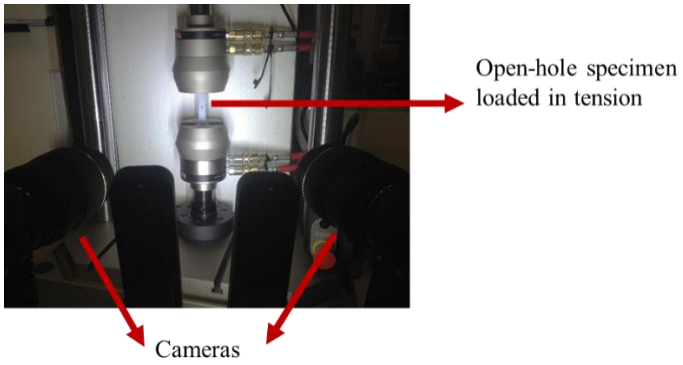

Figure 3.3: Test setup for open-hole testing

Table 3.4: Stereo DIC measurement specifications.

Specimen Type	T300-T300 $[\pm 26_5/0]_s$	MR60-YSH70 $[\pm 25_2/0]_s$
Technique	Stereo DIC	
Software	LaVision DaVis 8.3.1	
Subset size (Pixels)	29	35
Step size (Pixels)	3	3
Camera	VC-Imager 16M	
Lens	Tokina ATX AF 100/2.8	
Resolutions (Pixels)	5065 x 3336	5283 x 3408
Field of view (mm)	101.4 x 66.8	63.0 x 40.6
Spatial resolution (μm)	60	36
Strain resolution (μs)	114	68

Acoustic emission (AE) also has been employed in the open-hole tensile test for detecting damage onset as shown in Figure 3.4. Based on the different energies produced in the different damage modes, damage mechanisms can be identified. Two acoustic emission sensors were bonded to the surface of the open-hole specimens to monitor the real-time damage sequence during loading and they were connected to an AE data acquisition system (PAC) PCI2 for further analysis.

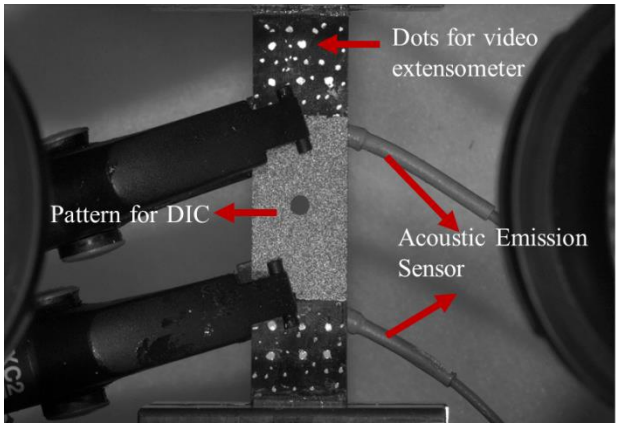

Figure 3.4: Details of the pattern used for tracking the overall longitudinal strain with a video extensometer and local strain distribution by DIC, and the position of acoustic emission.

3.3 Unnotched tension testing results

3.3.1 T300-T300 $[\pm 26_5/0]_s$ laminates

The stress-strain behaviour of the T300-T300 $[\pm 26_5/0]_s$ laminates is given in Figure 3.5 and the mean values of the key mechanical properties are summarised in Table 3.5. All five specimens showed consistent pseudo-ductile stress-strain behaviour. In the initial stage of loading, the stress increased approximately linearly with strain and a slight softening was observed after a strain of 1.0% was reached. Therefore, the modulus presented in Table 3.5 is the chord modulus, estimated between the strains of 0.1% and 0.3%. When the specimen was loaded beyond the fracture strain of the T300 fibre ($\varepsilon_x = 1.6\%$), an approximately constant stress plateau was observed. During this stage, the fibres in the central 0° plies fragmented progressively and dispersed delamination occurred. The last stage of the curve is a small amount of additional loading after saturation of the fragmentation until the mean failure strain of 3% was reached when the angle plies failed. This stress-strain curve is similar to the one presented in [11], using the same layup but a different fibre type TR30. Overall, gradual failure has been successfully achieved in this configuration, with a "yield" stress of 792 MPa and a pseudo-ductile strain of 1.39%.

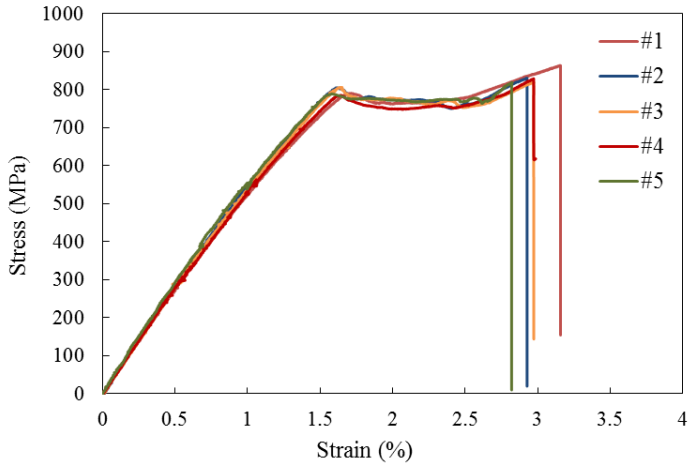

Figure 3.5: The unnotched tensile stress-strain behaviour of T300-T300 laminates.

Table 3.5: Mean values for mechanical testing results of T300-T300 $[\pm 26_5/0]_s$ and MR60-YSH70 $[\pm 25_2/0]_s$ laminates. The coefficients of variation (CV) for each mechanical property are shown in parentheses. Note: the symbol of each property was defined in the chapter 1.

	σ_Y [MPa]	σ^* [MPa]	ε_Y [%]	ε^* [%]	ε_d [%]	$\varepsilon_d/\varepsilon_Y$	E [GPa]
T300-T300 $[\pm 26_5/0]_s$	792 (1.1%)	814 (2.1%)	1.62 (1.2%)	3.00 (4.6%)	1.39 (4.6%)	0.86	57 (1.8%)
MR60-YSH70 $[\pm 25_2/0]_s$	642 (2.0%)	828 (2.4%)	0.51 (2.0%)	2.22 (6.8%)	1.54 (5.2%)	3.02	130 (3%)

3.3.2 MR60-YSH70 $[\pm 25_2/0]_s$ laminates

Figure 3.6 shows the un-notched tensile stress-strain behaviour of the MR60-YSH70 $[\pm 25_2/0]_s$ laminate and the mechanical properties are summarised in Table 3.5. All five specimens showed consistent favourable pseudo-ductile tensile stress-strain behaviour although slight discrepancies were observed in the failure strain. From the stress-strain curve, an initial linear response was observed, with an initial chord modulus of 130 GPa, measured in the region of 0.1% to 0.3% strains. This modulus is similar to the modulus of a standard modulus carbon fibre unidirectional prepreg such as Skyflex USN020A with T300 fibre, and it shows the potential of introducing pseudo-ductile sub-laminates to replace conventional standard modulus carbon fibre plies. The response was then followed by an approximately constant stress plateau,

with multiple small stress variations along the plateau. These stress variations could be due to delaminations at the 0/-25 interface initiating immediately from fragmentations of the high modulus carbon fibre layer. Another possible explanation is the relatively high thickness (t_{UD}/t_{AP}) and modulus (E_{UD}/E_{AP}) of the central 0° plies, which therefore carry a high proportion of the load compared with the angle plies, which could result in a noticeable stress reduction when they fragment. From the end of the plateau to final failure, further load was mainly carried by the angle plies.

The MR60-YSH70 $[\pm 25_2/0]_s$ laminate showed pseudo-ductility with a pseudo-ductile strain of 1.54%. Also, it is worth noting that a pseudo-ductile strain to initial strain ratio of 3.02 was achieved. This ratio satisfies the design criterion of obtaining a strain ratio higher than 3 and provides a contrast with the strain ratio of 0.86 for the T300-T300 laminate.

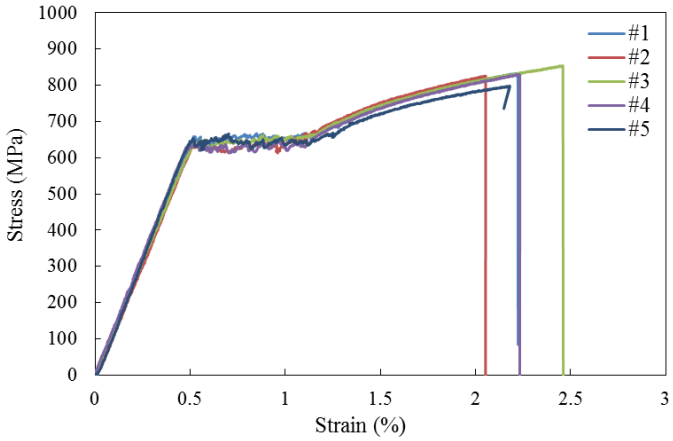

Figure 3.6: The unnotched tensile stress-strain behaviour for MR60-YSH70 laminates.

3.4 Damage mode analysis of unnotched specimens

To understand the damage mechanisms and damage evolution of these two laminates over the tensile loading, the specimens from both configurations were loaded to various different positions in the stress-strain curve and were then unloaded and analysed using X-ray CT-scanning. All the specimens were immersed in a zinc iodide dye penetrant for at least 24 hours and then scanning was performed using a Nikon XTN320 X-Ray CT inspection machine. Since a very detailed damage

analysis of $[\pm 26_5/0]_s$ laminates with TR30 fibres can be found in previous work [11], only one specimen of T300-T300 $[\pm 26_5/0]_s$ is also presented here. A detailed characterisation of the MR60-YSH70 $[\pm 25_2/0]_s$ laminates is presented in this section since damage analysis with a similar configuration has not previously been published.

3.4.1 X-ray CT-scan of T300-T300 laminates

The detailed X-ray analysis of the $[\pm 26_5/0]_s$ laminates made from thin ply prepreg with TR30 fibre presented by Fuller shows that the critical damage is observed when the fibre fragmentation strain has been reached [11]. Therefore, one T300-T300 specimen was loaded to a strain of 1.8%, which is 0.2% higher than the nominal fracture strain of the T300 fibre (1.6%), then scanned by X-ray with a resolution of 0.078 mm. Figure 3.7 shows the X-ray image of this specimen.

At this strain, fragmentations in the central 0° plies and dispersed delaminations at the 0/-26 interface were expected to have initiated, and the X-ray images shows that this is the case. Due to the low ply thickness (t=0.022mm), interference from surrounding plies occurred, resulting in the captured image at the central 0° layer from CT scanning showing multiple failure modes in varying intensities. The fragmentation showed inclined thin white lines, which can be seen propagating from the edge towards to the centre of the specimen. A larger, but less intense white region can be seen around these fragmentations, which is the dispersed delamination at the 0/-26 interface. It is also worth noting that delamination developed from the free-edge at the -26/26 interface adjacent to the central 0° plies and is shown by a white triangular shape. Some of the edge delaminations joined with dispersed delaminations, forming a larger damaged region.

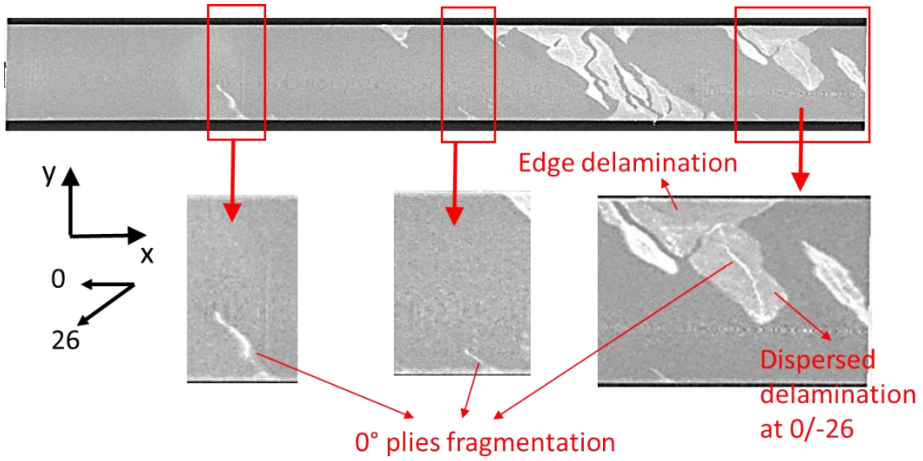

Figure 3.7: X-ray images of T300-T300 unnotched tensile specimen.

3.4.2 X-ray CT-scan of MR60-YSH70 laminates

Figure 3.9 shows the X-ray images of the MR60-YSH70 $[\pm 25_2/0]_s$ specimens which were loaded to three different strain levels of 0.58%, 1.2% and 2.1%. The interrupted positions in the stress-strain curve are shown in Figure 3.8. One ultrasonic C-scan image per specimen is also presented to help locate the damage in each specimen, since the X-ray scan was carried out smaller segments along the length of each specimen.

In the X-ray image for 0.58% strain, a few inclined thin white lines are observed in the upper region and it shows that fragmentation in the central 0° plies has initiated. Since the strain of 0.58% is close to the fibre fracture strain of 0.5%, only limited numbers of fibre fragmentation have occurred and dispersed delaminations at 0/-25 interface were developed over only small distances. Also, it is worth noting that all these fragmentations have been observed across the entire width, although the specimen was loaded to just after the fragmentation strain.

The images of the specimen - halted at a strain of 1.2% show that the fragmentations were fully saturated along the gauge length and the delamination extended further compared to the strain of 0.58%. Even though some of these inclined strips did not extend fully across the width, these regions were considered to be fragmented, since Fuller et al showed that the gap at the fragmentations in the

middle could be too small for dye solution to penetrate. Similar to the X-ray image taken at the end of the plateau, the fragmentation of the central 0° plies is fully saturated.

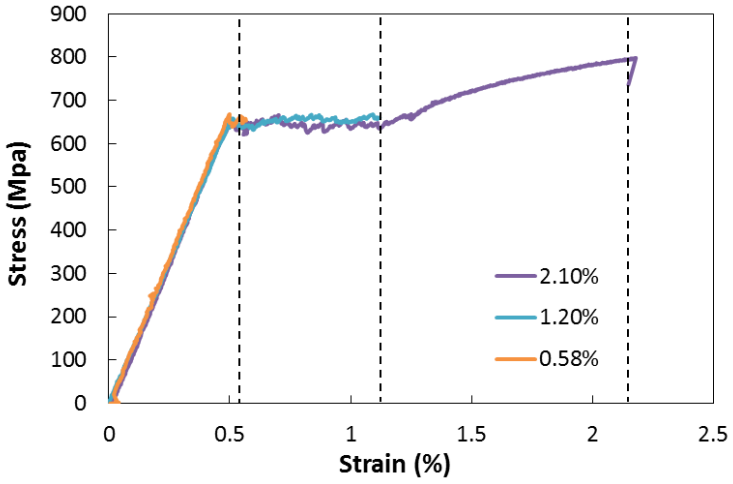

Figure 3.8: Stress-strain plot for showing the load/strain levels of the MR60-YSH70 specimens for the X-ray scans.

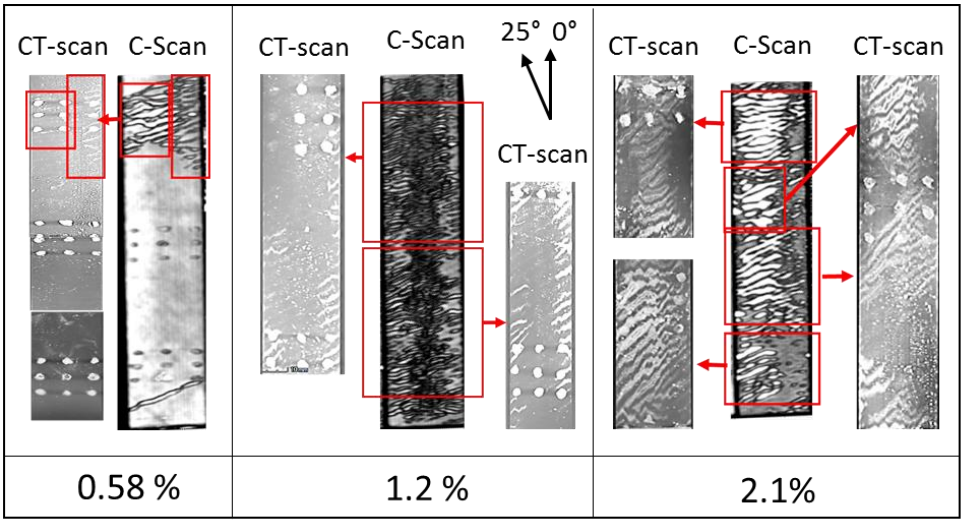

Figure 3.9: X-ray images of three MR60-YSH70 unnotched tensile specimens loaded to three different levels. C-scan images from the same specimens here show the global position of the damage in the specimens. The white dots in each X-ray image are the white paint.

When the specimen was interrupted at a strain of 2.1% very close to the ultimate failure strain, the dispersed delaminations had propagated extensively and some of the adjacent delaminations were joined together, forming a complete failure. No further fragmentation could be observed at this stage and this indicated that the angle plies carried the majority of the additional load in the final loading stage. No obvious edge delamination at the 25/-25 interface was observed in the specimen.

Overall, the T300-T300 $[\pm 26_5/0]_s$ and MR60-YSH70 $[\pm 25_2/0]_s$ laminates both have shown a promising pseudo-ductile stress-strain behaviour, and they gave very different pseudo-ductile strain to "yield" strain ratios of 0.86 and 3.02 respectively. The damage mechanisms of 0° ply fragmentation and dispersed delamination have been observed in both cases.

3.5 Open-hole tensile testing results

From section 3.3, the T300-T300 $[\pm 26_5/0]_s$ and MR60-YSH70 $[\pm 25_2/0]_s$ laminates both have shown a promising pseudo-ductile stress-strain behaviour, and they gave very different pseudo-ductile strain to "yield" strain ratios of 0.86 and 3.02 respectively. The damage mechanisms of 0° ply fragmentation and dispersed delamination have been observed in both cases.

X-ray images show that at the end of the stress plateau, the fragmentation in the 0° plies and local dispersed delamination were saturated along the entire gauge length, which means that any further loading was primarily carried by the angle plies and the laminate no longer has pseudo-ductility. As a result, in the open-hole tensile loading, once the ligament section has reached the end of the stress plateau in the unnotched stress-strain curve, this section is expected to be fully fragmented and the stress is not able to redistribute any further. Therefore, in the following paragraphs, the open-hole performance is assessed against both the unnotched "yield" stress and the ultimate strength, but the comparison is primarily focused on the unnotched "yield" stress since the unnotched "yield" stress is similar to the stress at the end of the stress plateau.

The two laminates have been tested in open-hole tension with all the specimen's design and testing set-up given in section 3.2. Two different definitions of open-hole strength are used here: net-section notched strength ($\sigma_{net\text{-}section}$) and gross notched strength (σ_{gross}), where P is the applied load.

$$\sigma_{net-section} = \frac{P}{t \times (w-d)} \tag{3.3}$$

$$\sigma_{gross} = \frac{P}{t \times w} \tag{3.4}$$

3.5.1 T300-T300 laminates

The open-hole tensile gross stress is plotted versus the "global" strain measured by the video gauge as shown in Figure 3.10, and the unnotched tensile curve of the same laminate is also presented as a reference. The averaged mechanical properties are summarised in Table 3.6. All five specimens exhibited a similar response: approximately linear up to ultimate net-section failure at the hole. The average net-section ultimate open-hole tensile strength is 527 MPa, which showed a 34% reduction compared to the unnotched "yield" strength - the maximum stress at which the pseudo-ductile laminates can normally be operated and 37% less when compared to the unnotched ultimate strength. The significant strength reduction and failure mode of this open-hole specimen is similar to those that have been presented in the studies of thin ply laminates under open-hole tension [45–47]. This brittle and net-section failure as shown in Figure 3.10, could be attributed to the lack of significant fragmentation and all other damage mechanisms being suppressed. The lack of subcritical damage for blunting the stress concentration resulted in a large strength reduction and brittle failure.

3.5.2 MR60-YSH70 laminate

The open-hole tensile gross stress-strain curves for all five MR60-YSH70 specimens are presented in Figure 3.11 and averages of key mechanical properties are tabulated in Table 3.6. All five specimens exhibited a similar linear response in the initial stage,

and then a small amount of non-linearity was shown when a strain of 0.17% was reached. This is due to the stress concentrations in the area around the hole - the fragmentation strain of the 0° plies was reached here. In this laminate, an average net-section strength of 627 MPa was achieved, which reached 97% of the unnotched "yield" strength of 642 MPa of the same laminate. If compared to its unnotched ultimate strength, the strength reduction increased to a higher figure of 24%, but it still shows that a higher open-hole strength was retained in the MR60-YSH70 laminate than in the T300-T300 laminate. This is due to the higher strain ratio in the MR60-YSH70 laminate than for the T300-T300 laminate. When the strain ratio is sufficiently large, the subcritical damage of 0° ply fragmentation and dispersed delamination can develop to blunt the stress concentration in the MR60-YSH70 laminate. Similar to the failed specimen of T300-T300 laminate presented in Figure 3.10, brittle failure mode with a clean fracture surface was also observed in the MR60-YSH70 laminate. It could be due to the delamination being localised to the fragmentation area without extensive delamination occurring across the entire width.

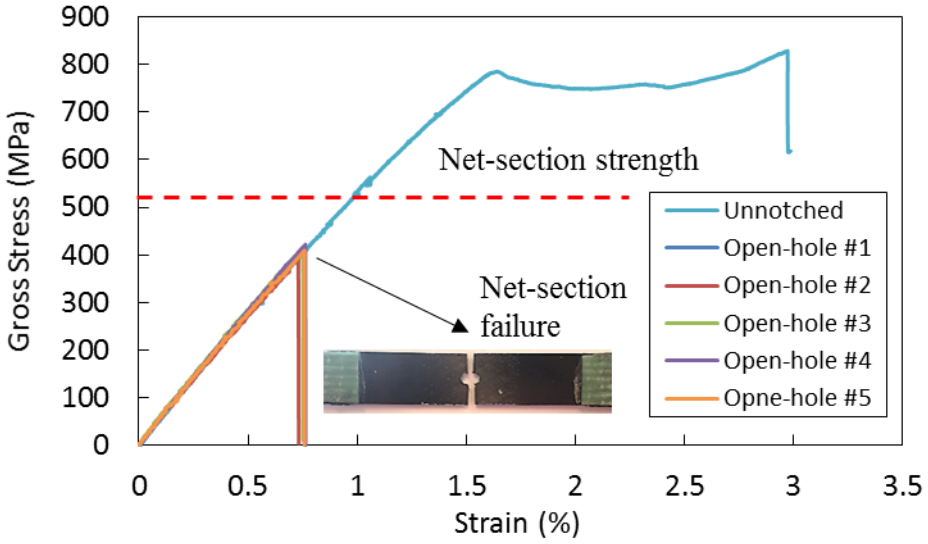

Figure 3.10: Stress-strain curves for T300-T300 $[\pm 26_5/0]_{s2}$ laminate subjected to open-hole tensile loading. An image of a failed specimen shows net-section failure. A dashed red line presents the net-section strength.

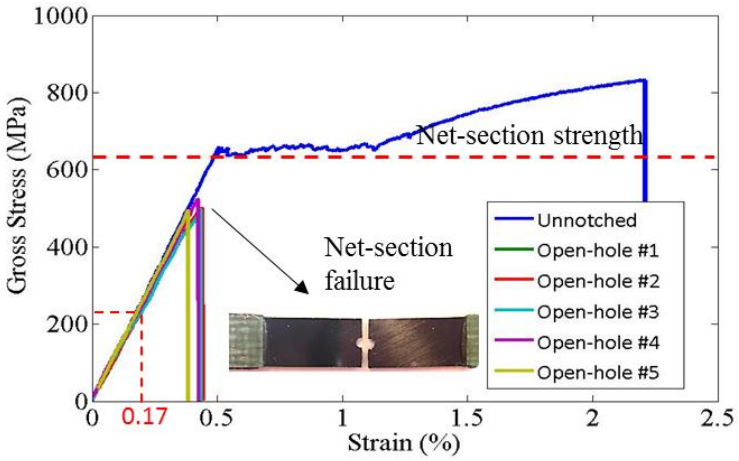

Figure 3.11: Stress-strain curves of MR60-YSH70 $[\pm 25_2/0]_{s4}$ laminate subjected to open-hole tensile loading. An image of a failed specimen shows net-section failure. A dashed red line presents the net-section strength

Table 3.6: Average test results for open-hole testing of T300-T300 $[\pm 26_5/0]_{s2}$ and MR60-YSH70 $[\pm 25_2/0]_{s4}$ laminates. The gross strength σ_{gross} was calculated from the full width and the net-section strength $\sigma_{net\text{-}section}$ was calculated from the reduced width across the hole. $\sigma_{net\text{-}section}$ is used as the critical strength in this study. CV for each mechanical property are shown in parentheses. Note the E presented in this table refers to the stiffness of the stress-strain curve, not Young's modulus as the strains were measured over the notched and unnotched sections.

		T300-T300 $[\pm 26_5/0]_{s2}$	**MR60-YSH70 $[\pm 25_2/0]_{s4}$**
Unnotched	σ_{yield} [MPa]	792 (1.1%)	642 (2.0%)
	ε_{yield} [%]	1.62 (1.2%)	0.51 (2.0%)
Open-hole	σ_{gross} [MPa]	413 (4.8%)	502 (2.4%)
	$\sigma_{net\text{-}section}$ [MPa]	516 (4.8%)	627 (2.4%)
	$\varepsilon_{failure}$* [%]	0.76 (5.3%)	0.42 (2.3%)
	E [GPa]	56 (5.4%)	122 (3.3%)
	$\sigma_{net\text{-}section}/\sigma_{yield}$	0.65	0.97

3.6 Damage analysis of open-hole specimens

As seen from the open-hole stress-strain behaviour of the two different laminates in Figure 3.10 and Figure 3.11, the open-hole strength has been retained in the MR60-

YSH70 $[\pm 25_2/0]_{s4}$ laminates, but not in the T300-T300 $[\pm 26_5/0]_{s2}$ laminates. To further understand the damage mechanisms causing the different notched performances in these laminates and the damage evolution during the loading, in-situ techniques of acoustic emission and DIC, and post-failure analysis methods such as Ultrasonic C-scan and X-ray CT-scanning were employed in this study.

3.6.1 Acoustic emission

In the acoustic emission, different damage modes can be distinguished by the different energies detected. In the study conducted by Fotouhi et al. [29], it is shown that the damage initiation energy of delamination and fibre breakage are 200aJ and 500aJ respectively.

Based on this, Figure 3.12 shows AE events of the T300-T300 Open-hole specimen during loading and the corresponding stress-strain curve also plotted for tracking the damage onset stress. At the early stage from 0 to 0.67% strain, apart from a few low energy noises, there is no significant high energy event detected. It indicates that the critical damage has not initiated at this stage. When the strain of 0.67% was reached, a few high energy events were detected and the energy levels of these events were associated with fibre fragmentation. In overall terms, only limited damage developed in the T300-T300 specimen before ultimate failure. The stress concentration around the hole and the nature of damage suppression in the thin-ply laminates result in this brittle and catastrophic failure, due to lack of damage mechanisms that can reduce the stress concentration.

Figure 3.13 shows the AE events of the MR60-YSH70 specimen combined with the gross stress-strain curve. Similar to Figure 3.12, only noise signals were detected in the beginning of loading. The first major energy event that was detected when the global strain reached 0.18% was presumed to be the first damage initiation. In the later stage in the stress-strain curve, a large number of high energy fragmentation and delamination events were captured, particularly after a strain of 0.35% had been reached.

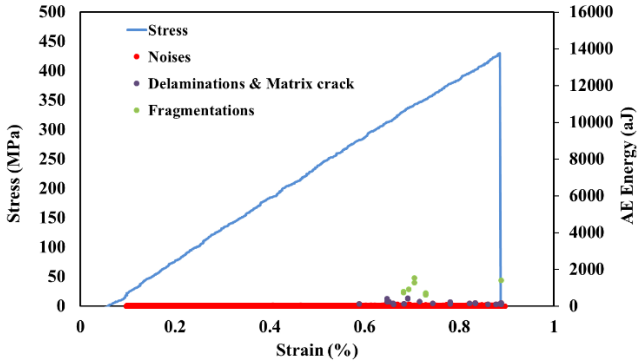

Figure 3.12: Stress-strain curve and acoustic emission energy distribution for T300-T300 laminates under open-hole tension testing

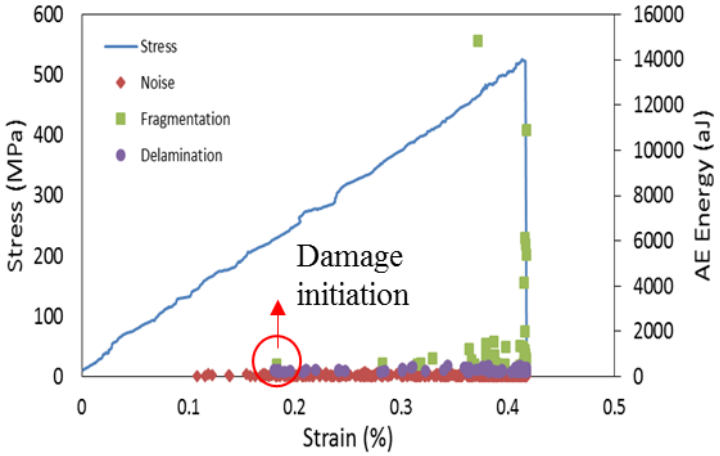

Figure 3.13: Stress-strain curve with Acoustic Emission energy results for open-hole MR60-YSH70 specimen

3.6.2 Damage analysis via digital image correlation (DIC)

Although DIC is not able to show the damage directly, it can be a useful tool for preliminary analysis of surface strain variation of these pseudo-ductile laminates under open-hole tension and for comparing these two different configurations.

Surface longitudinal strain fields taken at 98% of the failure load of the T300-T300 and MR60-YSH70 open-hole tensile specimens are plotted in Figure 3.14. The surface strain images on the left hand side of Figure 3.14 are plotted within a colour map, and the strains in both images can be seen highly concentrated next to the hole edge. However, it is hard to tell any difference between them as the images

are shown with the same colour contours. Since there was no observable block of delamination in the open-hole specimen, the strain in the central 0° plies can be assumed to be the same as the surface ply as all the plies are still connected. If the fibre fracture strain of the central 0° plies is used as a relative point – the surface strains higher than the fibre fracture strain (1.6% for T300-T300 laminate and 0.5% for MR60-YSH70 laminate) are plotted in white, whilst the remaining parts are plotted dark. The surface strain distribution is plotted like this in the two images on the right-hand side of Figure 3.14 and these images are called "strain damage maps" in the following paragraphs. As discussed in the damage analysis of the unnotched specimen, fibre fragmentation in the central 0° plies is the first damage to occur, so all of the area in white is likely to be fragmented.

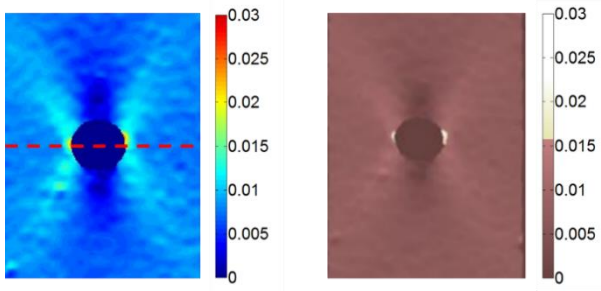

(a) T300-T300 $[\pm 26_5/0]_s$

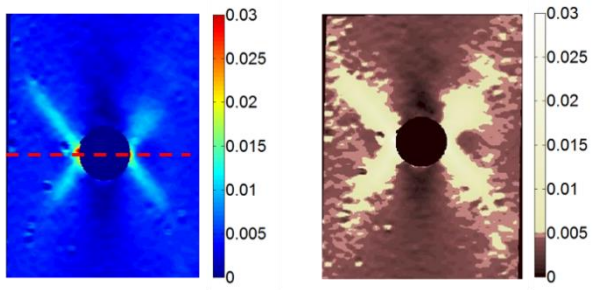

(b) MR60-YSH70 $[\pm 25_2/0]_s$

Figure 3.14: Original and scaled longitudinal surface strain map of (a) T300-T300 $[\pm 26_5/0]_{s2}$ laminate and (b) MR60-YSH70 $[\pm 25_2/0]_{s4}$ laminate. All images were taken at 98% of the ultimate strength.

In the "strain damage map" of the T300-T300 laminates, the fragmentation strain has been reached only in the area close to the hole edge. However, in the

MR60-YSH70 laminates, the white areas extend from the hole boundary approximately parallel to diagonal line, indicating the appearance of fibre fragmentation in the central 0° plies and presumably also some dispersed delaminations at the 0/−25 interface.

It can be clearly seen that more damage is present in the MR60-YSH70 laminate than the T300-T300 laminate at 98% of ultimate load, and this damage relieved the stress concentration at the hole edge. Further understanding of how the damage developed during the loading can be gained through several surface strain maps taken at different positions along the stress-strain curves as indicated on the local strain versus applied load relation.

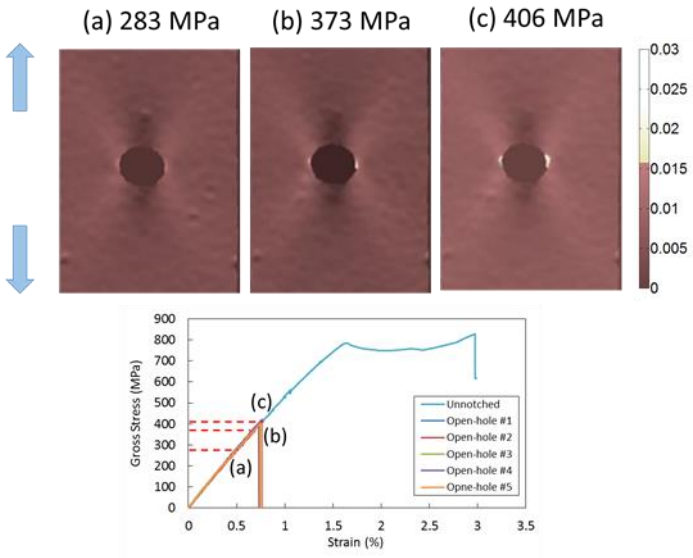

Figure 3.15: Scaled longitudinal surface strain maps for T300-T300 $[\pm 26_5/0]_{s2}$ laminate at various applied stresses.

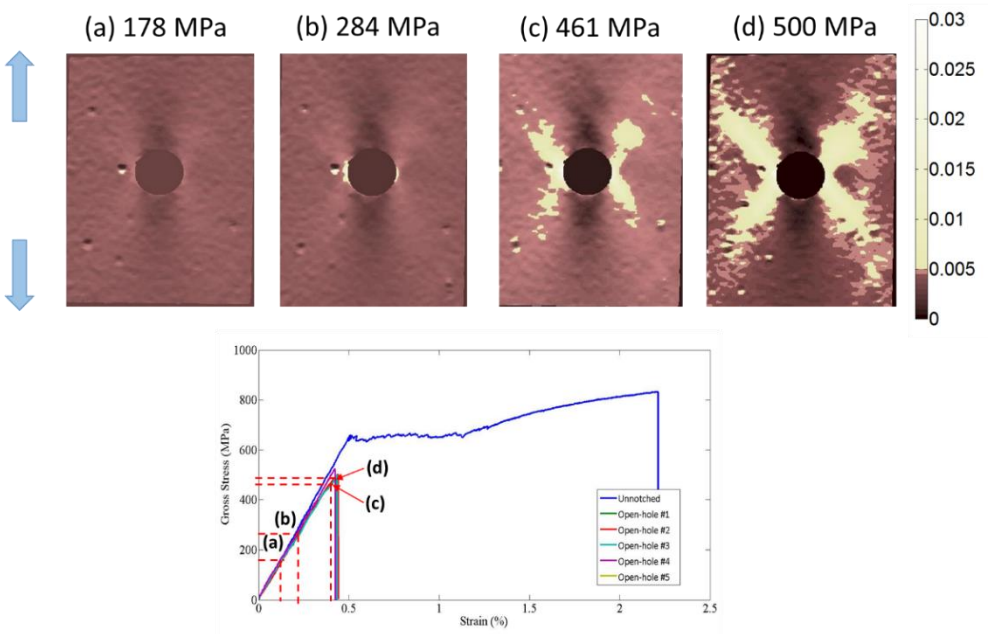

Figure 3.16: Scaled longitudinal surface strain maps for MR60-YSH70 $[\pm 25_2/0]_{s4}$ laminate at various applied stresses.

Figure 3.15 and Figure 3.16 show the "strain damage maps" of the T300-T300 $[\pm 26_5/0]_{s2}$ and MR60-YSH70 $[\pm 25_2/0]_{s4}$ laminates respectively. For the T300-T300 laminate, no damage could be seen until the applied stress reached 373 MPa, 90% of the ultimate stress. After that, the damage only extended to a slightly larger region before ultimate failure. In the "strain damage maps" of the MR60-YSH70 specimen, early fibre fragmentation can be observed when the applied stress is 284 MPa, 44% of the open-hole ultimate strength and at a corresponding laminate strain of about 0.17%, which is similar to the first major energy event detected in Figure 3.13. Consequently, a small amount of nonlinearity can be seen in the gross stress-strain curve starting from this stress.

From Figure 3.15 and Figure 3.16, the hole edge was shown as the first region that has been damaged, therefore the curves of local strain at the hole edge were plotted against load in Figure 3.17 (a) and (b). The hole edge strain of the T300-T300 specimen increases approximately linearly with the applied load and only at 98% of ultimate load is there an increase in the slope. By contrast, the MR60-YSH70

laminates present a more complicated three-stage local strain variation in Figure 3.17 (b). The first sharp increase in slope occurred when the specimen was loaded to 46% of ultimate load. At this load, the corresponding strain is 0.5%, the same as the YSH70 fibre fracture strain. It means that fragmentation initiated in the central 0° plies and resulted in a local stiffness loss. The second critical point in terms of the rate of change of strain happened at 94% of the ultimate load. At this point, the area around the hole was already close to its unnotched ultimate failure strain and the hole edge was fully damaged in the 0° plies and the 0/-25 interface. The angle plies carried most of the load and the fracture process zone started to develop.

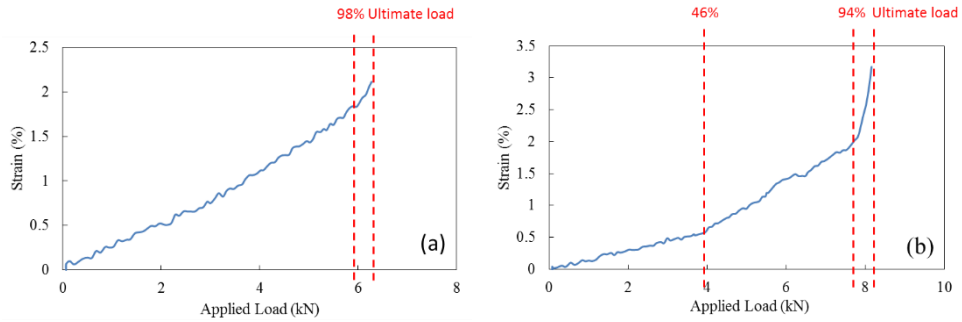

Figure 3.17: The strain at the critical point variation with the applied load of (a) the T300-T300 laminate and (b) the MR60-YSH70 laminates

Further investigation of the strain distributions across the entire width of the specimens at different loads have been plotted in Figure 3.18 (a) and (b). Both tested laminates have shown strain concentrations near the hole, but the strain concentration factor varies in different cases. The strain concentration factor (SCF), determined from the strain at the hole edge divided by the far-field strain, for the T300-T300 laminate remains at almost the same level, changing from 2.5 at loading initiation to 2.8 at just before failure. However, for the MR60-YSH70 laminates, the SCF increases from roughly 3.03 at the start of loading to 7.1 at ultimate load. These observations in SCF can identify that the T300-T300 laminate remained in the linear region and the MR60-YSH70 laminate reached non-linearity and achieved local strain redistribution after a certain applied load. Although the calculation of strain concentration based on the surface strain measurement were not precise due to lack

of resolution close to the hole edge, the large strain concentration increase can still indicate more stiffness loss and deformation at the hole edge in the MR60-YSH70 laminate than in the T300-T300 laminates.

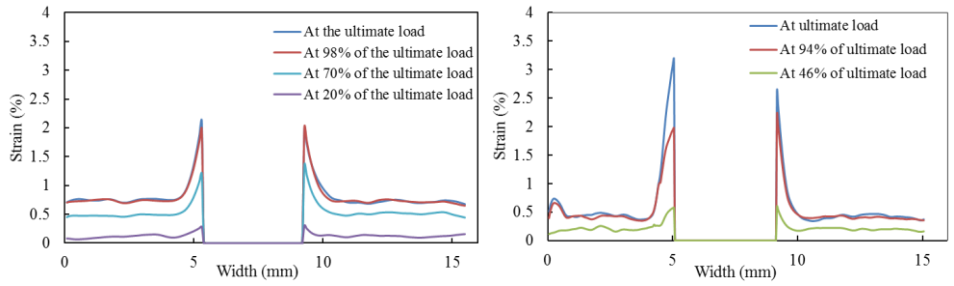

Figure 3.18: Strain distribution across the width at various loading stages for (a) T300-T300 laminate and (b) MR60-YSH70 laminate.

3.6.3 Damage analysis via ultrasonic C-scan

Even though the surface strain map taken by the DIC can identify possible damage within the laminate during loading and explain the differences between the two configurations, it is not a direct technique to observe damage in the laminates. To investigate the damage that has developed in the open-hole tensile loading more accurately, ultrasonic C-scan and X-ray CT imaging were used here.

One specimen from each configuration was loaded to 90% of the open-hole ultimate strength and then immersed in a water tank for an ultrasonic C-scan with frequency 5kHz. Both C-scan images present the front view at the 0/-θ interfaces. In the C-scan image of the T300-T300 laminate as shown in Figure 3.19(a), there are some highlighted areas around the hole, which are suspected to be drilling damage. Apart from that, there is no obvious delamination observed. In the C-scan image of the MR60-YSH70 laminate, the delamination highlighted in the bright white colour is located on both sides of the hole and extends in the direction of diagonal line. However, due to the rather low ply thickness and lack of delamination in these laminates, Ultrasonic C-scan was not sufficient in this case and X-ray CT-scan imaging was required as the resolution of available X-ray machine can be less than the ply thickness of these laminates.

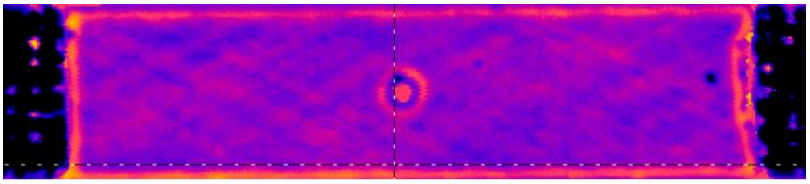

(a) T300-T300 $[\pm 26_5/0]_s$

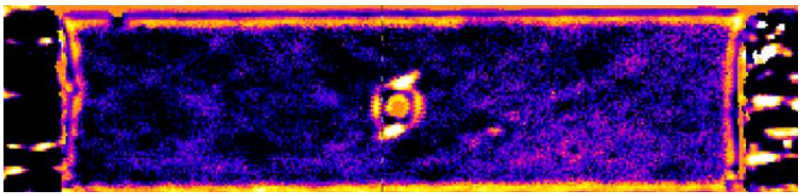

(b) MR60-YSH70 $[\pm 25_2/0]_s$

Figure 3.19: Ultrasonic C-scan images of open-hole specimens for both layups interrupted at 90% of the ultimate load.

3.6.4 Damage analysis: X-ray CT imaging

The same specimens used for ultrasonic C-scans were submerged in a zinc iodide dye penetrant solution and then analysed using X-ray CT scans. The X-ray images of the T300-T300 and the MR60-YSH70 laminates are presented in Figure 3.20 and Figure 3.21 respectively. All damage has been highlighted as a white colour and the grey areas correspond to undamaged material, as discussed in the unnotched tensile testing. The corresponding DIC images from the same specimen at the same load level are also included.

Figure 3.20 shows the X-ray images for the T300-T300 specimen taken at two different locations of the 0/-θ interfaces through the thickness, illustrated by a red dashed line. The scan resolution is 0.0376 mm. In both images, no critical damage can be observed. The only area highlighted in white is the small region around the hole, which may be machining damage and need not be taken into account. These X-ray images are similar to the X-ray images for open-hole thin ply QI laminates – no visible damage at the hole edge or free-edge due to the damage suppression in thin ply laminates. This indicates that the damage mechanisms observed in the unnotched pseudo-ductile laminates have not occurred in the open-

hole specimen with the same layup, due to the insufficient strain ratio margin. The "strain damage map" taken at the same load level for the same specimen is shown in Figure 3.20 (c). No damage is visible, which correlates well with the X-ray images.

Figure 3.21 (a – d) presents the X-ray images of the MR60-YSH70 laminates captured at four different 0/-25 interfaces through the thickness with a scan resolution of 0.044 mm. The DIC "strain damage map" taken at the same loading (90% of ultimate load) is given in Figure 3.21(e), showing that fragmentation of the central 0° plies has initiated. The X-ray images show a similar pattern of damage located on both sides of the hole edge and roughly parallel to the diagonal line direction. The white strips shown in the red bounded boxes have a certain width and are not exactly straight, correspond to the central 0° plies fragmentation and associated dispersed delamination. This is totally different from the micro-cracks/splitting in angle plies or 0° plies that has been observed in most open-hole testing of laminates.

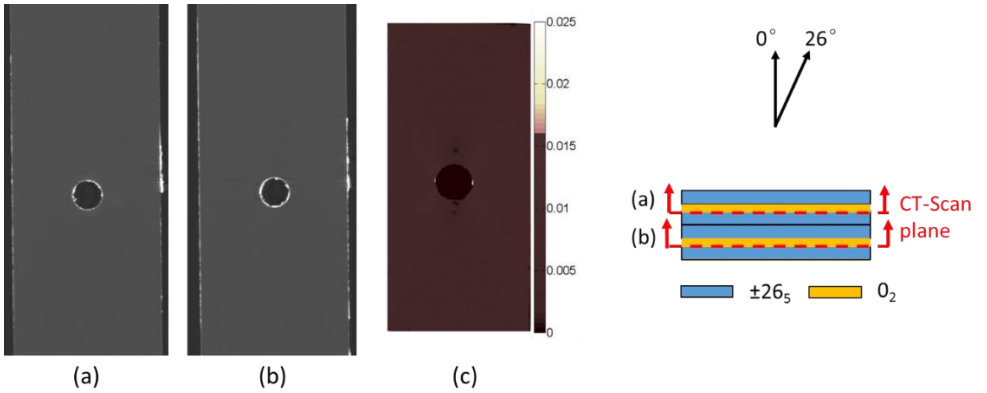

Figure 3.20: (a) (b) X-ray images for the open-hole T300-T300 $[\pm 26_5/0]_{s2}$ laminate, taken at two different 0/-26 interfaces shown as the red dashed line. (c) The "strain damage map" of the same specimen at the same load (90% of ultimate load)

The X-ray images confirmed that the higher open-hole strength in the MR60-YSH70 laminates compared with the T300-T300 laminates is due to the reduction of stress concentrations around the hole after the damage initiated by 0° ply fragmentation and dispersed delamination. 0° ply splitting, as the main mechanism for blunting the stress concentration in the laminates made from

conventional thickness ply, was not seen in these pseudo-ductile laminates. Therefore, the hole size effect - the stress blunting effects of the 0° splitting reduced with the increase of hole diameter [176], observed in the conventional laminates was not applicable to this study. Increasing the hole diameter from 3.175 mm to higher values, is not expected to significantly reduce the strength of these pseudo-ductile laminates, since the stressed and damaged area will also increase with further relief of the stress concentration. However, hole size studies in notched pseudo-ductile thin ply angle-ply laminate with central 0° plies are still worth carrying out as future work.

It is also shown that the DIC technique is a sufficient tool to determine where the damage is likely to have occurred and for a preliminary verification of what the possible damage mechanisms are in the pseudo-ductile thin ply angle-ply laminates under open-hole loading.

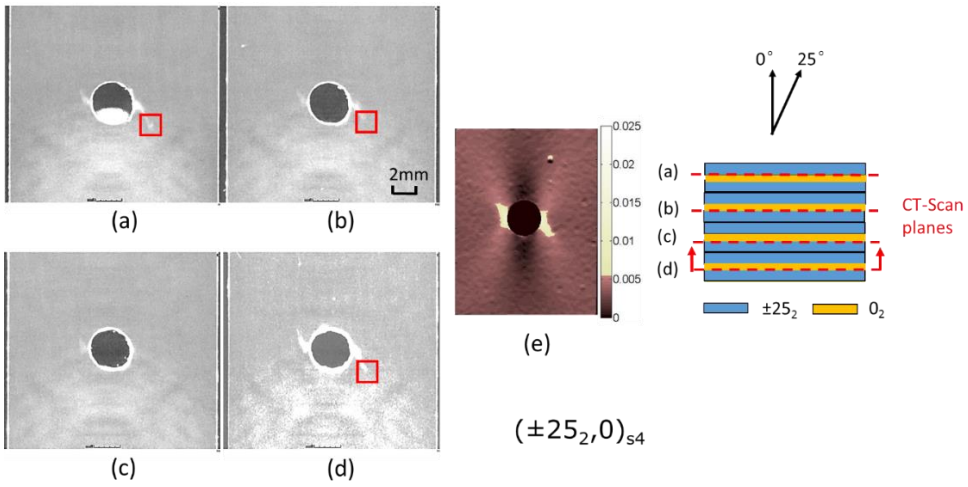

Figure 3.21: X-ray images for the open-hole MR60-YSH70 $[\pm 25_2/0]_{s4}$ laminate, taken at four different -25/0 interface shown in the red dashed lines from (a) to (d). It should be noted that the large white region at the bottom of all four images and the white "ellipse" in the hole in (a) are the rubber used to hold the specimen during CT scan, so do not constitute any damage. (e) "Strain damage map" predicted from DIC in the same specimen at the same load level (90% of ultimate load).

3.7 Conclusions

Pseudo-ductile tensile stress-strain behaviour has been demonstrated in unnotched T300-T300 $[\pm 26_5/0]_s$ and MR60-YSH70 $[\pm 25_2/0]_s$ laminates. The ratio of pseudo-

ductile strain to "yield" strain for the T300-T300 laminate and MR60-YSH70 laminate were 0.86 and 3.02 respectively. Central 0° ply fragmentation and dispersed delaminations have been shown as the main damage mechanisms in both tested laminates via X-ray CT scanning. However, their performance was different in the presence of stress concentrations when they were subjected to open-hole tensile loading: the T300-T300 laminate is sensitive to the stress concentrations, but the notch sensitivity in MR60-YSH70 laminate is reduced. The open-hole net-section strength is similar to the unnotched "yield" strength of the MR60-YSH70 laminate and less strength reduction is observed in the MR60-YSH70 laminate than the T300-T300 laminate, when comparing the notched strength to the unnotched ultimate strength.

The X-ray images showed a larger damaged area in the MR60-YSH70 specimen than in the T300-T300 at 90% of ultimate loading. The damage mechanisms of unnotched MR60-YSH70 laminates, with 0° ply fragmentation and dispersed delamination, have also been seen in the open-hole specimens with the same layup. These damage mechanisms relieved the stress concentration around the hole in the MR60-YSH70 laminate, resulting in an enhanced notched strength and reduced notch-sensitivity of the MR60-YSH70 laminates compared with the T300-T300 laminates. If the strain ratio is low, the strain at the hole edge reaches the unnotched ultimate tensile failure strain, whilst the rest of the region is still below the fibre fragmentation strain and damage progression and associated stress redistribution is limited in the laminate. But if the strain ratio is high, full load redistribution can take place.

Digital image correlation has been found to be a useful tool to identify damage development in pseudo-ductile thin ply angle-ply laminates with central 0° plies. From the surface longitudinal strain distribution and the local strain variation around the hole, the initial damage in the open-hole T300-T300 specimens was found to occur at 98% of the ultimate load. However, damage was found in the MR60-YSH70 specimen when the specimen was loaded to only 46% of its ultimate load. The presence of damage at an early stage relieved the stress concentration by the damage developed within the laminates.

From the study of both laminates presented above, it has been successfully demonstrated that the notch-sensitivity can be reduced in thin ply laminates by taking advantage of the damage mechanisms of pseudo-ductile thin ply angle-ply laminates with central 0° plies. It also showed the potential that by proper selection of materials and layup in these laminates, the behaviour of the laminate can be tailored to either unnotched or notched critical applications.

4 Exploration of potential pseudo-ductility in compression

Compressive failure is critical in many loading cases, potentially limiting the applications of pseudo-ductile $[\pm\theta_m/0_n]_s$ laminates which have successfully demonstrated tensile metal-like gradual failure. The aim of this work is to experimentally explore the potential of using the thin ply angle-ply concept for achieving compressive pseudo-ductility in carbon fibre laminates. A laminate with a $[\pm27_7/0]_s$ configuration was selected and tested in compression, via a sandwich beam subjected to four-point bending. From the stress- strain curve, a significant amount of non-linearity has been observed and an average failure strain of 1.08% has been attained. Visual damage observation of a single fracture parallel to the angle-ply direction suggested that the compressive failure could be attributed to the high transverse tensile and in-plane shear stresses. X-ray analysis and microscopic observations revealed that 0° ply fragmentation was the main mechanism for gradual failure, inhibiting delamination at the 0/-27 interface.

4.1 Introduction

To be able to extend the pseudo-ductile thin ply angle-ply laminates to wider applications, compressive performance needs to be considered as it is usually much lower than the tensile performance [83]. Compressive failure is the dominant failure mode in many combined loading cases, such as bending, static indentation and impact.

In carbon fibre laminates made from standard thickness plies, the main compressive failure mode is plastic microbuckling or kinking [84,177–179]. Previous studies showed that in the case of off-axis laminates with internal 0° plies $[\pm\theta_m/0_n]_s$ subjected to compressive loading, laminates failed catastrophically by microbuckling the of 0° plies and followed by delamination, leading to the internal 0° plies not being supported by the angle plies [177,180]. Studies conducted on the scaling and thickness effect on compressive behaviour of CFRPs suggested that the number of delaminations and matrix cracks decreases with the reduction of ply thickness [181]. Similar observations have also been seen in laminates made with thin ply prepregs [43,45]. A uniform microstructure with better fibre alignment and a small resin rich region enables a better compressive performance and less delamination in thin ply laminates compared to laminates with thicker plies.

The aim of this chapter is to avoid the catastrophic failure in compression of thin ply angle-ply laminates containing 0° plies, since the research presented thus far has shown that delamination can be suppressed in tensile or compressive loading if the plies are sufficiently thin, to achieve similar pseudo-ductility in compression [43].

4.2 Laminate design and material selection

As an initial investigation, a similar layup to the tension tests of $[\pm\theta_n/0_m]_s$ was used in compression. Progressive fibre fractures of high modulus carbon fibre in compression were observed in a glass-carbon hybrid beam under four-point bending loading [15]. To promote progressive fibre fractures in the central 0° plies of a pseudo-ductile thin ply angle-ply laminate, high modulus fibre prepreg was selected for the central 0° plies. The compressive fracture strains of three different high

modulus fibres and the ratio of the compressive facture strain to tensile fracture strain are presented in Table 4.1. The M55 fibre shows the highest compressive fracture strain and compressive to tensile strain ratio among all three fibres. Therefore, the M55 fibre was selected for the 0° plies in this study.

Table 4.1: Compressive failure strain and the ratio of compressive strain to tensile strain of three different high modulus fibre types.

	YSH70A	M55	XN80
E [GPa]	720	540	780
ε_c [%]	0.12	0.46	0.073
ε_t [%]	0.5	0.8	0.5
$\varepsilon_c/\varepsilon_t$	0.24	0.57	0.15

Similar to the tensile testing, the stress in the angle plies at the fracture of the 0° ply needs to be taken into consideration (equation (3.1)) to promote fibre fragmentation in the central 0° plies instead of single-fracture of the laminate. Intermediate modulus fibre prepregs were selected for the angle plies. A $[\pm 27_7/0]_s$ combination was tested, since ±27° is expected to show a promising combination of nonlinearity and considerable strength. Seven pairs of ±27° angle plies were selected enabling the angle plies are strong enough to take the non-uniform stress distribution around them once the compressive fracture of the central 0° plies occurred.

Table 4.2: Cured ply properties of UD laminates

		MR60/Epoxy	M55/Epoxy [15]	IM7/8552[182]
E_1	[GPa]	146	280	164
E_2	[GPa]	6.6	6.2	11.4
σ_1	[MPa]	2800	2240	2723
G_{12}	[GPa]	2.97	5.0	5.17
ε_{1c}	[%]	-	0.456	-
t	[mm]	0.028	0.032	0.125
v_f	[%]	50	50	60

The material selected for the angle plies was the Skyflex UIN020 prepreg (termed MR60), the same as used in chapter 3. For the 0° plies, the North M55JB-

ThinPreg120EPHTg-402 prepreg with M55 high modulus fibre (termed M55) was selected. The North M55/epoxy prepreg uses the same resin system as the North YSH70A/epoxy prepreg that was used in chapter 3, therefore the curing cycles of the two prepregs are the same as previously mentioned. The key mechanical properties of the cured prepregs are given in Table 4.2.

4.3 Compression test method selection

A number of test methods are available to determine the compressive behaviour of carbon fibre laminates[15,183–185]. Illustrations of these test methods are shown in Figure 4.1. Different test methods can bring significant discrepancies in measurements, therefore the selection of a test method needs to be well considered [186].

Firstly, some of these methods often require highly precise and complex machining. For example, the Imperial College of Science, Technology and Medicine (ICSTM) Method via end-loading and shear in the tab requires a high precision in specimen machining and can easily fail in undesirable modes, such as failure in the end-tabs due to the formation of stress-concentration. Another method - ASTM D-695 - requires specimens to be in a dog-bone shape, which can bring more complexities in specimen machining. The second consideration is for the material usage efficiency. Due to the low ply thickness (t = 0.03 mm), many plies are required to satisfy the thickness requirement for direct testing. For instance, 80 plies are needed for maintaining a specimen thickness of 2 mm. Thirdly, a short specimen gauge length of 10 mm is usually used in direct compression. This is not ideal for testing angle-ply laminates, since the fibre rotation is constrained by the end-tabs. In the hybrid beam bending method, the specimen is placed on the top of a glass substrate and then the entire hybrid beam is tested in a four-point bending configuration. However, due to the significant fibre rotation of angle plies and the mismatch between the Poisson ratio of the angle-ply laminate and the glass substrate, the hybrid beam bending method is not suitable for this case.

Following all the considerations discussed above, an indirect compression test method via 4-point bending of a sandwich beam was selected. In this method, the laminate to be examined is used as the top skin of a sandwich beam, which is loaded in compression under flexural loading. Since the laminate to be examined is bonded to a honeycomb core and the overall deflection is small, specimen buckling that was observed in a direct compression test would not be expected to be observed in this method. There are a few drawbacks using this method, such as the possibility of premature core failure - core crushing and core shear failure, and the difficulty of measuring the stress directly in a bending test. Premature core failure can be avoided via sandwich beam design. A method has also been developed to derive the stress and will be presented in section 4.6.2.

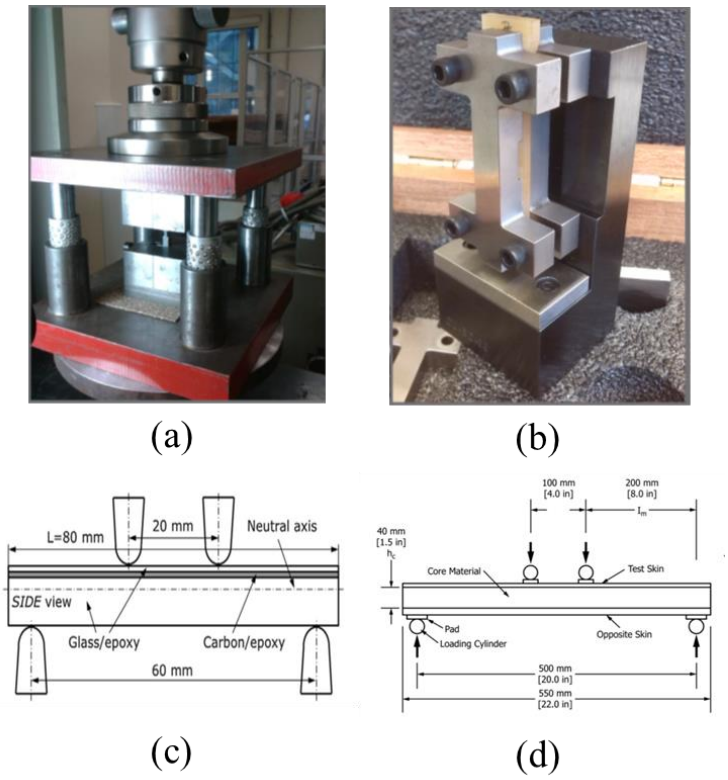

Figure 4.1: Common ompression test methods (a) ICSTM , (b) ASTM D695, (c) hybrid beam method [15] and (d) ASTM D5467 [182].

4.4 Sandwich beam design

4.4.1 Skin and core design considerations

The design of the top skin, sandwich core and the bottom skin were considered separately when designing the sandwich beam. The MR60-M55 $[\pm 27_7/0]_s$ laminate was selected for the top skin. The ASTM standard D5467 recommends that the thickness of the bottom skin should be at least twice that of the top skin to avoid failure in the tensile side. Large amounts of material would be required if using the same thin ply prepreg in the bottom skin. As an alternative, a layup of $[\pm 27_3/0]_s$ using the Hexcel IM7/8552 prepreg (t = 0.125 mm) was selected in the bottom skin. The similar orientation of angle plies in the bottom skin to the top skin is chosen to match fibre angles between the two skins as much as possible, whilst the 0° plies should add extra stiffness to ensure the bottom skin behaves linearly. The material properties of the Hexcel IM7/8552 prepreg are given in Table 4.2 and the estimated modulus of the skins from Classical Laminate Analysis (CLA) is presented in Table 4.3.

Table 4.3: The estimated modulus in longitudinal direction of the top and bottom skins (calculated from CLA).

	MR60-M55 $[\pm 27_7/0]_s$	IM7/8552 $[\pm 27_3/0]_s$
E_x [GPa]	59.0	82.3

The core material selection is also critical for the beam performance. A couple of considerations have been made here:

- Core material: subject to material availability, core selection focused on the use of a Nomex honeycomb with a cell size of 3.2 mm, as it has shown the best range of compression strengths among all cell sizes.
- Density of the honeycomb: the density of the Nomex honeycomb has a significant influence on both the compressive and shear strengths. For instance, the Nomex honeycomb with the highest density (144 kg/m^3) shows three times higher compressive modulus and shear strength in the ribbon direction compared to the same grade honeycomb with a lower density (64 kg/m^3). To maintain the

beam rigidity and to avoid any premature core failure, the Nomex honeycomb with a density of 144 kg/m^3 was selected.

- Height of the honeycomb: core height determines both the bending and core shear rigidities of a sandwich beam. Further detail will be given in section 4.4.2.

4.4.2 Beam design considerations

To estimate the stress in the skins and bending stiffness of the beam, the neutral axis position needs to be determined. Due to the property mismatch of the top and bottom skins, the neutral axis position can be found using the following equations [187]. The graphical representation of all the parameters in the equations are presented in Figure 4.2, where subscripts t, b, and c denote the properties of the top skin, the bottom skin and core respectively:

$$y_{NA} = \frac{t_t\left(d-\frac{t_t}{2}\right)+\left(\frac{E_c}{E_t}\right)t_c\left(t_b+\frac{d-t_t-t_b}{2}\right)+\left(\frac{E_b}{E_t}\right)t_b\left(\frac{t_b}{2}\right)}{t_t+\left(\frac{E_c}{E_t}\right)t_c+\left(\frac{E_b}{E_t}\right)t_b} \quad (4.1)$$

The effective second moment of area I for each part as well as the combined sandwich beam can be expressed as:

$$I_{top} = \frac{wt_t^3}{12} + wt_t\left(d-\frac{t_t}{2}-y_{NA}\right)^2 \quad (4.2)$$

$$I_{core} = \frac{wE_ct_c{}^3}{12E_t} + w\frac{E_c}{E_t}t_c\left(t_b+\frac{d-t_t-t_b}{2}-y_{NA}\right)^2 \quad (4.3)$$

$$I_{bottom} = \frac{wE_bt_b{}^3}{12E_t} + w\frac{E_b}{E_t}t_b\left(y_{NA}-\frac{t_b}{2}\right)^2 \quad (4.4)$$

$$I = I_{top} + I_{core} + I_{bottom} \quad (4.5)$$

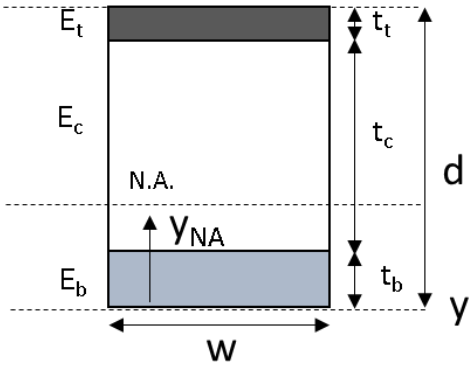

Figure 4.2: Schematic shows the cross-section of a sandwich beam. All the symbols used in the equations are presented here.

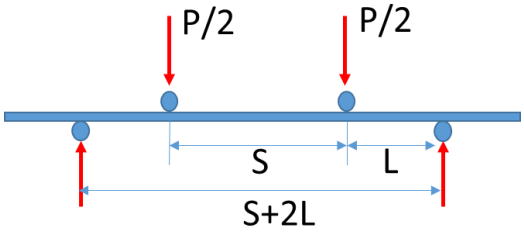

Figure 4.3: Schematic of a four-point bending condition.

When the entire sandwich beam is loaded in four-point bending as shown in Figure 4.3, the deflection and bending moment M are found to be a maximum between the two loading rollers. At the same time, the shear force V is a maximum in the regions between the supporting and loading rollers and is zero between the loading rollers. The in-plane stresses in the top and bottom skins σ_{top} and σ_{bottom}, and core shear stress τ_c can be calculated as follows:

$$M_{\max} = \frac{PL}{2} \tag{4.6}$$

$$V = \frac{P}{2} \tag{4.7}$$

$$\sigma_{top} = \frac{M(d - y_{NA})}{I} \tag{4.8}$$

$$\sigma_{bottom} = \frac{M(y_{NA})}{I} \times \frac{E_b}{E_t} \tag{4.9}$$

$$\tau_c = \frac{V}{w(d - t_t - t_b)} \tag{4.10}$$

4.4.3 Beam geometry

Once the layups of the top and bottom skins, and core material type were determined, the main focuses of beam design were the test configuration and core dimensions. The span between the loading and support rollers has a large effect on the core shear stress and deflection of the beam. Minimising the core shear stress can avoid premature core shear failure and reduce the shear deflection of the beam, therefore the moment arm L needs to be sufficiently long. A supporter span distance of 340 mm and a loading span of 40mm were used in this case. In terms of the core dimensions, the height of the core also influences the core shear stress and shear deflection. The final dimensions of the sandwich beam are summarised in Table 4.4.

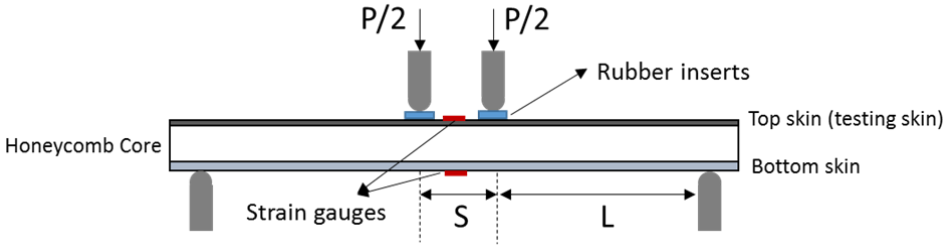

Figure 4.4: Specimen schematic for a sandwich beam geometry and test setup

4.5 Manufacture and testing procedures

The sandwich beam was manufactured using a post-cure bonding method, since the two skin laminates require different curing cycles. Firstly, the top and bottom skins were cured separately in the autoclave using their specific cure cycles. The cure cycle of the top skin was the same as the one for the MR60-YSH70 laminate in chapter 2 and the bottom skin was cured using a standard cure cycle for IM7/8552 prepreg [188]. Both skins were bonded to the honeycomb core with a layer of FM

73M epoxy adhesive film, and the entire assembled structure was cured in the oven at 120 °C, following the specified cure cycle [189]. The sandwich panel was then machined into the required dimensions as specified in Table 4.4.

Table 4.4: Sizing results for the sandwich beam.

Sizing results		$[\pm 27_7/0]_s$
Total beam length	[mm]	400
Support span (S+2L)	[mm]	340
Loading span S	[mm]	40
t_{top}	[mm]	0.83
t_{core}	[mm]	13.75
t_{bottom}	[mm]	1.75
Width w	[mm]	30
Load	[N]	1932
Deflection	[mm]	5.87
τ_c	[MPa]	2.15

Five specimens were tested using a four-point bending test fixture, with loading and support roller diameters of 10 mm each. Two strain gauges were placed on the surface of the top and bottom skins to measure longitudinal strains, and another strain gauge was placed perpendicularly on the surface of the top skin to measure transverse strain. The schematic diagram of the test set-up is presented in Figure 4.4. All tests were performed using an Instron 25 kN hydraulically-actuated testing machine with a loading rate of 2 mm/min. The test configuration is shown in Figure 4.5.

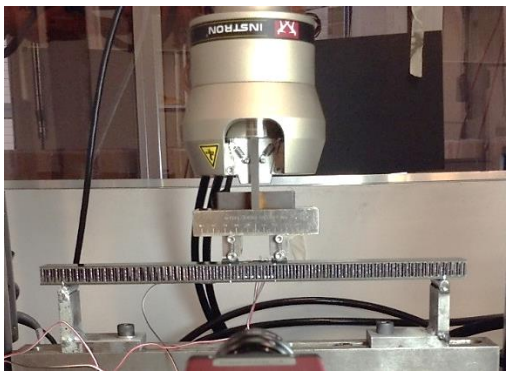

Figure 4.5: Four-point bending test setup.

4.6 Experiment results

4.6.1 General behaviour

As expected, all five specimens failed in the compressive skin and no undesirable failure modes occurred. The applied moment was calculated from the product of the applied load and a constant moment arm L. The moment is plotted versus the surface strains of the beam in Figure 4.6. In the initial stage, the compressive longitudinal strain, ε_{tx}, increased linearly with the applied moment. When the compressive fibre fracture strain of the M55 fibre was reached, the slope of the moment-strain curve reduced significantly. The specimen did not fail immediately due to the fracture of the 0° plies, instead showing progressive failure. This could be attributed to the fragmentation of the central 0° plies under compression, which is a less common compressive damage mechanism but was observed in the study of thin carbon-glass hybrid beams [15]. Detailed damage analyses will be presented in sections 4.6.4 and 4.6.5. It is also worth noting that a significant amount of non-linearity developed in the transverse direction of the compressive skin, and the transverse strain was almost twice that of the longitudinal strain. From Figure 4.7, the moment-strain curve of the lower tensile skin showed a linear behaviour as the tensile skin operated at a low strain range. Although a small amount of non-linearity due to the neutral axis shift can be seen, it was negligible compared with the non-linearity of the top compressive skin and so a linear elastic behaviour was assumed in the tensile skin.

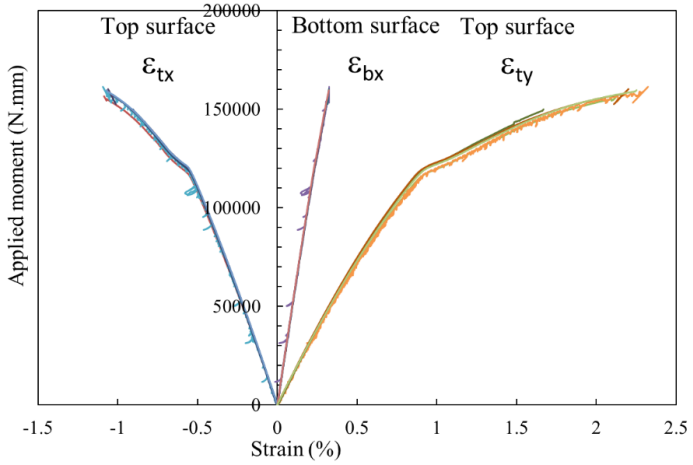

Figure 4.6: Applied moment versus the surface strains of test beam under four-point bending

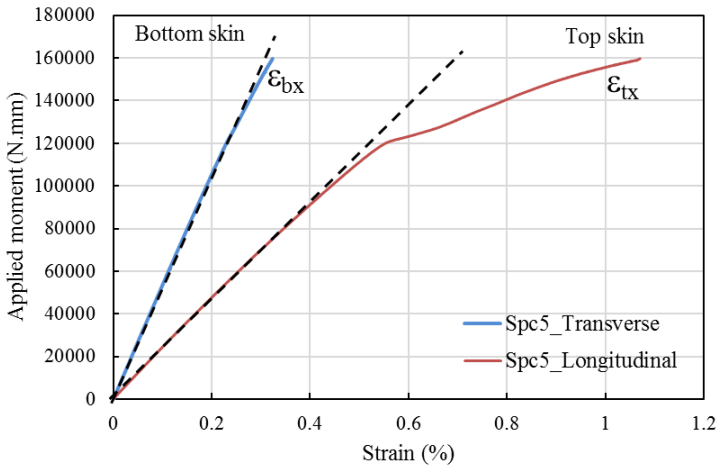

Figure 4.7: The applied moment versus the longitudinal strains of the top and bottom surfaces. Two dashed lines were plotted with original curves, highlighting linear region.

4.6.2 Stress evaluation

Fragmentation of the central 0° plies within the compressive skin significantly reduced the stiffness in the top skin and resulted in a neutral axis shift towards the bottom skin. Evaluation of the compressive strength cannot follow the ASTM D5467 guidelines, since the method is based on a constant neutral axis position and modulus. Compressive stress calculations based on the surface strain measurements with several assumptions, is presented here. The graphical representation of all the parameters used in the calculation are presented in Figure 4.9. In all of these expressions, subscripts t and b denote the properties of the top and bottom skins respectively

The neutral axis position, $y_{NA,}$, relative to the lower surface of the bottom skin, y_b, was estimated from the surface strain measurements. Since the beam was under pure bending and the cross-section remained plane during bending, a linear strain variation assumption was made:

$$y_{NA} = y_b - \frac{y_t - y_b}{\varepsilon_t - \varepsilon_b}\varepsilon_b \qquad (4.11)$$

Where y_t is the position of upper surface of the top skin relative to the bottom y_b=0.

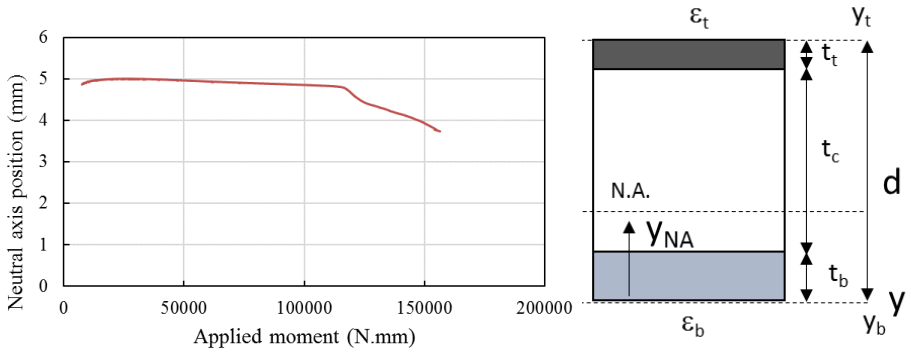

Figure 4.8: A plot shows the position of neutral axis relative to the bottom skin moving with the applied moment.

The centroid position is plotted against the applied moment in Figure 4.8. The centroid position was found to move towards the bottom skin under bending and the effect of N.A shifting on moment-surface strain behaviour will be investigated in section 4.8. Based on the real time neutral axis position, the position and strain in the mid-plane of the top and bottom skins relative to the neutral axis, y_t', y_b', ε_t', and ε_b' were determined.

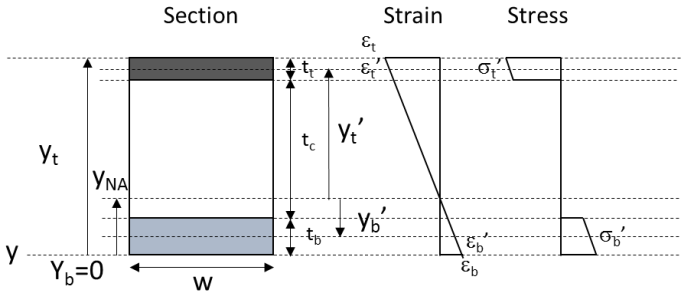

Figure 4.9: Graphical representations of all the parameters, stress and strain variations through the thickness.

The couple of assumptions are made here: an elastic response in the tensile bottom skin is assumed, as the strain on the bottom skin is less than 0.4%. The core is assumed to have negligible stiffness contribution to the beam and the total moment M is contributed by the top and bottom skins only as a much lower core longitudinal

stiffness compared with the skin materials. It also assumed negligible geometrical non-linearity as an overall small beam deflection observed in the test.

$$M = f_t y_t' + f_b y_b' \tag{4.12}$$

where

$$M = \frac{PL}{2} \tag{4.13}$$

$$f_b = \varepsilon_b' E_b w t_b \tag{4.14}$$

$$f_t = \sigma_t w t_t \tag{4.15}$$

Where M is the applied bending moment which can be assumed to be constant between the loading points, P is the applied load, L is the initial moment arm and assumed to remain the same during loading, E_b is the modulus of the bottom skin, w is the width of beam and t_b is the thickness of the bottom skin.

Substituting equations (4.13) - (4.15) with equation (4.12) gives:

$$\frac{PL}{2} = \sigma_t w t_t y_t' + \varepsilon_b' E_b w t_b y_b' \tag{4.16}$$

The averaged compressive stress, σ_t in the top skin can be expressed as:

$$\sigma_t = \frac{PL - 2E_b \varepsilon_b' w t_b}{2 y_t' w t_t} \tag{4.17}$$

The stress-strain behaviour for all five specimens is plotted in Figure 4.10 and the key compressive properties are summarised in Table 4.5. All five specimens exhibited consistent stress-strain curves, although minor noise was seen in Spc2 (red line). The stress-strain curve consisted of three stages. In the initial stage of loading, the stress increased approximately linearly with strain up to the fibre fracture strain, although a small amount of non-linearity was observed due to the carbon fibre non-linearity. Between the strains of 0.55% and 0.68%, the stiffness reduced gradually due to the progressive damage of the M55 fibres in the 0° plies. The third part of the curve showed the further loading ability of the laminate, although the 0° plies were

presumed to be fully damaged. This three-stage behaviour in compression is like the tensile stress-strain curve of the pseudo-ductile thin ply angle-ply laminates. However, in contrast to the flat stress plateau in the tensile stress-strain curve, the 2nd stage of the compressive curve showed an inclined response and was termed as "sloped stress plateau" in this thesis.

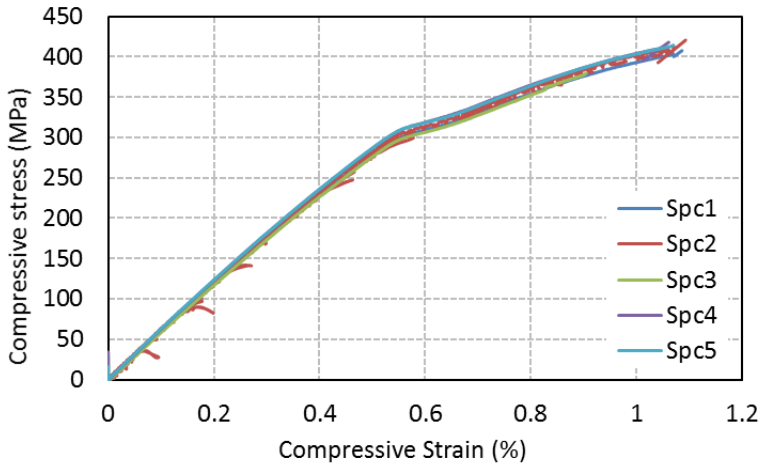

Figure 4.10: Compressive stress-strain curves for all five MR60-M55 specimens. Note: the red lines traces to the right are the noisiness in the strain measurement of specimen 2, which can be explained by voltage fluctuations in the analogue output from the strain gauge data log equipment.

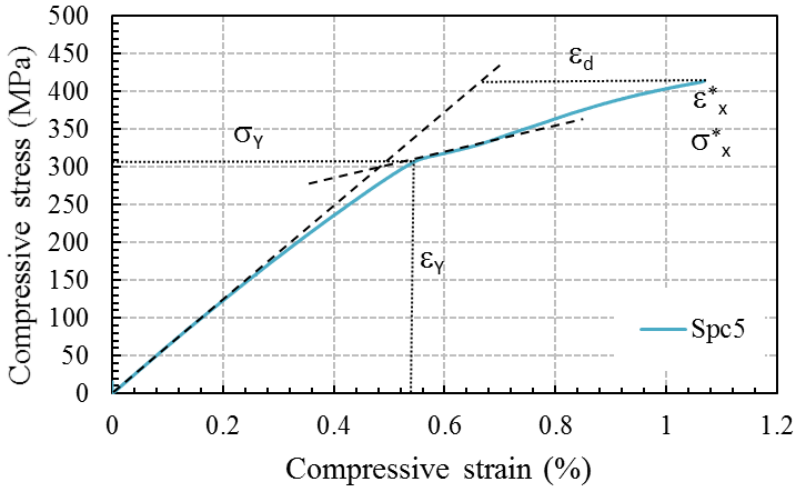

Figure 4.11: An example stress-strain curve, annotated with graphic definitions of all the key results.

Table 4.5: Mean values for compressive testing results of MR60-M55 laminate. The coefficient of variation for each property are shown in parentheses.

			MR60-M55 $[\pm 27_7/0]_s$
ε_d	Pseudo-ductile strain	[%]	0.41 (1.23%)
ε_Y	"Yield" strain	[%]	0.55 (1.73%)
ε^*_x	Failure strain	[%]	1.08 (1.39%)
σ_Y	"Yield" stress	[MPa]	306 (1.38%)
σ^*_x	Ultimate stress	[MPa]	412 (1.02%)
E_x	Modulus	[GPa]	60 (3.4%)

4.6.3 Visual inspection

Visual inspection presented in Figure 4.12 revealed that the specimen failed by a single-fracture through the thickness and across the entire width of the compressive skin, parallel to the 27° direction. This has been shown as a common compressive failure mode in angle-ply laminates with angles being in the region between 15° to 30° [101,105]. The high shear stress and transverse tensile stress in the angle-ply laminates in compression, resulted in a reduction in the compressive strength [105]. The failure modes in this case include matrix failure in the 27° plies, fibre fracture in the -27° plies and damage due to fragmentation in the central 0° plies. Due to the delamination at the 0/−27 interface being inhibited, the laminate did not fail immediately after the fracture of the central 0° plies. The angle plies and the fragmented 0° plies took up further loading until final failure.

As can be seen in Figure 4.12, the fracture developed from one end of the specimen to the other end. Localised core damage was seen (see the red-box), but this occurred after compressive failure of the skin with no load drop occurring prior to final failure, as can be observed in Figure 4.10. The core damage was crushing due to the large amount of energy that was released in the compressive fracture of the skin. In addition, no core-skin separation can be observed, which indicates the adhesive film chosen for bonding was strong enough and interface failure was avoided. Overall, the visual observation provided a good indication that the sandwich

beam effectively failed in the compressive skin, without any premature failure in the bottom skin, sandwich core or core-skin interfaces.

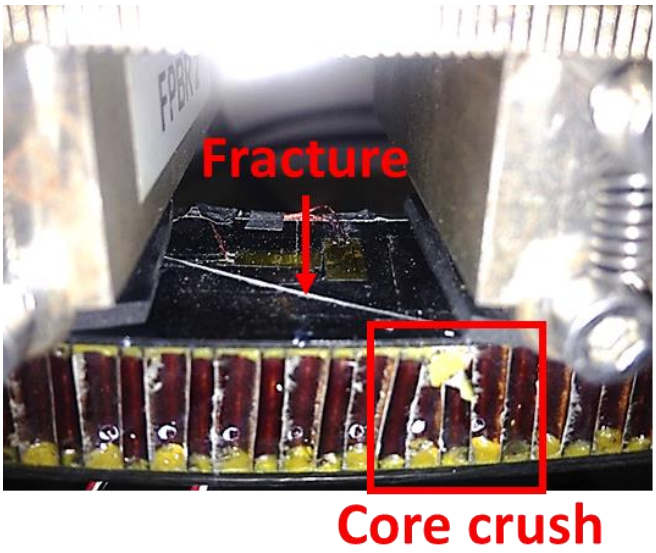

Figure 4.12: Visual damage observation shows the failure modes exhibited in the sandwich beam.

4.6.4 X-ray CT-scan of the MR60-M55 $[\pm 27_7/0]_s$ laminates

Due to the localised internal damage within the compressive skin being invisible, X-ray CT-scanning was employed. To further understand the internal damage within the specimen, only the compressive skin between two loading rollers was removed from the test beam (including fracture surfaces), immersed in a dye penetrant and then scanned using a Nikon XTN320 X-ray CT inspection machine. The X-ray image captured at the central 0° plies of the laminate is presented in Figure 4.13. No obvious damage can be observed in the X-ray image of the entire pieces (the middle image in Figure 4.13). Higher magnification images of the edge of the specimen reveal either the free-edge or fracture edge, where multiple small white strips can be seen. These short length strips are suspected to be fragmentations and a small amount of localised delamination, similarly observed for the tensile case. The damage is only seen close to the edge and cannot be seen in the middle part of the specimen, since the gap at the fractured 0° plies is too small for the dye solution to penetrate.

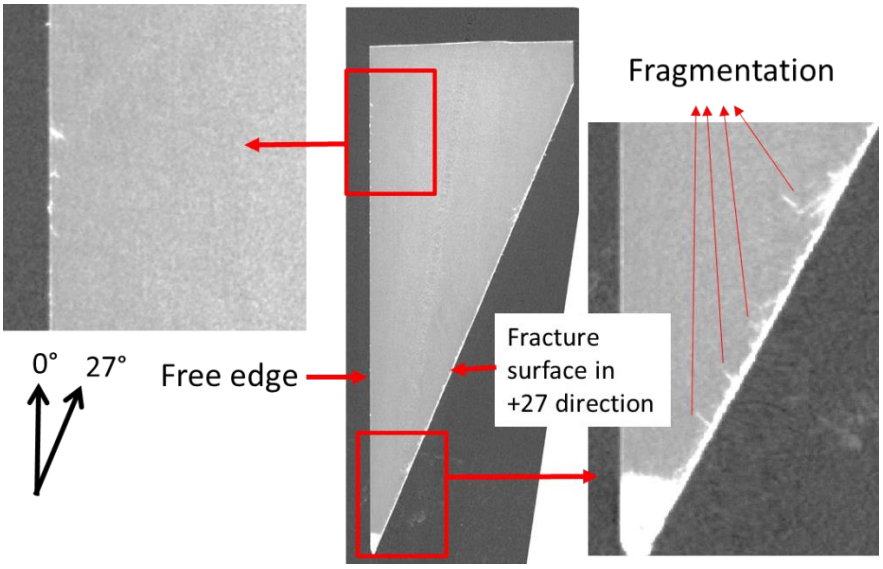

Figure 4.13: X-ray images of the MR60-M55 laminates in compression.

4.6.5 Microscopy of compressive skin

The X-ray images of the specimen suggested that the fragmentations occurred close to the edge of the specimen, but with no damage observed in the middle of the specimen. Further analysis of the damage away from the edges was undertaken using optical microscopy. This was conducted by grinding the angle plies off ply-by-ply in the through-thickness direction until the 0° plies were visible. An example of the microscopic images taken at the 0° plies are shown in Figure 4.14. Fragmentations in the central 0° plies are clearly shown as dark lines across the width. Carbon layers were broken into small pieces across the entire width under compressive loading once the M55 fibre fracture strain was reached, in contrast to a previous study [177], where a kink-band in the 0° layer and delamination growth at the 0/–27 interface were shown in the $[\pm\theta_m/0_n]_s$ laminates with standard thickness.

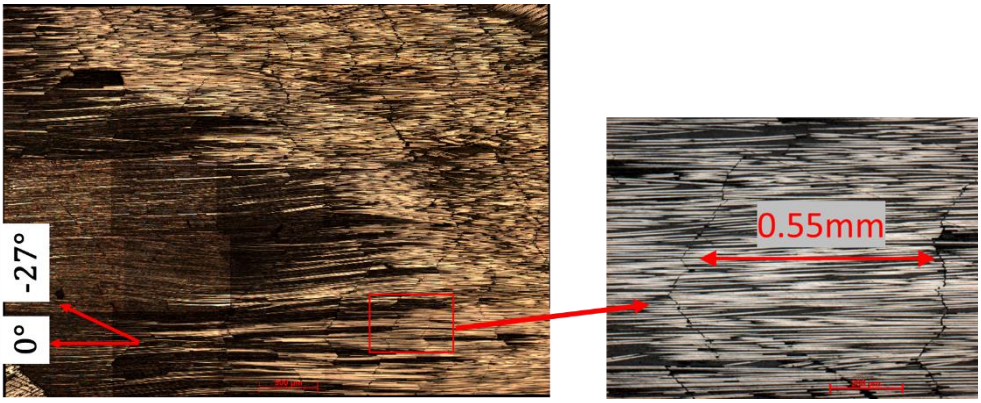

Figure 4.14: An example of a microscopic image of fragmentation in the central 0° plies. Note: the ply adjacent to the 0° ply is a -27° ply.

By measuring the length of the fragmented ply presented in Figure 4.15, the distribution of fragment lengths is plotted in Figure 4.16. It is worth noting that the measurement of fragment length (X_n) was performed at regular intervals across the width of the specimen (as shown from Line 1 to Line n in Figure 4.15), since the fragment lengths are not completely straight. Most of the fragmented fibre lengths can be seen to be in the range between 0.3 and 0.6 mm. The critical fibre length l_c of the central 0° plies is 1.2 mm and was calculated using equation (4.18), assuming a linear elastic-perfectly plastic response in the matrix with a constant shear stress:

$$l_c = \frac{E_c \varepsilon_c t_c}{\tau_c} \tag{4.18}$$

Where E_c, ε_c, and t_c are the Young's modulus, compressive failure strain and thickness of the central 0° plies (the North M55/epoxy prepreg) respectively. τ_c is shear yield stress, taken as the interlaminar shear strength of the central 0° plies.

The fragmented lengths are found to be less than half of the critical ply length l_c. This indicates the load transfer mechanism between the fibre was not the same to the tensile case, once the compressive fracture occurred. Due to the absence of delamination at the 0/-27 interface and kink-band of 0° plies, the first fracture did not lead to instability. Instead, the two adjacent fragments 0° plies were expected to compress against each other during further loading. The contact between the two

fragments allowed further loading, leading to fibre direction stress and shear stress in the fragments. The fibres in contact fragmented into even small segment, supported by the surrounding angle plies. These observations explain the "sloped stress plateau" presented in Figure 4.10, since the central 0° plies still contributed to the overall stiffness during fragmentation. Similar observation has been found in a glass-M55 fibre hybrid laminate under compression. A fractured surface in an angle of approximately 45° enables the compressive load transferred within the laminate via contact force as well as sliding along the fracture surfaces [108].

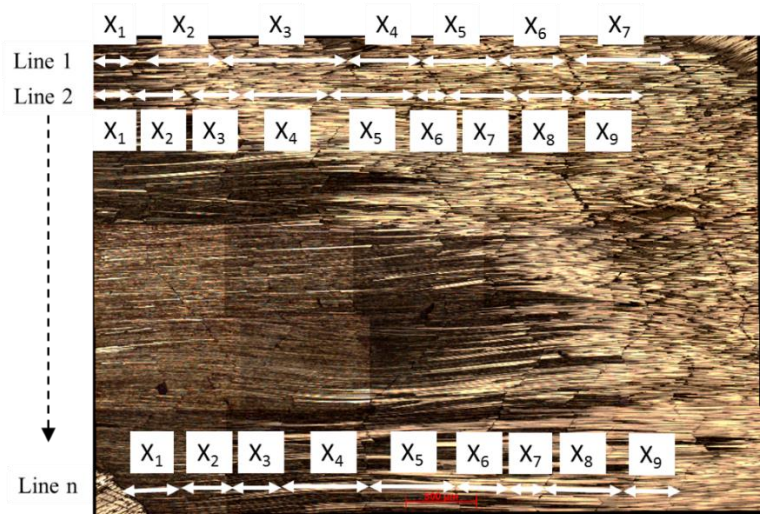

Figure 4.15: Method to measure the fragmentation length.

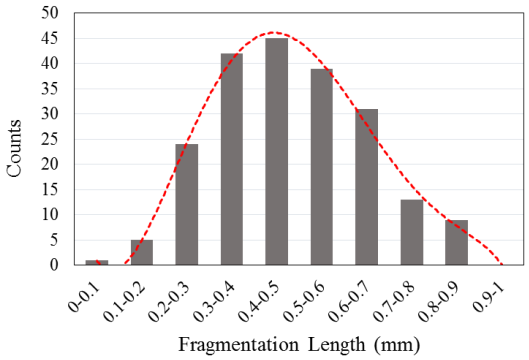

Figure 4.16: Distribution of fragmentation length in the central 0° plies.

4.7 Investigation of the observed low strain to failure (CLA)

To understand the ply-level behaviour further in compression, ply level stresses and strains were calculated using Classical Laminate Analysis (CLA). The calculation was based on the experimental surface strain measurements, assumed constant material properties, and negligible fibre rotation. The results of σ_{11}-ε_{11}, σ_{22}-ε_{22} and τ_{12}-γ_{12} on the surface 27° ply are plotted in Figure 4.17.

As seen from the stress-strain curves in Figure 4.17, the stress level in the fibre direction σ_{11} was the greatest. However, comparing those values with the material properties presented in Table 4.6, the relative ply level stresses of τ_{12} and σ_{22} are very high. The calculated shear stress τ_{12} reached the material in-plane shear yield stress of the Skyflex UIN020 prepreg, and the stress developed in the transverse direction σ_{22} was also close to the transverse tensile strength of the same prepreg. This suggests that the low stress at failure of the angle-ply laminates under compressive loading with failure modes being a clean break parallel to the fibres can be attributed to a combination of high in-plane shear and transverse tensile stresses.

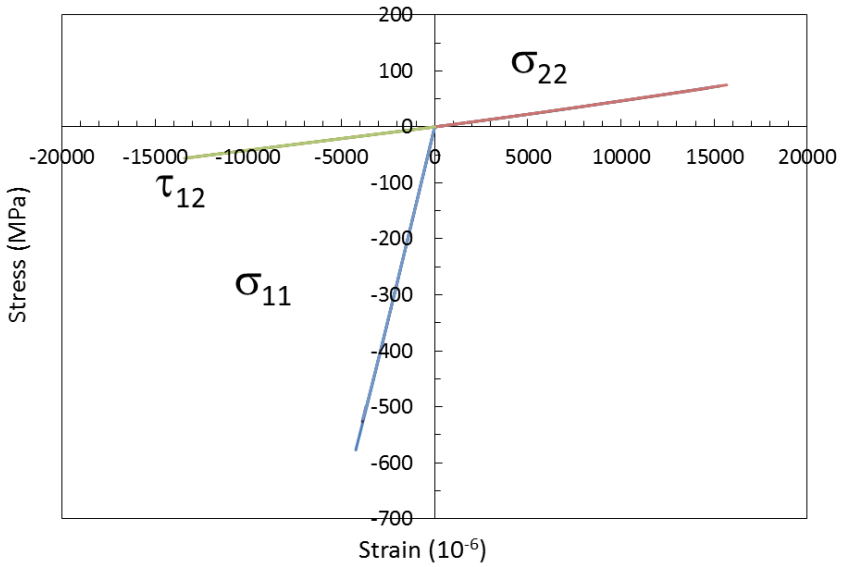

Figure 4.17: Material direction stress-strain curves in the surface 27° ply for the top compressive skin.

Table 4.6: Stresses in the material directions in the surface 27° ply for the top skin, calculated from Classical Laminate Analysis (CLA)

		From CLA	Strength
σ_{11}	[MPa]	-518	-1440
σ_{22}	[MPa]	75	82
τ_{12}	[MPa]	56	55

4.8 Investigation of bending effects

The compressive test was carried out via an indirect bending method and an inclined moment-strain "plateau" was observed which could also be affected by the neutral axis shift during loading. To investigate this "bending effect", a 2D finite element (FE) model was developed.

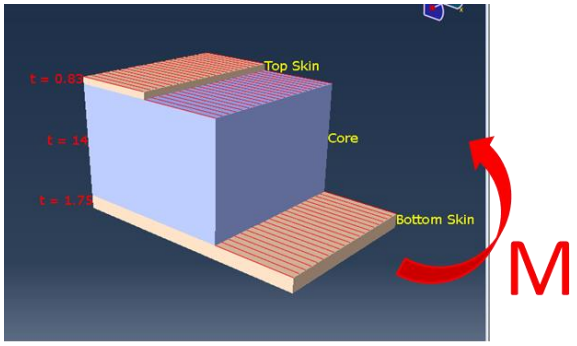

Figure 4.18: A schematic diagram of a sandwich beam. To improve visualisation, the schematic diagram in the through thickness direction has been exaggerated.

4.8.1 Modelling procedure

A 2D plane stress FE model was developed to investigate the bending effect on compressive behaviour in a sandwich beam. The model geometry was the same as the beam tested experimentally (given in Table 4.4 and Figure 4.4). The model shown in Figure 4.19 was built with the Abaqus Composites Layup toolbox, using quadratic plane stress elements of type CPS8 with the smallest mesh and element size of 0.5 mm applied between the loading rollers. The element has three integration points in the thickness direction, representing the top skin, honeycomb core and the bottom skin respectively. A schematic representation is presented in Figure 4.18.

The thickness of each layer was the same as those used in the experiment. The elastic constant material properties (Table 4.7) were assigned to the bottom skin and the material of the top skin was defined using a user defined material subroutine (UMAT) and will be discussed later. The core was treated as a homogenous material, with a relative low elastic modulus E = 0.6 GPa and a Poisson ratio of 0.3. The displacement was applied at two reference points and both points constrained to the lines that represent the contact region between the loading rollers and the specimen.

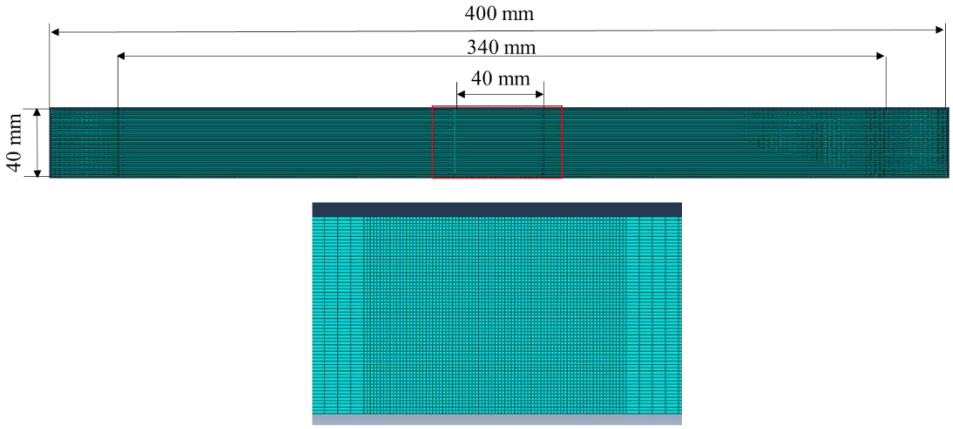

Figure 4.19: Meshed bending specimen. The bottom image shows a finer mesh between two rollers.

To understand the origin of the inclined "plateau" that was observed in the experimental moment-strain response, the UMAT defined a non-linear material property compromising of a bilinear response as shown in Figure 4.20. The first part is a linear elastic response and the second part of the response is an inclined line, with the same slope of the second stage of the compressive strain curve as presented in Figure 4.9, representing the stress plateau which is dominated by the mechanisms of fibre fragmentation and dispersed delamination in a pseudo-ductile laminate. The idea was to see change in the slope due to the neutral axis shift from the output moment-strain curve. This 2-line response is defined by seven independent parameters: initial longitudinal modulus E_1, transverse modulus E_2, major Poisson ratio v_{12}, in-plane shear modulus G_{12}, initial strain ε_1, saturation strain ε_2 and the stress σ_m at saturation strain ε_2. The details of the input properties that were used are

given in Table 4.7, where the experimentally measured E_X and ε_Y were used for the longitudinal modulus E_1 and ε_1. The slope of the 2nd line is also the same to the 2nd stage of the compressive stress-strain curve. The longitudinal modulus E_1 remains constant when the current strain is lower than ε_1, otherwise it is a secant modulus which is calculated from the yield stress and the current strain value. Other properties of E_2, G_{12} and v_{21} are assumed to be constant.

Table 4.7: Input material properties for the bottom skin (from CLA).

	Bottom skin: IM7/8552 $[\pm 27_3/0]_s$
E_1 [GPa]	82.3
E_2 [GPa]	12.6
G_{12} [GPa]	25.6
G_{13} [GPa]	5.2
G_{23} [GPa]	4.0
v_{12}	0.6

Table 4.8: Input material properties for the top skin (in UMAT). The values were adjusted from the experimental measurements presented in Table 4.5.

	Top skin: MR60-M55$[\pm 27_7/0]_s$
E_1 [GPa]	60
E_2 [GPa]	6.0
v_{12}	0.6
G_{12} [GPa]	2.5
ε_1 [%]	0.56
ε_2 [%]	0.7
σ_m [MPa]	400

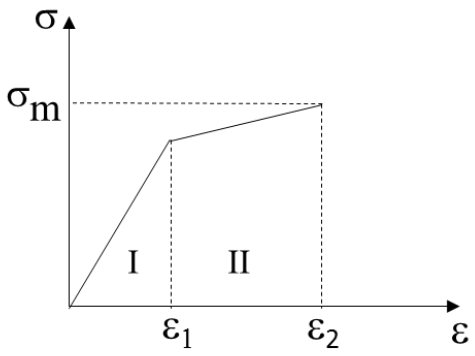

Figure 4.20: Input stress-strain curve for UMAT

4.8.2 Modelling results

The output of the applied moment is plotted against the compressive strain in Figure 4.21, along with the experimental moment-strain curve in the same figure. Note that the non-linearity in fibre direction has been neglected in the FE model. Comparing the slope of the 2nd stage of FE model to the experimental result, the gradient of the inclined moment "plateau" in the FE model is nearly identical to the experimental results. This observation can explain that the inclined moment "plateau" in the moment-strain curve was nearly independent of the neutral axis shifts during bending, and predominantly caused by the damage mechanism of the fragmentation of 0° plies as discussed previously.

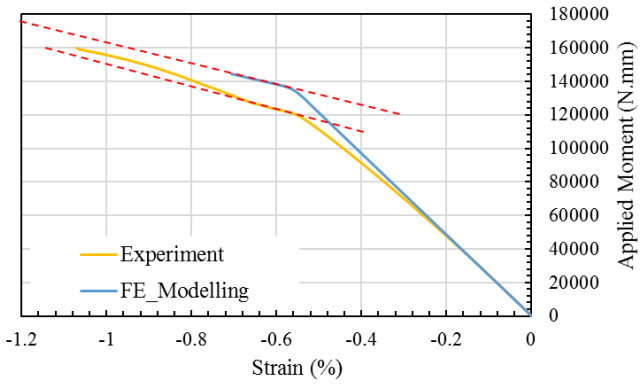

Figure 4.21: A comparison between FE and experimental applied moment versus strain curves. Red dashed-lines are added in both cases to fit the slope of the 2nd stage of the curves.

4.9 Conclusions

In this chapter, a thin ply angle-ply laminate with internal 0° plies has been designed and tested via an indirect compressive test method using a sandwich beam. The laminate exhibited a non-linear compressive stress-strain curve consisting of an initial elastic region, compressive fibre fragmentation in the central 0° plies, and a section of further loading of the angle plies. The failure mode of the specimen was a single fracture, parallel to the -27° direction due to the combination of high transverse tensile stress and in-plane shear stress within the angle-ply laminate. Delamination has been suppressed in the tested laminate and multiple fibre fractures have been promoted, instead of a single complete delamination initiating from the fibre fracture surface.

Progressive compressive fibre fractures of the 0° plies have been also achieved in the present study. Fragmentation lengths are smaller than the critical length. This indicates that the load transfer in compression was not the same as in tension once the compressive fractures occurred. Instead, as delamination at the 0/-27 interfaces has been inhibited, the load transfer between the adjacent fragmented fibres is via a mix of direct contact at the fractured surfaces and sliding between them during further compressive loading. This mechanism enables the central 0° plies to still contribute to the overall stiffness during fragmentation.

In addition, the moment-strain response obtained from the FE model indicates that the effect of the neutral axis shift has only small amounts of influence on the slope of moment-strain curve. The inclined “plateau” observed in the compressive test was primarily attributed to the mechanisms of compressive fibre fragmentation.

5 Exploring pseudo-ductility of thin ply angle-ply laminates with central 0° plies in flexural loading

Angle-ply laminates containing 0° plies have been found to show gradual failure but behave differently in uniaxial tensile and compressive loading. Once such laminates are tested under flexural loading, dissimilar non-linear responses in tension and compression could bring more complicated flexural responses. Therefore, the aim of this work is to understand the flexural behaviour of these pseudo-ductile $[\pm\theta_m/0_n]_s$ *laminates and to explore the non-linearity of these laminates under flexural loading. In the present work, two typical pseudo-ductile laminates were tested under a four-point flexural loading: the first one has pseudo-ductile stress-strain behaviour in both tension and compression and the second one has only pseudo-ductility in tension. The flexural results show that laminates with both layups failed on the compressive sides due to the high in-plane shear stress in the angle plies on the outer compressive side. However, due to the fragmentation on the tensile side, the failure was delayed and therefore a higher failure strain and more gradual failure were achieved.*

5.1 Introduction

Gradual failure of carbon fibre composites in tensile and compressive loading has been achieved in the thin ply angle-ply laminates with central 0° plies. This is achieved via combining the non-linearity of angle plies with the damage mechanisms of fragmentation of the central 0° plies and localised dispersed delamination. Via this approach, the pseudo-ductile strain has been found to be up to 2.2% in tension and 0.41% in compression in section 3.3.1 and section 4.6.2. Once the uniaxial tensile and compressive behaviour of these materials has been understood, the next stage of the work aims to understand their performance in flexural loading, as it is a more complex loading case involving both tension and compression.

So far, bending testing has shown its importance in composites characterisation, as it is one of the major loading cases in real structures. The pseudo-ductile stress-strain response is very different in tension and compression and some of the pseudo-ductile laminates with high fracture strain fibre in the 0° plies were found to have failed with no pseudo-ductile response in compression but did show pseudo-ductile response in tension. When these pseudo-ductile thin ply angle-ply laminates are subjected to flexural loading, the flexural behaviour of them will be influenced by the different non-linear behaviour in the tensile and compressive side.

In the present chapter, the laminates which have previously been demonstrated to show pseudo-ductility, were selected to be tested under bending loading. In these tests, the primary aim was to understand how the different non-linear compressive and tensile response of the laminates affects their bending behaviour, what the damage modes and their sequences are, and to explore the non-linearity and gradual failure in flexural loading.

5.2 Static tensile testing

Pseudo-ductile laminates with two different layups were selected to test under bending. The first one was a MR60-M55 $[\pm 27_7/0]_s$ layup (where MR60 denotes intermediate modulus MR60 fibre prepreg and M55 denotes high modulus M55 fibre prepreg), which has shown compressive pseudo-ductile stress-strain response

according to the previous compressive testing presented in Chapter 4. When such a laminate is tested under flexural loading, the different non-linear behaviour on the tensile and compressive sides of the bending beam would be expected to bring about an overall non-linear response. The second layup selected was TC35-TC35 $[\pm 26_6/0]_s$ (where TC35 denotes Skyflex prepreg with standard modulus TC35 fibre and the cured ply properties are shown in Table 5.1). This layup was selected to replace the T300-T300 $[\pm 26_5/0]_s$ laminate, which has shown pseudo-ductility in tension according to chapter 3 due to the T300 fibre prepreg is no longer available in the market. One extra pair of angle plies was used in the TC35-TC35 configuration than the T300-T300 configuration as the longitudinal modulus of TC35 fibre prepreg is slightly lower than the prepreg with T300 fibre. In the studies of $[\pm\theta_n/0_m]_s$ laminates subjected to compression, it has been found that the laminate with high strain carbon prepreg in the middle, tends to fail catastrophically with a kink-band forming in the 0° plies due to shear instability. Therefore, it is crucial to reduce the stress/strain on the compressive side and to promote damage initiation on the tensile side.

Prior to the monolithic bending testing, the tensile behaviour of the MR60-M55 $[\pm 27_7/0]_s$ laminate (termed as MR60-M55) and TC35-TC35 $[\pm 26_6/0]_s$ laminate (termed as TC35-TC35) were determined in order to analyse bending behaviour. The manufacture and preparation of laminates were the same as in the chapter 3 and chapter 4. The dimensions of specimen were the same as the unnotched tensile testing specimen as mentioned in chapter 3.

Table 5.1: Cured ply mechanical properties of UD laminates.

	E_1 [GPa]	E_2 [GPa]	σ_1 [GPa]	G_{12} [GPa]	ε_1 [%]	t [mm]	v_f
USN020A (T300 fibre)	121	5.4	1936	2.76	1.6	0.022	0.52
USN020A (TC35 fibre)	110	6.2	1780	3.0	1.6	0.027	0.52

Figure 5.1 shows the tensile stress-strain curves for all five specimens and the key mechanical properties are summarised in Table 5.2. Pseudo-ductile stress-

strain tensile behaviour can be observed with a pseudo-ductile strain of 3.08%. The laminate exhibited a three-stage pseudo-ductile stress-strain curve similar to the other layups tested previously: linear response in the initial stage before the "yield" stress, then followed by a gradual failure and short plateau due to fragmentation of the central 0° plies. A very large portion of reloading can be observed which was due to the angle plies carrying more load and having a higher failure strain.

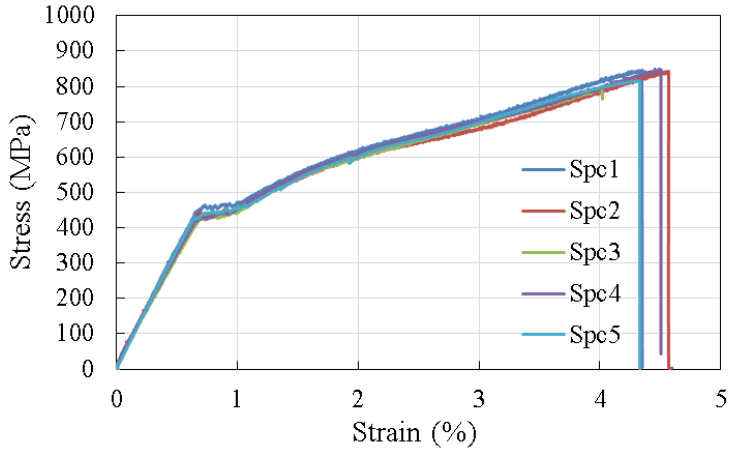

Figure 5.1: The experimental tensile stress-strain curves for the MR60-M55 laminates

Tensile stress-strain curve with simultaneous acoustic emission energy events as shown Figure 5.2 provides more information on damage evolution in the MR60-M55 specimen under tensile testing. In the linear region (stage I), no high energy event was captured. Significant amounts of high energy AE events were initiated from the "yield" stress and lasted until the first half of the second stage (stage II). These high energy events are associated with fibre fragmentation of the 0° plies. In the second half of the second stage, the total number of high energy events fell gradually, meaning the fragmentation in the gauge length of specimen tends to be saturated and localised dispersed delaminations were initiated from the fracture surfaces. In the third stage, only some medium level energy signals have been observed, associated with the dispersed delamination initiation from the fractured plies.

Table 5.2: The mean tensile results of the MR60-M55 and TC35-TC35 laminates.

	σ_Y [MPa]	σ^* [MPa]	ε_Y [%]	ε^* [%]	ε_d [%]	E [GPa]
MR60-M55	435	828	0.68	4.35	3.08	65
$[\pm 27_7/0]_s$	(2.7%)	(3.0%)	(1.7%)	(5.1%)	(5.9%)	(2.1%)
TC35-TC35	746	837	1.91	4.34	2.43	44
$[\pm 26_6/0]_s$	(1.3%)	(1.6%)	(2.5%)	(4.5%)	(1.0%)	(0.9%)

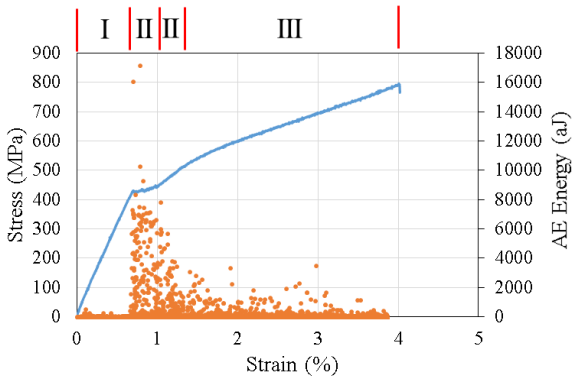

Figure 5.2 Acoustic emission events which occurred during the tensile testing of the MR60-M55 laminate.

Two MR60-M55 specimens were taken out from the testing machine when the strains of 1.2 % and 3.9 % were reached, and then X-ray CT-scans were performed. All X-ray images taken in the middle plies of the specimens are shown in Figure 5.3. Again, the thin white lines were the fibre fragmentations in the 0° plies and the less intensive regions around the white lines were the dispersed delaminations at the 0/-27 interface. At 1.2% strain, acoustic emission signals suggest the fibre fragmentation is saturated and the X-ray image at the same strain level shows this is the case. Fragmentation and dispersed delamination can be seen on both free edges over the entire gauge length with uniform fragment lengths and these fragmentations were shown to be approximately perpendicular to the loading direction. Some of this adjacent damage was found to be joined together across the width of the specimen. A finer scan was also performed at two locations of the specimen as shown in the two middle images of Figure 5.3. The information missing from the initial scan, can be observed in these finer scans. For example, some of the fragmentations are not

shown across the width in the initial scan, but can be seen in the finer images. In addition, the damage propagated between adjacent fragments can be seen in the matrix shear cracking in the 0° plies. In addition, some fragmentations are isolated away from the free edges, without any connection to the edge. This shows that fragmentations could existed in the area although there is no obvious dye penetration reflection can be seen. As a result, the observations above suggest the laminate was saturated with fragmentations and some localised delamination at the current strain level. When the strain was increased to very close to the ultimate point (3.9%), the specimen was fully damaged with fragmentation and extensive delamination.

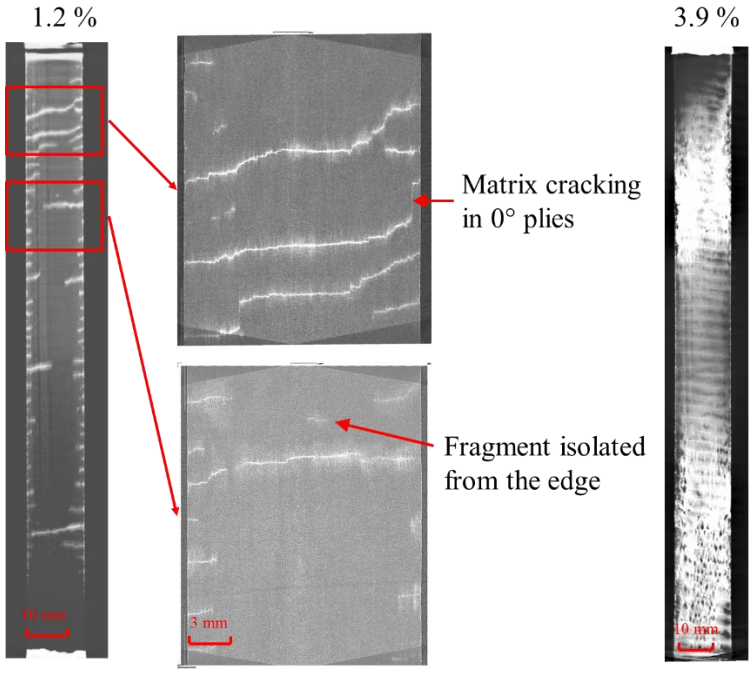

Figure 5.3: X-ray images of the MR60-M55 unnotched tensile specimen

The tensile stress-strain behaviour of the TC35-TC35 laminate is presented in Figure 5.4 and corresponding mechanical properties are given in Table 5.2. The overall gradual behaviour of the TC35-TC35 laminate is very similar to the one shown in the T300-T300 layup in Figure 3.5, but it has shown a higher "yield" stress and the ultimate failure strain. In general, this layup is a good candidate for replacing the T300-T300 layup used previously.

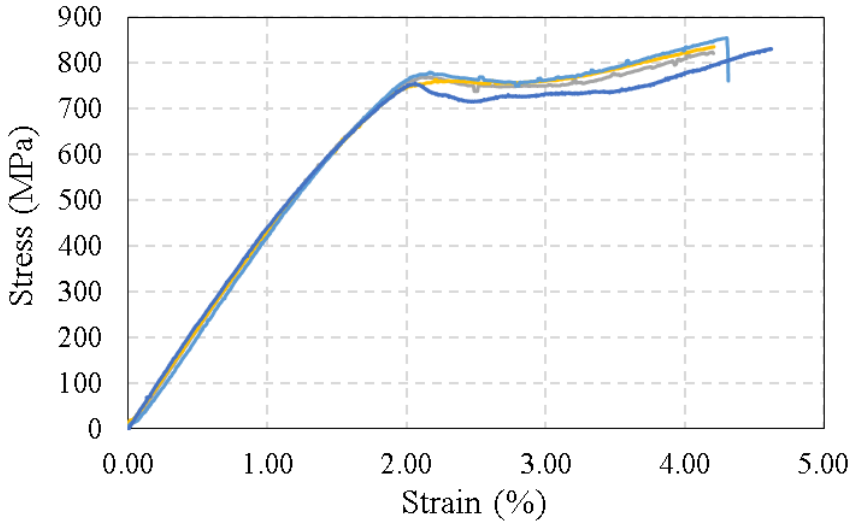

Figure 5.4: The experimental tensile stress-strain curves for the TC35-TC35 laminates

5.3 Monolithic bending testing

5.3.1 Specimen design and testing procedures

To investigate the bending behaviour of the pseudo-ductile MR60-M55 and TC35-TC35 laminates, a four-point loading configuration with fixed supporters and loading rollers was selected in this test since it allows zero shear forces between two loading rollers. An illustration of the testing configuration is presented in Figure 5.5. To introduce uniform contact and to reduce stress concentrations between the specimen and loading rollers, rubbery inserts were placed between them to avoid any premature fibre failure. Strain gauges were placed on both the top and bottom surfaces of the specimen for measuring strains during the loading.

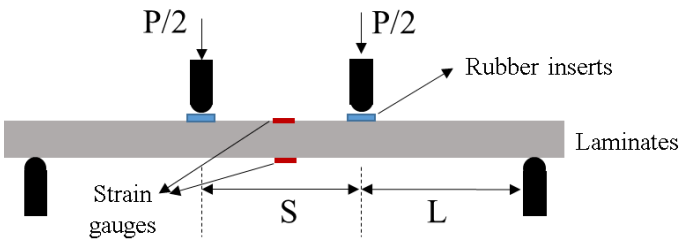

Figure 5.5: Illustration of testing configuration for a four-point bending test.

The design of specimen was primarily according to the ASTM standard D7264. The specimen was machined into a rectangular shape with parallel edges. One of the key parameters in designing bending specimens is the support span-to-thickness ratio. A low support span-to-thickness ratio can bring significant interlaminar shear stress and shear deformation, resulting in undesired failure. As per the ASTM standard, the recommended span-to-thickness ratio is 32:1. However, according to some preliminary bending tests of these pseudo-ductile specimens, a very large deflection was achieved if using this ratio. To minimise the total deflection and geometrical effect on the bending behaviour, in this chapter, a reduced span-to-thickness ratio around 25 was used. The dimensions for testing the MR60-M55 and TC35-TC35 laminates in a setup with a support span three times that of the loading span are presented in Table 5.2.

Table 5.3: Recommended specimen geometries for bending testing.

	Thickness [mm]	Width [mm]	Loading span (S) [mm]	Support span (S+2L) [mm]
TC35-TC35	2.65	20	20	60
MR60-M55	3.30	20	30	90

The experiments were performed in an Instron hydraulically-actuated system with a 25kN load cell. The load was applied at a loading rate of 1mm/min until the load drop was found to be higher than 30%. Vishay general purpose linear pattern strain gauges C2A-06-062LW-350 were used in this testing to obtain the strain measurements on both skins. Figure 5.6 shows the testing configuration of four-point bending test.

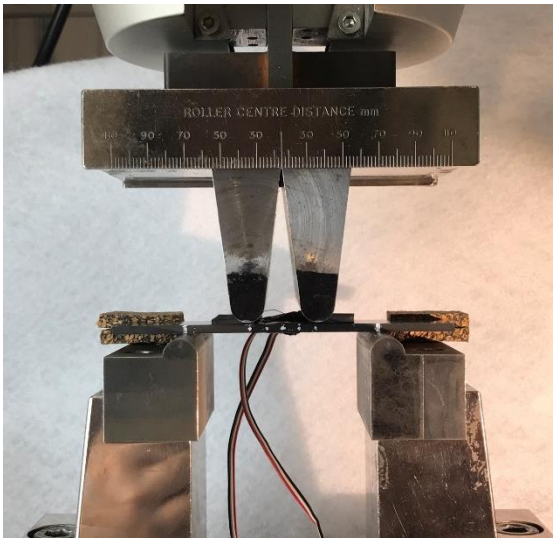

Figure 5.6: Experimental set-up for the four-point bending testing.

5.3.2 Bending results: the MR60-M55 $[\pm 27_7/0]_s$

The bending response of the laminate is presented as the moment per unit width against the surface strains from the strain gauges, where the applied moment was calculated from the applied load times an assumed constant moment arm. The top and bottom surface longitudinal strains were plotted against the applied moment per unit width of all the MR60-M55 specimens in Figure 5.7. The applied moment per unit width against displacement is presented in Figure 5.8. Non-linear behaviour and gradual failure are shown in the moment-displacement plot and moment-surface strain plot. Two dotted lines have been added to the moment-strain curves showing the degree of non-linearity. To give a better presentation, curves for a single specimen are also presented Figure 5.10. In the initial linear region, the curves for tensile and compressive sides are almost identical. It can be clearly seen that the non-linearity was initiated from around 0.7% strain on the compressive surface. Assuming a linear strain variation through the laminate thickness, a value of strain in the central 0° plies of the top sub-laminate (as shown ε4 in Figure 5.9) can be calculated to be 0.54% when the surface compressive strain of 0.7% has been reached. This strain is similar to the value of 0.56% for the "yield" strain of the same fibre type presented in chapter 4, therefore the non-linearity observed was related to

the fibre fragmentation of the central 0° plies on the compressive side of the beam. At the same time, the strain in the 0° plies on the tensile side was only 0.46%, which was lower than the tensile fibre fracture strain of the same laminate (0.7%) as determined in static tensile loading in section 5.2. With further applied load, the gradient of the moment-strain curve on the compressive side changed again at 1.2% surface strain. This could be related to the initiation of fragmentation of the central 0° plies on the tensile side and resulted in an increased non-linearity.

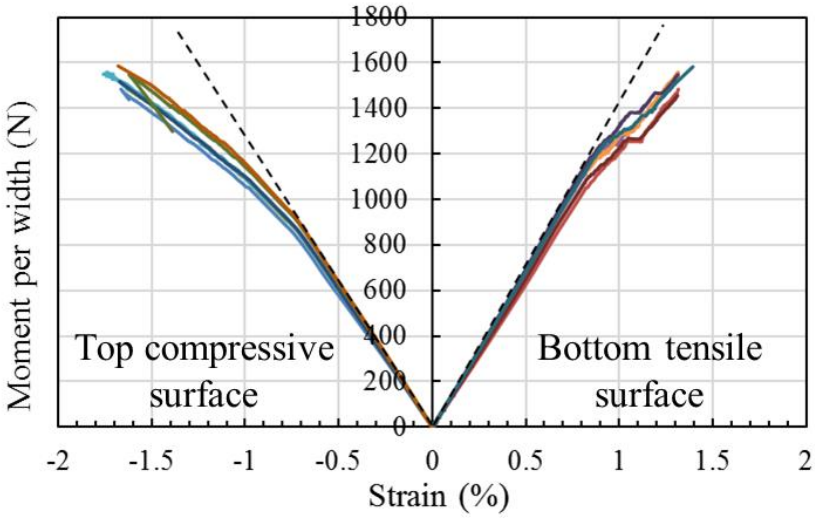

Figure 5.7: Applied moment per unit width versus surface strains for the MR60-M55 laminates under four-point bending.

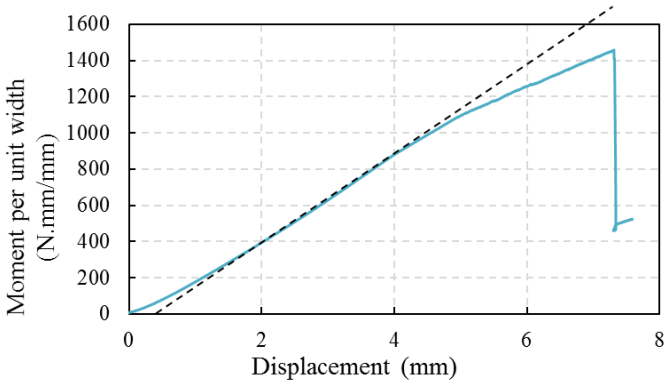

Figure 5.8: Applied moment per unit width versus displacement for the MR60-M55 laminates under four-point bending. The initial small amount of soft region is due to the rubber softness, which is not taking into consideration of material non-linearity.

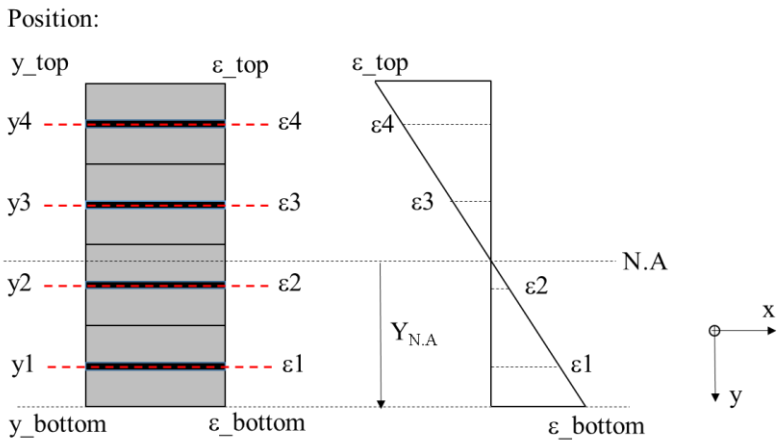

Figure 5.9: Graphical representation of a linear strain variation through the thickness

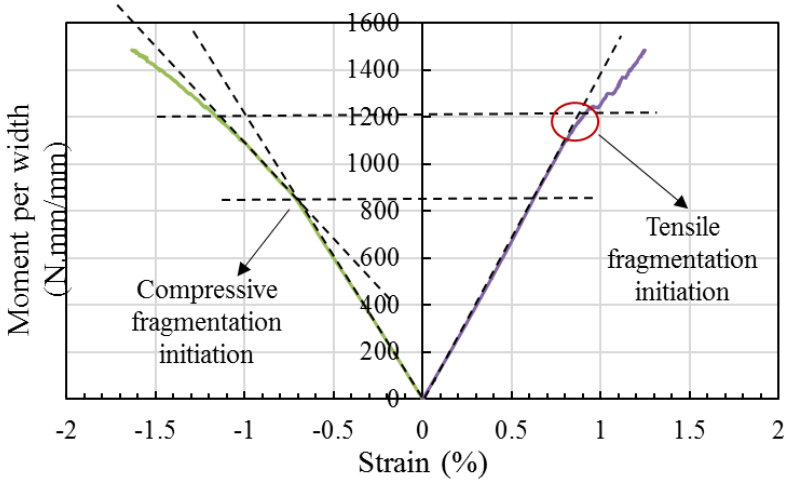

Figure 5.10: Moment-surface strain plot for single MR60-M55 specimen – showing the non-linearity and some characterization points on the curves.

On the tensile side of the bending beam, the moment-strain curves are nearly linear up to a strain close to 1%, followed by a stepwise behaviour – where multiple short plateaux can be observed with the increase of applied moment. One of the possible reasons for the short plateaux is that fragmentation was localised underneath the strain gauge, causing local strain variation. To investigate this, one extra set of bending tests was performed, using strain gauges with two different gauge lengths to determine the influence of gauge length on strain measurements.

In addition to the strain gauge with a 6.4 mm gauge length that was used previously, one extra long strain gauge with a gauge length of 11.18 mm was attached on both the tensile and compressive surfaces, parallel to the short one shown in Figure 5.11. The moment against surface strains from both the short and long strain gauges are plotted in Figure 5.11. Both strain gauges show almost identical behaviour on the compressive sides. On the tensile side, the overall trends for both strain gauges are similar, but the stress-strain curve plotted from the longer strain gauge is more gradual after the initial linear region and the obvious short plateaux have been eliminated compared with the shorter strain gauge. This confirms that the short plateaux observed on the tensile side of the bending beam are due to the localised fragmentation under the gauge length of strain gauges. However, since the overall shape of the moment-strain curves and tensile failure strain are similar, the tested results from short strain gauges are still valid.

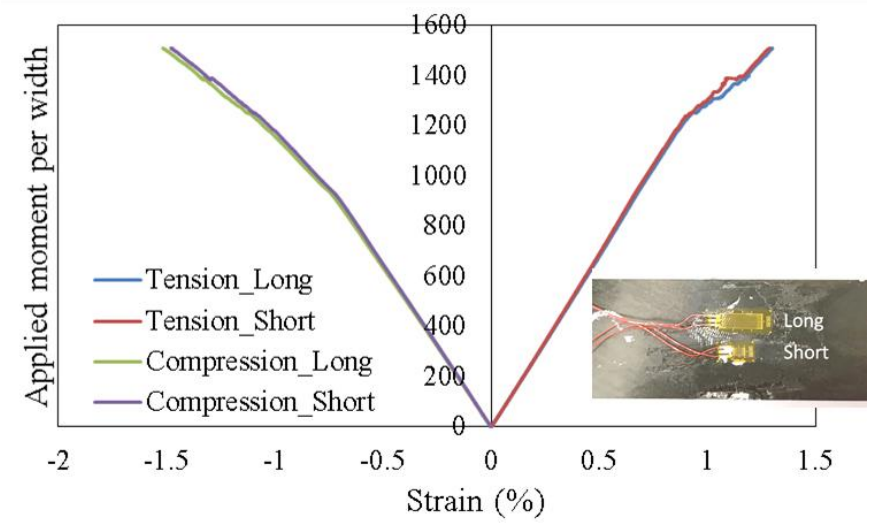

Figure 5.11: The measured moment-surface strain curves for strain gauges with two different gauge lengths. Results have been found to be almost identical.

The fragmentation of the 0° plies on the compressive side of the beam can therefore reduce the stiffness and result in the neutral axis shifting towards the tensile side (as shown in Figure 5.12). The neutral axis position relative to the bottom surface was determined from surface strain measurements using equation (4.11).

More specifically, at the beginning of testing, the neutral axis is almost in the middle of the specimen (the specimen is 3.3 mm thick) due to the very similar values of in tension and compression. With the load applied, the sub-laminate on the compressive side starts softening slowly due to non-linear elasticity of the carbon fibres in the 0° plies. The slope increases further around the compressive fragmentation load. When the 0° plies reach the compressive fracture strain, a clear change in the slope of the neutral axis curve can be seen and it moves toward the bottom skin. The neutral axis continuously moves downward as an increased level of compressive fibre fragmentation occurs. This trend changes once the fibre fracture strain is reached on the tensile surface and the neutral axis then moves back toward the top compressive skin. The fibre fragmentation on the compressive side makes the overall response more gradual and the fragmentation on the tensile side can slow down the strain accumulation on the compressive side. This results in a delay of the ultimate failure.

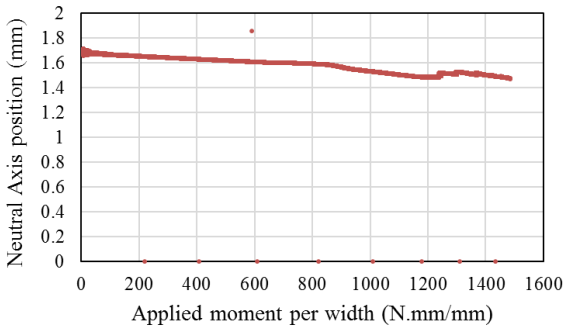

Figure 5.12: Neutral axis position relative to the bottom skin versus moment per unit width for the MR60-M55 specimen.

5.3.3 Damage analysis of the MR60-M55 laminate

All five specimens failed in the top compressive skins in a similar manner. A closer visual observation of the damage at the failure load is presented in Figure 5.13. The specimen failed by a single fracture through the thickness at the compressive side of the beam and across the entire width of the specimen, parallel to the direction of the 27° fibres. This single fracture mode was found to be the same as the compressive failure mode of the laminate with the same layup which was presented in chapter 4. The failure mode comprises the matrix failure between the

adjacent fibres in the 27° plies, fibre fracture in the -27° plies and 0° plies. As suggested in chapter 4, this compressive dominated failure mode was attributed to the combination of high in-plane shear and transverse tensile stresses. In addition to the compressive fracture, some apparent delaminations have been found to have initiated from the fracture surface of the angle plies, and propagated along different interfaces on the compressive side of the beam, induced by the fibre fracture and matrix cracking.

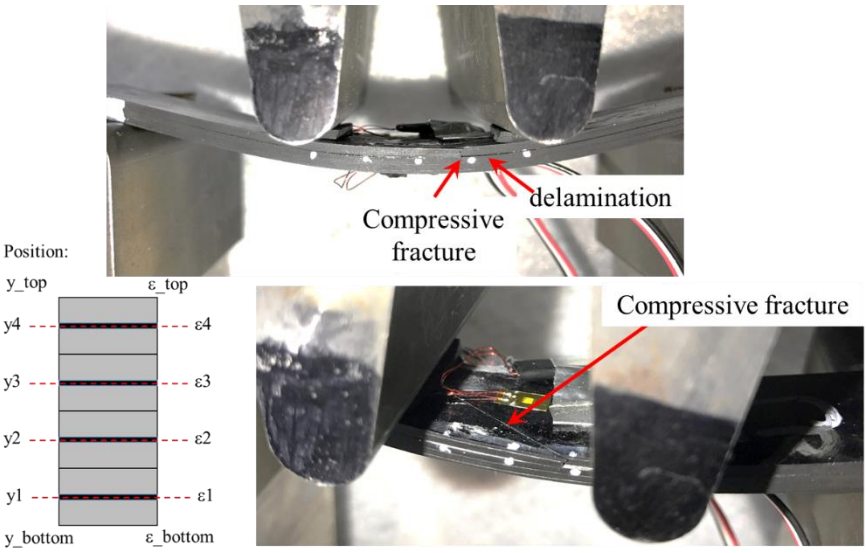

Figure 5.13: Visual observation of damage in the MR60-M55 specimen - failure exhibited on the compressive side of the beam.

To understand the damage within the specimens, further characterisation was carried out using Olympus and Zeiss microscopes, viewed from the free edge of the specimens. Figure 5.14 shows a typical microscopic observation of the MR60-M55 specimen at the failure load, with enlargements showing the details of damage. A complete fracture is found in the compressive side of the specimens across a large number of angle plies and 0° plies, perpendicular to the longitudinal direction. Delaminations at two different 0/-27 interfaces above the neutral axis are also observed in these specimens. Once the fracture of the 0° plies occurred, any further applied loading can bring the two fractured halves into contact and creates a stress concentration that favours a Mode-I delamination at the 0/-27 interfaces.

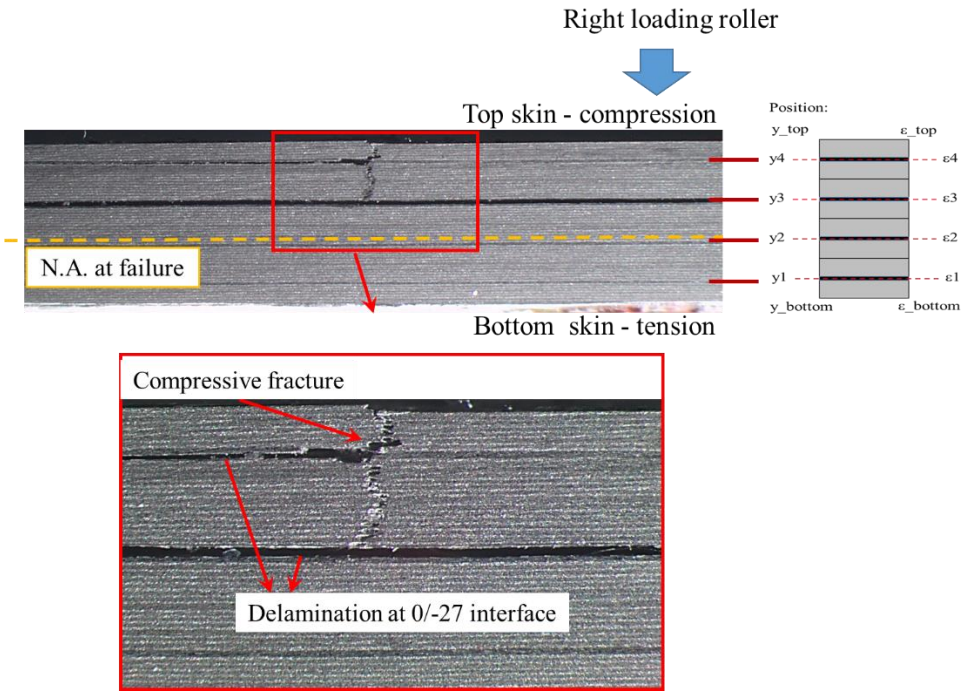

Figure 5.14: Microscopic images show the compressive fracture and delaminations above the neutral axis of the MR60-M55 specimen.

Further details of the localised damage were inspected via a Zeiss microscope. Figure 5.15 and Figure 5.16 show several portions of the laminate free-edge at the compressive side and the tensile side of the beam respectively. Figure 5.15 (a) and (b) show two typical observations on the compressive side. Both of them highlight that significant fragmentations of the central 0° plies in two different positions - "y3" and "y4" - on the compressive side (an image is attached to show the position of "y3" and "y4" in the through-thickness direction). These fragmented fibre lengths have been found in the range from 0.5mm to 0.7mm, for example 0.65mm in the presented portion. This observation shows a good agreement with the fragmented fibre length of the same layup that has been observed in compressive testing. It also confirms that the first major change in the gradient of moment-strain curves on the compressive side is attributed to fibre fragmentations in the compressive skins. Delaminations can be observed at the 0/-27 interfaces, as observed and discussed in the previous paragraphs.

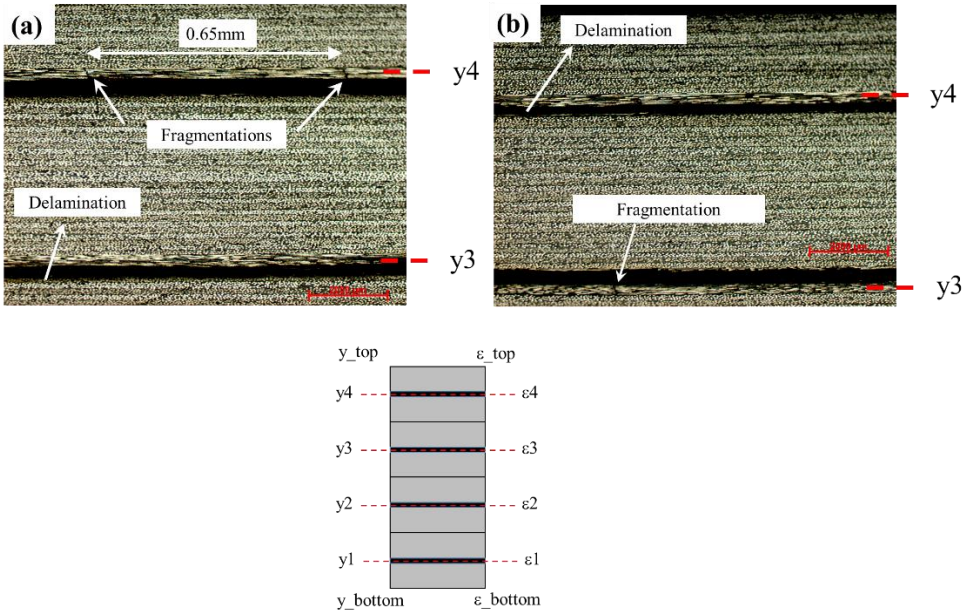

Figure 5.15: Typical microscopic images of the compression side of the MR60-M55 specimen, taken at two different position along the length of the beam

Similarly, Figure 5.16 (a) and (b) present two typical microscopic images taken on the tensile portion of the bending beam. Tensile fibre fragmentation can also be found in the central 0° plies of the outer MR60-M55 sub-laminate (the first one counted from the bottom skin). Localised dispersed delamination have initiated from the fractured ply and developed at the 0/-27 interfaces. Some of these delaminations have migrated through the -27° plies and joined with the edge delamination at the -27/27 interface adjacent to the central 0° plies. These damage modes are the same as the tensile damage modes of pseudo-ductile thin ply angle-ply laminates with central 0° plies, indicating that the neutral axis "shift-back" during the latter stage of the loading is attributed to fragmentation in the tensile skin. However, due to the 0° plies at the 2nd lowest sub-laminate being very close to the neutral axis, the strain level was insufficient to induce further fragmentation in this layer.

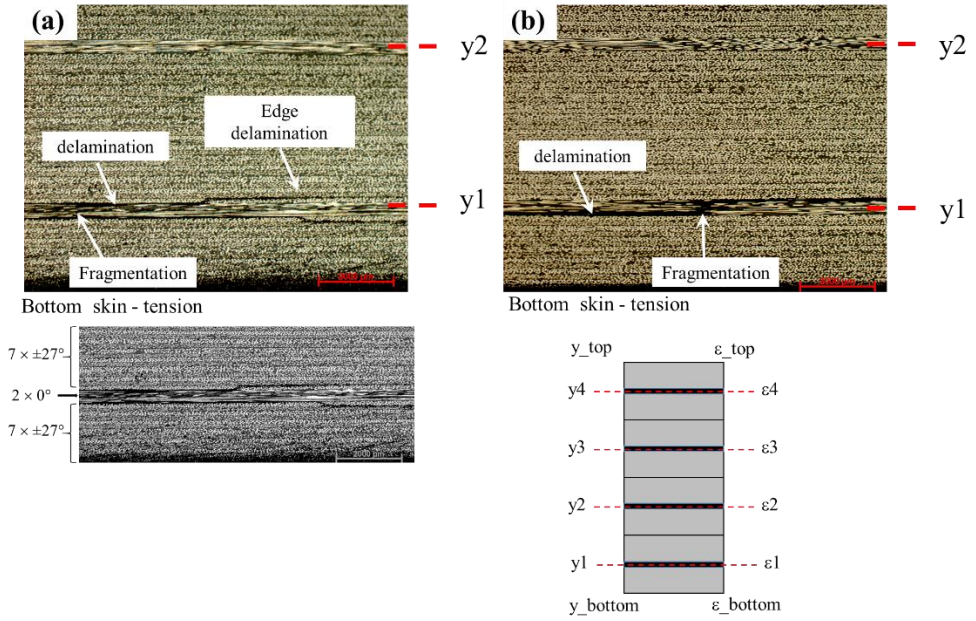

Figure 5.16: Typical microscopic images of the tensile side of the MR60-M55 specimen, taken at two different position along the length of the beam.

5.3.4 Bending results: the TC35-TC35 $[\pm 26_6/0]_s$

The applied moment per width versus the surface strains on the both sides of the bending beam are plotted in Figure 5.17 and the applied moment per unit width is also plotted against displacement in Figure 5.19. All the specimens generate consistent moment - strain behaviour apart from one specimen which shows a significant amount of noise in the load output, but this does not affect the overall shape of the curves. The averaged strains at failure on the tensile and compressive skins are 1.73% (2.6%) and -2.25% (4.0%) respectively, where coefficient of variation is shown in parentheses. The moment-displacement curve does not show any non-linearity until complete failure occurred. In the moment-strain curves, a small amount of hardening non-linear behaviour can be observed in tensile side and softening in compressive side, which are likely to be due to departure from linear elastic behaviour, with tensile modulus increasing with the increase of strain and the compressive modulus [123,190]. The degree of non-linearity in compression is often greater than that in tension, resulting in the position of neutral axis changed during loading. As shown in Figure 5.12, the position of neutral axis is at 1.33 mm above

the bottom surface at the beginning and gradually falls to 1.15 mm at the failure load. It gives an overall 0.18 mm shift of the neutral axis toward to the tensile bottom skin. This can slow down the strain increase on the tensile side and therefore the moment-strain curve presents more non-linearity on the tensile side than on the compressive side.

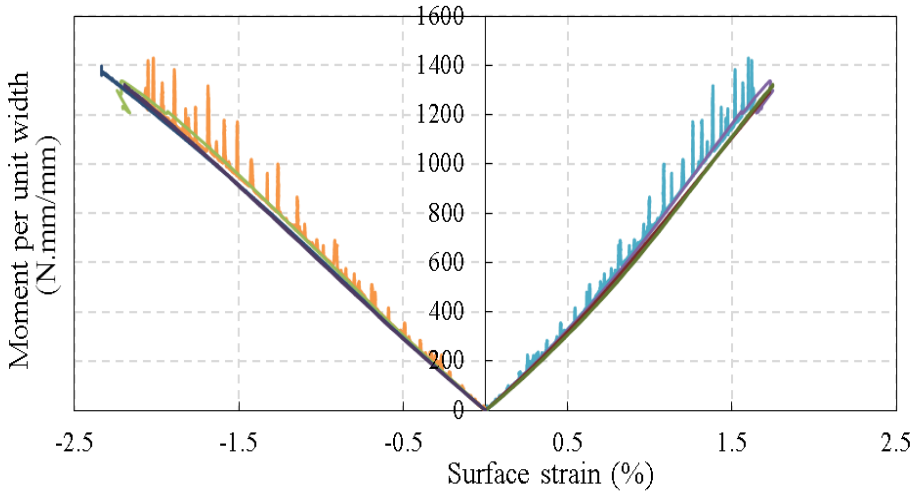

Figure 5.17: Applied moment per unit width versus surface strains of test beam for the TC35-TC35 laminates under four-point bending. Note, the spikes in yellow and blue are the noisiness in the load measurement of a single specimen, which can be explained by voltage fluctuations in the analogue output from the Instron testing machine.

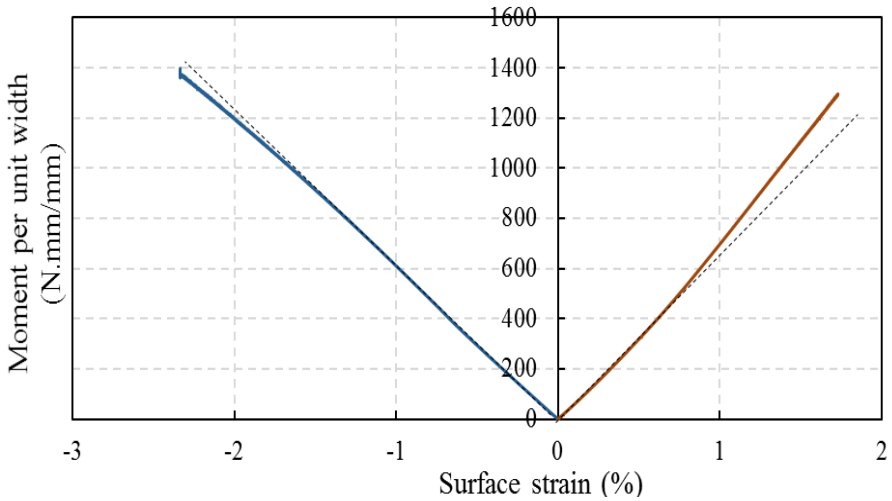

Figure 5.18: Moment-surface strain plot for single TC35-TC35 specimen. Two dashed lines were plotted with original curves, highlighting linear regions.

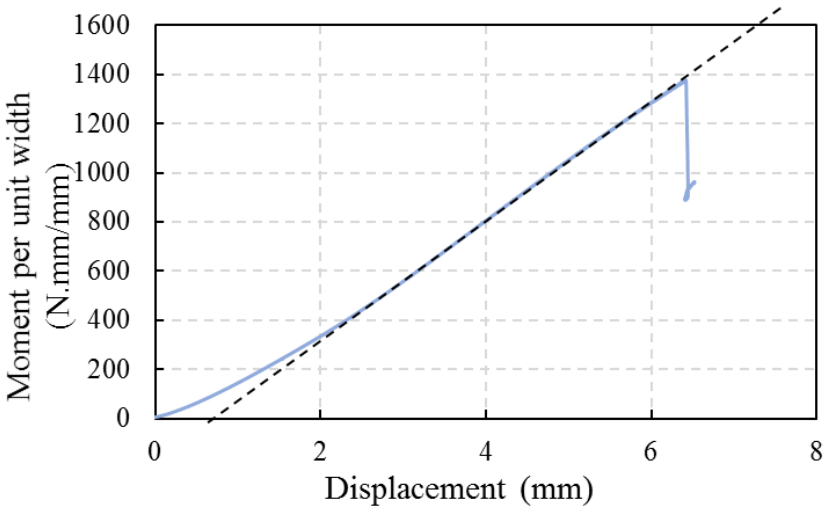

Figure 5.19: Applied moment per unit width versus displacement of the TC35-TC35 specimen under four-point bending. Dashed line was plotted with the original curve, highlighting linear region. The initial small amount of soft region is due to the rubber softness, which is not taking into consideration of material non-linearity.

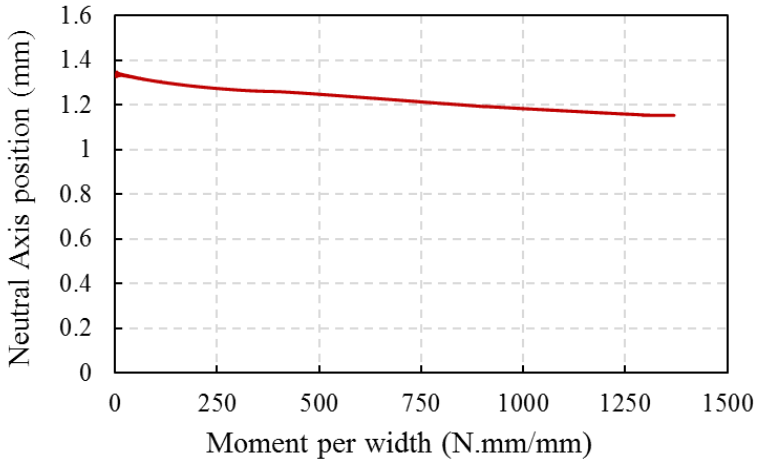

Figure 5.20: Neutral axis position relative to the bottom skin versus moment per unit width for the TC35-TC35 specimen.

5.3.5 Damage analysis of the TC35-TC35 laminates

The visual observation of the specimen at failure shows that the TC35-TC35 laminate also failed on the compressive side. Similar to the failure mode of the

MR60-M55 laminate, with the high in-plane shear stress and transverse tensile stress in the angle plies, compressive fracture was initiated, and parallel to the 26° fibre direction. The damage also involves matrix cracking in the 26° plies and fibre fracture of the 0° and -26° plies. Delaminations are also seen in the specimen on the compressive side and details of this damage will be observed and discussed in more detail together with the following microscopic observations.

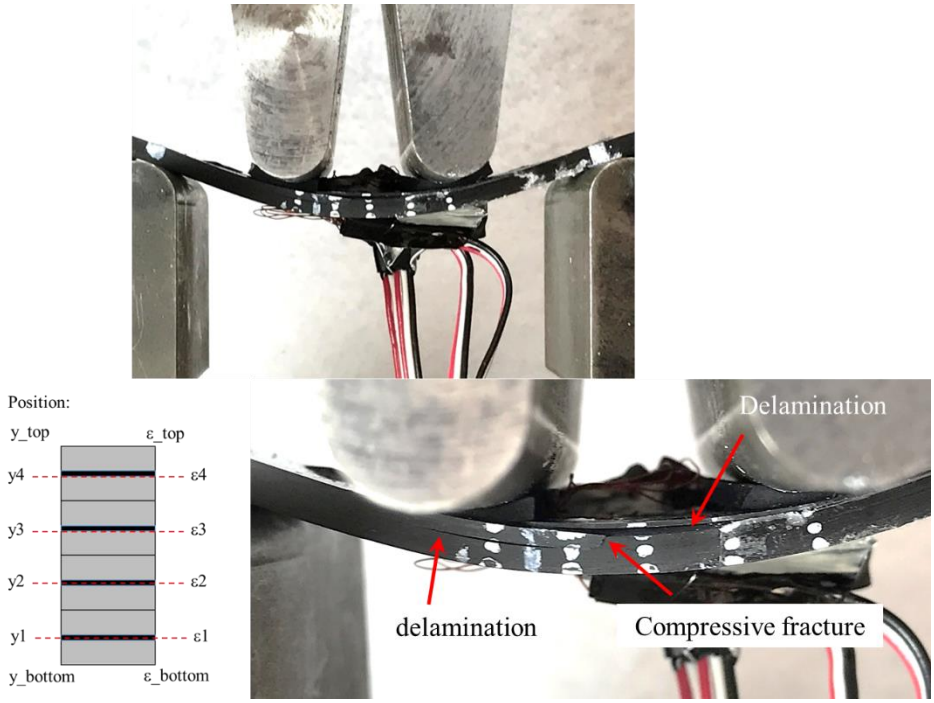

Figure 5.21: Visual observation of damage shows failure occurred on the compressive side of the TC3-TC35 specimen.

Figure 5.22 presents a microscopic image of TC35-TC35 specimens at the failure load. Two similar but slightly different damage morphologies have been observed in these laminates. In Figure 5.22 (a), the compressive fracture initiated and developed through the entire first two sub-laminates counting from the top skins. Several delaminations at different -26/26 interfaces were induced from the fractured fibres and matrix cracking, and the most severe one was found at one of the -26/26 interfaces close to the neutral axis. In Figure 5.22 (b), the fracture only occurred in the upper half of the topmost sub-laminate, also introducing several delaminations

at the -26/26 interfaces. No obvious damage can be seen on the tensile side according to the microscopic images at the current magnification.

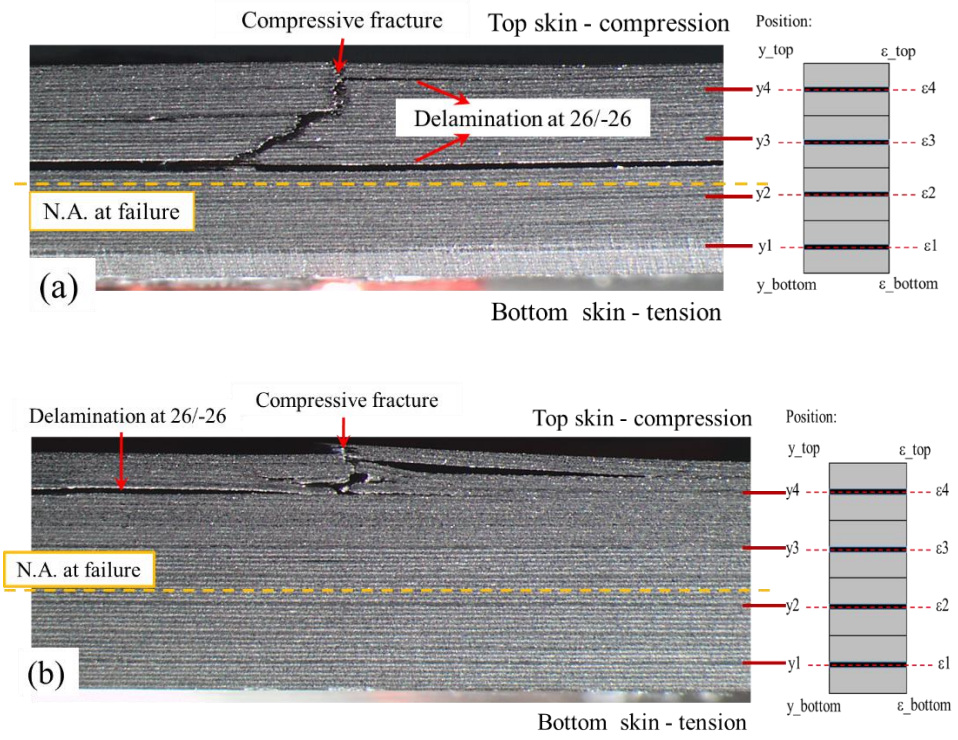

Figure 5.22: Microscopic images show the compressive fracture and delaminations above the neutral axis. There are two slightly different morphologies which are seen among all TC35-TC35 specimens.

The images taken under the Zeiss microscope show the damage at the free-edge of the specimen at a higher magnification and are presented in Figure 5.23, where (a) and (b) present typical observations on the compressive side and (c) presents the tensile side. Major damage and primary fibre failure are seen in the position where compressive fracture occurred. In the rest of the specimen, delamination initiated from the compressive fracture is the major damage on the compressive side, without any other damage observed. On the tensile side, 0° plies fragmentation and localised dispersed delamination are observed on the lower tensile sub-laminate. However, only a few fragmentations can be seen within the region between the loading span,

due to the premature fibre fragmentation. Therefore, the non-linearity on the tensile side was limited and the specimen failed in compression as a single fracture.

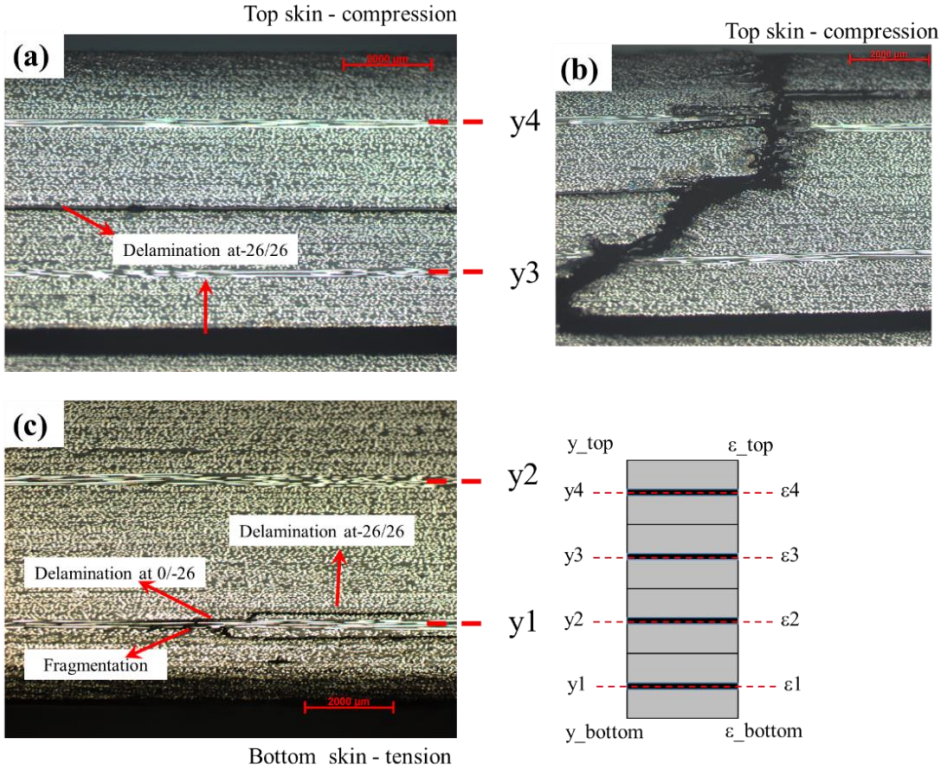

Figure 5.23: Microscopic images of (a)(b) compressive side and (c) tensile side of the TC35-TC35 specimen, taken at different positions along the length of the beam.

5.4 Conclusions

In this chapter, an experimental investigation into the bending behaviour of two different pseudo-ductile thin ply angle-ply laminates has been performed. The two layups tested in the bending were the MR60-M55 $[\pm 27_7/0]_s$ and TC35-TC35 $[\pm 26_6/0]_s$ laminates. The MR60-M55 laminate showed pseudo-ductile behaviour in both uniaxial tensile and compressive loading and this is achieved by the gradual fragmentation in the central 0° plies, as presented in Chapter 4. The TC35-TC35 laminate also showed pseudo-ductility and 0° ply fragmentation in tension and, is not expected to display pseudo-ductility in compression.

Both layups were found to fail on the compressive side of the bending beam, but they exhibited different moment-displacement and moment-strain behaviour in flexural loading. The MR60-M55 laminate was shown to have a more gradual failure and a larger amount of non-linearity according to the moment-displacement and the moment-strain curves. The non-linearity development was primarily due to the initial 0° ply fragmentation on both the compressive and tensile sides of the beam. The fragmentation on the tensile side resulted the position of neutral axis shifts up and down, to slow down the strain accumulation on the compressive skin and delay the final failure on the compressive surface. By contrast, the TC35-TC35 laminate has shown less non-linearity in the moment-displacement and moment-surface strain curves.

To understand the bending behaviour better and to examine damage within the specimen, both layups were characterised under microscope and found to fail in compression – a single fracture across the width and parallel to the angle ply direction. More detailed microscope images confirm that 0° ply fragmentation was observed in the sub-laminates on both the compressive and tensile sides of the MR60-M55 laminate. In the TC35-TC35 laminate, only a few premature fragmentations were found in the 0° plies on the tensile sides. In addition to the compressive fracture in angle plies and fibre fragmentation in the 0° plies, interlaminar shear delamination was also observed at multiple different location in both layups. These delaminations initiated from the compressive fracture surfaces and propagated along the 0/-27 interfaces for the MR60-M55 laminate and the 26/-26 interfaces for the TC35-TC35 laminate. These delaminations are more likely to be due to the stress concentrations at the fracture surfaces which favour a Mode-I delamination.

6 An investigation into fatigue behaviour and fatigue damage progression in Pseudo-ductile thin ply angle-ply laminates

Fatigue behaviour is another major consideration in the design of pseudo-ductile thin ply angle-ply laminates with central 0° plies. Fatigue loading was found to be a main cause of laminate failure, if the operating stress is too high during its service. Therefore, in this chapter, tension-tension fatigue loading was applied to the pseudo-ductile laminates. Two types of tests are presented: pristine specimens, tested at various peak amplitudes in the elastic region below the "yield" stress, and overloaded specimens with "pre-fractured" 0° plies, which were loaded in fatigue. The first experiment aims to determine the operating limits of these laminates and the latter one focuses on damage progression, particularly on the delamination onset and growth in these laminates.

6.1 Introduction

Pseudo-ductility has been observed in the thin ply angle-ply laminates with central 0° plies loaded in tension. The primary damage mechanisms in these laminates are fibre fragmentation in the internal 0° plies and localised delamination, although the damage morphologies are similar in these laminates, but still vary from case to case.

Fatigue is critical in the design of composites as structures have to bear a certain amount of fatigue loading during operation. Carbon fibre composites can usually sustain damage during cyclic loading, especially for thin ply carbon fibre laminates, but most tests have been conducted on conventional unidirectional or quasi-isotropic laminates, which behave linearly and have a sudden failure in static tension. Due to the unique failure mechanisms and pseudo-ductile stress-strain behaviour of $[\pm\theta_m/0_n]_s$ laminates, fatigue testing needs to be performed.

In this chapter, pseudo-ductile laminates with three different layups the TC35-TC35 $[\pm 26_6/0]_s$, MR60-YSH70 $[\pm 25_2/\underline{0}]_s$ and MR60-M55 $[\pm 27_7/0]_s$ presented in chapter 3 and chapter 5, were tested in tension-tension fatigue loading. Two types of tests were performed: pristine specimens were tested within the elastic region (below the "yield" stress) to determine the maximum stress level that these laminates can safely operate under and overloaded specimens with "built-in" initial 0° ply fragmentation, which were loaded in fatigue to investigate damage progression.

6.2 Testing arrangements

6.2.1 Specimens preparation and manufacture

The three different laminates TC35-TC35 $[\pm 26_6/0]_s$, MR60-YSH70 $[\pm 25_2/0]_s$ and MR60-M55 $[\pm 27_7/0]_s$ were all made from thin prepregs with different fibre types, different angles and different angle ply to 0° ply ratios.

These laminates were manufactured from commercially available thin ply prepregs. The curing cycles were the same as those used in static tension and can be found in chapters 3 to 5. Due to prepreg availability, the North prepreg with Nippon YSH70 fibre that was used in the MR60-YSH70 laminate, was replaced by the

Granoc prepreg with the same fibre type. The major difference between the two prepregs is the ply thickness, which is t = 0.05 mm for the Granoc prepreg compared to t = 0.032 mm for the North prepreg. Therefore, in the present study, the layup of the MR60-YSH70 laminate was modified to $[\pm 25_2/\underline{0}]_s$, where underline indicates only a single of 0° ply being used in the central ply. The cured prepreg properties are specified in Table 6.1 and the curing cycle is: dwell at 80°C for 75 mins and a curing temperature of 125°C for 165 mins. The laminates were machined to form specimens of the same dimensions as those used for the static tests, illustrated in Figure 3.2 in chapter 3.

Table 6.1: Cured prepreg properties for the YSH70/epoxy Granoc prepreg

		YSH70/epoxy (Granoc prepreg)
E_1	[GPa]	400
E_2	[GPa]	6.2
σ_1	[MPa]	2000
G_{12}	[GPa]	4.0
ε_1	[%]	0.5
t	[mm]	0.05
v_f	[%]	50

6.2.2 Test matrix

The pristine specimens underwent cyclic loading at several stress severities below the "yield" stress. As a starting point, the peak stress level used for all three configurations was 80% of the "yield" stress. Since there is no obvious stiffness loss in the specimen up to 1 x 10^5 cycles, the stress severity was then increased to 90% or higher. In the fatigue tests of "pre-fractured" specimens, the pristine specimens were first statically loaded to beyond the "yield" stress to introduce fragmentations in the specimen, called "pre-fractured" specimens. Then the "pre-fractured" specimens were tested under cyclic loading. The stress severity selected in the latter case is mainly focused on the maximum operating stress level determined from the first case. The details of the test matrix are shown in the Table 6.2.

Table 6.2: Summary of test matrix for three different configurations. Note: 4 specimens in each test were planned. This number is slightly modified based on the real test.

	Peak stress (as a percentage of "yield" stress)	TC35-TC35 $[\pm 26_6/0]_s$,	MR60-YSH70 $[\pm 25_2/\underline{0}]_s$	MR60-M55 $[\pm 27_7/0]_s$
Pristine	80%	4	5	4
	90%	4	4	4
	95%		5	2
Pre-fractured	80%	4	4	4
	85%			4
	90%			4

6.2.3 Testing procedures and set-up

All fatigue tests were performed using an Instron hydraulically-actuated system with a 5 kN load cell for the MR60-YSH70 laminate and a 25 kN load cell for the TC35-TC35 and MR60-M55 laminates, since the latter two were operated at greater load ranges. Testing was carried out in a load control mode at a series of different peak stresses (σ_{peak}) as stated previously in Table 6.2, with a constant load ratio of R = 0.1 and frequency of 2 Hz across all the tests. Strains, used for the modulus calculation, were recorded at different numbers of cycles using an Imetrum Video Extensometer. Each batch of specimens was tested to 1 x 10^5 cycles if no specimen failure occurred before this number. Due to the time limit, only one specimen in each batch was tested to 1 x 10^6 cycles at 80% and 90% stress severities, as 1 x 10^6 cycles is commonly used in the investigation of fatigue behaviour of carbon fibre composites. The relation between applied stress ($\sigma_{applied}$) and time (t) can be expressed in the following equation:

$$\sigma_{applied} = \left(\frac{1-R}{2}\sin t + \frac{1+R}{2}\right)\sigma_{peak} \quad (6.1)$$

The fracture of the 0° plies is found to be the first main damage mechanism and the material no longer behaves linearly when the "yield" stress has been reached, therefore the peak stress used in the fatigue tests was below the "yield" stress. In the pre-fractured fatigue tests, to introduce fragmentation in the 0° plies, the pristine

specimen was firstly loaded statically to a strain that is higher than the "yield" strain of the same laminate. In order to limit the number of fragmentations and minimise local delamination developed in the laminates, the strain just beyond the "yield" strain was selected as the "fracture" strain, which was 2.00% for the TC35-TC35 laminate (1.91%), 0.55% for the MR60-YSH70 laminate (0.49%) and 0.75% for MR60-M55 laminate (0.68%), where the numbers in the parentheses are the "yield" strains for each configuration. The selection of "fracture" strain was based on a ratio of the difference between fracture and "yield" strains to the total plateau strain. One of the major factors that can introduce variability in the results for "pre-fractured" fatigue is the number of fragmentations generated in the static "pre-fracture" tests. It is not easy to quantify and control the number of fragments within the specimens, since the carbon fibre laminates are not transparent and fragmentations randomly occur in the gauge length once the fibre fracture strain is reached. Therefore, acoustic emission was employed as a technique and sensors were attached to the specimen during the "pre-fracture" test. The reason for choosing acoustic emission is that amplitude and energy of acoustic emission events have been found to be useful in identifying the fibre fragmentation failure in previous studies [29]. An approximate number of fragments in the "pre-fracture" tests would be expected to be provided using acoustic emission. Figure 6.1 presents the test setup for the pre-fracture testing.

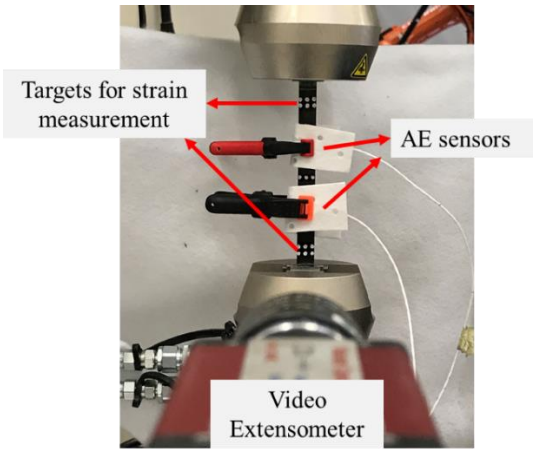

Figure 6.1: Setup for the pre-fractured testing. A video gauge was employed to measure the strain of the specimen before and after pre-fracture, and acoustic emission was used to quantify the number of fragmentations in "pre-fracture" testing.

6.3 Results of static tensile testing

Since the MR60-YSH70 $[\pm 25_2/\underline{0}]_s$ laminate with Granoc YSH70 fibre prepreg has not been previously tested, it was initially tested in static tensile loading using a loading rate of 2 mm/min. The tensile stress-strain response is plotted in the Figure 6.2. Similar pseudo-ductile stress-strain behaviour was observed in the $[\pm 25_2/0]_s$ laminate (two layers of 0° plies with nominal thickness 0.031mm in the centre) in Figure 2.7, and in the $[\pm 25_2/\underline{0}]_s$ laminate (single layer of 0° ply with nominal thickness 0.05mm in the middle). The major differences observed in $[\pm 25_2/\underline{0}]_s$ laminate compared to the $[\pm 25_2/\underline{0}]_s$ laminate is the lower "yield" stress and ultimate strength, which are due to there being only one 0° ply in the $[\pm 25_2/\underline{0}]_s$ laminate. The full set of key mechanical properties are summarised in the Table 6.3. From visual observation, the failure modes of $[\pm 25_2/\underline{0}]_s$ laminate are also similar to the $[\pm 25_2/0]_s$ laminate, but are not discussed here. Along with the mechanical properties of the TC35-TC35 and MR60-M55 laminates, their key mechanical properties referenced in fatigue testing are presented in Table 6.4 and static tensile stress-strain curves are in Figure 6.3.

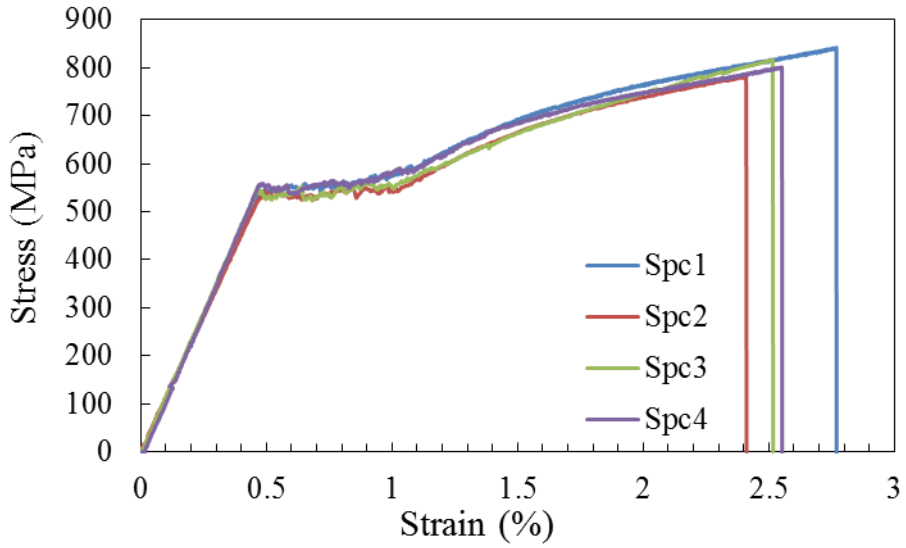

Figure 6.2: Tensile stress-strain curves for MR60-YSH70 (Granoc) laminates tested under static tensile loading

Table 6.3: Summary of mechanical testing results from static tension of MR60-YSH70 (Granoc prepreg)) laminate. The coefficient of variations (CV) for each mechanical property are shown in parentheses.

	σ_Y [MPa]	σ^* [MPa]	ε_Y [%]	ε^* [%]	ε_d [%]	E [GPa]
MR60-YSH70 $[\pm 25_2/\underline{0}]_s$	548 (1.5%)	811 (3.5%)	0.49 (1.1%)	1.87 (5.9%)	2.57 (4.6%)	115 (2.7%)

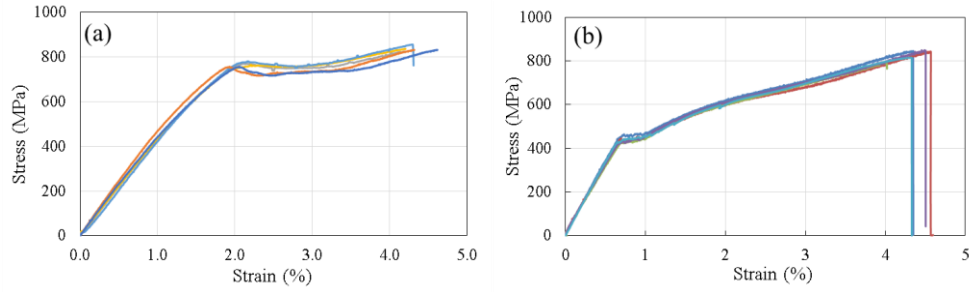

Figure 6.3: Recalling the tensile stress-strain curves for the (a) TC35-TC35 and (b) MR60-M55 laminates in static tensile loading.

Table 6.4: Summary of key parameters used in fatigue testing (obtained from static tensile testing).

	TC35-TC35 $[\pm 26_6/0]_s$	MR60-YSH70 $[\pm 25_2/\underline{0}]_s$	MR60-M55 $[\pm 27_7/0]_s$
ε_Y [%]	1.91	0.49	0.68
σ_Y [MPa]	737	548	435
E [GPa]	45	115	65

6.4 Fatigue test results of the TC35-TC35 laminates

6.4.1 Fatigue test of the pristine specimen

The first batch of specimens was tested in a cyclic loading at a peak stress level - 80% of the "yield" stress. The normalised modulus is plotted against the number of cycles in Figure 6.4. The normalised modulus is defined as the modulus measured between 0.1% and 0.3% strains, at the i_{th} cycle (E_i) divided by the modulus of the pristine

specimens (E_0), and it presents a straightforward way for observing damage evolution during loading. From Figure 6.4, it can be clearly seen that no obvious modulus reduction can be observed up to 1 x 10^5 cycles when the specimens were loaded at 80% stress severity and Spc4 even displayed no modulus reduction up to almost 1 x 10^6 cycles. From visual observation, only a few matrix cracks were observed from the surface of the specimens, but no other damage can be seen at this stage.

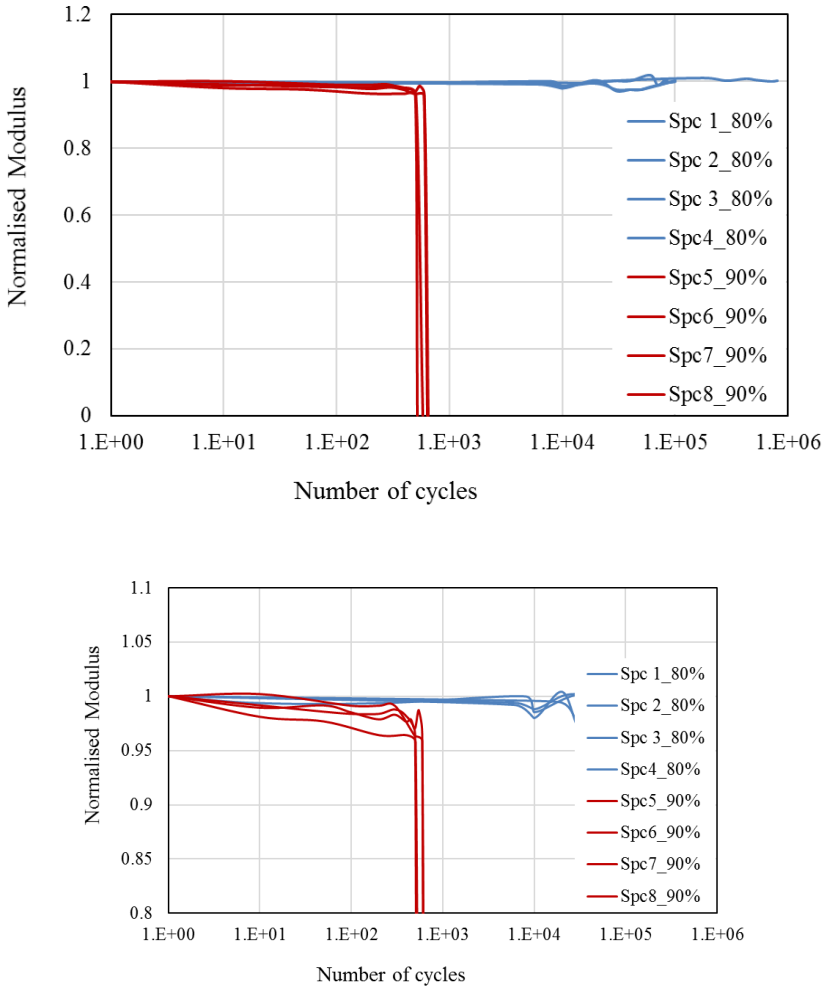

Figure 6.4: Fatigue stiffness curves for the TC35-TC35 laminate at 80% and 90% severity. The present normalised modulus is the modulus at the i^{th} cycle by initial modulus.The bottom figure shows the same figure, but zoomed in on the y-axis.

The specimens removed from testing machine after 1 x 10^5 cycles in cyclic loading, were submerged in zinc iodide dye penetration and then were characterised in an X-ray CT inspection machine in the same fashion to that in chapter 3. Since the fragmentation in the central 0° plies and delaminations at 0/-θ interfaces were found to be the major damage when the specimens were loaded in the static tension, the X-ray images were taken at the mid-plane of the laminates. One additional image was taken at the surface ply, since micro-cracks have visually been observed on the surface. From the X-ray images captured at the mid-plane (Figure 6.5 (a)), there is no significant fatigue damage developed in the TC35-TC35 laminate at this stress level. The image taken at the surface (Figure 6.5 (b)) shows a few bright lines near the free edge of the specimen, which are related to matrix cracks in the 26° ply. These matrix cracks on the surface ply are due to the lack of constraint from the adjacent plies and to the free-edge effect.

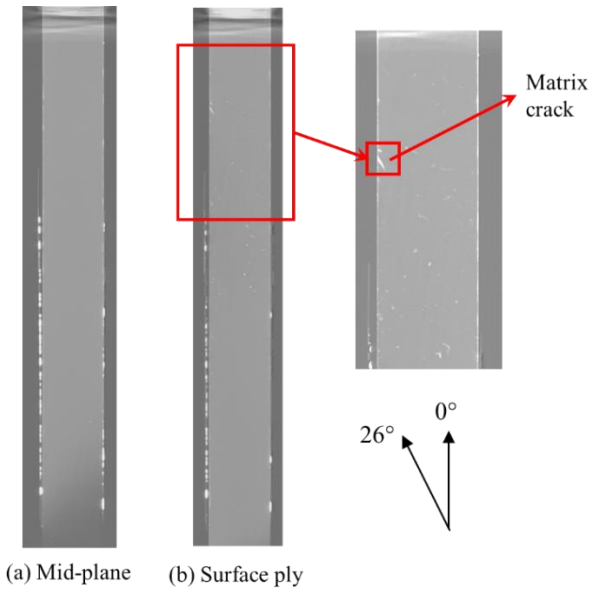

Figure 6.5: X-ray images of the pristine TC35-TC35 specimen tested to 1 x 10^5 cycles in fatigue loading at 80% severity.

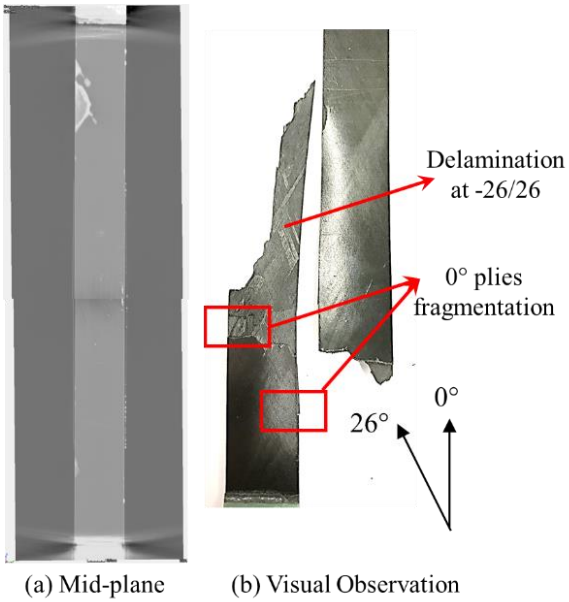

Figure 6.6: (a) The X-ray image of the pristine TC35-TC35 specimen interrupted at 400 cycles and (b) visual observation of fractured specimen for the TC35-TC35 specimen tested in fatigue loading at 90% severity.

Overall, the unchanged modulus and lack of critical fatigue damage in the laminates at 80% fatigue stress severity effectively demonstrate that the TC35-TC35 laminate can be operated at this cyclic peak stress to up to 1 x 10^6 cycles without obvious stiffness reduction. The peak stress was further increased to 90% of the "yield" stress and the normalised modulus against number of cycles plotted in Figure 6.4. All four specimens failed at an average 598 cycles (8.8% CV) and the average normalised modulus just before failure was 0.96 (0.3% CV). From visual observation presented in Figure 6.6 (b), the failed specimen displays some 0° ply fragmentation, complete fibre fracture in the angle plies and extensive delamination extended from the edge at the -26/26 interface. One specimen was interrupted at 400 cycles and inspected using X-rays, since the obvious modulus reduction can be observed at this number of cycles. In the X-ray image taken at the mid-plane of the laminate as shown in Figure 6.6 (a), a few inclined bright lines are observed in the top part of the gauge section and are identified as fragmentation of the 0° plies. These fragmentations were surrounded by a triangle shape with lower severity colour, which was found to be an edge delamination at the -26/26 interface. The delamination at -26/26 interface propagated quickly to form the final failure including the fracture of angle plies.

6.4.2 Fatigue testing with pre-fractured 0° plies

The pristine TC35-TC35 specimen displayed no modulus reduction at 80% of the "yield" stress, but showed poor performance in fatigue if the stress severity increased to 90%. To understand the ability of these laminates to withstand fatigue loading when the specimen contains "built in" fragmentation, fatigue tests with "pre-fractured" specimens were performed. The specimens were loaded in static tension to a strain of 2.0%, 0.1% higher than the "yield" strain of the TC35-TC35 laminate, and then underwent cyclic loading at 80% of the "yield" stress. The 80% value was selected since it is the maximum stress level at which the pristine specimen can be operated without obvious modulus reduction. The normalised modulus is plotted against number of cycles in Figure 6.7 and the typical acoustic emission events captured in the pre-fracture testing are shown in Figure 6.8. The modulus at the i^{th} cycle is normalised by the modulus of the pristine specimens, therefore the modulus reduction due to the pre-fracture can be seen from the same graph. The modulus was found to reduce significantly with the increase in number of cycles, and the specimens eventually failed at an average 2263 cycles (40% CV) with an average 10% reduction in modulus. Acoustic emission energy events in Figure 6.8 show that the large variation in the cycles to failure can be attributed to the number of fragmentations introduced in the pre-fracture. The total modulus reduction is higher than the pristine specimens at 90% loading, whilst it can last a larger number of cycles.

Visual observation of the failed specimen in Figure 6.9 shows damage initiation from the pre-fractured 0° plies. Instead of introducing more fragmentations in the 0° plies, the damage migrated from the 0° plies to the -26/26 interfaces adjacent to both sides of the central 0° plies and propagated extensively until the final fracture. The modulus reduction at the beginning of the fatigue modulus curve is attributed to 0° ply fragmentations, and the modulus reduction in the rest of the curve is primarily due to the delamination growth at -26/26 interfaces.

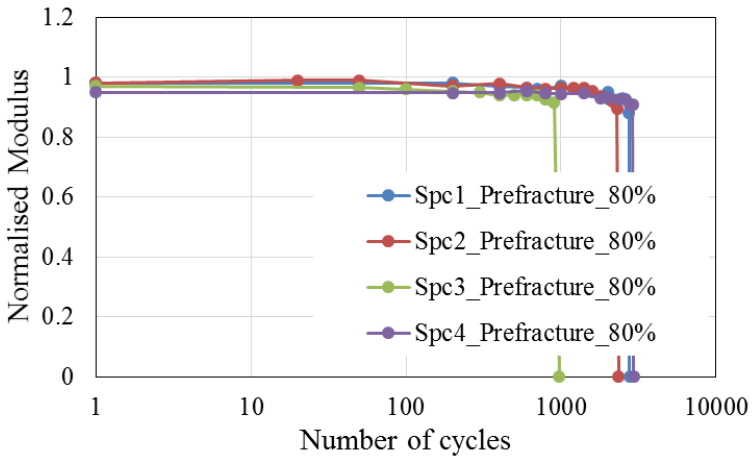

Figure 6.7: The modulus reduction in the TC35-TC35 laminate against number of cycles in "pre-fractured" fatigue loading at 90% severity.

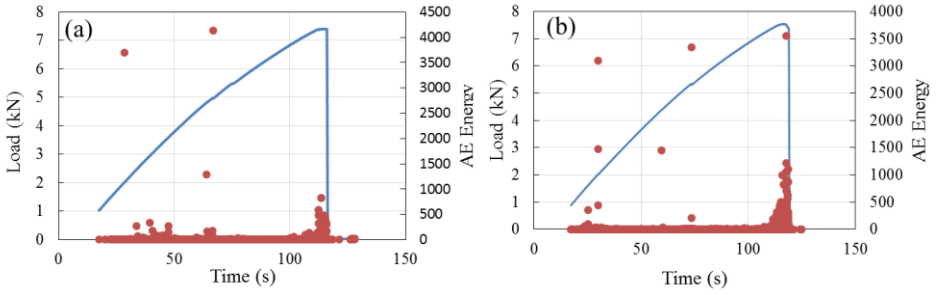

Figure 6.8: Typical acoustic emission energy events plots have shown the fragmentation in the pre-fracture testing of the TC35-TC35 specimens.

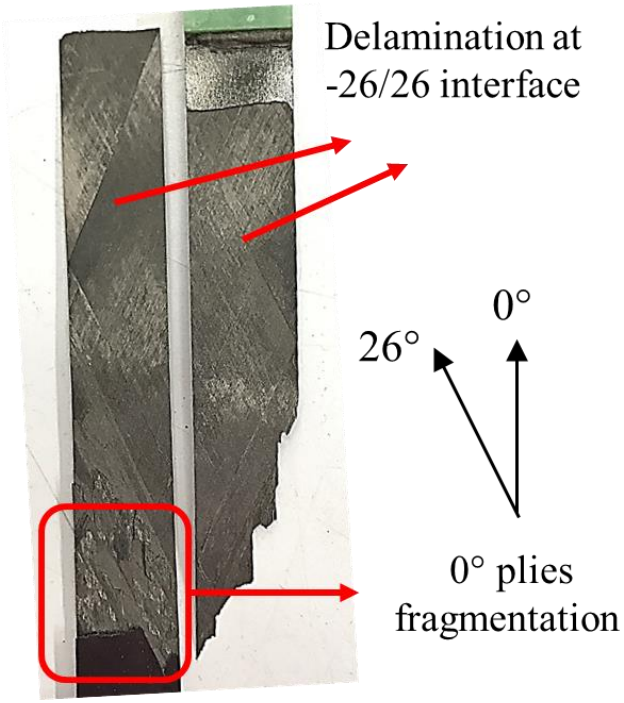

Figure 6.9: The failed TC35-TC35 specimen has shown fragmentation in 0° plies and complete delamination at -26/26 interface.

6.5 Fatigue results of the MR60-YSH70 laminates

6.5.1 Fatigue test of the pristine specimens

The pristine MR60-YSH70 specimens were tested at three different stress severities: 80%, 90% and 95% of the laminate's "yield" stress. The normalised modulus against the number of cycles for all three stress severities is plotted in Figure 6.10. At 80% and 90% severities, no observable modulus reduction can be seen when the specimen underwent cyclic loading to at least 1 x 10^5 cycles. When the specimen was loaded at 95% load severity, the modulus significantly dropped to about 51% (5.3% CV) of the initial modulus and the specimen failed at an average 60,000 (57% CV) cycles. All the curves display very similar trends, but show very large variation in the number of cycles. Considering the different number of cycles required for the weakest cluster of fibres to initiate fragmentation in different specimens and the average "yield" stress used for fatigue reference stress, the results still display good consistency. In general, 90% of the "yield" stress is the operating limit for the MR60-

YSH70 laminates. A red dashed-line is plotted in Figure 6.10 showing the modulus contribution from the angle plies calculated from Classical Laminate Analysis (CLA). It shows that the modulus of the specimen at failure point loaded at 95% severity is still higher than the angle-ply modulus contribution, which means the 0° plies still carry a certain amount of load before the final fracture.

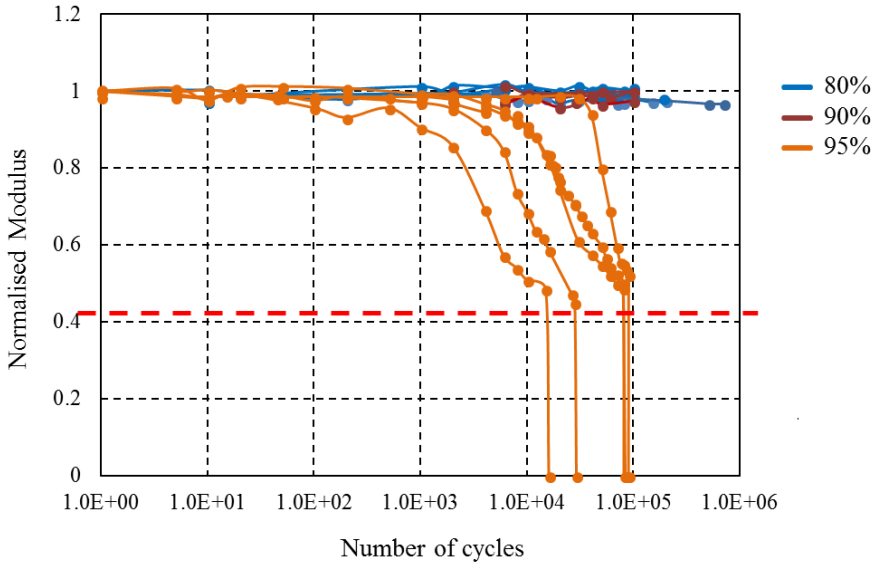

Figure 6.10: The normalised modulus against number of cycles plots for the MR60-YSH70 laminate at 80%, 90% and 95% severities. The red dashed-line is plotted, showing the modulus contribution from the angle plies calculated from (CLA).

Since the angle plies on each side of the central 0° plies are very thin, any delamination inside the laminates is reflected in the surface appearance. Figure 6.11 presents the damage evolution during cyclic loading via observation of the surface appearance changes for the Spc2 at 95% severity and Figure 6.12 indicates the number of cycles where the images were captured. The fragmentation is expected to have initiated between 0 and 1000 cycles according to the fragmentation sound captured during the test. However, due to the small gaps between adjacent fragmentations in the 0° plies, it did not cause any visual changes at 1000 cycles. At 16,000 cycles, inclined lines can be observed in the top of the specimen and at 28,000 cycles, these lines are extended to a wider range, along with the initiation of

delamination in a triangular shape at the free-edge. At 80,000 cycles just before the final failure, the area covered by the inclined lines increases to almost the entire gauge length and most of these lines are jointed together with edge delamination.

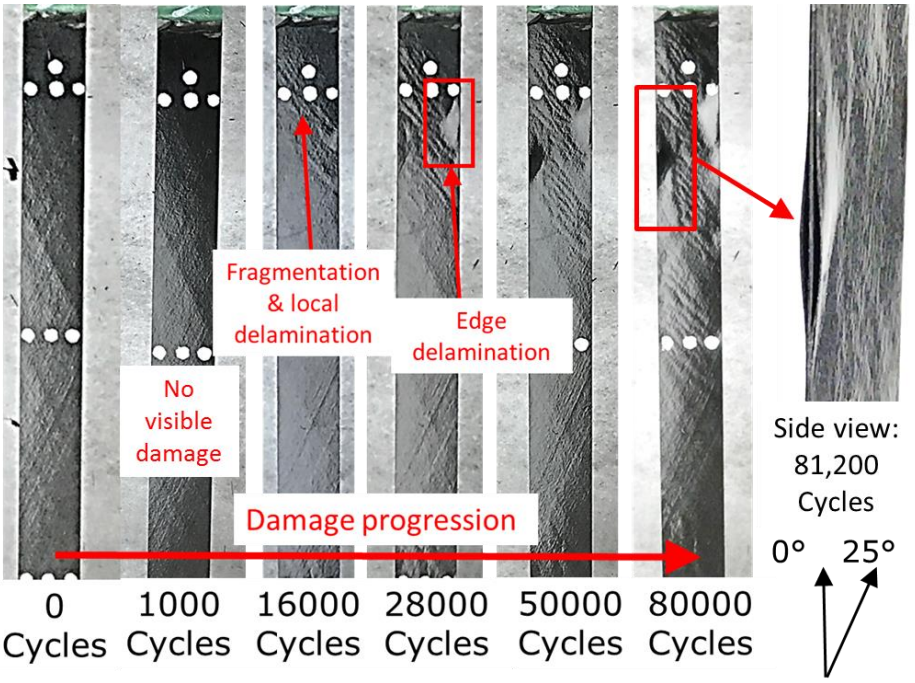

Figure 6.11: Damage progression of the MR60-YSH70 laminates at 95% severity. The damage is shown as the surface appearance change of the specimen during testing.

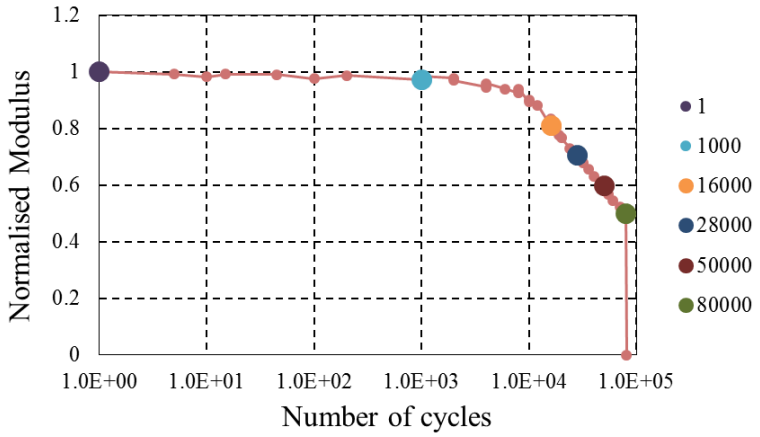

Figure 6.12: Stress-strain plot for showing the position of damage progression images for the pristine MR60-YSH70 specimens

.

6.5.2 Fatigue test with pre-fractured 0° plies

Four specimens were loaded in static tension to a strain of 0.55%, 0.06% higher than the "yield" strain of MR60-YSH70 laminate, and then tested in cyclic loading at 80% stress severity. The fibre fragmentation in the pre-loading was monitored by acoustic emission and a typical AE energy plot is shown in Figure 6.14. The normalised modulus against number of cycles is shown in Figure 6.13 and all the tests were manually terminated at 200,000 cycles. A 7% modulus drop is found in the pre-fracture and only a further 5% modulus drop is in the cyclic loading after 200,000 cycles. As opposed to the "pre-fractured" TC35-TC35 specimens that fail very quickly in cyclic loading, the "pre-fractured" MR60-YSH70 specimen retained good structural integrity.

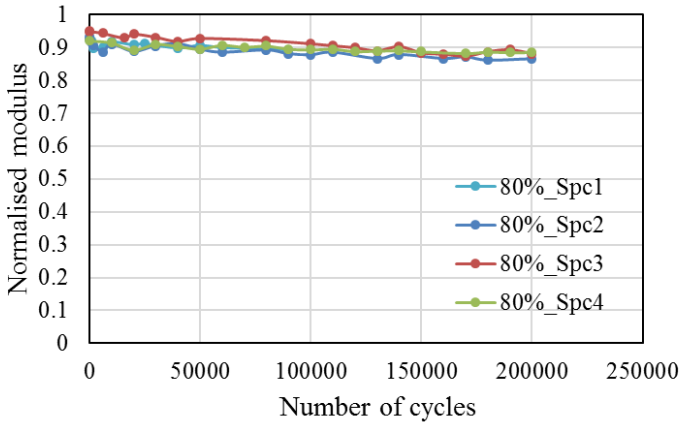

Figure 6.13: The normalised modulus against number of cycles plots for the "pre-fractured" MR60-YSH70 laminate at 80% fatigue severity.

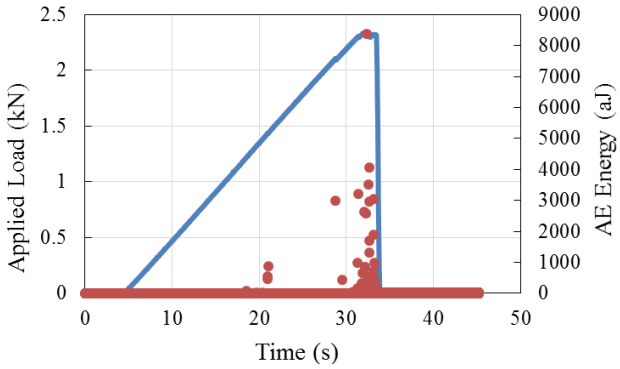

Figure 6.14: Typical acoustic emission energy events plot shows the amounts of fragmentation in the pre-fracture test for the MR60-YSH70 laminate.

To understand the different fatigue behaviour of the "pre-fractured" MR60-YSH70 specimen compared to the TC35-TC35 specimen, the specimens were removed from the testing machine after 200,000 cycles and analysed in the X-ray CT-scan. The X-ray images taken at the mid-plane of three specimens from Spc1 to Spc3 are shown in Figure 6.15 (a) to (c). It is worth noting that the images only present segments with observed damage, and the rest of the undamaged parts are not presented here.

Small amounts of damage – a few inclined thin white lines close to the free edge and small amounts of free edge delamination – can be observed in the X-ray images of all three specimens. As discussed in the context of the static tensile behaviour of the MR60-YSH70 laminate in Section 3.4.2, these thin white lines are the fibre fragmentation in 0° plies with small amounts of localised dispersed delamination around the fragmentation. These areas of delamination did not propagate any further. It would be interesting to assess the energy release rate and compare it to the critical energy release rate for Mode-II delamination G_{IIc}. The energy release rate G_{II} calculation is re-arranged from [11]:

$$G_{II} = \frac{{\sigma_{peak}}^2 E_{11} t_{UD} (t_{AP}+t_{UD})^2}{2E_x^{AP} t_{AP} (E_x^{AP} t_{AP}+E_{11} t_{UD})} \quad (6.2)$$

Where σ_{peak} is the peak stress, E_{11} and E_x^{AP} are the modulus of the central 0° plies and angle plies, t_{UD} and t_{AP} are the thickness of central 0° plies and angle plies respectively. At the peak fatigue stress, the calculated G_{II} is 0.2 N/mm, which is lower than the critical energy release rate G_{IIc} of 0.75 N/mm. Therefore, there is no further delamination propagation during cyclic loading at 80% severity.

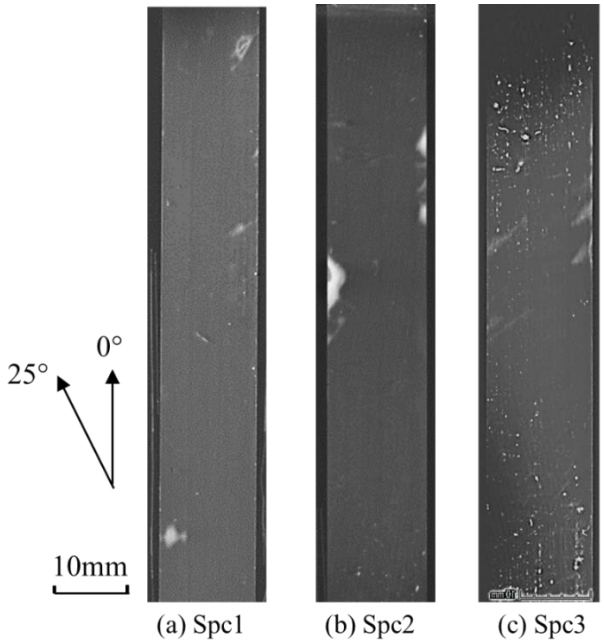

Figure 6.15: X-ray images for the pre-fractured MR60-YSH70 laminates after loading in fatigue to 200,000 cycles.

6.6 Fatigue test results of the MR60-M55 laminates

6.6.1 Fatigue testing of the pristine specimens

The pristine specimens were tested at three different stress severities: 80%, 90% and 95% of the "yield" stress. Figure 6.16 shows the plot of normalised modulus versus number of cycles for all three severities. At 80% severity, the modulus for all four specimens remains unchanged to at least 1 x 10^5 cycles. When the peak stress increases to 90% severity, the modulus for three out of four specimens is unchanged and only one specimen shows a small drop in modulus. Since the MR60-M55 laminate shows good behaviour at 90% severity, two specimens were then tested at a further higher load - 95% of the "yield" stress. The modulus drops very quickly from around 1 x 10^4 cycles, since fracture of the weakest 0° ply occurs and then introduces delamination as the operating stress level is close to the "yield" stress.

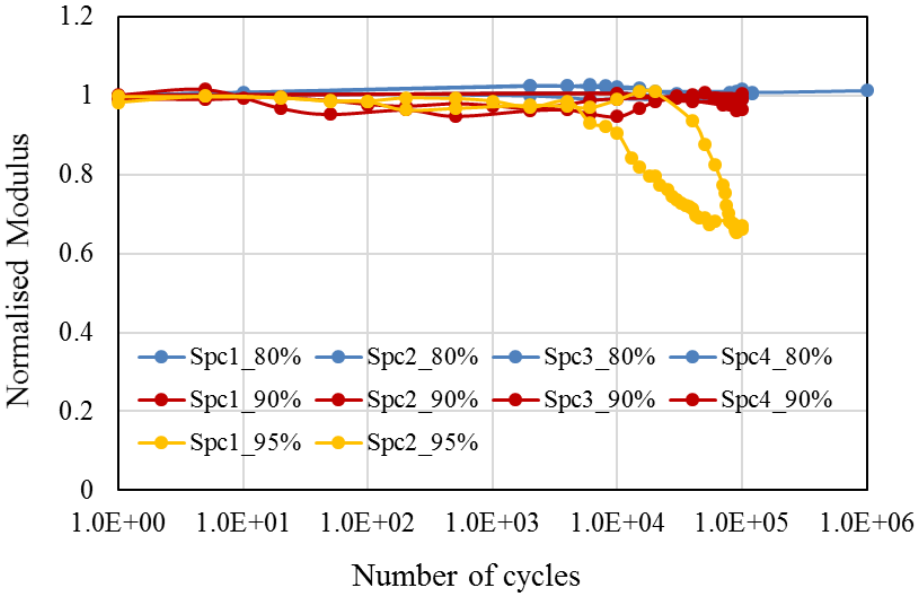

Figure 6.16: The normalised modulus against number of cycles plots for the MR60-M55 laminate in fatigue at 80%, 90% and 95% severities

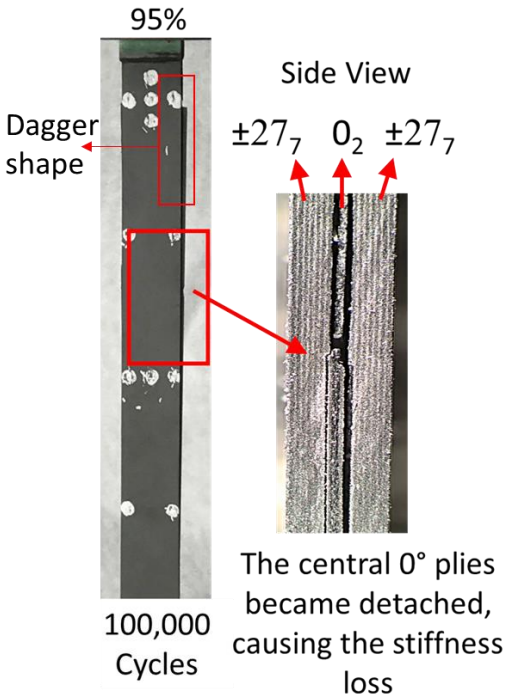

Figure 6.17: Images of the MR60-M55 specimen tested under 95% severity at 1 x 10^5 cycles shows that complete delamination at the 0/-27 interface is the main damage mechanism causing the modulus reduction in the laminate. The term "dagger" refers to the delaminated central 0 ply protruding from the side of the laminate.

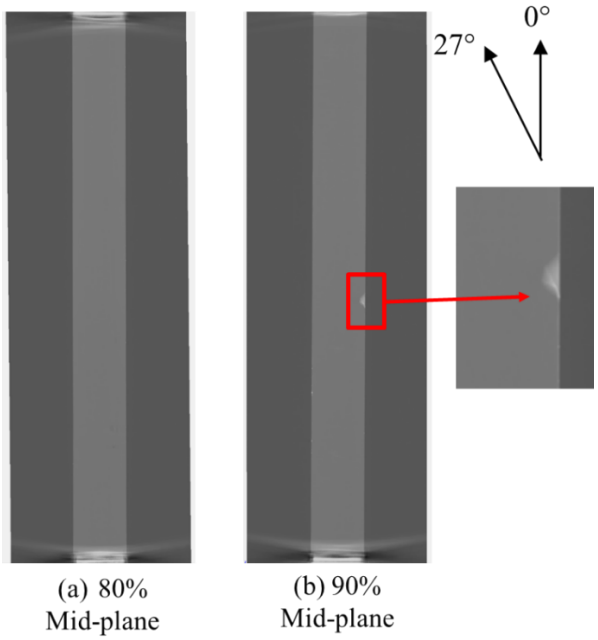

Figure 6.18: X-ray images for the MR60-M55 specimens at 80% and 90% fatigue severities, captured at 1 x 10^5 cycles.

No obvious visual damage was observed in the specimens tested at 80% and 90% severities. However, at the 95% severity, the specimen taken from 1 x 10^5 cycles was found to be saturated with damage. Figure 6.17 shows the visual observation from the front view and microscopic observation viewed from the side. The front view image shows a few "daggers" shapes at the free-edges of the specimen, which are assumed to be the central plies which have become detached from the outer angle plies. A higher magnification image from the side is evidence that this is the case. The delamination was found to be initiated from the 0° ply fracture, and then propagated either at the 0/-27 interfaces or -27/27 interfaces until the gauge length was saturated with complete delamination. The delamination contributed to the modulus reduction observed in the fatigue modulus plots.

From the X-ray images of the specimens loaded at 80% and 90% severities (Figure 6.18 (a) and (b)), no critical damage can be observed. However, a small, white triangular shape can be seen at the free edge of the specimen at 90% severity, attributed to free-edge delamination at the -27/27 interface adjacent to the central 0° plies.

6.6.2 Fatigue test of laminates with pre-fractured 0° plies

Laminates with the same configuration were then tested in fatigue with pre-fractured 0° plies. All the pristine specimens were loaded to a strain of 0.75%, which is 0.07% higher than the average "yield" strain. Figure 6.19 (a), (b) and (c) show two typical plots of acoustic emission energy events observed in the pre-fracture testing. All the tests were terminated at the same pre-fracture strain, but the acoustic emission shows two very different energy event plots: Figure 6.19 (a) and (b) represent moderate amounts of high energy events, with Figure 6.19 (c) showing small amounts of high energy events. The number of high energy events can represent the rough number of fragmentations in the "pre-fracture" testing – about ~6-8 fragments were observed in the specimen with moderate amounts of AE high energy events, and with 2 fragments in the lowest case. In the specimen with 2 fragments, the fragments were not across the entire width. To achieve a more consistent fatigue test performance, only the specimens displaying moderate high energy AE events were selected for further fatigue testing.

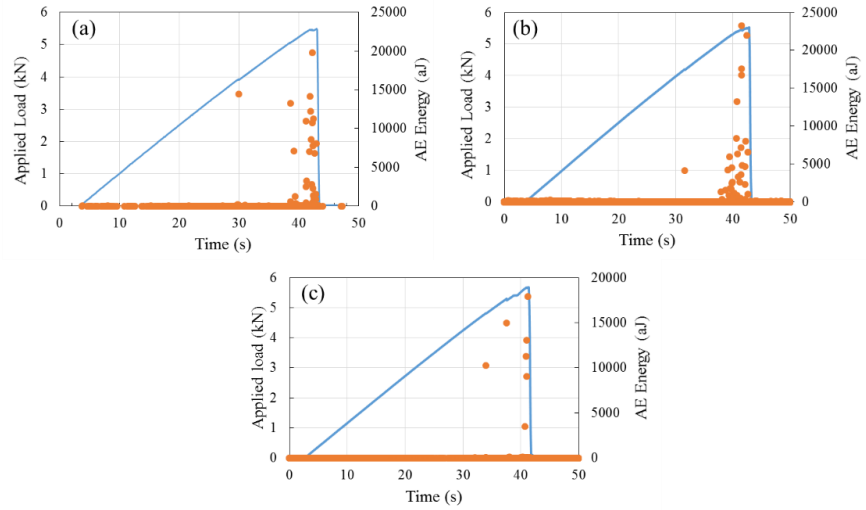

Figure 6.19: Two types of typical plots for acoustic emission energy events for the MR60-M55 specimen in "pre-fracture" test: (a) (b) have shown moderate number of fragmentation and (c) has shown very few fragmentations.

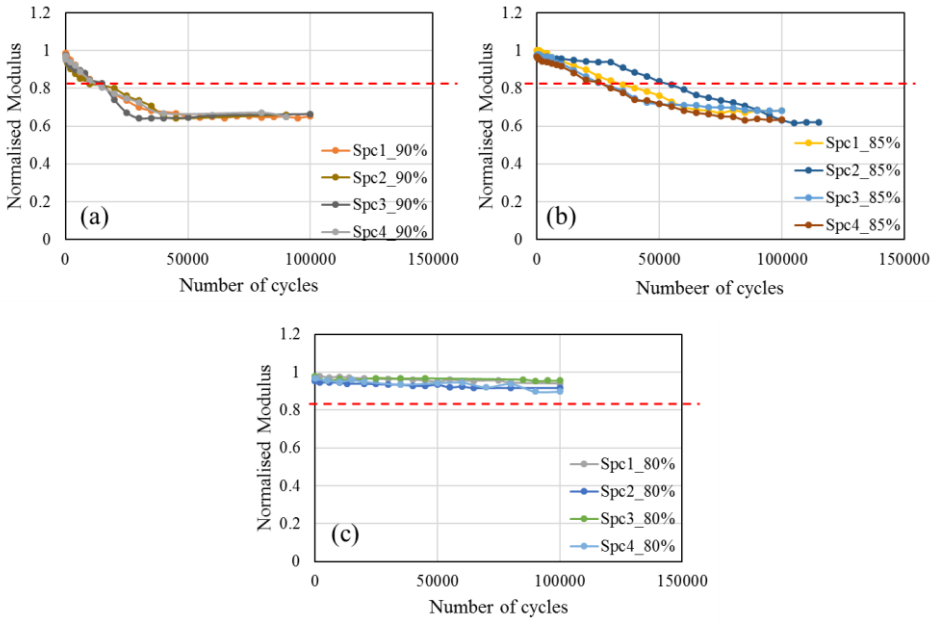

Figure 6.20: Normalised modulus plotted against number of cycles for the MR60-M55 laminate at three different severities: 80%, 85% and 90%. The modulus has been found to reduce gradually with different degradation rates in different severity. The red dashed-lines are plotted in each graph, showing the modulus contribution from the angle plies calculated from (CLA).

The selected specimens were tested under fatigue loading with 80%, 85% and 90% severities. Figure 6.20 shows the plots of normalised modulus versus number of cycles for three different stress severities and the red dashed line indicates the modulus contribution by angle plies calculated from CLA. All specimens in each batch show consistent trends –similar modulus reduction as a function of the number of cycles.

More specifically, the modulus degradation rate of the specimens at 90% severity is the highest and is the lowest at 80% severity among all three loading severities. At 90% severity, the modulus drops dramatically in the first 30,000 cycles and then remains constant at a normalised modulus close to 0.6. At 85% stress severity, it takes almost 80,000 cycles for the modulus to reduce to 0.6, which is more than twice of the number of cycles at 90% severity and the modulus stabilises with further loading. When the load severity decreases to 80%, the modulus degradation reduces significantly – less than 10% modulus reduction was observed after 1 x 10^5 cycles.

6.6.3 Damage analysis of fatigue specimen with pre-fracture

To understand the damage mode of the pre-fractured specimens operated at different fatigue loading severities and the damage mechanisms that contributed to the modulus reduction, the specimens were removed from the testing machine at 100,000 cycles, submerged in zinc iodide dye penetrant and examined in the X-ray CT-scanner. Figure 6.21 presents images captured at the central 0° plies and the edge view of the specimens, with all the damage highlighted in white.

At 80% severity, it is clear to see that the damage is located in the top and bottom of the specimen. Since the damage is localised and has not propagated further, the middle of the gauge length has been shown free of damage. A higher magnification view of the localised damage is shown in Figure 6.22. In these images, the thin white lines are fragmentations of the central 0° plies and the less intense bright regions on both side of these white lines are localised delamination areas at the 0/-27 interface. The distance these delamination areas have propagated to has been found to be similar to the localised delamination length in static tension, therefore the delamination observed at 80% severity probably occurs primarily in the pre-fracture testing. It means that at the current stress severity, the applied stress is lower than the delamination propagation stress of the laminate. The small amount of modulus reduction observed in fatigue loading with 80% severity is possibly attributed to the development of edge delamination and the extension of fragmentation.

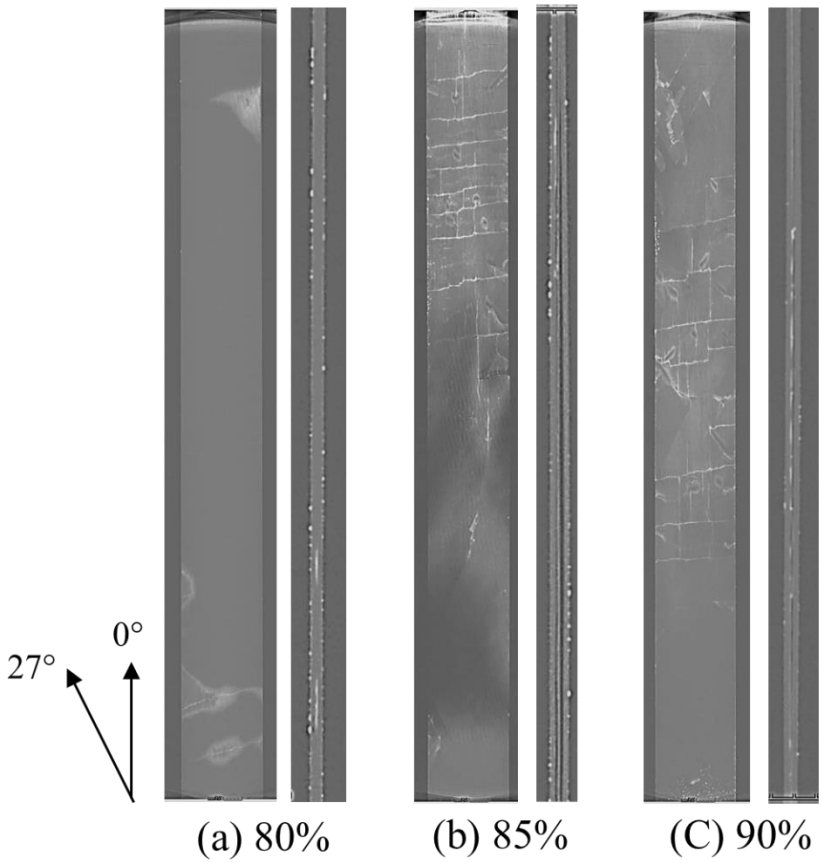

Figure 6.21: X-ray images of the "pre-fractured" MR60-M55 specimens tested at 80%, 85% and 90% severities, after $1x10^5$ cycles.

At 85% loading severity, extensive damage can be seen from either the front view or the edge view of the specimen as shown in Figure 6.23. Nine fragmentations across the entire width and some longitudinal 0° ply splitting seen as white thin lines are observed from the front view. From the edge view, complete delamination can be seen along the entire gauge length. At the top part of the specimen, the delamination is observed as a thin white line on one side of the 0/-27 interface. In the middle of the specimen, the delamination propagated to the 0/-27 interface on both sides of the 0° plies via the splitting in the 0° plies shown in the 2nd image viewed as a cross-section. At the bottom of the specimen, the delamination was even more severe, resulting in the 0° plies becoming completely detached from the angle plies on both sides. Small amounts of edge delamination at the -27/27 interface

adjacent to the central 0° plies can also be observed at the free edge and finally coalesces with the delamination at the 0/-27 interface.

The damage morphology of the specimen at 90% severity is very similar to what was observed for 85% severity – a similar number of fragmentations were observed in the laminate and delamination dominated failure modes were observed. From the damage mechanism observed at 85% and 90% severity, the significant modulus degradation at a constant rate observed in the fatigue modulus plot is mainly attributed to delamination. In theory, when the central 0° plies become separated from the surrounding angle plies as a consequence of the delamination at the 0/-27 interfaces, the normalised modulus of the remaining angle plies - ignoring completely the effect of the 0° plies - can be estimated from CLA shown in the red-dashed lines in Figure 6.20. The normalised modulus of 0.6 measured experimentally was found to be lower than the value of 0.8 calculated from CLA. In addition to the delamination at the 0/-27 interface, the damage in angle plies such as edge delamination at -27/27 interface and matrix cracking in angle plies shown in Figure 6.23 resulted in further modulus reduction.

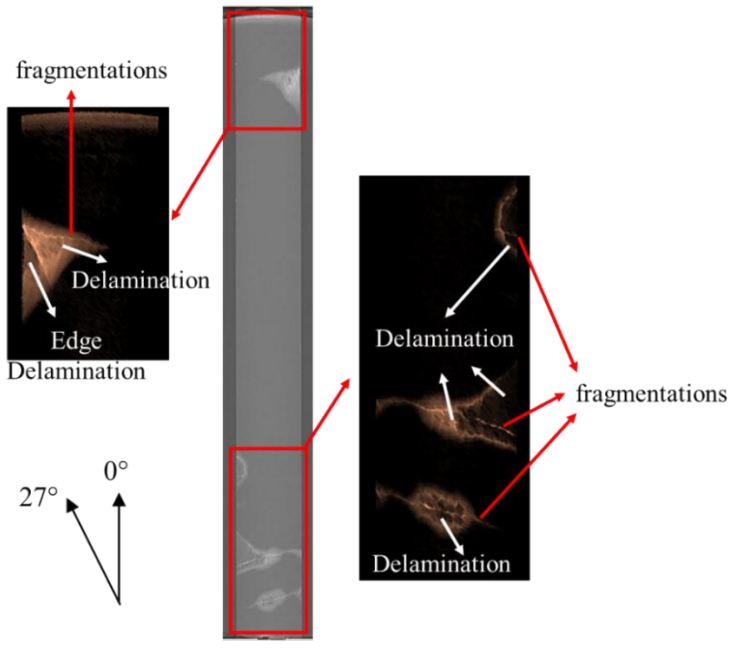

Figure 6.22: X-ray images detail the extent of the fragmentation and delamination for the MR60-M55 specimen at 80% load severity. The image was taken at the middle of the specimen.

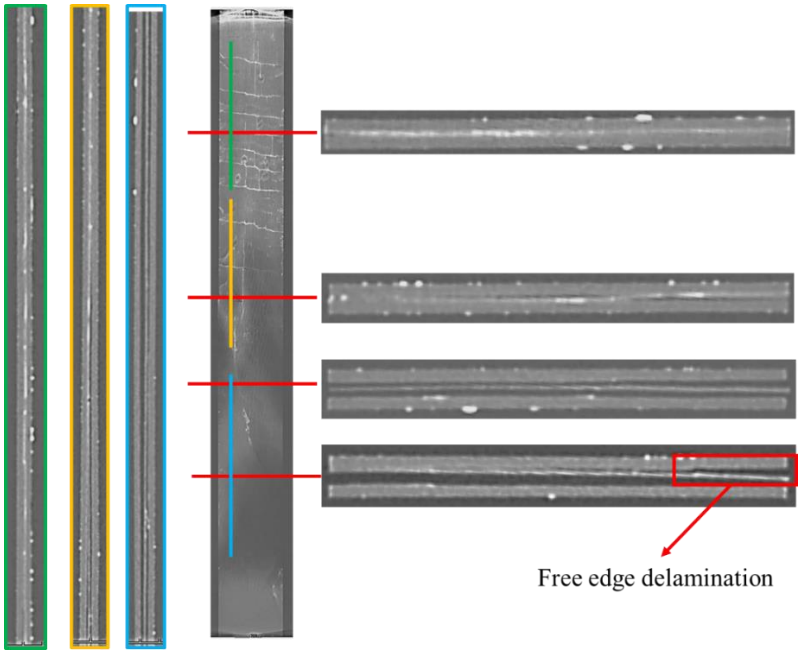

Figure 6.23: X-ray images captured at different planes of the specimen detail the extent of the fragmentation and delamination for the MR60-M55 specimen at 85% load severity, captured at 1 x 10^5 cycles.

6.6.4 Delamination analysis of the MR60-M55 specimen in fatigue loading

From the damage analysis presented in section 6.6.3, the major damage mode of the pre-fractured MR60-M55 laminate in fatigue loading is delamination. The growth of delamination area in fatigue loading is critical to the design of laminates, since a thorough understanding of the delamination growth rate could help to predict the laminate behaviour in fatigue loading. However, the delamination is primarily along the interface between the central 0° plies and angle plies, which is invisible in the carbon fibre laminate. In the present study, the area of delamination was estimated from a method from Wisnom et al. which is based on the measured modulus and the delamination is assumed to propagate along the 0/-θ interfaces [148]. The delamination length "a" can be therefore estimated as:

$$a = \frac{\left(1 - \frac{d_0}{d}\right) l_g E_0}{E_0 - E} \tag{6.3}$$

where d_0 and d are the cyclic displacement over the gauge length (l_g) before and after delamination initiation. E_0 is the original modulus of the laminate before the delamination and E is the modulus of the laminate once fully delaminated - ignoring the modulus contribution from the 0° plies. All these properties were measured or determined experimentally.

Figure 6.24 presents an example of estimated delamination length as a function of number of cycles. A reasonably linear change in delamination length with number of cycles can be found in the middle of the plot and the delamination growth tends to be slower and more stable after this region, therefore this region was used for establishing the delamination growth rate by using least squares fitting of the data.

Moreover, as another major parameter for delamination characterisation, a constant value of strain energy release rate can be estimated via:

$$G_{\max} = \frac{P^2 (k_0 - k)}{4 k_0 k} \tag{6.4}$$

Where P is the maximum cyclic load per unit width, "k_0" is the original normalised stiffness of the laminate (load per unit width per unit strain) before cyclic loading and "k" is the stiffness (load per unit width per unit strain) of the laminate without considering the central 0° plies contribution. Again, all these properties were determined experimentally.

It has only shown a small 4% modulus drop and that the delamination has not propagated when the specimens are loaded at 80% severity, only the delamination growth rate and strain energy release rate for 85% and 90% severities were calculated and summarised in Table 6.5. The delamination growth rate at 90% severity is 0.0031 (24%) mm/cycle, which is 50% higher than the value at 85%

severity. The strain energy release rate G_{max} of 0.271 N/mm was calculated for the specimen at 90% severity, which is approximately 10% higher than at 85% severity.

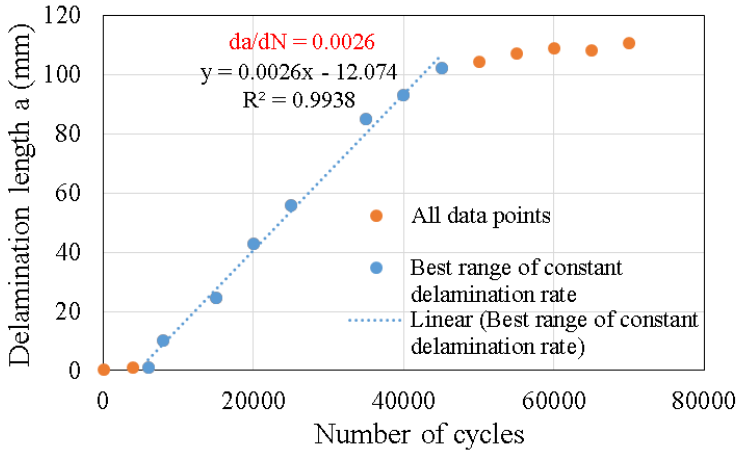

Figure 6.24: Typical plot of stiffness loss due to delamination for an overloaded MR60-M55 specimen at 85% severity. The delamination growth rate can be derived from the linear range of the curve.

Table 6.5: Results of calculated delamination growth rate and maximum strain energy release rate for MR60-M55 specimens at 85% and 90% severities

	85%		90%	
	da/dN [mm/cycle]	G_{max} [N/mm]	da/dN [mm/cycle]	G_{max} [N/mm]
Spc1	0.0019	0.232	0.0027	0.269
Spc2	0.0017	0.241	0.0026	0.276
Spc3	0.0026	0.267	0.0042	0.258
Spc4	0.0016	0.240	0.0030	0.279
Average	0.0020 (23%)	0.245 (6.2%)	0.0031(24%)	0.271 (3.5%)

6.7 Conclusions

Pseudo-ductile thin ply angle-ply laminates with central 0° plies were tested in tension-tension fatigue loading in order to determine their operation ranges and to understand the damage progression. Laminates with three different configurations

that have shown pseudo-ductility in static tension, were loaded in fatigue at several different severities from 80% to 95% of their "yield" stress respectively.

In the fatigue tests on pristine specimens, 80% severity was found to be the maximum stress for all three specimens where they can safely operate without obvious modulus reduction and damage observation. When the maximum fatigue stress increased to 90%, the TC35-TC35 specimen failed dramatically after less than only 1000 cycles. Premature fracture of the 0° plies and delamination at the 26/-26 interface dominated the dramatic failure. By contrast, the MR60-YSH70 and MR60-M55 laminates displayed no stiffness loss to at least 1 x 10^5 cycles and only a small amount of less critical damage was observed in the specimen at 90% severity. When the specimens were loaded in 95% severity, both of these two laminates showed a gradual modulus reduction as the number of cycles increased. The central 0° plies of the MR60-YSH70 specimen have been found to be significantly fragmented in the initial cycles and localised delamination at the 0/-25 interface leads to gradual modulus reduction. However, in the MR60-M55 specimen, the modulus reduction was as a result of delamination which was initiated from the tip of a single fragmentation and propagated along the entire gauge length.

In the pre-fractured fatigue test, all three types of specimens were loaded in static tension to a strain slightly higher than their "yield" strain and then were tested in fatigue. In the TC35-TC35 specimen, the laminate failed within 2000 cycles as a result of delamination at the -26/26 interface next to the central 0° plies. The "pre-fractured" MR60-YSH70 laminate displayed only a 5% modulus reduction over 200,000 cycles at 80% severity, which means it retained good structural integrity and mechanical properties in fatigue loading even after sustaining fragmentation in the laminate. In the MR60-M55 laminate, similar delamination dominated failure modes were observed at 85% and 90% severities. The delamination propagation stress was reached under these fatigue load and the delamination extensively extended at the 0/-27 interface. An estimated delamination growth rate based on the measured modulus shows that the delamination propagated 1.5 times faster in 90% severity than 85%.

7 Bearing failure of bolted pseudo-ductile thin ply angle-ply laminates

Pseudo-ductile $[\pm\theta_m/0_n]_s$ laminates have been previously tested in several different load-cases, such as open-hole tension and compression. These laminates have been found to exhibit different behaviour compared to laminates made from standard thickness plies or commonly used layups. As one of the major methods for joining carbon fibre composite components, mechanically fastened joints have been used and studied extensively. When mechanically fastened joints are loaded in tension, complicated damage modes are observed, including compressive and shear dominated bearing failure, shear-out failure and tensile failure. Therefore, it is necessary to understand the behaviour of these pseudo-ductile laminates containing bolted joints. As an initial investigation, two types of pseudo-ductile laminates were selected and specimens with single- or double-bolted joints were tested in double shear tensile loading. Gradual failure has been observed in all specimens with single- and double-bolts jointed laminates, but a higher bearing strength has been observed in the laminate containing standard modulus 0° plies. The failure modes have been found to be similar between the two layups, including bearing type of damage, followed by tear-out type of damage including splitting in angle plies and fibre microbuckling through the entire thickness.

7.1 Introduction

Up to now, CFRP composites have been introduced into a wide range of applications such as aerospace, automotive and sports. In all these applications, mechanical fastening is a common method to join the composite structures together. In the presence of holes and fasteners, the load carrying ability of the carbon fibre laminates is reduced significantly, due to the damage initiation in the early stage of loading and accumulation inside the laminates. The damage modes of jointed composites are significantly influenced by the laminate configuration and joint design, therefore the bearing performance, particularly for these pseudo-ductile laminates, needs to be understood.

In the previous chapters, these pseudo-ductile laminates have been tested under several different load cases, including open-hole tension and unnotched compression. The behaviour and damage mechanism observed in these laminates are very different from those laminates made from standard thickness plies or conventional layups, and are significantly influenced by the carbon fibre grades, the angles in angle plies and the ratio between 0° and angle plies. Therefore, the behaviour of these laminates with bolted joints is particularly crucial to be understood. The present work is primarily focused on experimentally characterising the bearing strength, bearing/bypass interaction and damage evolution within pseudo-ductile thin ply angle-ply laminates with single and double-bolted joints subjected to double lap shear loading and to compare the performance between the two different pseudo-ductile laminates.

7.2 Experimental procedures for bearing testing

7.2.1 Specimen design and test setup

Bearing tests were carried out in accordance to procedure “A” of the ASTM D5961 standard. A double shear-lap bolted joint test fixture with a single hole is recommended to be used in this test. A hole diameter of 3.175mm was used, to make it consistent with the open-hole tensile testing presented in chapter 3. The bearing force was applied by loading the fixture along with the test samples in tension in a

standard testing machine. Figure 7.1(a) shows a schematic of the double shear-lap bolted joint test fixture stated in ASTM D5961 and Figure 7.1(b) shows the fixture that was used in the current bearing testing. The specimen is mounted in the fixture and is sandwiched between two halves of a steel cylindrical block. The cylindrical block is designed to provide lateral support during loading. The amount of lateral support, or in other words clamping pressure, was applied by adjusting the tightness of the nuts on both sides of the cylinder quantitatively using a torque wrench.

Subject to the prepreg availability as mentioned in the previous chapters, in bearing testing, the TC35-TC35 $[\pm 26_6/0]_s$ and MR60-YSH70(Granoc) $[\pm 25_2/\underline{0}]_s$ laminates were used to replace the T300-T300 $[\pm 26_5/0]_s$ and MR60-YSH70(North) $[\pm 25_2/0]_s$ layups in open-hole testing, which give laminate thicknesses of 1.35 mm and 1.08 mm respectively. The underline indicates a single layer of 0 ply being used in the laminate. Other specimen geometric parameters, such as width-to-diameter ratio (w/d) and edge distance-to-diameter ratio (e/d) need to be well considered in the design of bearing specimens, since they have been found to influence the bolted bearing strength and failure modes significantly.

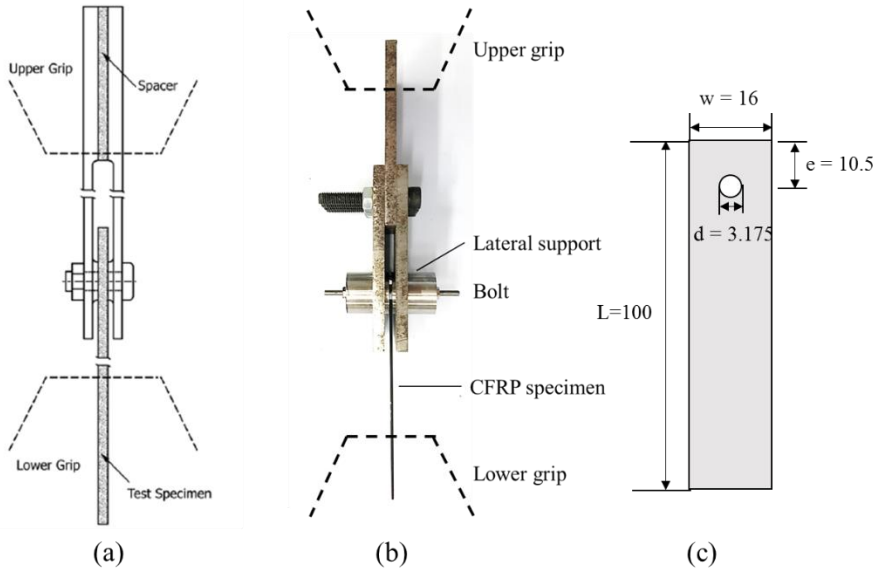

Figure 7.1: (a) Fixture assembly for a bearing test viewed from the side, (b) fixture assembly viewed from front side and (c) bearing test specimen drawing.

Different failure modes, such as cleavage, net-tension, shear-out, bearing and tear-out, are all commonly seen in bolted joint composite tests. An illustration of these damage modes is presented in Figure 2.12. As the aim of this investigation is to determine bearing dominated behaviour, the failure modes of net-tension and cleavage need to be avoided. The geometric dimensions of the specimens play an important role in controlling the failure modes in bolted joint composite tests. When a low width-to-diameter ratio w/d is used, the laminate tends to fail in a net-tension type of failure. To avoid it, a w/d ratio of 5 was used. The rest of the failure modes are primarily dependent on the edge distance-to-diameter ratio e/d. Previous studies on bolted composites suggest that the transition region of edge distance-to-diameter ratio from brittle failure modes to bearing falls within the region of 1 to 3 for the majority of reported laminates [149]. In theory, a very large e/d ratio could be used to ensure the specimen fails in bearing rather than shear-out. However, a redundant edge distance length could make the design less efficient. In the present chapter, as an initial investigation, an e/d ratio of 3.5 was selected, which is a common ratio used in bearing test of conventional laminates and would be expected to show bearing failure whilst not being over designed. The geometry of bearing specimen is illustrated in Figure 7.1 and all the key geometric parameters are summarised in Table 7.1.

Table 7.1: Key geometrical parameters for the TC35-TC35 and MR60-YSH70 specimens tested in single bolted joint bearing.

		MR60-YSH70 $[\pm 25_2/\underline{0}]_s$	TC35-TC35 $[\pm 26_6/0]_s$
Fastener diameter, D	[mm]	3.00	3.00
Hole diameter, d	[mm]	3.175	3.175
Thickness, t	[mm]	1.35	1.08
Length, L	[mm]	100	100
Width, w	[mm]	16.0	16.0
Edge distance, e	[mm]	10.5	10.5

7.2.2 Specimen preparation and testing procedures

Laminates with both configurations were manufactured from prepregs and the details of the manufacturing procedures are the same as for the laminates used in chapter 4 and chapter 5. The laminate panels were then machined into the required size as mentioned in Figure 7.1 and Table 7.1. The fastener hole of diameter 3.175 mm was drilled using a carbide drill.

The bearing tests were performed using an Instron hydraulically-actuated system with a 25 kN load cell, at loading rates of 0.5 mm/min. The lower edge of the specimen was clamped into the lower grip and the upper specimen was mounted in the fixture, and then the entire structure was fixed into the testing machine. Previous studies on the effect of clamping pressure on bearing behaviour show that bearing strength is found to be a function of clamping pressure [151,156,191–193]. To minimise the influences of clamping pressure on the bearing strength measurement and provide consistency across all specimens, a relatively low level of torque of 0.5 N.m (finger-tight condition) was applied to the fastener using a torque wrench. The displacement was recorded using a video extensometer, by tracking the movement of the bolt. According to the standard ASTM D5961, the bearing stress can be expressed as:

$$\sigma_{bearing} = \frac{k \times P}{d \times t} \tag{7.1}$$

Where k is the load per hole factor: 1.0 for single bolt joint.

7.3 Results and discussion of bearing testing

7.3.1 Overall bearing behaviour

Figure 7.2 shows the bearing stress-displacement curve for all the TC35-TC35 specimens and consistent behaviour among all specimens can be seen in these curves. The curves are predominantly linear up to the first load drop, followed by a less stiff but more gradual increase up to the ultimate stress, although multiple small load drops can be seen within this region. This means that the laminate is still carrying sufficient load although damage has initiated. In the present study, two stresses are

used to characterise the bearing behaviour: the stress at the first peak and the ultimate stress as illustrated in Figure 7.3. The first peak stresses and ultimate stresses for all four specimens are summarised in Table 7.2. The failure of the laminate is defined as when the load drop is more than 30% and based on that, the overall displacement, which is primarily contributed by the hole edge deformation, is found to be around 1.35 mm over the bearing load.

The bearing stress for the MR60-YSH70 laminate is plotted against displacement in Figure 7.4. All four specimens also show good consistency in the curves before the ultimate point, but quite large differences can be observed after this point. Unlike the TC35-TC35 specimen, the load increases up to the maximum load, and then drops gradually, including a large load drop (more than 30%). The MR60-YSH70 laminate shows an elastic deformation in the initial stage and then the curve tends to be more gradual up to the maximum stress. It also can be seen in this laminate that the hole deformation is only about one third of the TC35-TC35 laminate, which is due to the higher stiffness of the MR60-YSH70 laminate. Again, the stresses at the first peak and ultimate point are summarised in the Table 7.3. It shows that both stresses are lower than for the TC35-TC35 laminate.

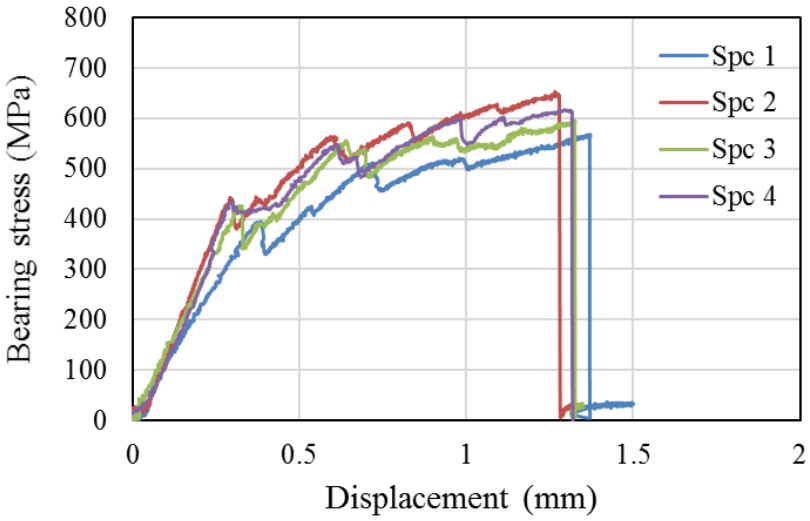

Figure 7.2: Bearing stress - displacement curves for the TC35-TC35 laminates.

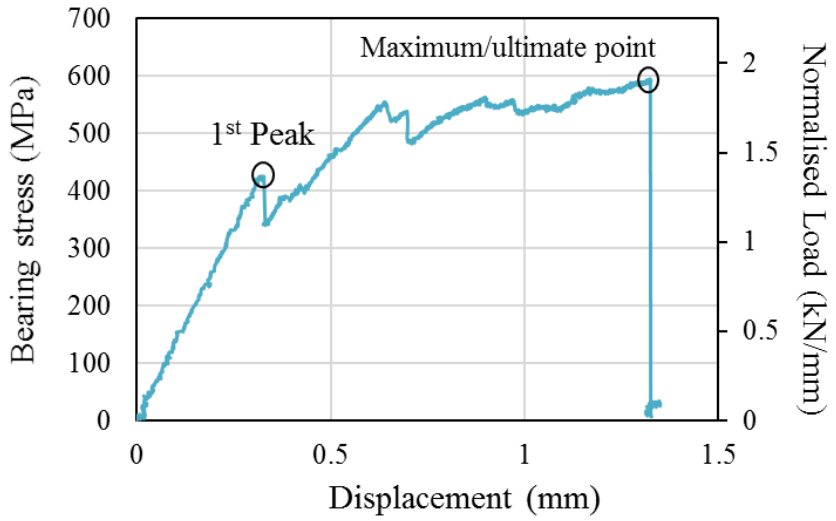

Figure 7.3: A typical bearing stress-displacement curve for the TC35-TC35. The definition of the first peak and ultimate stress are presented in the curve. The secondary axis shows the applied load normalised with the thickness for the same specimen, will be used in the comparison and analysis with double-bolted joint specimens in the Section 7.5.

Table 7.2: Summary of the bearing strength and the failure modes for the individual TC35-TC35 specimens

	1st peak bearing stress [MPa]	Ultimate bearing stress [MPa]	Failure mode
Spc1	425	567	bearing, tearout
Spc2	442	653	bearing, tearout
Spc3	436	596	bearing, tearout
Spc4	434	618	bearing, tearout
Average	432	609	
CoV	2.0%	5.9%	

From the stress-displacement curves, gradual failure is achieved for both laminates and the curves are primarily in two stages. In the initial stage, the displacement increases almost linearly with the applied load. The bolt starts to contact with the laminate at the hole edge, resulting in the compressive deformation at the hole edge of the laminate in this region. Instead of a smooth load-displacement

curve, small load drops can be seen in these curves. These multiple load drops would be related to the damage initiation and accumulation. The appearance of damage brings down the overall stiffness. It can also be seen that the total displacement of the bolted laminates loaded to the first load drop for the TC35-TC35 laminate is 3 times higher than the MR60-YSH70 laminate, since YSH70 fibres fracture at a compressive strain of 0.12% [175] much lower than the TC35 fibres as well as due to the higher stiffness of the MR60-YSH70 laminate.

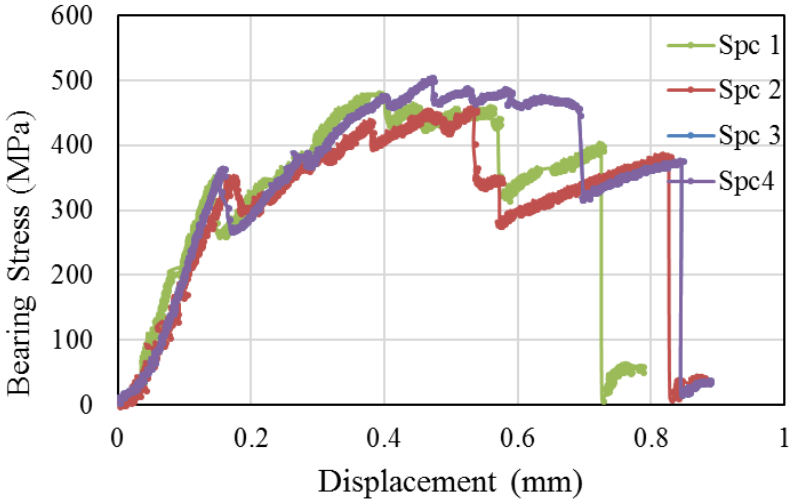

Figure 7.4: Bearing stress - displacement curves for the MR60-YSH70 laminates.

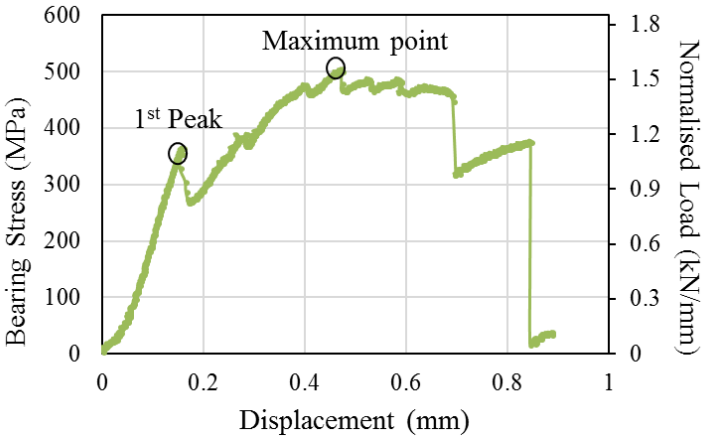

Figure 7.5: A typical bearing stress-displacement curve for the MR60-YSH70 laminates. The definition of first peak and ultimate strength have been drawn in the curve. The secondary axis shows the applied load normalised with the thickness for the same specimen, will be used in the comparison and analysis with double-bolted joint specimens in the Section 7.5.

Table 7.3: Summary of the bearing strength and the failure modes for the individual MR60-YSH70 specimens

	1st peak bearing stress [MPa]	Ultimate bearing stress [MPa]	Failure mode
Spc1	371	485	bearing, tearout
Spc2	351	460	bearing, tearout
Spc3	363	482	bearing, tearout
Spc4	388	507	bearing, tearout
Average	368	484	
CoV	4.2%	4.0%	

7.3.2 Visual observation of damage

The damage modes of these tested specimens were visually observed to help validate the bearing test. Visual observation shows that similar failure modes can be observed in all specimens for both laminate configurations and are summarised in Table 7.2 and Table 7.3. Since the damage modes for all the specimens are the same, only two specimens for each configuration are presented in Figure 7.6. From the surface inspection of the two failed specimens as presented in Figure 7.6 (a) and (b), the failure modes of bearing (can be seen as crushing at the hole edge), along with secondary tear-out failure mode including in-plane micro-buckling in the -θ° plies and splitting in the fibre direction of θ° plies are observed. The latter failure mode occurred as a result of bearing failure. Red and yellow circles were added to each image to identify the deformation of the hole and show that the hole deformed more in the TC35-TC35 laminate than the MR60-YSH70 laminate. Small amounts of fractured fibres and wrinkles have been found in the small region near the contact hole edge, indicating the damage in this region is bearing failure.

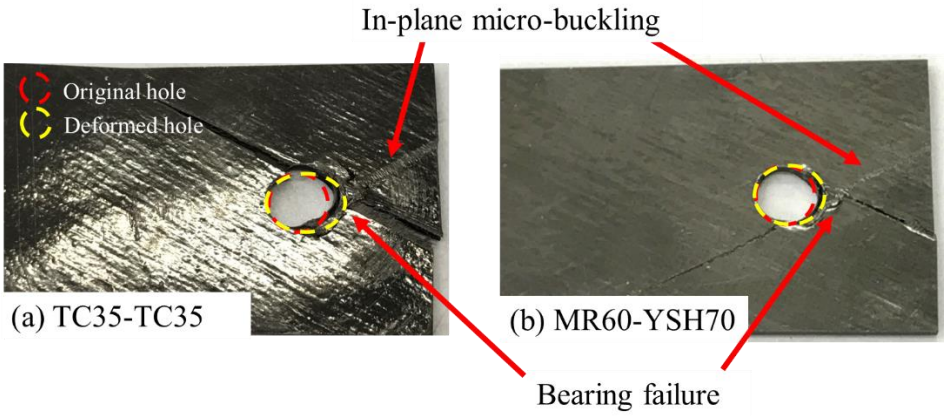

Figure 7.6: Photographs on the surface of the damaged (a) the TC35-TC35 and (b) the MR60-YSH70 specimens.

7.3.3 Damage analysis via X-ray analysis and microscopy

In both layups, multiple characteristic load drops have been seen in the stress-displacement curves. To get a better understanding of what these load drops were associated with, a few of specimens were loaded to two different load levels, both averaged of all four specimens from the previous tests, submerged in dye penetrate solution and then scanned in the Nikon XTN320 X-ray CT inspection machine. More specifically, specimens were loaded to the first load drops and the maximum loads respectively.

Figure 7.7 shows X-ray images for the TC35-TC35 specimens taken at the first peak load. All the images were captured at three different planes to provide a complete observation. In these images, several thin white curves are found to be at the bolt-laminate contact edge, which is the same morphology as a typical bearing damage mode. Inspecting the damage in the bearing plane of the laminate (mid-side view), the damage is found to be close to the hole edge. Out-of-plane fractures, as one of the typical bearing failure modes, are shown in the angled white line through the thickness. From the image of the cross-section at the bolt-laminate edge, two white lines are observed in the 0° plies at two different locations. When the specimen is loaded to the ultimate load, the damage in the bearing plane is found to be more severe as shown in Figure 7.8. Due to the higher stress level, the total number of

angled fractures increases and most of these fractures propagated outward from the 0° plies to the outer surface. The bearing damage is extended from the hole edge to a wider range as seen in the image viewed from the mid-side.

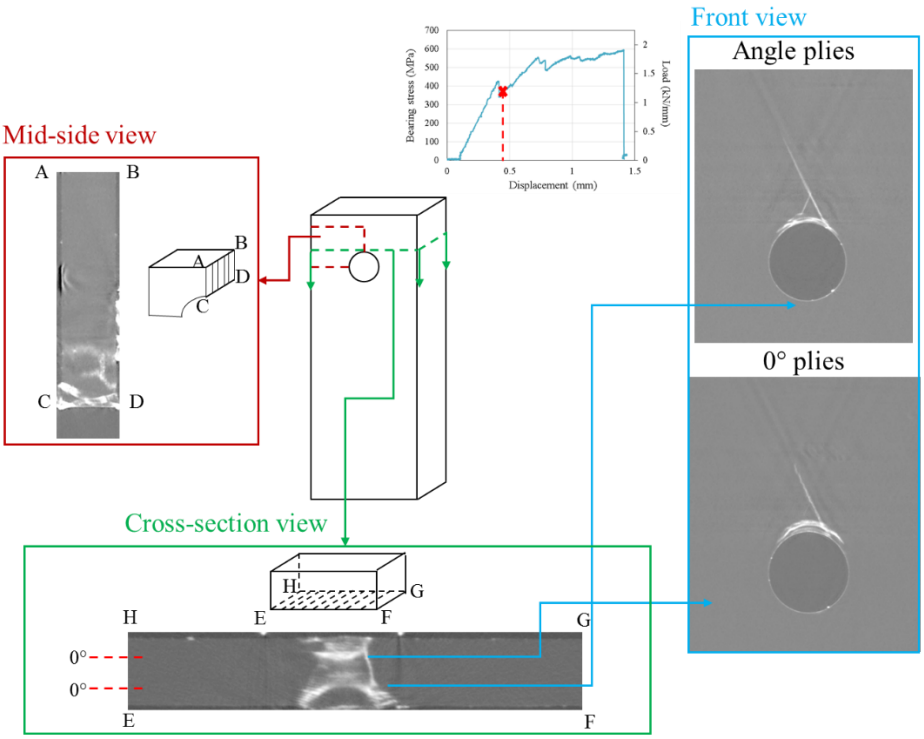

Figure 7.7: X-ray images showing the damage in the TC35-TC35 specimen at the first peak load drop. The images have been taken from three different planes. To improve the visualisation, the thickness (edge AB and CD) of the schematic diagram has been exaggerated.

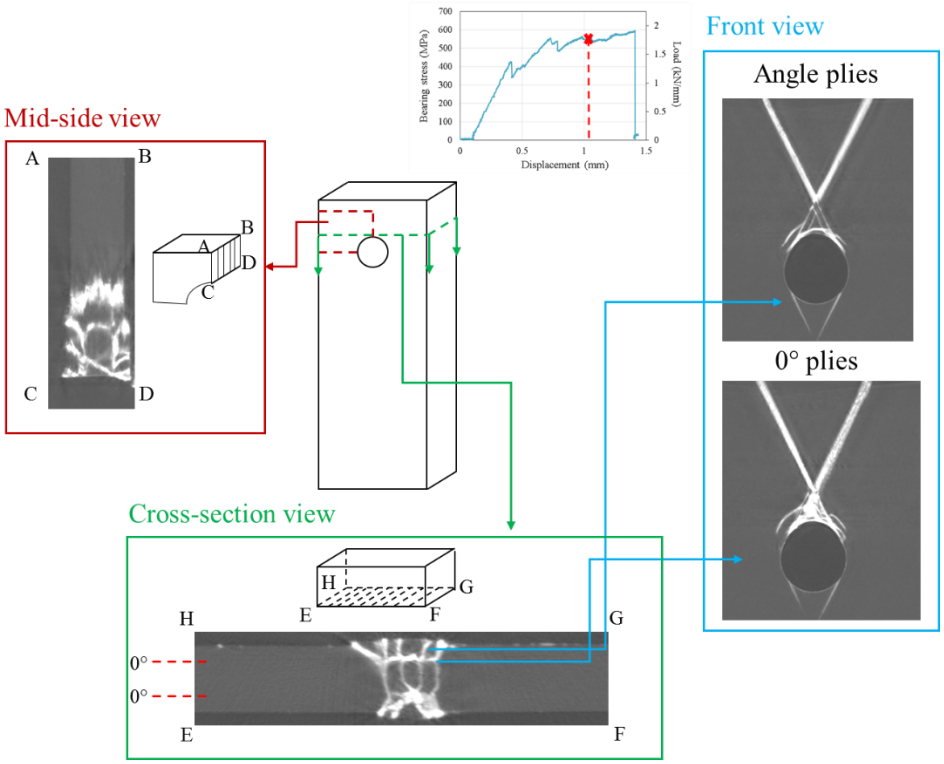

Figure 7.8: X-ray images showing the damage in the TC35-TC35 specimen at the ultimate load. The images have been taken from three different planes. To improve the visualisation, the thickness (edge AB and CD) of the schematic diagram has been exaggerated.

The details of the bearing damage in the TC35-TC35 specimen were studied via microscopy. The microscopic images were taken near the centre of the bearing plane of a specimen that was loaded to the maximum stress and are presented in Figure 7.9. In the microscopic image taken at the entire bearing plane "ABCD", the damage primarily can be seen from two locations: one is bearing damage at the bolt-laminate edge and another one is away from the hole edge. The latter one corresponds to the bold white strip that was observed in the mid-side view of the X-ray image, which involves splitting in the θ° plies, fibre fracture in the 0° plies and in-plane fibre kinking in the -θ° plies. In the images taken at the hole edge at a high magnification, no obvious delamination can be observed in the fractured 0° plies and surrounding angle plies. This allows the compressive fracture of the 0° plies (kink band) to gradually expand in the in-plane direction as well as these kink bands gradually propagated to the adjacent angle plies in the out-of-plane direction.

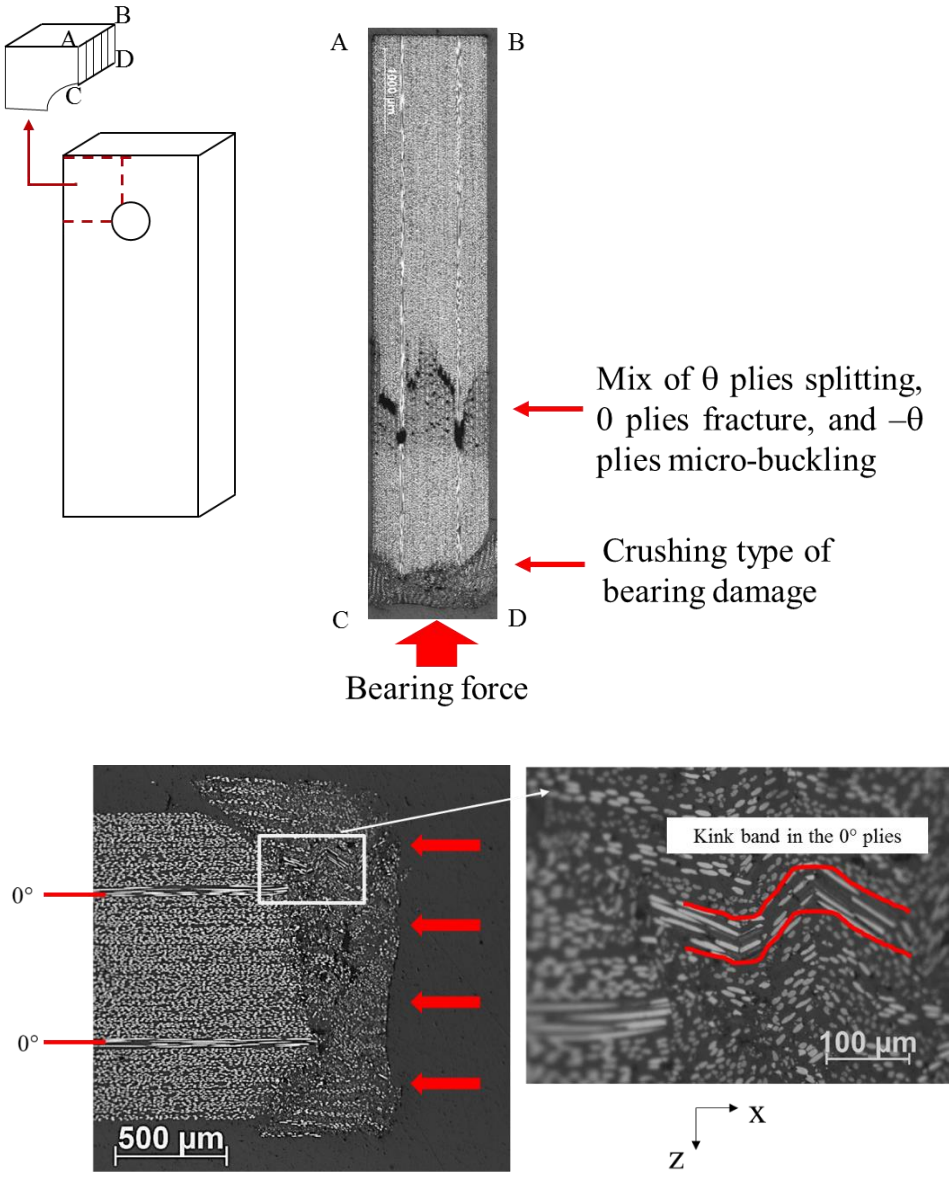

Figure 7.9. Microscopic images of the TC35-TC35 specimen, viewed from the middle slides of bearing plane. The lower two images present the view of bolt-laminate contact region at large magnifications. To improve the visualisation, the thickness (edge AB and CD) of the schematic diagram has been exaggerated.

X-ray images of the MR60-YSH70 specimens interrupted at the first load drop are presented in Figure 7.10. At the first peak load drop, the damage is mainly observed in the 0° plies at different locations through the thickness from the cross-

section view. In addition, the front view image taken at these 0° plies shows the region with an intensive and a less intensive white colour. Due to the compressive force applied by the bolt to the hole edge, the laminate at the hole edge was expected to be compressively deformed and the 0° fibres were expected to be fractured in compression once the fibre compressive strain has been reached. It has been previously reported in chapter 4 that under compressive deformation, high modulus fibres in the 0° plies were progressively fragmented into small segments and localised delamination was initiated at the crack tip due to the sliding between two adjacent fragmented fibres. Therefore, the region with intensive white colour observed in the 0° plies is the compressive fragmentation of the central high modulus YSH70 fibres and the region with a less intensive white colour would be localised delamination at the 0/-25 interface.

When the load increases to the ultimate load, extensive angled fractures can also be observed in this layup shown as the angled white lines in Figure 7.11. To understand the damage at the bearing plane in detail, the middle of the bearing plane of the MR60-YSH70 specimen at maximum load was examined via microscopy and is presented in Figure 7.12. The laminate at the hole edge deformed extensively in the out-of-plane direction. The image at the higher magnification clearly presents that different damage modes accumulated in the laminate, including compressive fragmentation in the 0° plies, out-of-plane kink-band in the 0° plies and in the angle plies, and micro-cracks. Out-of-plane kink-bands can be clearly seen that initiated from the hole edge and grew inward. The extensive out-of-plane damage propagating inward indicates that the lateral constraints (clamping pressure) provided is insufficient to prevent inward out-of-plane damage growth. No blocks of delamination can be seen in the damaged area due to the crack suppression ability of the thin ply prepreg and the damaged material can continue to carry the additional load to achieve a gradual bearing failure.

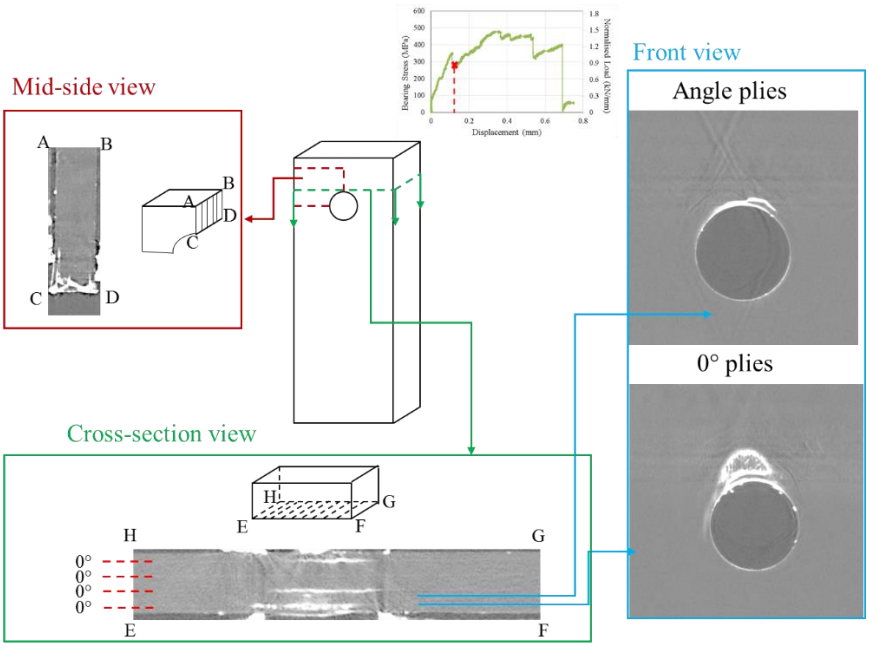

Figure 7.10: X-ray images showing the damage in the MR60-YSH70 specimen at the first peak drop load. The images have been taken from three different planes. To improve the visualisation, the thickness (edge AB and CD) of the schematic diagram has been exaggerated.

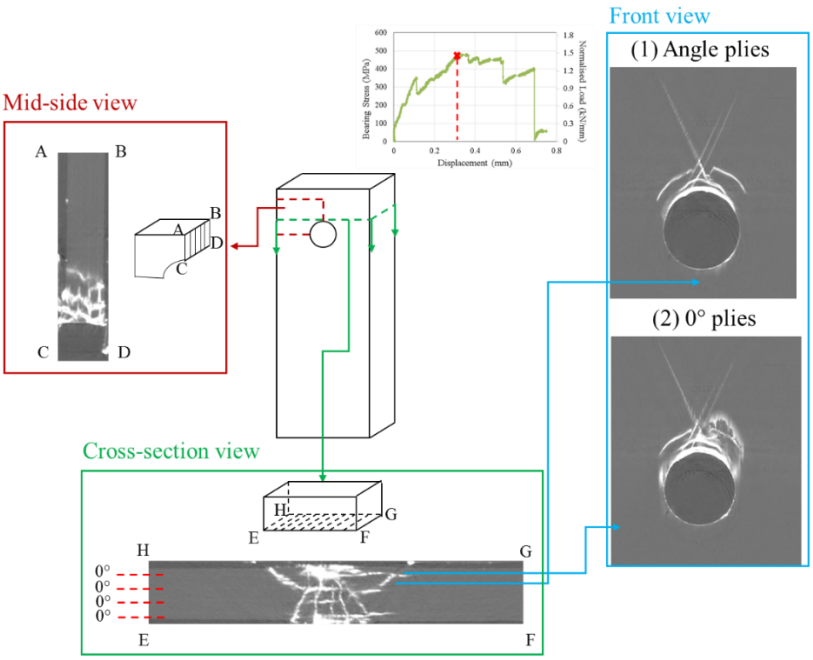

Figure 7.11: X-ray images of showing the damage in the MR60-YSH70 specimen at the ultimate load. The images have been taken from three different planes. To improve the visualisation, the thickness (edge AB and CD) of the schematic diagram has been exaggerated.

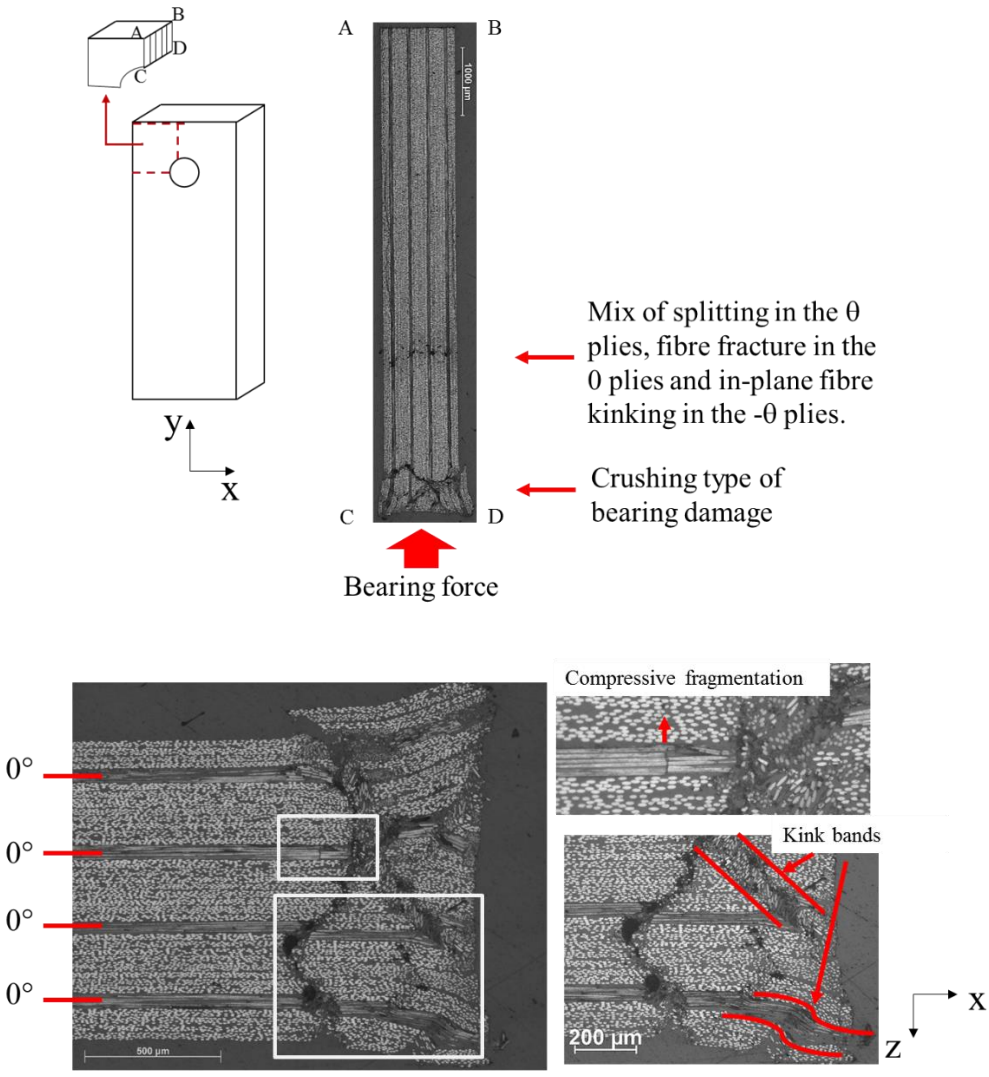

Figure 7.12. Microscopic images of the MR60-YSH70 specimen, viewed in the middle slide of bearing plane. The lower two images present the view of bolt-laminate contact region at large magnifications. To improve the visualisation, the thickness (edge AB and CD) of the schematic diagram has been exaggerated.

Both the TC35-TC35 and MR60-YSH70 laminates were shown to have similar gradual bearing failures with complex damage sequences: elastic compressive deformation at the hole edge, fracture of the 0° ply fibres – either kink-band or compressive fragmentation, out-of-plane kink-band propagation followed by splitting and in-plane kink band formation in the angle plies. Common failure

modes that have been reported in laminates with standard thickness plies - namely extensive delamination initiated from local failure, were not seen in these laminates due to the crack suppression ability of thin ply prepreg. This is aiding the laminate to sustain additional bearing load and allowing more damage accumulation within the laminate before ultimate failure.

7.4 Experimental procedures for double-bolted joints test:

Once the fundamental bearing behaviour of the laminates with a single bolted joint was established, the characterisation was extended to understand the multi-bolted joint response – where multi-bolted joints were loaded in a row. The material and layups remain the same to those used in the single-bolted bearing test.

In the multi-bolted joint tests, the analysis of the laminate becomes more complicated than the case with a single bolt, since the load transfer in such laminates includes bearing load around each individual hole and load that bypasses between each hole. Previous studies showed that the response is affected by several independent parameters such as end distance, plate width, number of bolts, the bolt spacing and the load distribution between the bolts. To start with, a laminate with two bolts was selected to test in a double shear tensile loading to investigate the bearing/bypass interaction response.

The specimen design and test set-up follow the ASTM-D7248 standard. The geometrical drawing and parameter specifications of the specimens are given in Figure 7.13(c). To make a consistent comparison with the open-hole tensile response and bearing behaviour of the laminate with a single-bolted joint, a hole diameter of 3.175 mm has been selected. In addition, the double-bolted joint specimens were cut from the same panels as the bearing test specimens to reduce the variation due to manufacture. The ASTM standard suggests that a width to diameter ratio of 5 and a bolt spacing to diameter ratio of 6 is adequate for the laminate to fail in tension. The edge distance to diameter ratio of the first hole remains the same as those that have been used in the bearing tests. The details of the specimen dimensions for both laminates are presented in Table 7.4.

The specimen was mounted with a double lap joint fixture as illustrated in Figure 7.13(a) and (b), and the two metal loading strips were manufactured from the 316 stainless steel with a thickness of 3 mm. When the bolts are fastened, a 0.5 N.m torque was applied to each bolt by using a torque wrench, as per the bearing tests to maintain a uniform and consistent clamping force among each batch of specimens. The entire fixture along with the specimen was gripped into an Instron hydraulically-actuated testing machine with a tensile loading rate of 0.5 mm/min to allow progressive damage development.

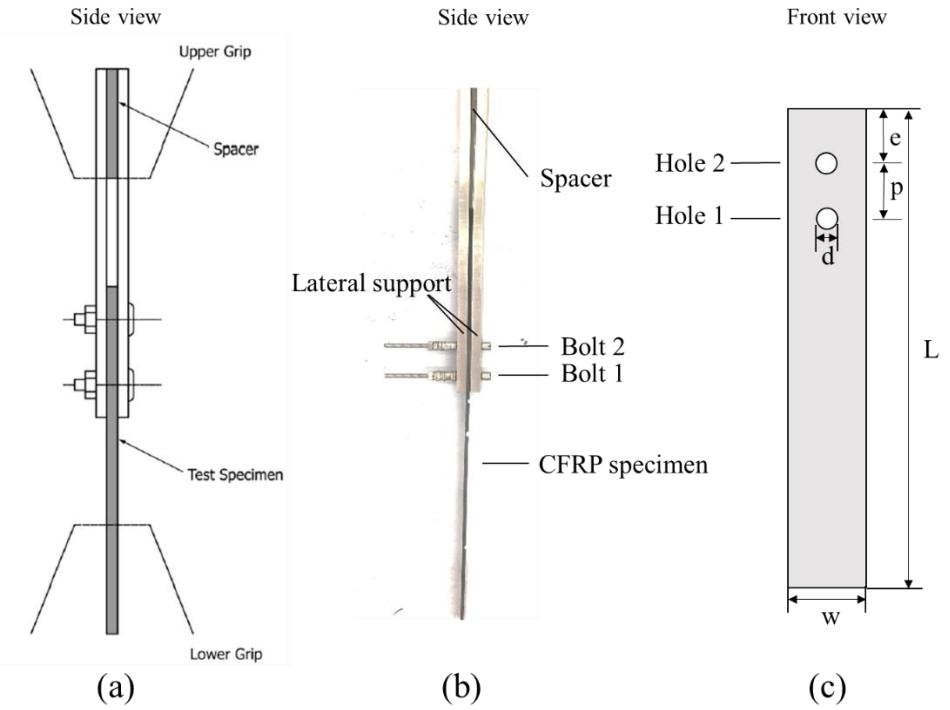

Figure 7.13: (a) Schematic diagram of a fixture assembly for a double-bolted joint test, suggested from ASTM D7248, (b) Photograph illustration of the fixture used in the testing and (c) schematic diagram of a double-bolted joint testing specimen drawing.

According to the standard, bypass stress for all specimens was calculated based on the specimen gross cross-sectional area. Bearing stress in this case was then calculated based on the bolt-specimen contact region – assumed to be the hole diameter by the specimen thickness. Therefore, the expression of ultimate bypass and bearing strength are:

$$\sigma_{bypass} = \frac{(1-k_1)P_{max}}{wt} \quad (7.2)$$

$$\sigma_{bearing} = \frac{k_1 P_{max}}{dt} \quad (7.3)$$

Where k_1 is the proportion of total force transferred through the fastener #1 and it can be calculated in the following equations according to the ASTM D7248 standard:

$$k_1 = \frac{2C_p + C_{F2}}{(2C_p + C_S + C_{F1} + C_{F2})} \quad (7.4)$$

$$k_2 = 1 - k_1 \quad (7.5)$$

$$C_P = \frac{p}{t_P w_P E_{xP}} \quad (7.6)$$

$$C_S = \frac{p}{t_{S1} w_{S1} E_{xS1}} \quad (7.7)$$

$$C_{F1} = \frac{8(2t_{S1}+t_P)(1+v_{F1})}{3\pi E_{F1} d_1^2} + \frac{64\left(8t_{S1}^3 + 16t_{S1}^2 t_P + 8t_{S1}t_P^2 + t_P^3\right)}{192\pi E_{F1} d_1^4} + \frac{2t_{S1}+t_P}{t_{S1}t_P E_{F1}} + \frac{1}{t_{S1}E_{xS1}} + \frac{2}{t_P E_{xP}} \quad (7.8)$$

$$C_{F2} = \frac{8(2t_{S2}+t_P)(1+v_{F2})}{3\pi E_{F2} d_2^2} + \frac{64\left(8t_{S2}^3 + 16t_{S2}^2 t_P + 8t_{S2}t_P^2 + t_P^3\right)}{192\pi E_{F2} d_2^4} + \frac{2t_{S2}+t_P}{t_{S2}t_P E_{F2}} + \frac{1}{t_{S2}E_{xS2}} + \frac{2}{t_P E_{xP}} \quad (7.9)$$

Where k_1, k_2 are proportion of total force transferred through fastener #1 and #2, C_P, C_S, C_F are the flexibilities of test specimen, metal loading strips and fasteners respectively, t_p, t_S are the thickness of test specimen and metal loading strips, w_P, w_S are the width of test specimen and metal loading strips, E_{xP}, E_{xS}, E_F are the modulus of the test specimen, metal loading strips and fasteners, v_F is fastener's Poisson's ratio, p is the distance between fastener centrelines. Subscripts "1" and "2" denote the properties at the position of fastener #1 and #2 respectively. The properties of the metal loading strips and fasteners are presented in Table 7.5. Based on this, k_1 is 0.87 and 0.79 for the TC35-TC35 and MR60-YSH70 specimens respectively. These k_1 values suggested that the majority of load is carried by fastener #1. It is worth noting that these calculated k_1 values are valid to use only in the elastic deformation range before the initial failure.

Table 7.4: Key geometrical parameters for the TC35-TC35 and MR60-YSH70 specimens tested in double-bolted joints.

		TC35-TC35 $[\pm 26_6/0]_s$	MR60-YSH70 $[\pm 25_2/\underline{0}]_s$
Fastener diameter, D	[mm]	3.0	3.0
Hole diameter, d	[mm]	3.175	3.175
Thickness, t	[mm]	1.35	1.08
Length, L	[mm]	180	180
Width, w	[mm]	16.0	16.0
Edge distance, e	[mm]	10.5	10.5
Bolt spacing, p	[mm]	21	21

Table 7.5: Loading strip and fastener properties for double-bolted joints tests.

		Properties
Loading strip thickness, t_{S1}, t_{S2}	[mm]	3.0
Loading strip width, w_{S1}, w_{S2}	[mm]	16.0
Loading strip modulus, E_{S1}, E_{S2}	[MPa]	190000
Fastener diameters, d_1, d_2	[mm]	3.0
Fastener modulus, E_{F1}, E_{F2}	[MPa]	190000
Fastener Possion's ratio, υ_{F1}, υ_{F2}		0.28
Fastener centreline distance, p	[mm]	21

7.5 Results and Discussion of multi-bolted joint tests

7.5.1 General behaviour

The applied load is plotted against displacement for all the TC35-TC35 and MR60-YSH70 specimens and is shown in Figure 7.14 and Figure 7.15 respectively.

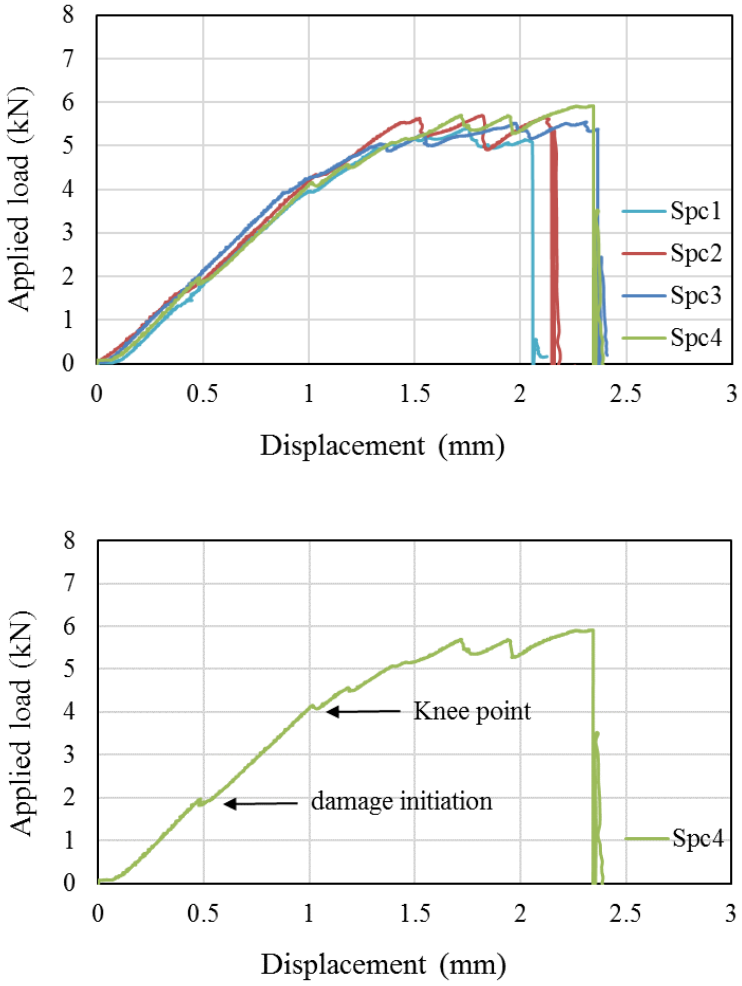

Figure 7.14: Applied load versus displacement curves for the TC35-TC35 laminates with double-bolted joints.

From the load-displacement curve for the TC35-TC35 laminate, the specimen initially deformed linearly, followed by a gradual deformation and failure, with multiple small load drops observed prior to ultimate failure. The slope of the initial part of the curve is similar to the initial slope of single-bolted joint test for the same laminate as presented in Figure 7.3. The initial linear behaviour was assumed to be primarily attributed to the compressive deformation at both the bolt-laminate contact regions. The point at which a small but distinct drop in the load-displacement curve occurs corresponds to an applied load of 1.6 kN (1.4kN at the hole #1), which

is very similar to the first peak load of 1.5 kN in the single bolt joint bearing testing. The bearing damage accumulated within the laminates, resulting in the change of slope.

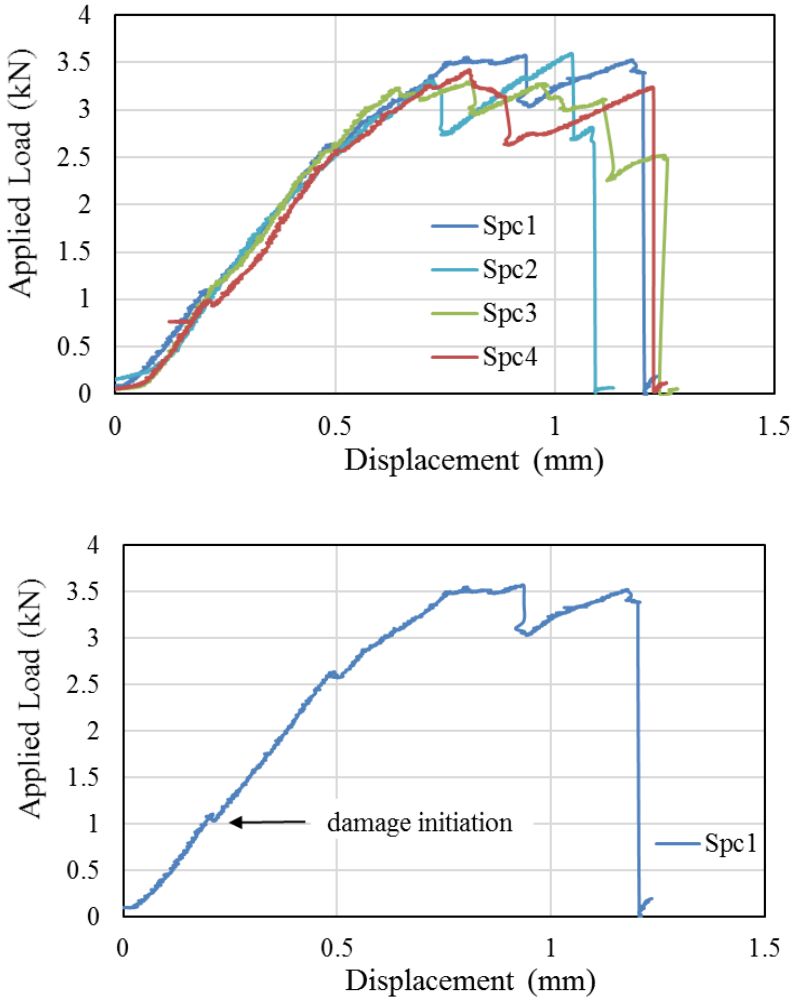

Figure 7.15: Applied load versus displacement curves for the MR60-YSH70 laminates with double-bolted joints.

In the MR60-YSH70 laminate, the major slope reduction of the applied load-displacement curve is seen following the initial linear region. Similarly, the initial slope of the curve is similar to the one in the single-bolted joint as shown in Figure 7.5. The damage initiation is found to be around an applied load of 1.1 kN, which is also close to the applied load at the first peak of 1.1 kN in the single bolted test for

the same laminate. Like in the single bolted joint testing, the gradual failure after the first peak is due to the damage accumulation within the laminate, resulting in the stiffness reduction.

Since damage has initiated in the early stage of loading, the load distribution around the hole and the total force transferred through the two fasteners are expected to change. In the initial stage of testing, the hole #1 carried majority of load according to the factor k_1 values of 0.87 and 0.79. With damage occurring and accumulating at the hole #1, the deformation redistributes the load at the hole #1 whilst the load carried increases at the hole #2. The proportion of the total force transferred through the two fasteners #1 and #2 can be assumed to be equal eventually, and therefore k_1 and k_2 of 0.5 were used in equation (7.2) and (7.3) for calculating bearing and bypass stresses after damage initiation in this case.

Table 7.6. Summary of key results from unnotched tensile, single- and double-bolted joints tests. Pure bearing properties refer to the values obtained from single-bolted joint test. Bearing and bypass stresses at knee point, first peak and ultimate load were calculated using the k_1 of 0.5. The coefficients of variation (CV) for each mechanical property are shown in parentheses.

	TC35-TC35	MR60-YSH70
Bypass stress at ultimate load [MPa]	130 (3.9%)	100 (4.0%)
Bearing stress at knee point [MPa]	463 (9.4%)	382 (7.0%)
Bearing stress at ultimate load [MPa]	659 (3.9%)	501 (4.0%)
Pure bearing stress at first peak [MPa]	432 (2.0%)	368 (4.2%)
Pure bearing strength [MPa]	609 (5.9%)	484 (4.0%)
Unnotched tensile yield stress [MPa]	746 (1.3%)	548 (1.5%)

Table 7.6 lists a summary of bypass and bearing stresses at maximum load from the double-bolted joint testing, pure bearing stresses at first peak and maximum load from single-bolted joint testing and the unnotched "yield" stresses of both laminates. The TC35-TC35 laminate shows higher values in all these properties compared to the MR60-YSH70 laminate. The bearing stresses are higher than the

bypass stresses, suggesting that the results should be dominated by bearing. The bearing stress at the ultimate load is slightly higher than the pure bearing strength. In the single-bolted joint bearing test, the specimen failed in a bearing induced tear-out mode and this failure mode is controlled by the end-distance to hole diameter ratio. In the double-bolted joint test, the end-distance at the hole #1 is larger than the previous case, resulting in a higher bearing stress at failure.

7.5.2 Damage observation

The failure modes were then examined via visual observation of all failed specimens in each batch as shown in Figure 7.16 and Figure 7.17. The visual observation indicates that the primary failure modes are bearing damage at the contact hole edge in both holes, tear-out at the hole #1 and cleavage near both holes. More specifically, the damage mode at the hole #2 (the hole close to the edge) of the TC35-TC35 and MR60-YSH70 specimens is the same bearing damage mode that was observed in the single-bolted bearing test. The damage modes at the hole #1 are slightly different between specimens. Bearing and cleavage have been found to be the main damage modes for the hole #1 of the TC35-TC35 laminate, but one out of four specimens showed net-tension and bearing failure modes. For the hole #1 of the MR60-YSH70 laminate, bearing, tensile damage and cleavage initiated from the tensile damage dominated the failure. Overall, the double-bolted joint test performed in this chapter is a bearing and bearing induced tear-out dominated bearing/bypass test. The applied load was primarily carried by the fastener #1 in the initial stage, and then the two fasteners are believed to have carried similar loads until the hole #2 failed in a bearing induced tear-out. Due to the larger end-distance at the hole #1, the fastener #1 carried further loading until the final failure. A significant amount of cleavage damage in the specimen for both configurations is due to lack of lateral constraint of these particular layups.

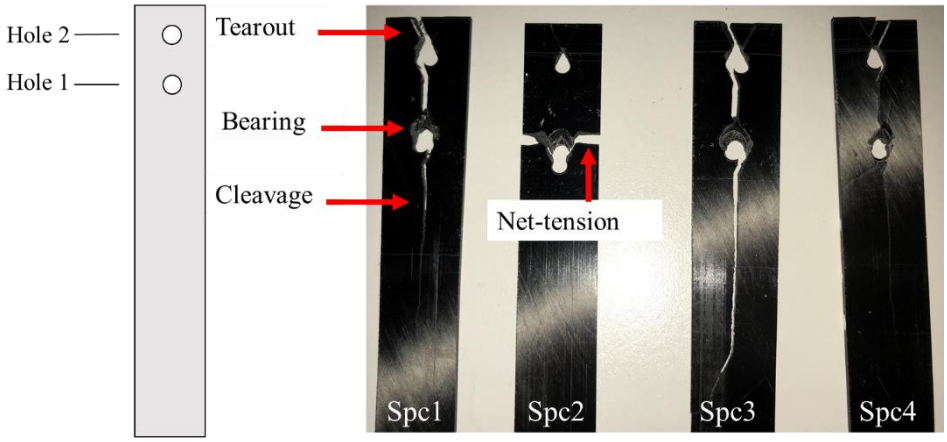

Figure 7.16: Photographs of the surface view of the damaged TC35-TC35 specimens.

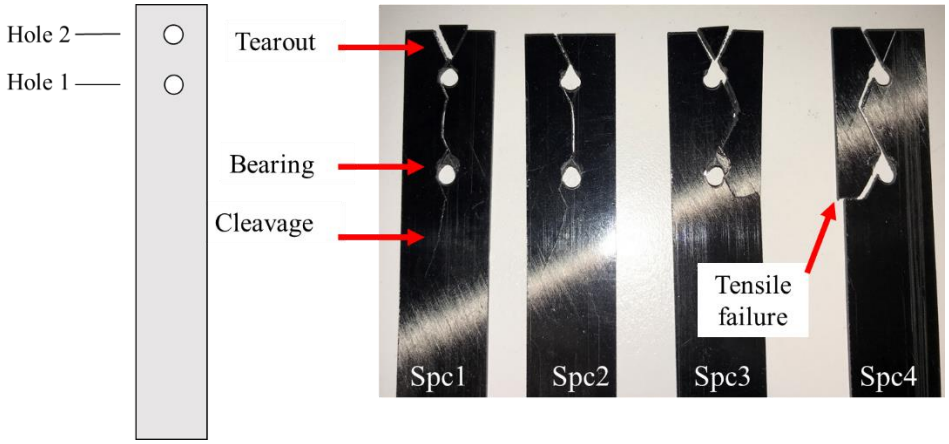

Figure 7.17: Photographs of the surface view of the damaged MR60-YSH70 specimens.

7.5.3 Damage analysis via X-ray

To further aid understanding of the damage development within the double-bolted joint laminates, specimens taken at several positions along the load-displacement curves, were scanned by X-ray using a Nikon XTN320 X-Ray CT inspection machine. As the specimens were immersed in a zinc iodide dye penetrant for at least 24 hours before scanned in X-ray, all the damage within the specimen is shown in bright white in the X-ray images.

Figure 7.18 shows the X-ray images viewed from the in-plane direction for the two TC35-TC35 specimens which were loaded to 1.5 mm and 1.9 mm displacements respectively. The damage around the hole #2 presented in the two top images, is the same as the damage mode of a single bolted laminate under the bearing load. This is not surprising to see due to the edge distance to diameter ratio e/d being the same as the bearing test, and the bearing strength was reached at the current load level. In the hole #1, the damage is different to the hole #2. The damage is observed primarily close to the bolt-laminate contact region and is a crushing type of bearing failure. The damaged region was found to be larger than the region damaged by bearing load around the hole #1 and no tear-out failure is observed due to the bolt spacing to diameter ratio p/d being twice the edge distance to diameter ratio e/d for the hole #2. Due to the bolt spacing, the shear stress in the angle plies was sufficiently reduced at the same applied load and thus tear-out failure is avoided at the hole #1. In addition, at 1.5 mm displacement, a small amount of damage was initiated on both sides of the hole edges. This is very similar to the damage that was seen in the specimen loaded in open-hole tension. When the specimen was further loaded to a displacement of 1.9 mm, the tensile damage propagated to a wider region and joint bearing damage occurred (as shown in white curves parallel to the hole edge).

The damage at the hole #1 has also been analysed via the X-ray images in the through thickness direction and is presented in Figure 7.19 and Figure 7.20. The red and yellow lines in the top left image indicate the directions where these images were taken. The images in the red rectangle present the cross-section view at four different positions from (1) to (4). In the image taken at the position (1) of the centre of the hole, the damage can only be observed in the 0° plies, which is the small amount of tensile fragmentation of the central 0° plies due to the stress concentration at the hole edge. In the image taken at the bearing plane, a large number of shear fractures in the through thickness direction, can be observed, which is the same as the bearing damage that was shown in Figure 7.7 for the same layup. The images in the yellow rectangle indicate the side view of the damaged specimen. At the right hole edge, fragmentation in the central 0° plies and fractures through the thickness can be seen. The damage morphology at the centre of the bearing plane is the same as the bearing damage modes observed at the ultimate bearing stress shown in Figure

7.8. These X-ray images indicate that the damage modes dominating at the hole hole #1 are the bearing damage at the bolt-hole contact region and a small amount of tensile damage. However, the fragmentation in the 0° plies can redistribute the stress around the hole, allowing the laminate to fail in cleavage rather than the typical net-section failure.

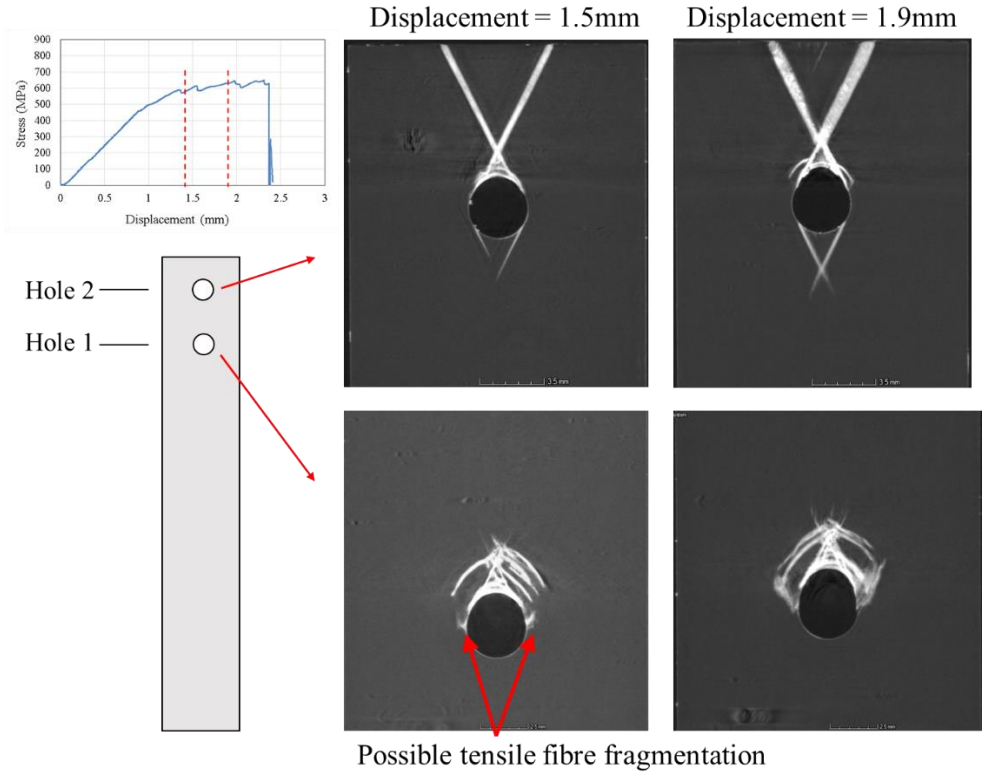

Figure 7.18: X-ray images for the TC35-TC35 laminates with double-bolted joints at two different load levels. All four images were taken at the 0° plies.

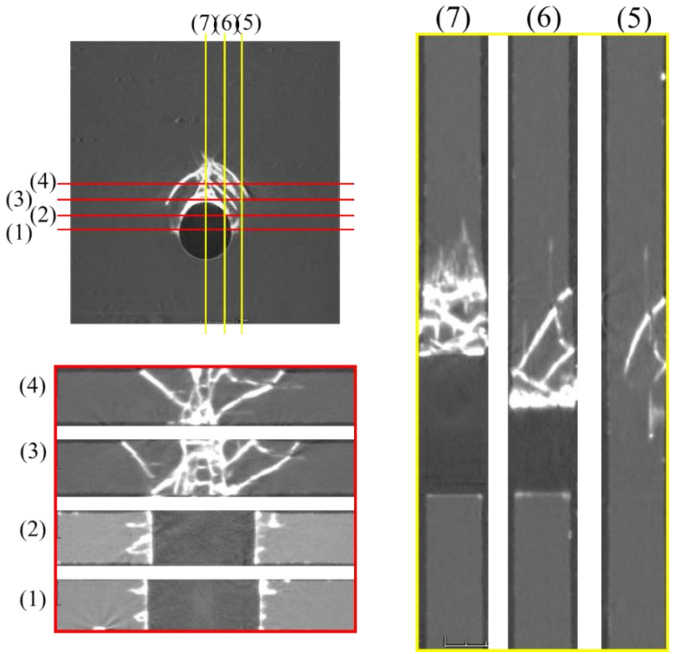

Figure 7.19: Detailed X-ray images for the TC35-TC35 specimen loaded to 1.5 mm displacement. All the images were taken in the through-thickness direction, either viewed from the cross-section or side of the hole #1 of the specimen.

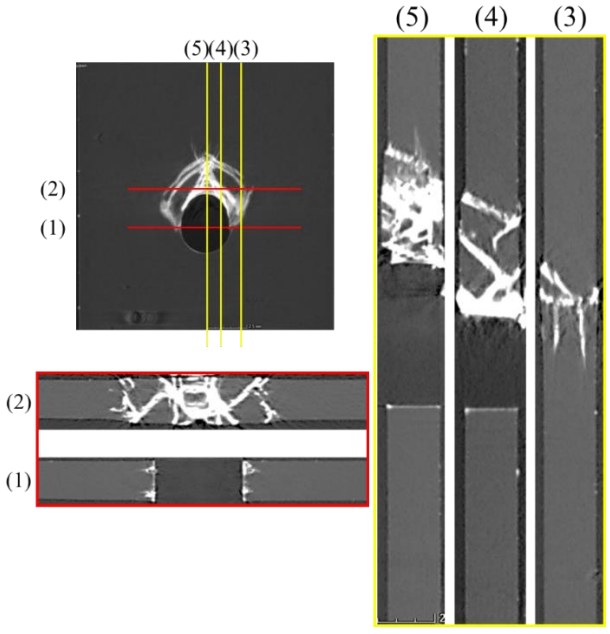

Figure 7.20: Detailed X-ray images for the TC35-TC35 specimen loaded to 1.9 mm displacement. All the images were taken in the through thickness direction, either viewed from the cross-section or side of the hole #1 of the specimen.

Similarly, the X-ray images taken at the two 0° plies for the two MR60-YSH60 specimens loaded to displacements of 0.7 mm and 1.1 mm respectively are presented in Figure 7.21. For the specimen loaded to the displacement of 0.7 mm at the first load drop, damage modes at the hole #2 (the one close to the edge) are the same as the bearing test specimen at its ultimate load. At the hole #1, the damage is primarily around the bearing plane without extended splitting and in-plane kink-bands in the angle plies. When the specimen was loaded to a displacement of 1.1mm, damage can be seen to have grown significantly – a complete fracture was formed from the edge of the hole #2 to the edge of the specimen, extended bearing damage at the hole #1 and cleavage were initiated from the side of the hole #2.

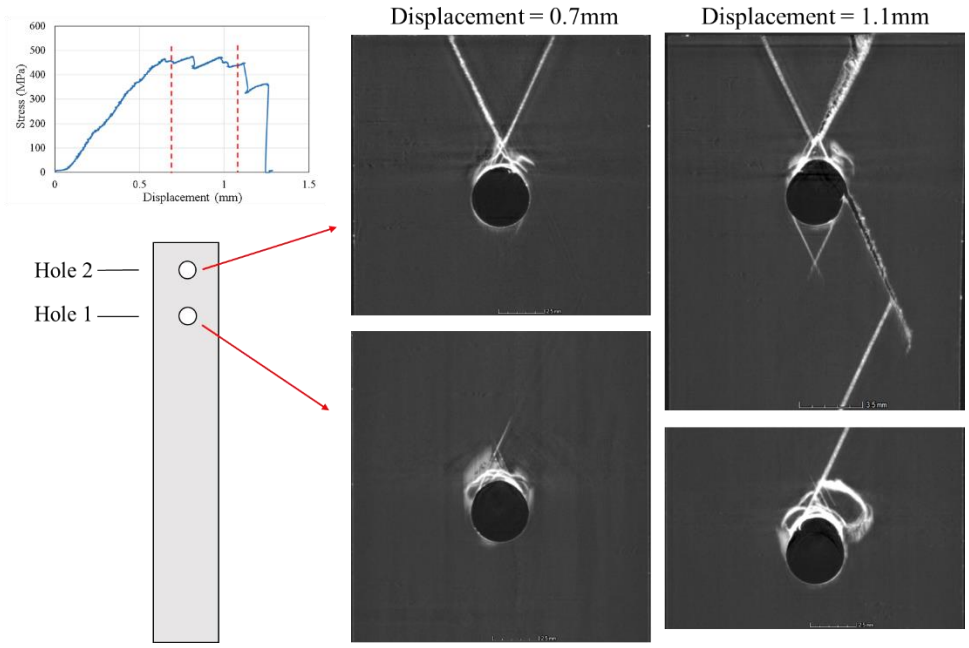

Figure 7.21: X-ray images for the MR60-YSH70 laminates with double-bolted joints at two different load levels. All four images were taken at the 0° plies.

X-ray images of the specimen were taken at several through-thickness positions at the hole #1 are shown in Figure 7.22 and Figure 7.23, from either a cross-section view or side view. At the two side edges of the hole (at the positions (1) and (2)), the damage appears primarily in the 0° plies and can be identified as fragmentation of the 0° plies and possibly localised dispersed delamination at the 0/-

25 interface due to the stress concentration of the hole #1 under tensile loading. In the image taken in the bearing region, the damage modes observed in the single-hole bearing test, included angled fracture through the thickness (shown as the inclined white strips), kink-bands and splitting in the angle plies (shown as the thin straight lines perpendicular to the plies), compressive fragmentation and out-of-plane kink-band in the 0° plies.

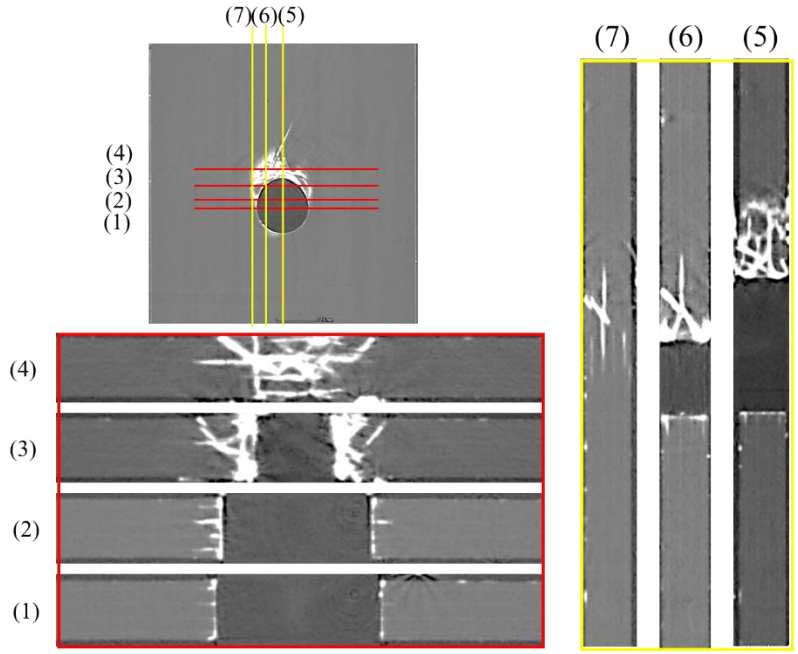

Figure 7.22: Detailed X-ray images for the MR60-YSH70 specimen loaded to 0.7 mm displacement. All the images were taken in the through thickness direction, either viewed from the cross-section or side of the hole #1 of the specimen.

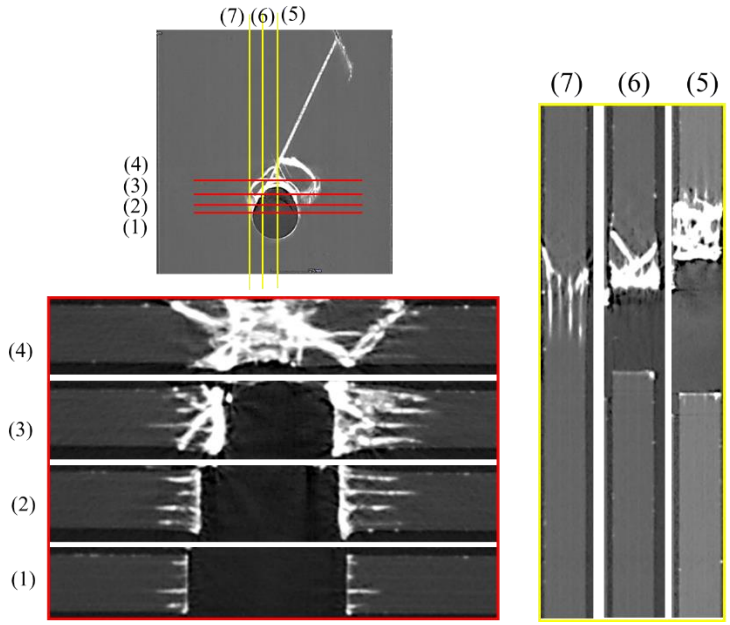

Figure 7.23: Detailed X-ray images for the MR60-YSH70 specimen loaded to 1.1 mm displacement. All the images were taken in the through thickness direction, either viewed from the cross-section or side of the hole #1 of the specimen.

7.6 Conclusions

In this chapter, bearing responses of pseudo-ductile thin ply angle-ply carbon fibre laminates have been investigated by loading the laminates in single- and double-bolted joint configurations in double shear tension. The main objectives were to understand the fundamental bearing behaviour of pseudo-ductile laminates with different materials and layups. The investigation was focused on fixed test parameters such as hole/pin diameter, width-to-hole ratio w/d, edge distance-to-hole ratio e/d, clamping pressure, and hole spacing to diameter p/d in the double-bolted joint test.

Gradual failure in bearing is achieved in both the TC35-TC35 $[\pm 26_6/0]_s$ and MR60-YSH70(Granoc) $[\pm 25_2/\underline{0}]_s$ laminates. Both laminates show elastic deformation in the initial region, then present a gradual reduction in stiffness until the final failure. More specifically, in the first stage, the linear behaviour shown in the bearing stress-displacement curve is primarily attributed to compressive deformation of the laminate at the hole contact edge. With further applied load, the

compressive damage in the central 0° plies within both laminates was initiated, resulting in the first major load drop in the stress-displacement curve. However, due to the crack and delamination suppression ability of thin ply laminates, the damage in the 0° plies – either fibre kinking in the TC35-TC35 laminate or compressive fibre fragmentation in the MR60-YSH70 laminate, does not lead to a catastrophic failure. Instead, with a further increase in applied load, a kink-band propagates in the out-of-plane direction via the adjacent angle plies to allow this gradual failure.

In the double-bolted joint tests, gradual failure was also achieved in both laminate configurations. The bearing stress at the ultimate load is 5% to 8% higher than the pure bearing strength obtained from the equivalent single-bolted joint bearing test. This is due to the larger end-distance at the hole #1 in the double-bolted joint test than in the single-bolted joint test. The bypass stresses at the ultimate load for both configurations are lower than the bearing stresses, suggesting that the tests with present configurations are dominated by bearing and bearing induced tear-out. The damage modes at the hole #2, which is the one closest to the edge of the specimen, are the same as the damage modes of the single-bolted joint laminates. At the hole #1, the damage is primarily at the bolt/laminate contact plane. Eventually the laminate failed in a cleavage type mechanism due to the lack of 90° plies to provide lateral constraint.

8 Conclusions and future work

8.1 Conclusions

This thesis has presented a comprehensive investigation on thin ply angle-ply laminates with central 0° plies subjected to several different load cases including open-hole tension, compression, bending, fatigue loading and bearing/bypass loading. In general, the overall aim of this thesis has been achieved. The behaviour of the laminates in each load case was shown to be significantly dependent on the selection of material and the design of the relevant stacking sequences. The damage suppression as observed in thin ply laminates assures the presence of other failure mechanisms, e.g. fibre fragmentation, which leads to different failure behaviour compared to traditional laminates under given specific load cases. Some key findings of each chapter have been summarised in the following paragraphs.

Chapter 3: Open-hole tensile behaviour of two different laminates: the T300-T300 $[\pm 26_5/0]_s$ and MR60-YSH70 $[\pm 25_2/0]_s$ laminates have been investigated experimentally. Initially, these laminates were tested in unnotched tension and pseudo-ductile tensile stress-strain responses have been demonstrated in both layups. Two different pseudo-ductile strain to "yield" strain ratios have been seen in the two layups, which are 0.86 and 3.02 respectively. When these two laminates were loaded in open-hole tensile loading, 96% of the unnotched "yield" stress has been retained in the MR60-YSH70 laminate, whilst only 63% has been retained in the T300-T300 laminate. Via in-situ and post-failure analysis, significant amounts of 0° ply fragmentation and dispersed delamination have been observed around the hole edge which relieved the stress concentration around the hole in the MR60-YSH70 laminate. This observation suggested that an important factor for the open-hole performance of pseudo-ductile laminates is the strain ratio – if the strain ratio is sufficiently high, full load redistribution could be achieved.

Chapter 4: The thin ply angle-ply laminate with central 0° plies has been tested in compression via a sandwich beam subjected to four-point bending load. Overall, non-linear compressive stress-strain curves and progressive failure have

been achieved in the MR60-M55 $[\pm 27_7/0]_s$ laminate. Common compressive failure modes - fibre kinking and complete delamination at the 0/θ interface were not seen in this laminate. Instead, progressive fibre fractures were promoted, and delamination was successfully suppressed in this specimen. The fragmented fibre length was found to be around half of the critical fibre length, showing the different load transfer mechanism in compression and tension. The final failure of the laminate was due to the combination of high transverse tensile stress and in-plane shear stress within the angle plies in compression. In addition, incorporating the high modulus 0° plies into angle-ply laminates has shown a significant increase in the initial modulus of angle-ply laminates.

Chapter 5: Flexural testing was carried out on pseudo-ductile thin ply angle-ply laminates with two configurations, where the MR60-M55 $[\pm 27_7/0]_s$ laminate showed fibre fragmentation in both tensile and compressive loading, and the TC35-TC35 $[\pm 26_6/0]_s$ laminate showed fibre fragmentation only in tension. Non-linearity in the load-displacement curve, and progressive failure have been successfully demonstrated in the MR60-M55 laminate under flexural loading. Damage was initiated from the compressive side by 0° ply fragmentation, followed by fragmentation on the tensile side. The fragmentation on the tensile side successfully slowed down damage accumulation on the compressive side and achieved a gradual failure in bending. Fragmentation in tension and compression showed the potential of slowing down the damage accumulation, but it has only shown a small effect on the overall load-displacement behaviour.

Chapter 6: Investigations on the fatigue life and damage progression under fatigue loading of pseudo-ductile thin ply angle-ply laminates have been presented. All three types of pristine specimens (TC35-TC35 $[\pm 26_6/0]_s$, MR60-YSH70 $[\pm 25_2/\underline{0}]_s$ and MR60-M55 $[\pm 27_7/0]_s$), have been found able to be safely operated up to 1×10^6 cycles at 80% of each laminate "yield" stress. When overloaded specimens with pre-fractured 0° ply fibres were loaded in cyclic loading, the damage progression in each configuration behaved differently. The MR60-YSH70 laminate has shown only a 5% modulus reduction at 80% stress severity over 200,000 cycles and only a small amount of delamination propagated under cyclic loading. The

TC35-TC35 laminate sustained fatigue load at 80% severity only up to 2,000 cycles and failed by complete delamination at the -26/26 interface. In the MR60-M55 specimen, a less than 10% stiffness reduction has been observed up to 100,000 cycles at 80% stress severity, and the delamination propagated at the 0/-27 interface with different delamination rates at 85% and 90% severities. Due to the energy release rate for the MR60-YSH70 and MR60-M55 laminates at 80% severity being lower than the critical energy release rate, the delamination did not propagate further.

Chapter 7: Bearing of the TC35-TC35 $[\pm 26_6/0]_s$ and MR60-YSH70 $[\pm 25_2/\underline{0}]_s$ laminates have been investigated via loading the laminates in single- and double-bolted joint configurations in double shear tension. Gradual failure in bearing has been achieved in both laminates with an initial elastic deformation and then gradual deformation due to the damage accumulation within the laminates. Compressive damage – fibre microbuckling and fragmentation of the 0° plies has initiated in the laminates and fibre microbuckling propagated in the through-thickness direction through the adjacent plies due to the delamination suppression ability of thin ply laminates, enabling gradual failure. In the double-bolted joint tests, the failure of these pseudo-ductile laminates was dominated by bearing. In both load cases, the damage modes were similar in both laminates, including bearing damage at the bolt-hole contact surface and secondary tear-out damage due to lack of lateral constraint in laminates.

In general, thin ply angle-ply laminates with central 0° plies have shown promising behaviour, including reduced notch-sensitivity, gradual failure and good fatigue performance of damaged specimens. The mechanical behaviour is found to be reliant on a combination of material, layup and angles in angle-ply selections, and there are trade-offs between each mechanical property. For example, in the structure a notch present, laminates with high modulus central plies were found to be a better candidate than those made with standard modulus plies. On the contrary, in applications where strength is more critical, the laminate with standard modulus 0° plies is favourable as it has a high the "yield" strength. This indicates that the design of pseudo-ductile thin ply angle-ply laminates can be flexible and tailored to meet the specific requirements for different applications.

Compared with conventional carbon fibre laminates, thin ply angle ply laminates with central 0° plies lose some stiffness and strength due to the low mechanical properties of angle plies. However, taking into consideration the benefits of additional pseudo-ductile strain and the residual load carrying capacity of these pseudo-ductile materials, reduced safety margins would be required in design than current conventional laminates. Along with the good fatigue performance of pristine and damaged specimens and improved notched-behaviour, the actual load design limit of pseudo-ductile laminates can be very close to the "yield" stress of them, and therefore can improve the structural efficiency of the laminate. In addition, progressive damage and failure can ensure the structure will not fail catastrophically, and any over-loading can be easily visually inspected.

However, there are also some limitations of these pseudo-ductile laminates slowing their use in industrial applications. The first limitation is the high cost of thin ply laminates. As mentioned in chapter 2, many more plies will be required to maintain thickness requirement of the structures, which will increase the total cost of materials and time for layup. This limitation can be potentially minimised by using pre-manufactured pseudo-ductile tape. For instance, the MR60-YSH70 $[\pm 25_2/\underline{0}]_s$ configuration can be made into a prepreg tape to replace conventional UD prepreg, since its modulus is similar to the standard modulus carbon fibre UD prepreg and its total thickness is only 0.25 mm, similar to conventional prepregs. In addition, each sublaminate has a low thickness, enabling it to build up to different thickness required in applications.

Another limitation is the laminates can only be used in the case where the structure is primarily loaded in the longitudinal direction or off-axis load at small angles (less than 10°) due to the lack of 90° plies in these laminates, which is not realistic in many real-world applications. As in these laminates, 90° plies can limit fibre scissoring in angle plies and therefore restrict the development of pseudo-ductility. However, it can be a good candidate for tubular structures, as these pseudo-ductile thin ply angle-ply laminates can withstand longitudinal tension, compression as well as some torsion and shear load. One of the examples is to use as struts in any

pin-jointed truss structure since they usually experienced only in longitudinal tension and compression.

8.2 Recommendations for future work

Several key areas deserve further investigation and are summarised as follows:

- **Open-hole tension and compression:** in the present work, the characterisation has focused on a single hole size of d = 3.175mm. In previous literature on the hole size effect, the notched strength of the laminate made from standard thickness plies tends to decrease with the increase of the hole size. However, due to the different damage mechanisms for the reduction of notch sensitivity, the hole size effect observed in conventional laminates is not expected to apply to the pseudo-ductile laminates. With increasing hole size, the damaged area would be expected to increase with further relief of the stress concentration. Therefore, a further investigation on the hole size effect is recommended to verify this hypothesis.

  Similar work would also be worth carrying on open-hole compression. As specimen with thicker plies was shown a higher open-hole compressive strength than the one with thinner plies, due to the local damage e.g. fibre-matrix splitting, in the first one redistributed the stress around the hole. The compressive fibre fragmentation would be expected to redistribute the stress around the hole in the pseudo-ductile laminates in compression.
- **Compressive loading:** Although progressive failure and fibre fragmentation have been achieved in compressive loading, the compressive strength and failure strain were still found to be lower than the tensile properties due to the high transverse tensile stress and in-plane shear stress. It is worth designing and testing pseudo-ductile laminates with angle plies made from prepreg with an enhanced shear property, where increased pseudo-ductility would be expected to be achieved.
- **Flexural loading:** Some degree of non-linearity and progressive failure have been achieved in the MR60-M55 $[\pm 27_7/0]_s$ laminate in flexural loading through fibre fragmentation in the 0° layers on both the compressive and tensile side of

the beam. To achieve an increased non-linearity and pseudo-ductility, two proposed methods could be used. (1) Design the bending specimen to be thicker and to have more sub-laminates (which is 4 for the present design) ensuring the strain gradient between the adjacent two sub-laminates will be reduced and fragmentation in more 0° layers will be introduced. (2) Use standard modulus fibres in the 0° plies on the compressive side of the beam and use fibres with lower strain to failure on the tensile side. The fragmentation would then only be expected on the tensile side, avoiding catastrophic failure on the compressive side of the beam.

- **Bearing:** In bearing tests of either single-bolted or double-bolted composite joint, the specimens failed by a combination of bearing and tear-out due to lack of lateral constraint in these $[\pm\theta_n/0_m]_s$ laminates. This suggests that for the pseudo-ductile thin ply angle-ply laminates, a higher edge distance to hole diameter ratio would be desirable to fully exploit the bearing strength of laminate and it is worth investigating in future work.
- **Other load cases: Indentation and compression after impact (CAI)** are also worth investigating as the behaviour of laminates with "uncontrolled defects" is crucial in real applications. Delamination and intralaminar failure such as matrix cracking and fibre breakage, are found to be the main damage mechanisms in indentation and impact loading. When the pseudo-ductile thin ply angle-ply laminate is subjected to indentation or low-velocity impact, the matrix cracking would expect to be suppressed and delamination would be less compared to conventional laminates. The compression after impact properties of the laminate should be promising too since the inner plies are well-protected by adjacent plies. It is also essential to understand the behaviour of pseudo-ductile thin ply angle-ply laminates under non-standard environmental conditions such as hot-wet condition on a coast in tropical climate or low temperature in the stratosphere. From the present work, pseudo-ductile thin ply angle-ply laminates failed in a matrix dominant mode in many load cases. Therefore, it is also essential to understand their behaviour under different **environmental conditions** such as in hot-wet tropical climate region or in low temperature stratosphere, since the

matrix properties, e.g. glass transition temperature T_g, can be significantly affected by the hydrothermal conditions.

9 Bibliography

[1] Wu X, Fuller JD, Longana ML, Wisnom MR. Reduced notch sensitivity in pseudo-ductile CFRP thin ply angle-ply laminates with central 0° plies. Compos Part A Appl Sci Manuf 2018;111. doi:10.1016/j.compositesa.2018.05.011.

[2] Wu X, Fuller JD, Wisnom MR. Open-hole response of pseudo-ductile thin-ply angle-ply laminates. In: Procedding of the 17th European Conference on Composites Materials., Munich, Germany, 26-30th June, 2016.

[3] Wu X, Fuller JD, Wisnom MR. Combining the non-linearity of angle-plies and fibre fragmentation in carbon fibre laminates under compressive loading. In: Procedding of the 21st International Conference on Composites Materials., Xi'an, China, 20-35th August, 2017.

[4] Wu X, Fotouhi M, Fuller JD, Wisnom MR. Bearing Failure of Pseudo-Ductile Thin Ply Angle-Ply Laminates. In: Procedding of the 18th European Conference on Composites Materials., Athens, Greece, 25-28th June, 2018.

[5] Hale J. Boeing 787 from the Ground Up. Boeing Aero Mag, 2006:17–23.

[6] Airbus Group. A350 XWB Family aircraft, http://www.airbus.com/aircraft/passenger–aircraft/. Accessed on [18/09/2018]

[7] Foust J. SpaceX's Mars plans call for massive 42-engine reusable rocket. SpaceNews 2016. http://spacenews.com/spacex-unveils-mars-mission-plans/. Accessed on [18/09/2018].

[8] EPSRC. High Performance Ductile Composite Technology (HiPerDuCT) 2011. http://gow.epsrc.ac.uk/NGBOViewGrant.aspx?GrantRef=EP/I02946X/1.

[9] High Performance Ductile Composite Technology (HiPerDuCT)

http://hiperduct.ac.uk/. Accessed on [18/09/2018].

[10] Fuller J, Wisnom M. Pseudo-ductility and damage suppression of thin ply CFRP angle-ply laminates. Compos Part A Appl Sci Manuf 2015;69:64–71. doi:10.1016/j.compositesa.2014.11.004.

[11] Fuller JD, Jalalvand M, Wisnom MR. Combining fibre rotation and fragmentation to achieve pseudo-ductile CFRP laminates. Compos Struct 2016;142:155–66. doi:10.1016/j.compstruct.2016.01.073.

[12] Fuller JD, Wisnom MR. Exploration of the potential for pseudo-ductility in thin ply CFRP angle-ply laminates via an analytical method. Compos Sci Technol 2015;112:8–15. doi:10.1016/j.compscitech.2015.02.019.

[13] Czél G, Wisnom MR. Demonstration of pseudo-ductility in high performance glass/epoxy composites by hybridisation with thin-ply carbon prepreg. Compos Part A Appl Sci Manuf 2013;52:23–30. doi:10.1016/j.compositesa.2013.04.006.

[14] Czél G, Jalalvand M, Wisnom MR. Design and characterisation of advanced pseudo-ductile unidirectional thin-ply carbon/epoxy-glass/epoxy hybrid composites. Compos Struct 2016;143:362–70. doi:10.1016/j.compstruct.2016.02.010.

[15] Czél G, Jalalvand M, Wisnom MR. Hybrid specimens eliminating stress concentrations in tensile and compressive testing of unidirectional composites. Compos Part A Appl Sci Manuf 2016;91:436–41. doi:10.1016/j.compositesa.2016.07.021.

[16] Jalalvand M, Czél G, Wisnom MR. Parametric study of failure mechanisms and optimal configurations of pseudo-ductile thin-ply UD hybrid composites. Compos Part A Appl Sci Manuf 2015;74:123–31. doi:10.1016/j.compositesa.2015.04.001.

[17] Jalalvand M, Czél G, Wisnom MR. Numerical modelling of the damage modes in UD thin carbon/glass hybrid laminates. Compos Sci Technol 2014;94:39–47. doi:10.1016/j.compscitech.2014.01.013.

[18] Jalalvand M, Czél G, Wisnom MR. Damage analysis of pseudo-ductile thin-ply UD hybrid composites - a new analytical method. Compos Part A Appl Sci Manuf 2015;69:83–93. doi:10.1016/j.compositesa.2014.11.006.

[19] Wisnom MR, Czél G, Swolfs Y, Jalalvand M, Gorbatikh L, Verpoest I. Hybrid effects in thin ply carbon/glass unidirectional laminates: Accurate experimental determination and prediction. Compos Part A Appl Sci Manuf 2016;88:131–9. doi:10.1016/j.compositesa.2016.04.014.

[20] Wisnom MR. Mechanisms to create high performance pseudo-ductile composites. IOP Conf Ser Mater Sci Eng 2016;139:012010. doi:10.1088/1757-899X/139/1/012010.

[21] Yu H, Potter KD, Wisnom MR. A novel manufacturing method for aligned discontinuous fibre composites (High Performance-Discontinuous Fibre method). Compos Part A Appl Sci Manuf 2014;65:175–85. doi:10.1016/j.compositesa.2014.06.005.

[22] Yu H, Longana ML, Jalalvand M, Wisnom MR, Potter KD. Pseudo-ductility in intermingled carbon/glass hybrid composites with highly aligned discontinuous fibres. Compos Part A Appl Sci Manuf 2015;73:35–44. doi:10.1016/j.compositesa.2015.02.014.

[23] Longana ML, Yu HN, Jalavand M, Wisnom MR, Potter KD. Aligned discontinuous intermingled reclaimed/virgin carbon fibre composites for high performance and pseudo-ductile behaviour in interlaminated carbon-glass hybrids. Compos Sci Technol 2017;143:13–21. doi:10.1016/j.compscitech.2017.02.028.

[24] Bunsell AR, Harris B. Hybrid carbon and glass fibre composites. Composites 1974;5:157–64. doi:10.1016/0010-4361(74)90107-4.

[25] Swolfs Y, Gorbatikh L, Verpoest I. Fibre hybridisation in polymer composites: A review. Compos Part A Appl Sci Manuf 2014;67:181–200. doi:10.1016/j.compositesa.2014.08.027.

[26] Aveston J, Kelly A. Tensile First Cracking Strain and Strength of Hybrid

Composites and Laminates. Philos Trans R Soc A Math Phys Eng Sci 1980;294:519–34. doi:10.1098/rsta.1980.0061.

[27] Manders PW, Bader MG. The strength of hybrid glass/carbon fibre composites - Part 2 A statistical model. J Mater Sci 1981;16:2246–56. doi:10.1007/BF00542387.

[28] Jalalvand M, Czél G, Wisnom MR. Reducing the Notch Sensitivity of Quasi-Isotropic Layups using Thin-Ply Hybrid Laminates. In: Proceedings of the 30th Annual Technical Conference of the American Society for Composites 2015. East Lansing, Michigan, USA, 28-30th September; 2015

[29] Fotouhi M, Suwarta P, Jalalvand M, Czel G, Wisnom MR. Detection of fibre fracture and ply fragmentation in thin-ply UD carbon/glass hybrid laminates using acoustic emission. Compos Part A Appl Sci Manuf 2016;86:66–76. doi:10.1016/j.compositesa.2016.04.003.

[30] Fuller JD, Wisnom MR. Ductility and pseudo-ductility of thin ply angle-ply CFRP laminates under quasi-static cyclic loading. Compos Part A Appl Sci Manuf 2018;107:31–8. doi:10.1016/j.compositesa.2017.12.020.

[31] Wisnom MR. The effect of fibre rotation in ±45° tension tests on measured shear properties. Composites 1995;26:25–32. doi:10.1016/0010-4361(94)P3626-C.

[32] Herakovich CT, Schroedter RD, Gasser A, Guitard L. Damage evolution in $[\pm 45]_s$ laminates with fiber rotation. Compos Sci Technol 2000;60:2781–9. doi:10.1016/S0266-3538(00)00091-9.

[33] Xu X, Wisnom MR. An experimental and numerical investigation of the interaction between splits and edge delaminations in $[+20_m/-20_m]_{ns}$ carbon epoxy laminates. In: Procedding of the 15th European Conference on Composites Materials., Venice , Italy, 24-28th June, 2012.

[34] Ogihara S, Kobayashi S, Reifsnider KL. Characterization of nonlinear behavior of carbon/epoxy unidirectional and angle-ply laminates. Adv Compos Mater Off J Japan Soc Compos Mater 2003;11:239–54.

doi:10.1163/156855102762506281.

[35] Wang SD, Palo L. Initiation and growth of transverse cracks and edge delamination in composites laminates: Part 1. an energy method. J Compos Mater Suppl 1980;14:71–87.

[36] Crossman FW, Warren WJ, Wang ASD, Law GE. Initiation and Growth of Transverse Cracks and Edge Delamination in Composite Laminates Part 2. Experimental correlation. J Compos Mater 1980;14:88–108. doi:10.1177/002199838001400106.

[37] Sasayama H, Kawabe K, Tomoda S, Ohsawa I, Kageyama K, Ogata N. Effect of lamina thickness on first ply failure in multidirectionally laminated composites. J Japan Soc Compos Mater 2004;30:142–8. doi:10.1024/0301-1526.32.1.54.

[38] Saito H, Morita M, Kawabe K, Kanesaki M, Takeuchi H, Tanaka M, et al. Effect of ply-thickness on impact damage morphology in CFRP laminates. J Reinf Plast Compos 2011;30:1097–106. doi:10.1177/0731684411416532.

[39] Herakovich CT. Influence of layer thickness on the strength of angle-ply laminates. J Compos Mater 1982;16:216–27.

[40] Kim K, Hong C. Delamination growth in angle-ply laminated composites. J Compos Mater 1986;20:423–37.

[41] Kawabe K, Tomoda S, Matsuo T. Technology for Spreading Tow and its Application to Composite Materials. Part 1. A New Pneumatic Method for Spreading Carbon Tow. J Text Mach Soc Japan 1997;50:68–75.

[42] Kawabe K. New Spreading Technology for Carbon Fiber Tow and Its Application to Composite Materials. Fiber 2008;64:P.262 – P.267. doi:10.2115/fiber.64.P_262.

[43] Amacher R, Cugnoni J, Botsis J, Sorensen L, Smith W, Dransfeld C. Thin ply composites: Experimental characterization and modeling of size-effects. Compos Sci Technol 2014;101:121–32.

doi:10.1016/j.compscitech.2014.06.027.

[44] Arteiro A., Catalanotti G, Xavier J, Camanho PP. Large damage capability of non-crimp fabric thin-ply laminates. Compos Part A Appl Sci Manuf 2014;63:110–22. doi:10.1016/j.compositesa.2014.04.002.

[45] Arteiro A, Catalanotti G, Xavier J, Camanho PP. Notched response of non-crimp fabric thin-ply laminates. Compos Sci Technol 2013;79:97–114. doi:10.1016/j.compscitech.2013.02.001..

[46] Furtado C, Arteiro A, Catalanotti G, Xavier J, Camanho PP. Selective ply-level hybridisation for improved notched response of composite laminates. Compos Struct 2016;145:1–14. doi:10.1016/j.compstruct.2016.02.050.

[47] Sihn S, Kim RY, Kawabe K, Tsai SW. Experimental studies of thin-ply laminated composites. Compos Sci Technol 2007;67:996–1008. doi:10.1016/j.compscitech.2006.06.008.

[48] Yokozeki T, Aoki T, Ogasawara T, Ishikawa T. Effects of layup angle and ply thickness on matrix crack interaction in contiguous plies of composite laminates. Compos Part A Appl Sci Manuf 2005;36:1229–35. doi:10.1016/j.compositesa.2005.02.002.

[49] Yokozeki T, Aoki Y, Ogasawara T. Experimental characterization of strength and damage resistance properties of thin-ply carbon fiber/toughened epoxy laminates. Compos Struct 2008;82:382–9. doi:10.1016/j.compstruct.2007.01.015.

[50] Yokozeki T, Kuroda A, Yoshimura A, Ogasawara T, Aoki T. Damage characterization in thin-ply composite laminates under out-of-plane transverse loadings. Compos Struct 2010;93:49–57. doi:10.1016/j.compstruct.2010.06.016.

[51] Arteiro A, Catalanotti G, Xavier J, Linde P, Camanho PP. Effect of tow thickness on the structural response of aerospace-grade spread-tow fabrics. Compos Struct 2017;179:208–23. doi:10.1016/j.compstruct.2017.06.047.

[52] Yamashita S, Sonehara T, Takahashi J, Kawabe K, Murakami T. Effect of thin-ply on damage behaviour of continuous and discontinuous carbon fibre reinforced thermoplastics subjected to simulated lightning strike. Compos Part A Appl Sci Manuf 2017;95:132–40. doi:10.1016/j.compositesa.2017.01.010.

[53] Amacher R, Cugnoni J, Brunner J, Kramer E, Dransfeld C, Smith W, et al. Toward Aerospace Grade Thin-Ply Composites. In: Proceeding of the 17th European Conference on Composites Material, Munich, Germany, 26-30th June, 2016.

[54] Bullegas G, Pinho ST, Pimenta S. Engineering the translaminar fracture behaviour of thin-ply composites. Compos Sci Technol 2016;131:110–22. doi:10.1016/j.compscitech.2016.06.002.

[55] Frossard G, Cugnoni J, Gmür T, Botsis J. Mode I interlaminar fracture of carbon epoxy laminates: Effects of ply thickness. Compos Part A Appl Sci Manuf 2016;91:1–8. doi:10.1016/j.compositesa.2016.09.009.

[56] Frossard G, Cugnoni J, Gmür T, Botsis J. Ply thickness dependence of the intralaminar fracture in thin-ply carbon-epoxy laminates. Compos Part A Appl Sci Manuf 2018;109:95–104. doi:10.1016/j.compositesa.2018.03.001.

[57] Reinoso J, Arteiro A, Paggi M, Camanho PP. Strength prediction of notched thin ply laminates using finite fracture mechanics and the phase field approach. Compos Sci Technol 2017;150:205–16. doi:10.1016/j.compscitech.2017.07.020.

[58] Sebaey TA, Mahdi E. Using thin-plies to improve the damage resistance and tolerance of aeronautical CFRP composites. Compos Part A Appl Sci Manuf 2016;86:31–8. doi:10.1016/j.compositesa.2016.03.027.

[59] Wagih A, Maimí P, González E V., Blanco N, De Aja JRS, De La Escalera FM, et al. Damage sequence in thin-ply composite laminates under out-of-plane loading. Compos Part A Appl Sci Manuf 2016;87:66–77. doi:10.1016/j.compositesa.2016.04.010.

[60] Arteiro A, Catalanotti G, Melro AR, Linde P, Camanho PP. Micro-mechanical analysis of the in situ effect in polymer composite laminates. Compos Struct 2014;116:827–40. doi:10.1016/j.compstruct.2014.06.014.

[61] Arteiro A, Catalanotti G, Melro AR, Linde P, Camanho PP. Micro-mechanical analysis of the effect of ply thickness on the transverse compressive strength of polymer composites. Compos Part A Appl Sci Manuf 2015;79:127–37. doi:10.1016/j.compositesa.2015.09.015.

[62] Guillamet G, Turon A, Costa J, Linde P. A quick procedure to predict free-edge delamination in thin-ply laminates under tension. Eng Fract Mech 2016;168:28–39. doi:10.1016/j.engfracmech.2016.01.019.

[63] Fuller J. Pseudo-ductility of thin ply angle-ply laminates. University of Bristol, 2015.

[64] Sun CT, Chen JL. A Simple Flow Rule for Characterizing Nonlinear Behavior of Fiber Composites. J Compos Mater 1989;23:1009–20. doi:10.1177/002199838902301004.

[65] Yuan Y, Yao X, Liu B, Yang H, Imtiaz H. Failure modes and strength prediction of thin ply CFRP angle-ply laminates. Compos Struct 2017;176:729–35. doi:10.1016/j.compstruct.2017.06.005.

[66] Fotouhi M, Jalalvand M, Wisnom MR. Notch insensitive orientation-dispersed pseudo-ductile thin-ply carbon/glass hybrid laminates. Compos Part A Appl Sci Manuf 2018;110:29–44. doi:10.1016/j.compositesa.2018.04.012.

[67] Czél G, Rev T, Jalalvand M, Fotouhi M, Longana ML, Nixon-Pearson OJ, et al. Pseudo-ductility and reduced notch sensitivity in multi-directional all-carbon/epoxy thin-ply hybrid composites. Compos Part A Appl Sci Manuf 2018;104:151–64. doi:10.1016/j.compositesa.2017.10.028.

[68] Lagace PA. Notch sensitivity and stacking sequence of laminated composites. In: Proceeding of Comference of Composite Materials: Testing and Design, Philadelphia, USA, 2-4th April, 1984.

[69] Kortschot MT, Beaumont PWR. Damage mechanics of composite materials. IV: The effect of lay-up on damage growth and notched strength. Compos Sci Technol 1991;40:167–79. doi:10.1016/0266-3538(91)90095-7.

[70] Hallett SR, Green BG, Jiang WG, Wisnom MR. An experimental and numerical investigation into the damage mechanisms in notched composites. Compos Part A Appl Sci Manuf 2009;40:613–24. doi:10.1016/j.compositesa.2009.02.021.

[71] Tan SC. Notched Strength Prediction and Design of Laminated Composites Under In-Plane Loadings. J Compos Mater 1987;21:750–80. doi:10.1177/002199838702100804.

[72] Belingardi G, Koricho EG, Beyene AT. Characterization and damage analysis of notched cross-ply and angle-ply fabric GFRP composite material. Compos Struct 2013;102:237–49. doi:10.1016/j.compstruct.2013.03.006.

[73] Hallett SR, Jiang W, Wisnom MR. The Effect of Stacking Sequence on Thickness Scaling of Tests on Open Hole Tensile Composite Specimens. 48th AIAA/ASME/ASCE/AHS/ASC Struct. Struct. Dyn. Mater. Conf., 2007, p. 1–10. doi:10.2514/6.2007-2334.

[74] Potter RT. On the mechanism of tensile fracture in notched fibre reinforced plastics. In: Proceedings of the Royal Society of London. Series A, Mathematical and Physical Sciences, 1st June, 1978, London, UK.

[75] O'Higgins RM, McCarthy MA, McCarthy CT. Comparison of open hole tension characteristics of high strength glass and carbon fibre-reinforced composite materials. Compos Sci Technol 2008;68:2770–8. doi:10.1016/j.compscitech.2008.06.003.

[76] Liu CJ, Sterk JC, Nijhof AHJ, Marissen R. Matrix-dominated damage in notched cross-ply composite laminates: Experimental observations. Appl Compos Mater 2002;9:155–68. doi:10.1023/A:1014705100947.

[77] Liu G, Tang K. Study on stress concentration in notched cross-ply laminates under tensile loading. J Compos Mater 2016;50:283–96.

doi:10.1177/0021998315573802.

[78] Kortschot MT, Beaumont PWR. Damage mechanics of composite materials: I- Measurements of damage and strength. Compos Sci Technol 1990;39:289–301. doi:10.1016/0266-3538(90)90077-I.

[79] Harros CE., Morris DH., Role of Delamination and Damage Development on the Strength of Thick Notched Laminates, Delamination and Debonding of Materials. W S Johnson, Ed, Am Soc Test Mater ASTM STP 876 1985:424–47. doi:10.1520/STP36318S.

[80] Green BG, Wisnom MR, Hallett SR. An experimental investigation into the tensile strength scaling of notched composites. Compos Part A Appl Sci Manuf 2007;38:867–78. doi:10.1016/j.compositesa.2006.07.008.

[81] R. Wisnom M, Chang FK. Modelling of splitting and delamination in notched cross-ply laminates. Compos Sci Technol 2000;60:2849–56. doi:10.1016/S0266-3538(00)00170-6.

[82] Wang W, Zhang W, Liu S, Jin X. Investigation on the behavior of tensile damage evolution in T700/6808 composite based on acoustic emission technology. Shock Vib 2016;2016. doi:10.1155/2016/6364205.

[83] Wisnom MR. The effect of fibre misalignment on the compressive strength of unidirectional carbon fibre/epoxy. Composites 1990;21:403–7. doi:10.1016/0010-4361(90)90438-3.

[84] Budiansky B, Fleck NA. Compressive failure of fibre composites. J Mech Phys Solids 1993;41:183–211. doi:10.1016/0022-5096(93)90068-Q.

[85] Lee J. Measuring the notched compressive strength of composite laminates: Specimen size effects. Compos Sci Technol 2008;68:2359–66. doi:10.1016/j.compscitech.2007.09.003.

[86] Jumahat A, Soutis C, Jones FR, Hodzic A. Fracture mechanisms and failure analysis of carbon fibre/toughened epoxy composites subjected to compressive loading. Compos Struct 2010;92:295–305.

doi:10.1016/j.compstruct.2009.08.010.

[87] Jelf PM, Fleck NA. Compression Failure Mechanisms in Unidirectional Composites. J Compos Mater 1992;26:2706–26. doi:10.1177/002199839202601804.

[88] Frost SR. Compressive Behaviour of Long-Fibre Unidirectional Composites. J Compos Mater 1992;26:1151–72. doi:10.1177/002199839202600804.

[89] Chung I, Weitsman Y. A mechanics model for the compressive response of fiber reinforced composites. Int J Solids Struct 1994;31:2519–36. doi:10.1016/0020-7683(94)90035-3.

[90] Camponeschi ET. Compression of composites materials: a review. Am Soc Test Mater 1991:550–78.

[91] Camanho PP, Mayugo JA. A Micromechanics-Based Damage Model for the Strength Prediction of Composite Laminates. III Eur Conf Comput Mech Solids, Struct Coupled Probl Eng 2006;58:5–8.

[92] Budiansky B, Fleck NA. Compressive Kinking of Fiber Composites: A Topical Review. Appl Mech Rev 1994;47:S246. doi:10.1115/1.3124417.

[93] Wung ECJ, Chatterjee SN. On the Failure Mechanisms in Laminate Compression Specimens and the Measurement of Strengths. J Compos Mater 1992;26:1885–914. doi:10.1177/002199839202601302.

[94] Wisnom MR. Analysis of Shear Instability in Compression Due to Fibre Waviness. J Reinf Plast Compos 1993;12:1171–89. doi:10.1177/073168449301201103.

[95] Wisnom MR. Effect of shear stresses in indirect compression tests of unidirectional carbon fiber/epoxy. AIAA J 1991;29:1692–7. doi:10.2514/3.10792.

[96] Wang B, Uda N, Ono K, Nagai H. Effect of micro in-plane fiber waviness on compressive properties of unidirectional fabric composites. J Compos Mater 2017:002199831774019. doi:10.1177/0021998317740197.

[97] Soutis C. Measurement of the Static Compressive Strength of Carbon-Fiber Epoxy Laminates. Compos Sci Technol 1991;42:373–92. doi:Doi 10.1016/0266-3538(91)90064-V.

[98] Montagnier O, Hochard C. Compression characterization of high-modulus carbon fibers. J Compos Mater 2005;39:35–49. doi:10.1177/0021998305046433.

[99] Rosen BW. Mechanisms of Composite Strengthening. Fibre Compos. Mater., American Society of Metal Seminar; 1965.

[100] Jelf PM, Fleck NA. The failure of composite tubes due to combined compression and torsion. J Mater Sci 1994;29:3080–4. doi:10.1007/BF01117623.

[101] Shuart MJ. Failure of Compression-Loaded Multidirectional Composite Laminates. AIAA J 1989;27:1274–9. doi:10.2514/3.10255.

[102] Teresa SJ De. Effect of an Angle-Ply Orientation ‘ on Compression Strength of Composite Laminates. Mater Res 1999.

[103] Khatibzadeh M. The Strength of Angle-Ply Laminates and Composites with Misaligned Fibres. University of Toronto, 1997.

[104] Kim RY. On the Off-Axis and Angle-Ply Strength of Connposites, Test Methods and Design Alloables for Fibrous Composites, ASTM STP 734, 1981:91–108.

[105] Peel LD, Hyer MW, Shuart MJ. Compression failure of angle-ply laminates. Ninth DoD(NASA)FAA Conf Fibrous Compos Struct Des 1992:185–96.

[106] Berbinau P, Soutis C, Guz IA. Compressive failure of 0° unidirectional carbon-fibre-reinforced plastic (CFRP) laminates by fibre microbuckling. Compos Sci Technol 1999;59:1451–5. doi:10.1016/S0266-3538(98)00181-X.

[107] Kim RY. On the Off-Axis and Angle-Ply Strength of Connposites. Am Soc Test Mater 1981:91–108.

[108] Czél G, Suwarta P, Jalalvand M, Wisnom MR, Building Q, Kingdom U. Investigation of the Compression Performance and Failure Mechanism of Pseudo-Ductile Thin-Ply Hybrid, In: Proceeding of the 18th European Conference on Composites Material, Athens, Greece, 24-28th June, 2018.

[109] Sensmeier MD, Griffin OH Jr, Johnson ER. Static and dynamic large deflection flexural response of Graphite epoxy beams. NASA contractor report 4118, March 1988.

[110] Wisnom MR, Atkinson JW. Reduction in tensile and flexural strength of unidirectional glass fibre-epoxy with increasing specimen size. Compos Struct 1997;38:405–11. doi:10.1016/S0263-8223(97)00075-5.

[111] Wisnom MR. The effect of fiber waviness on the relationship between compressive and flextural strengths of unidirectional composites. J Compos Mater 1993;28:66–76.

[112] ASTM. D 7264 Standard Test Method for Flexural Properties of Polymer Matrix Composite Materials. ASTM Stand 2007;i:1–11. doi:10.1520/D7264.

[113] Davies IJ, Hamada H. Flexural properties of a hybrid polymer matrix composite containing carbon and silicon carbide fibres. Adv Compos Mater 2001;10:77–96. doi:10.1163/15685510152546376.

[114] Wisnom MR. The effect of specimen size on the bending strength of unidirectional carbon fibre-epoxy. Compos Struct 1991;18:47–63. doi:10.1016/0263-8223(91)90013-O.

[115] Jackson KE, Kellas Sotiris, Morton J. Scale Effects in the Response and Failure of Fiber Reinforced Composite Laminates Loaded in Tension and in Flexure, J Compos Mater 1992;2674-2705.

[116] Caminero AM, Rodriguez GP, Munoz V. Effect of stacking sequence on Charpy impact and flexural damage behavior of composite laminates. Compos Struct 2016;136.

[117] Serna Moreno MC, Romero Gutiérrez A, Martínez Vicente JL. First flexural

and interlaminar shear failure in symmetric cross-ply carbon-fibre laminates with different response under tension and compression. Compos Struct 2016;146:62–8. doi:10.1016/j.compstruct.2016.03.003.

[118] Serna Moreno MC, Romero Gutiérrez A, Martínez Vicente JL. Different response under tension and compression of unidirectional carbon fibre laminates in a three-point bending test. Compos Struct 2016;136:706–11. doi:10.1016/j.compstruct.2015.06.017.

[119] Serna Moreno MC, Horta Muñoz S, Romero Gutiérrez A, Rappold C, Martínez Vicente JL, Morales-Rodríguez PA, et al. Pseudo-ductility in flexural testing of symmetric ±45° angle-ply CFRP laminates. Compos Sci Technol 2018;156:8–18. doi:10.1016/j.compscitech.2017.12.015.

[120] Serna Moreno MC, Gutiérrez AR, Vicente JLM. Flexural testing on carbon fibre laminates taking into account their different behaviour under tension and compression. IOP Conf Ser Mater Sci Eng 2016;139. doi:10.1088/1757-899X/139/1/012047.

[121] Jones RM. Apparent Flexural Modulus and Strength of Multimodulus Materials. J Compos Mater 1976;10:342–54. doi:10.1177/002199837601000407.

[122] Kam TY, Sher HF, Nonlinear and First-Ply Failure Analyses of Laminated Composite Cross-Ply Plates. J Compos Mater, 1995;29:463-482 ..

[123] Wisnom MR. Limitations of Linear Elastic Bending Theory Applied to Four Point Bending of Unidirectional Carbon Fibre-Epoxy. In: Proceeding of 31st Structure, Structure Dynamics and Materials Conference 1990. doi:10.2514/6.1990-960

[124] Wisnom MR. Relationship between strength variability and size effect in unidirectional carbon fibre/epoxy. Composites 1991;22:47–52. doi:10.1016/0010-4361(91)90102-M.

[125] Vassilopoulos AP, Keller T. Fatigue of Fiber-reinforced Composites. London, UK: Springer-Verlag; 2011.

[126] Henaff-gardin C, Henaff-gardin R, Mahi E. Influence of the Stacking Sequence on Fatigue Transverse Ply Cracking in Cross-Ply Laminates. Am Soc Test Mater 1992:236–55.

[127] Ogihara S, Takeda N, Kobayashi S, Kobayashi A. Effects of stacking sequence on microscopic fatigue damage development in quasi-isotropic CFRP laminates with interlaminar-toughened layers. Compos Sci Technol 1999;59:1387–98. doi:10.1016/S0266-3538(98)00180-8.

[128] Luterbacher R, Acher R, Trask RS, Bond IP. Static and fatigue tensile properties of cross- ply laminates containing vascules for self- healing applications. Smart Mater Struct 2016;25.

[129] Adam TJ, Horst P. Fatigue damage and fatigue limits of a GFRP angle-ply laminate tested under very high cycle fatigue loading. Int J Fatigue 2017;99:202–14. doi:10.1016/j.ijfatigue.2017.01.045.

[130] Masters JE, Reifsnider KL. An Investigation of Cumulative Damage Development in Graphite/Epoxy Laminates. Am Soc Test Mater 1982:40–62.

[131] Gao F, Boniface L, Ogin SL, Smith PA, Greaves RP. Damage accumulation in woven-fabric CFRP laminates under tensile loading : Part 1 . Observations of damage accumulation. Compos Sci Technol 1999;59:123–36.

[132] Ratwani MM, Kan HP. Effect of Stacking Sequence on Damage Propagation and Failure Modes in Composite Laminates. Am Soc Test Mater 1982:211–28.

[133] Rotem A. Load frequency effect on the fatigue strength of isotropic laminates. Compos Sci Technol 1993;46:129–38. doi:10.1016/0266-3538(93)90168-G.

[134] Eftekhari M, Fatemi A. On the strengthening effect of increasing cycling frequency on fatigue behavior of some polymers and their composites: Experiments and modeling. Int J Fatigue 2016;87:153–66. doi:10.1016/j.ijfatigue.2016.01.014.

[135] Saff CR. Effect of Load Frequency and Lay-Up on Fatigue Life of

Composites. Am Soc Test Mater 1983:78–91.

[136] C.Tsai G, Sun CT, Doyle JF. Frequency Effects on the Fatigue Life and Damage of Graphite / Epoxy Composites Tposite. J Compos Mater 1987;21:2–13.

[137] Schaff JR, Davison BD. Life Prediction Methodology for Composite Structures. Part I—Constant Amplitude and Two-Stress Level Fatigue. J Compos Mater 1997;31:128–57.

[138] Harris CE, Morris DH. An Evaluation of the Effects of Stacking Sequence and thickness on the Fatigue Life of Quasi-lsotropic Graphite/Epoxy Laminates. Am Soc Test Mater 1985:153–72.

[139] Harris B. Fatigue in Composites. Boca Raton: Woodhead Publishing Ltd; 2003.

[140] Miyano Y, Nakada M, Muki R. Applicability of fatigue life prediction method to polymer composites. Mech Time-Dependent Mater 1999;3:141–57. doi:10.1023/A:1009873124095.

[141] Adolfsson E, Gudmundson P. Matrix crack induced stiffness reduction in $[(0_m/90_n/+\theta_p/-\theta_p)_s]_m$ composite laminate. Compos Eng 1995;5:107–23.

[142] Ogin SL, Smith PA, Beaumont PWR. Matrix cracking and stiffness reduction during the fatigue of a $(0/90)_s$ GFRP laminate. Compos Sci Technol 1985;22:23–31. doi:10.1016/0266-3538(85)90088-0.

[143] O'Brien TK. Local Delamination in Laminates with Angle Ply Matrix Cracks , Part II Delamination Fracture Analysis and Fatigue Characterization. ASTM Int 1993:507–37.

[144] O'Brien TK. Characterization of Delamination Onset and Growth in a Composite Laminate. Damage Compos Mater Basic Mech Accumulation, Toler Charact 1982:140–67. doi:10.1520/STP34325S.

[145] Poursartip A, Ashby MF, Beaumont PWR. The fatigue damage mechanics of a carbon fibre composite laminate: I-development of the model. Compos Sci

Technol 1986;25:193–218. doi:10.1016/0266-3538(86)90010-2.

[146] Poursartip A, Ashby MF, Beaumont PW. The fatigue damage mechanics of a carbon fibre composite laminate: II Life prediction. Compos Sci Technol 1986;25:283–99. doi:10.1016/0266-3538(86)90045-X.

[147] Salpekar SA, O'Brien TK, Shivakumar KN. Analysis of Local Delaminations Caused by Angle Ply Matrix Cracks. J Compos Mater 1996;30.

[148] Wisnom MR, Jones MI, Cui W. Delamination in composites with terminating internal plies under tension fatigue loading. ASTM Spec Tech Publ 1995:486–508. doi:10.1520/STP14031S.

[149] Wisnom MR, Jones MI, Cui W. Failure of tapered composites under static and fatigue tension loading. AIAA J 1995;33:911–8. doi:10.2514/3.12510.

[150] Zhang J, Liu F, Zhao L, Zhi J, Zhou L, Fei B. Influence of end distances on the failure of composite bolted joints. J Reinf Plast Compos 2015;34:388–404. doi:10.1177/0731684415572199.

[151] Wang H, Hung C-L, Chang F-K. Bearing failure of bolted composite joints. Part 1: Experimental characterization. J Compos Mater 1996;30:1284–313.

[152] Hamada H, Haruna K, Maekawa Z. Effects of Stacking Sequences on Mechanically Fastened Joint Strength in Quasi-Isotropic Carbon-Epoxy Laminates. J Compos Technol Res 1995;17:249–59.

[153] Park HJ. Effects of stacking sequence and clamping force on the bearing strengths of mechanically fastened joints in composite laminates. Compos Struct 2001;53:213–21. doi:10.1016/S0263-8223(01)00005-8.

[154] Khashaba UA, Sallam HEM, Al-Shorbagy AE, Seif MA. Effect of washer size and tightening torque on the performance of bolted joints in composite structures. Compos Struct 2006;73:310–7. doi:10.1016/j.compstruct.2005.02.004.

[155] Kelly G, Hallström S. Bearing strength of carbon fibre/epoxy laminates: Effects of bolt-hole clearance. Compos Part B Eng 2004;35:331–43.

doi:10.1016/j.compositesb.2003.11.001.

[156] Ataş A, Mohamed GF, Soutis C. Effect of clamping force on the delamination onset and growth in bolted composite laminates. Compos Struct 2012;94:548–52. doi:10.1016/j.compstruct.2011.08.014.

[157] Xiao Y, Ishikawa T. Bearing strength and failure behavior of bolted composite joints (part I: Experimental investigation). Compos Sci Technol 2005;65:1022–31. doi:10.1016/j.compscitech.2005.02.011.

[158] Okuta Baba B. Behavior of pin-loaded laminated composites. Exp Mech 2006;46:589–600. doi:10.1007/s11340-006-8735-z.

[159] Thoppul SD, Finegan J, Gibson RF. Mechanics of mechanically fastened joints in polymer-matrix composite structures - A review. Compos Sci Technol 2009;69:301–29. doi:10.1016/j.compscitech.2008.09.037.

[160] Okutan B, Karakuzu R. The failure strength for pin-loaded multi-directional fiber-glass reinforced epoxy laminate. J Compos Mater 2002;36:2695–712. doi:10.1177/002199802761675502.

[161] Camanho PP, Matthews FL. Stress analysis and strength prediction of mechanically fastened joints in FRP: A review. Compos Part A Appl Sci Manuf 1997;28:529–47. doi:10.1016/S1359-835X(97)00004-3.

[162] Camanho P, Bowron S, Matthews FL. Failure Mechanism Bolted CFRP. J Reinf Plast Compos 1998;17:205–33.

[163] Okutan B, Karakuzu R. The strength of pinned joints in laminated composites. Compos Sci Technol 2003;63:893–905. doi:10.1016/S0266-3538(02)00313-5.

[164] Sola C, Castanié B, Michel L, Lachaud F, Delabie A, Mermoz E. On the role of kinking in the bearing failure of composite laminates. Compos Struct 2016;141:184–93. doi:10.1016/j.compstruct.2016.01.058.

[165] Nanda Kishore A, Malhotra SK, Siva Prasad N. Failure analysis of multi-pin joints in glass fibre/epoxy composite laminates. Compos Struct 2009;91:266–

77. doi:10.1016/j.compstruct.2009.04.043.

[166] Godwin EW, Matthews FL, Kilty PF. Strength of multi-bolt joints in grp. Composites 1982;13:268–72. doi:10.1016/0010-4361(82)90009-X.

[167] Crews JH, Naik RA. Combined bearing and bypass loading on a graphite/epoxy laminate. Compos Struct 1986;6:21–40. doi:10.1016/0263-8223(86)90066-8.

[168] Lawlor VP, McCarthy MA, Stanley WF. An experimental study of bolt-hole clearance effects in double-lap, multi-bolt composite joints. Compos Struct 2005;71:176–90. doi:10.1016/j.compstruct.2004.09.025.

[169] McCarthy CT, McCarthy MA, Lawlor VP. Progressive damage analysis of multi-bolt composite joints with variable bolt-hole clearances. Compos Part B Eng 2005;36:290–305. doi:10.1016/j.compositesb.2004.11.003.

[170] Yun JH, Choi JH, Kweon JH. A study on the strength improvement of the multi-bolted joint. Compos Struct 2014;108:409–16. doi:10.1016/j.compstruct.2013.09.047.

[171] Eriksson I, Bäcklund J, Möller P. Design of multiple-row bolted composite joints under general in-plane loading. Compos Eng 1995;5:1051–68. doi:10.1016/0961-9526(95)00044-N.

[172] Rahman MU, Rowlands RE. Finite element analysis of multiple-bolted joints in orthotropic plates. Comput Struct 1993;46:859–67. doi:10.1016/0045-7949(93)90148-7.

[173] Torayca. T300 Data Sheet 2002:6–7.

[174] PYROFIL™ MR60H 24K Data Sheet 2008.

[175] Nippon Graphite Fiber Corporation. Nippon Granoc Yarn YSH-A Series Data sheet 2010:1–2.

[176] Xu X, Wisnom MR, Chang K, Hallett SR. Unification of strength scaling between unidirectional, quasi-isotropic, and notched carbon/epoxy laminates. Compos Part A Appl Sci Manuf 2016;90:296–305.

doi:10.1016/j.compositesa.2016.07.019.

[177] Berbinau P, Soutis C, Goutas P, Curtis PT. Effect of off-axis ply orientation on 0-fibre microbuckling. Compos Part A Appl Sci Manuf 1999;30:1197–207. doi:10.1016/S1359-835X(99)00026-3.

[178] Chowdhury NT, Wang J, Chiu WK, Yan W. Matrix failure in composite laminates under compressive loading. Compos Part A Appl Sci Manuf 2016;84:103–13. doi:10.1016/j.compositesa.2016.01.007.

[179] Jelf PM, Fleck NA. Compression Failure Mechanisms in Unidirectional Composites. J Compos Mater 1992;26:2706–26. doi:10.1520/STP35345S.

[180] Berbinau P, Soutis C. a Study of 0 °-Fibre Microbuckling in Multidirectional Composite Laminates n.d.

[181] Lee J, Soutis C. Measuring the notched compressive strength of composite laminates: Specimen size effects. Compos Sci Technol 2008;68:2359–66. doi:10.1016/j.compscitech.2007.09.003.

[182] HexTow ® IM7 Datasheet 2016;000:1–2.

[183] ASTM D5467. Standard Test Method for Compressive Properties of Unidirectional Polymer Matrix Composite Materials Using a Sandwich Beam. ASTM Stand 2010;97:1–9. doi:10.1520/D5467.

[184] ASTM D3410M - Standard Test Method for Compressive Properties of Polymer Matrix Composite Materials with Unsupported Gage Section by Shear Loading. Annu B ASTM Stand 2003;15.03:1–16. doi:10.1520/D3410..

[185] Compressive Properties of Rigid Plastics 1. Annu B ASTM Stand 2008;i:1–8. doi:10.1520/D0695-15.2.

[186] Adams D. Current compression test methods. CompositesWorld 2005. https://www.compositesworld.com/articles/current-compression-test-methods [accessed August 24, 2018].

[187] Bitzer T. Honeycomb Technology: Materials, Design, Manufacturing, Applications and Testing. Glasgow: Springer Science Business Media

Dordrecht; 1997.

[188] Hexcel. HexPly ® 8552 - Product Data Sheet - EU Version 2016:1–6.

[189] Fm 73 epoxy film adhesive Datasheet.

[190] Vandreumel WHM, Kamp JLM. Non-Hookean Behavior in Fiber Direction of Carbon-Fiber Composites and Influence of Fiber Waviness on Tensile Properties. J Compos Mater 1977;11:461–9. doi:Doi 10.1177/002199837701100408.

[191] Kumar TVV, Shankar GSS, Shankar BL. Experimental Study on Effect of Stacking Sequence, Clearance and Clamping Torque on Strength of FRP Composite Bolted Joints. Mater Today Proc 2017;4:10746–50. doi:10.1016/j.matpr.2017.08.022.

[192] Stockdale JH, Matthews FL. The effect of clamping pressure on bolt bearing loads in glass fibre-reinforced plastics. Composites 1976;7:34–8. doi:10.1016/0010-4361(76)90279-2.

[193] Rosales-Iriarte F, Fellows NA, Durodola JF. Experimental evaluation of the effect of clamping force and hole clearance on carbon composites subjected to bearing versus bypass loading. Compos Struct 2011;93:1096–102. doi:10.1016/j.compstruct.2010.09.016.